

SWINBURNE UNIVERSITY OF TECHNOLOGY

Faculty of Science, Engineering and Technology

Centre for Astrophysics and Supercomputing



**Scaling relations
between the supermassive black hole mass
and the host spheroid properties**

Giulia A. D. Savorgnan

Presented in fulllment of the requirements
of the degree of Doctor of Philosophy

2016

Abbandona questo mestiere non appena smette di essere un gioco.

Peppo Gavazzi (and, before him, Beppo Occhialini)

Abstract

Supermassive black holes in local galaxies obey a surprisingly large number of scaling laws that involve the black hole mass and various properties of the host spheroid or galaxy. These “black hole mass scaling relations” reveal a strong symbiosis between galaxies and black holes, define important constraints about their co-evolution through the cosmic time, and set the boundary conditions (at $z = 0$) for theoretical models and simulations of galaxy evolution.

Using *Spitzer* observations at $3.6 \mu\text{m}$, which is the best available wavelength band to trace the stellar mass, we performed state-of-the-art structural decompositions for 66 galaxies with a direct measure of their black hole mass, M_{BH} . Thanks to a meticulous inspection of each galaxy’s substructure – by means of photometric and isophotal analysis, unsharp masking, auxiliary information extracted from the literature, and, for the first time, kinematic maps – we were able to identify *a priori* the physical galaxy components. The combination of photometric and kinematic information was crucial to confirm the presence of rotationally supported components in most early-type (elliptical+lenticular) galaxies, and to identify their radial extent (nuclear, intermediate-scale or large-scale discs). Upon performing galaxy decompositions with both one-dimensional (1D) and two-dimensional (2D) parametric techniques, we observed no systematic differences between the results from 1D and 2D methods, but we found more advantages in the former. Our 66 galaxies constitute the largest sample to date for which the following two conditions are satisfied: (*i*) the spheroid structural parameters have been measured accurately and homogeneously; (*ii*) and the black hole mass has been securely estimated with a direct method. This thesis presents updates and modifications to several black hole mass scaling relations, and discusses important implications for galaxy evolution models.

For early-type (elliptical + lenticular) galaxies only, the black hole mass correlates equally well with galaxy luminosity, L_{gal} , and spheroid luminosity, L_{sph} , or spheroid stellar mass, $M_{*,\text{sph}}$. However, when all galaxies (early- and late-type) are considered together, the $M_{\text{BH}} - L_{\text{sph}}$ relation has a lower level of intrinsic scatter than the $M_{\text{BH}} - L_{\text{gal}}$ relation. In the $M_{\text{BH}} - M_{*,\text{sph}}$ diagram, early-type galaxies define a tight linear correlation (a *red sequence*), whereas late-type (spiral) galaxies follow a 2 – 3 times steeper *blue sequence*. The spheroid Sérsic index, n_{sph} , scales with M_{BH} in the same way for early- and late-type galaxies. Black holes that appear to be “overmassive” compared to expectations from the stellar velocity dispersion, σ_* , have been theoretically explained with their host galaxies having experienced more dry mergers than any other galaxy. In spite of that, we present empirical evidence supporting a scenario where the host galaxies of such overmassive black holes have undergone the lowest degree of dry merging. Finally, we debunk claims of four overmassive black holes in the $M_{\text{BH}} - M_{*,\text{sph}}$ diagram by demonstrating that the luminosity of their host spheroids had been considerably underestimated. We show that these four spheroids are unevolved relics of $z = 2$ quiescent compact massive spheroids, and we confer about the significant consequences of this.

Acknowledgements

First thanks go to my supervisor Alister, for offering me a PhD project in the country I always dreamt to live in, for guiding me during this long journey, for his patience and support, for all the lessons I've learnt, and for being constantly available to all of his students, regardless of how many late nights he had to spend in the office correcting my writings. Second thanks go to my co-supervisor Duncan for the constructive scientific conversations that we had, for his useful comments and suggestions, and for his genuine interest in making sure that at any stage everything was going well with me. Very special thanks are reserved to Chris Blake, Duncan, Greg, and Karl, for their invaluable, immediate, unconditionate support when I most than ever needed it.

Declaration

I herewith declare that this thesis contains no material that has been accepted for the award to the candidate of any other degree or diploma. To the best of my knowledge, this thesis contains no material previously published or written by another author, except where due reference is made. The work presented in this thesis has been carried out in the Centre for Astrophysics and Supercomputing at Swinburne University of Technology between September 2012 and April 2016. The content of the chapters listed below has appeared or will appear in refereed journals.

- Chapter 2 has been published as “The supermassive black hole mass – Sérsic index relations for bulges and elliptical galaxies” in 2013, MNRAS, 434, 387, by Giulia A. D. Savorgnan et al.
- Chapter 3 has been published as “Supermassive black holes and their host spheroids I. Disassembling galaxies” in 2016, ApJS, 222, 10, by Giulia A. D. Savorgnan & Alister W. Graham.
- Chapter 4 has been published as “Supermassive black holes and their host spheroids II. The red and blue sequence in the $M_{\text{BH}} - M_{*,\text{sph}}$ diagram” in 2016, ApJ, 817, 21, by Giulia A. D. Savorgnan et al.
- Chapter 5 has been accepted for publication in *The Astrophysical Journal* as “Supermassive black holes and their host spheroids III. The $M_{\text{BH}} - n_{\text{sph}}$ correlation” by Giulia A. D. Savorgnan.
- Chapter 6 has been published as “Overmassive black holes in the $M_{\text{BH}} - \sigma$ diagram do not

belong to over (dry) merged galaxies" in 2015, MNRAS, 446, 2330, by Giulia A. D. Savorgnan & Alister W. Graham.

- Chapter 7 has been published as "Explaining the reportedly over-massive black holes in early-type galaxies with intermediate-scale discs" in 2016, MNRAS, 457, 320, by Giulia A. D. Savorgnan & Alister W. Graham.

I warrant that I have obtained, where necessary, permission from the copyright owners to use any third part copyright material reproduced in the thesis, or to use any of my own published work in which the copyright is held by another party.

Contents

| | | |
|----------|---|------------|
| 1 | Introduction | 3 |
| 1.1 | Supermassive Black Holes | 4 |
| 1.1.1 | Measuring Black Hole Masses | 5 |
| 1.1.2 | Scaling Relations | 8 |
| 1.1.3 | Spheroid | 9 |
| 1.1.4 | Co-evolution and AGN Feedback | 10 |
| 1.1.5 | The Sérsic/Core-Sérsic Paradigm | 11 |
| 1.1.6 | Sérsic and Core-Sérsic Spheroids | 13 |
| 1.1.7 | Origin of Supermassive Black Holes | 15 |
| 1.1.8 | Monster Black Holes | 17 |
| 1.2 | Galaxy Decomposition | 18 |
| 1.2.1 | Photometry and Kinematics | 22 |
| 1.2.2 | A Compendium of the Previous Literature | 24 |
| 1.3 | Thesis Outline | 25 |
| 2 | The Recovery of the $M_{\text{BH}} - n_{\text{sph}}$ Relation | 29 |
| 3 | Galaxy Vivisection | 43 |
| 4 | $M_{\text{BH}} - L_{\text{gal}}$, $M_{\text{BH}} - L_{\text{sph}}$ and $M_{\text{BH}} - M_{*,\text{sph}}$ | 103 |
| 5 | $M_{\text{BH}} - n_{\text{sph}}$ | 117 |

| | | |
|----------|---|------------|
| 6 | Monster Black Holes in Massive Galaxies | 129 |
| 7 | Monster Black Holes in (Compact) Massive Spheroids with Intermediate-Scale Discs | 139 |
| 8 | Final Remarks and Future Perspectives | 149 |
| | Bibliography | 157 |

last print: April 1, 2016

1

Introduction

In the 1790s, John Michell of England and Pierre-Simon Laplace of France independently imagined an “invisible star”, an object whose escape velocity is greater than the speed of light, and they both used Newton’s gravitational laws to calculate the mass and size of such object (Montgomery et al., 2009).

A century ago, in 1915, Albert Einstein completed his General theory of Relativity and submitted to the Prussian Academy of Sciences a seminal paper where he published the full treatment of his “field equations”. Einstein’s theory finally explained the anomalous precession of the perihelion of Mercury, and predicted the deflection of light by means of gravitational fields and the gravitational redshift of light. Albert Einstein willingly embraced these three implications of his theoretical work, and was confident about a timely verification of the last two. However, he never accepted nor demonstrated any interest in another conclusion of General Relativity, i.e. the existence of regions of the space-time where the force of gravity is so strong that not even light can escape. Ironically, while some of his colleagues were fascinated by these exotic, dark objects – first of all the American physicist John Archibald Wheeler, who coined and popularised the term “black hole” – Einstein strongly opposed and fought against the idea of those weird mathematical singularities for all his life (Thorne, 1994). In his 1939 article, Einstein derived the relativistic equations that describe a stationary cluster of particles orbiting on the surface of a sphere. He imagined to gradually reduce the radius of the sphere, forcing the particles to move faster and faster, and demonstrated that the velocity of the particles was reaching the speed of light before the cluster was small enough to become a black hole. Einstein interpreted his calculations as a proof of the fact that black holes cannot exist. He concluded the article writing

"The essential result of this investigation is a clear understanding as to why the Schwarzschild singularities do not exist in physical reality. [...] The Schwarzschild singularity does not appear for the reason that matter cannot be concentrated arbitrarily".

Today, not only their existence is unanimously taken for granted by the scientific community, but black holes are at the centre of some of the most active research fields of astronomy. We know that they come in different flavours and they occupy a wide range of masses, going from the hypothetical, minuscule, primordial black holes (e.g. Carr & Hawking 1974), generated by density fluctuations of matter during the very first moments of the Universe's expansion after the Big Bang, through the well understood stellar black holes (e.g. Shahbaz 1999), remnant products left behind after the death of a massive star, to the so called "massive black holes", occupying the centre of nuclear star clusters and galaxies. Massive black holes are further differentiated into two classes according to their mass: Intermediate Mass Black Holes (within the mass range $100 - 10^5 M_{\odot}$, e.g. Miller & Colbert 2004; van der Marel 2004), still lacking many incontrovertible direct detections (but for which we might accumulate evidence over the next years, e.g. Pasham et al. 2014), and Supermassive Black Holes (e.g. Ferrarese 2006), which are the focus of this thesis.

1.1 Supermassive Black Holes

An astrophysical black hole is a region of the space-time whose escape velocity is greater than the speed of light. Black holes are the simplest objects in the Universe. They are completely characterised by three properties: mass, spin (or angular momentum) and electric charge.

Supermassive black holes (SMBHs) are the most massive black holes known, with typical masses $M_{\text{BH}} \approx 10^6 - 10^9 M_{\odot}$. This class of black holes was first theorised (Lynden-Bell, 1969; Wolfe & Burbidge, 1970) after the discovery of quasars. Quasars can be as luminous as galaxies ($\approx 10^{46} \text{ erg s}^{-1}$). However, their rapid variability ($\approx \text{minutes}$) at high energies implies tiny sizes for these objects ($\approx 10^{-6} \text{ pc}$), even smaller than the Solar System. Small sizes and powerful energy outputs led to the conclusion that accreting SMBHs are the engine of quasars (Salpeter, 1964; Zel'dovich & Novikov, 1964; Lynden-Bell, 1978).

Because quasars were numerous at high redshift, the Universe should be populated with relic black holes (Soltan, 1982). Assuming that the luminosity of quasars is produced by accretion of mass onto the central black hole, Andrzej Soltan calculated a lower limit for the integrated energy density due to quasar light, derived the corresponding value of mass density of accreted material, and showed that, because this mass must be discretely distributed in today's Universe, then most, if not all, nearby galaxies host quiescent black holes in their nuclei, each black hole having a mass in the $10^8 - 10^9 M_{\odot}$ range. This realisation motivated the search of SMBHs at the centre of galaxies, i.e. at the bottom of the potential well, where dynamical friction is expected to drag compact massive objects.

The gravitational potential of a SMBH dominates over the gravitational potential of the host galaxy within the sphere-of-influence radius

$$r_h = \frac{GM_{\text{BH}}}{\sigma_*^2} \approx 0.45 \left(\frac{M_{\text{BH}}}{10^6 M_{\odot}} \right) \left(\frac{100 \text{ km s}^{-1}}{\sigma_*} \right) \text{ pc}, \quad (1.1)$$

where G is the gravitational constant and σ_* is the velocity dispersion of the stars in the host galaxy's bulge. A dynamical detection of a black hole requires the ability to resolve its sphere-of-influence. For local galaxies ($\lesssim 20$ Mpc), it demands a subarcsecond spatial resolution. It is only after the introduction of CCD on spectrographs ('80s) that stellar dynamical detections of black holes became possible (see the references in the reviews by Kormendy & Richstone 1995 and Richstone et al. 1998). The number of dynamical black hole mass measurements has increased with time and it has recently become a statistically meaningful sample with which one can study SMBH demographics. It is now generally accepted that SMBHs reside at the centre of most, if not all, massive galaxies, either quiescent or active.

1.1.1 Measuring Black Hole Masses

Techniques to measure the mass of SMBHs can be divided into two main categories: direct and indirect methods (see Ferrarese & Ford 2005 for a thorough review). In direct methods, the mass of a black hole is determined from its gravitational imprint in the motion of the surrounding stars or gas. The spatial resolution of the observing instrument has to be smaller than the size of the black hole sphere-of-influence, which implies challenging technology and time-consuming observations. In indirect methods, one adopts approximations to the direct methods or uses a parameter of the host galaxy as a proxy to infer the black hole mass on the basis of observed

scaling relations.

Sgr A*, the radio source associated with the Galactic black hole, represents a special case study. Thanks to its proximity (8.28 ± 0.33 kpc, Genzel et al. 2010), near infrared techniques have made possible to resolve and follow each individual star orbiting around Sgr A*. From the analysis of these orbits, Ghez et al. (2008) derived a best-fit central mass of $(4.5 \pm 0.4) \times 10^6 M_{\odot}$.

When measuring black hole masses in gas-poor early-type galaxies, the primary method of choice is based on modelling the integrated kinematics of stars acquired through high spatial resolution spectroscopy. Because to a good approximation the stars in a local galaxy constitute a collisionless system, it is possible to describe their motion analytically and constrain the central gravitational potential. The best-fit model to the observed integrated stellar kinematics returns an estimate of the black hole mass and the stellar mass-to-light ratio, which are treated as free parameters. Although modelling the integrated stellar kinematics can in principle return robust black hole mass estimates, this method is not exempted from systematics and degeneracies, which are mainly caused by our poor ability to resolve the tiny black hole sphere-of-influence even in the most nearby galaxies (Valluri et al., 2004). Gebhardt & Thomas (2009) first explored the effects of including the additional contribution from a dark matter halo when modelling the central stellar kinematics of the galaxy M87. Their measurement of the black hole mass was over a factor of two larger than previous stellar dynamical measurements which did not account for dark matter. Upon deriving 10 new black hole mass measurements from the analysis of two-dimensional stellar kinematics, Rusli et al. (2013) concluded that the omission of dark matter systematically overestimates the stellar mass-to-light ratio and underestimates the black hole mass; this bias does not significantly affect the estimate of the black hole mass only if the spatial resolution of the observations is at least a factor of 10 smaller than the size of the black hole sphere-of-influence. Merritt (2013a) reminds that, among all current black hole mass measurements based on stellar-dynamics, only three cases were carried out with enough spatial resolution to detect a convincing Keplerian rise in the central stellar velocities, as expected from the presence of a central massive object. From this consideration, he raises doubts about the majority of such black hole mass detections, and pessimistically cautions that they should be interpreted as upper limits only.

When water maser clouds are present in an Active Galactic Nucleus (AGN) in the form of a thin disc (with sub-parsec size) rotating around the central engine and heated by the X-ray photons emitted by the AGN accretion disc, the gas dynamics can be studied with radio interferometric techniques (e.g. with the Very Long Baseline Array) and the central gravitational potential constrained, benefiting from a spatial resolution that can be up to ≈ 200 times higher than that allowed by the Hubble Space Telescope (e.g. the black hole mass measurement in the galaxy NGC 4258, Miyoshi et al. 1995). Water masers allow the most accurate mass measurements for SMBHs in galaxies other than the Milky Way.

More than half of massive early-type (elliptical + lenticular) galaxies and virtually all spiral galaxies have detectable warm ionised gas in their nuclei (Ho et al., 1997), whose emission lines are easier to measure than stellar absorption lines. In principle, under the assumption that the ionised gas is distributed in a rotationally-supported Keplerian disc, where the effects of stellar orbital anisotropy, triaxiality or dark matter are negligible, modelling the gas dynamics is conceptually simpler than modelling the integrated stellar kinematics. However, as Kormendy & Ho (2013) pointed out, unlike stars, gas is subject to non-gravitational perturbations (turbulence, shocks, radiation pressure, magnetic fields, etc.), hence its dynamics could be much more complicated than the ordered motion assumed within a Keplerian disc model. Kormendy & Ho (2013) compared the common black hole mass measurements obtained from gas and stellar dynamics for eight galaxies and concluded that the gas-based measurements are systematically underestimated when the modelling of the gas dynamics does not include corrections for large emission-line widths, which are speculated to imply significant random motions of gas perturbed by non-gravitational phenomena, such as radio jets.

Other black hole mass determination methods can be applied to some AGNs and quasars. These techniques rely on fitting accretion disc models to multiwavelength continua spectra (Shields, 1978; Malkan, 1983) or studying the emission line due to iron fluorescence (e.g. Fabian et al. 2000; Reynolds & Nowak 2003). Reverberation mapping (e.g. Peterson 1993) consists of modelling the structure of the broad emission-line region of an AGN, as probed by the short-term variability of the ionising continuum, and estimating the black hole mass by assuming a calibration factor that depends on an observed correlation between the black hole mass and some host

galaxy parameter¹.

Building on past catalogs of direct black hole mass measurements obtained with stellar-kinematics, gas-dynamics, or water maser techniques, Graham & Scott (2013) compiled a sample of ≈ 80 galaxies with a reliable measure of M_{BH} . The galaxy sample used in this work is based on that published by Graham & Scott (2013).

1.1.2 Scaling Relations

Over the last three decades, observations have demonstrated that the black hole mass scales with a number of properties of its host spheroid (see Section 1.1.3 for the meaning of the term “spheroid”), on scales much larger than the black hole sphere-of-influence. The black hole mass has been shown to correlate with the spheroid luminosity L_{sph} (Dressler, 1989; Kormendy & Richstone, 1995), the spheroid stellar velocity dispersion σ_* (Ferrarese & Merritt, 2000; Gebhardt et al., 2000), the spheroid central radial concentration of stars (Graham et al., 2001; Graham & Driver, 2007a), the spheroid dynamical mass $M_{\text{dyn,sph}}$ (Magorrian et al., 1998; Marconi & Hunt, 2003; Häring & Rix, 2004), the spheroid gravitational binding energy (Aller & Richstone, 2007), the spheroid kinetic energy of random motion (Feoli & Mele, 2005; Feoli & Mancini, 2009), the spheroid effective radius (Sani et al., 2011), and the spheroid stellar mass (e.g. Magorrian et al. 1998; Sani et al. 2011; Beifiori et al. 2012; Scott et al. 2013). Other correlations with host galaxy parameters – as opposed to spheroid parameters – have been proposed, such as with the spiral arm pitch angle (Seigar et al., 2008; Berrier et al., 2013), the number of globular clusters (Burkert & Tremaine, 2010; Snyder et al., 2011), the dark matter halo (Ferrarese, 2002) and the velocity dispersion of the globular clusters (Sadoun & Colin, 2012; Pota et al., 2013). Very recently, Läsker et al. (2014b) claimed that the black hole mass correlates equally well with the spheroid and the total galaxy luminosity.

The astrophysical interest in black hole mass scaling relations can be summarised in three points. First, the correlations probe a strong connection between SMBHs and their host spheroids. Exploring how scaling relations have changed throughout the cosmic time could help identify the driving mechanisms of the black hole – galaxy co-evolution. Observations at

¹Typically, this scaling factor is calibrated on the $M_{\text{BH}} - \sigma_*$ relation, i.e. the observed correlation between black hole mass and host spheroid stellar velocity dispersion (e.g. Ferrarese & Merritt 2000; Gebhardt et al. 2000).

$z = 0$ are the most accurate and therefore the most important. Second, *all* of the observed scaling relations must be taken into account by any complete theory or model describing the co-evolution of galaxies and SMBHs². A fundamental, but non-trivial, requirement is that all the correlations have to be consistent with each other. Third, scaling relations can be employed to predict the masses of SMBHs in other galaxies, where a direct measure of M_{BH} would be extremely time consuming or simply impossible due to technological limitations. Many accurate M_{BH} predictions would help derive the local black hole mass function (e.g. Salucci et al. 1999; Graham et al. 2007) and space density (Graham & Driver 2007b and references therein), and aid study of SMBH demographics.

1.1.3 Spheroid

Throughout the text, the term “spheroid” will be used to indicate either a pure elliptical galaxy or the bulge component of a disc galaxy. Obviously, if a galaxy is composed of a relatively flat stellar disc embedded in a triaxial, elliptically-shaped stellar system which dominates the light at large radii (a “discy elliptical”, Michard 1984; Nieto et al. 1988), the term “spheroid” designates the latter component. Providing a self-sufficient definition of a galaxy’s “bulge” is not trivial. In Laurikainen et al. (2016), B. Madore retraces the history of the origin of this term, from its first legitimation as “Galactic bulge”, to the modern, ordinary acceptation that all extragalactic astronomers embrace when they think about lenticular or early-type spiral galaxies. A bulge can be identified photometrically, as the central component rising above the inward extrapolation of the disc’s surface brightness profile, or morphologically, as a 3-dimensional rounded swelling which emerges from the disc plane (best visible in the vast majority of massive, edge-on galaxies, e.g. Kautsch et al. 2006), or also kinematically, by distinguishing a structure with low-angular momentum and higher vertical dispersion at the centre of a high-angular momentum thin disc (e.g. Fabricius et al. 2014). It is common practice to make a distinction between *classical bulges* and *pseudobulges*. Classical bulges are merger-built, pressure-supported systems, whereas pseudobulges are disc-like, rotation-supported systems, originated from secular evolution processes such as disc or bar instabilities (Kormendy, 1982; Kormendy & Kennicutt, 2004).

²Modern semi-analytic models use the observed black hole mass scaling relations to constrain the black hole accretion rate (\dot{M}_{BH}).

1.1.4 Co-evolution and AGN Feedback

The tightness (or small scatter) of the observed black hole mass correlations led to the idea that SMBHs and host galaxies have co-evolved with some sort of self-regulated growth. AGN feedback has been proposed as the process by which this occurs (e.g. Silk & Rees 1998; Fabian 1999; Ostriker & Ciotti 2005; see Fabian 2012 for a review). The AGN is believed to emit intense flux of photons and particles which can sweep the gas from the host spheroid and terminate both star formation and gas accretion onto the black hole. This idea is motivated by the fact that the black hole binding energy ($\propto M_{\text{BH}}c^2$) is much larger than the bulge binding energy ($\propto M_{\text{dyn,sph}}\sigma_*^2$). Therefore, if just a very small percentage of the AGN energy output couples to the gas, all of the gas reservoir can be blown away from the host galaxy. The current picture distinguishes between “quasar mode AGN feedback”, which takes place when the AGN energy output is close to the Eddington limit³ and whose main effect is to blow gas away from the spheroid, and “radio mode AGN feedback”, also known as “maintenance mode”, which injects energy into the interstellar gas and prevents it from cooling.

Although observational evidence is not always clear, the AGN feedback scenario is consistent with some direct observations, such as the X-ray cavities of giant ellipticals, galaxy groups and clusters, thought to be inflated by AGN jets (e.g. McNamara & Nulsen 2012), or the blue-shifted quasar absorption lines, signature of high-velocity winds (e.g. Tombesi et al. 2012), or the ionised gas outflows seen in radio galaxies (e.g. Nesvadba et al. 2006). Many mechanisms, either radiative (through photons) or mechanical (through high-energy particles, winds or jets), can be responsible for AGN feedback, but it has not yet been established which ones are dominating. For each AGN feedback mechanism, theoretical models predict how the black hole mass scales with the host spheroid properties. These predictions can be compared with the observed scalings of the empirical black hole mass correlations to constrain the models and understand which mechanisms are prevailing. Part of the popularity of the AGN feedback scenario resides in its ability to resolve some open questions in galaxy formation. For instance, AGN feedback is invoked to explain the “cooling flow problem”, which states that, in the absence of an energy input, the X-ray halos of the most massive galaxies known, Brightest Cluster Galaxies (BCGs), and galaxy clusters would cool quickly, producing cold gas and associated giant bursts of star

³The Eddington limit is the maximum luminosity at which an object can emit owing to balance between the outward radiation pressure and the inward gravitational force.

formation activity that are not observed in the predicted large amounts (e.g. Ostriker & Ciotti 2005). AGN activity is also believed to quench star formation in high-mass galaxies, explaining why the galaxy mass function (at high masses) drops more quickly than expected from our standard cosmology (e.g. Croton et al. 2006).

An alternative idea to explain the empirical black hole mass correlations without calling into play AGN feedback was explicitly proposed for the first time by Peng (2007), and similar conclusions were reached later by Gaskell (2010), Hirschmann et al. (2010) and Jahnke & Macciò (2011). These studies showed that, starting from a distribution of small progenitor {galaxy – black hole} pairs, regardless of whether or not the initial black hole masses correlate with the initial galaxy masses, and building bigger galaxies through a succession of dry mergers (where galaxy masses and black hole masses add separately), as a consequence of the central limit theorem, after several mergers one obtains a near-linear correlation between black hole mass and galaxy mass, whose scatter decreases with increasing mass. In addition to this, the central limit theorem guarantees that, regardless of the nature of the initial distributions of galaxy and black hole masses, the final distributions converge to Gaussians. However, this scenario does not fit in with the non-linear $M_{\text{BH}} - L_{\text{sph}}$ correlation found by Graham & Scott (2013), as explained in Section 1.1.5.

1.1.5 The Sérsic/Core-Sérsic Paradigm

For many years, the samples of galaxies with a direct measurement of their black hole mass had been dominated by early-type, high-luminosity galaxies, hosting the most massive black holes known. From these samples, the $M_{\text{BH}} - M_{\text{dyn,sph}}$ and $M_{\text{BH}} - L_{\text{sph}}$ log-linear relations had been reported to have an exponent β close to 1 (i.e. $M_{\text{BH}} \propto M_{\text{dyn,sph}}^{\beta \approx 1}$). However, Graham (2012) addressed a crucial inconsistency, that becomes clear when one considers the following points.

- 1) The $L_{\text{sph}} - \sigma_*$ log-linear relation is not described by a single power law. In fact, this correlation has a different slope if one considers only the bright core-Sérsic spheroids ($L_{\text{sph}} \propto \sigma_*^5$) rather than the fainter Sérsic spheroids ($L_{\text{sph}} \propto \sigma_*^2$). Core-Sérsic spheroids display a central deficit of light relative to the inward extrapolation of their outer Sérsic light profile, whereas Sérsic spheroids do not. The different behaviour of their central light

profile is thought to be indicative of distinct formation scenarios (see Section 1.1.6 for a digression on this topic). Davies et al. (1983) and Matković & Guzmán (2005) showed that the change in slope of the $L_{\text{sph}} - \sigma_*$ relation occurs at the B-band absolute magnitude $M_B \approx -20.5$ mag ($\sigma_* \approx 200 \text{ km s}^{-1}$) and corresponds to the division between core-Sérsic and Sérsic spheroids (e.g. Graham & Guzmán 2003).

- 2) The $M_{\text{BH}} - \sigma_*$ relation, instead, does not have a bent nature, being well described by a single power law (Graham, 2012).
- 3) The dynamical mass-to-light ratio scales with the luminosity as $(M/L)_{\text{dyn}} \propto L^{1/4}$ (e.g. Faber et al. 1987).

These three points put together led to the conclusion that the $M_{\text{BH}} - L_{\text{sph}}$ and $M_{\text{BH}} - M_{\text{dyn,sph}}$ log-linear relations could not be fit with a single power law. Core-Sérsic spheroids were expected to follow $M_{\text{BH}} \propto L_{\text{sph}}^{1.0}$ and $M_{\text{BH}} \propto M_{\text{dyn,sph}}^{1.0}$. Sérsic spheroids, instead, were predicted to define a much steeper sequence, having $M_{\text{BH}} \propto L_{\text{sph}}^{2.5}$ and $M_{\text{BH}} \propto M_{\text{dyn,sph}}^{2.0}$. Therefore, the $M_{\text{BH}} - L_{\text{sph}}$ and $M_{\text{BH}} - M_{\text{dyn,sph}}$ log-linear relations should be better described by a broken (or *bent*) power law.

Upon re-analysing the sample of ≈ 30 galaxies presented by Häring & Rix (2004), Graham (2012) derived linear regressions for Sérsic and core-Sérsic spheroids, separately, in the $M_{\text{BH}} - M_{\text{dyn,sph}}$ diagram, and reported on the bent nature of this correlation. The findings of Graham (2012) were later confirmed by Graham & Scott (2013), who expanded the galaxy sample with ≈ 40 additional objects and converted B- and K-band observed, total galaxy magnitudes of disc galaxies into dust-corrected, bulge magnitudes. Rather than do this galaxy by galaxy, which would require careful bulge/disc decompositions, they employed a mean statistical correction based on each object's morphological type and disc inclination. These mean statistical bulge-to-total ratios were derived from the results of two-component (Sérsic-bulge/exponential-disc) models taken from Graham & Worley (2008, and references therein). Graham & Scott (2013) found $M_{\text{BH}} \propto L_{\text{sph}}^{1.10 \pm 0.20}$ for their core-Sérsic subsample and $M_{\text{BH}} \propto L_{\text{sph}}^{2.73 \pm 0.55}$ for their Sérsic subsample (using K-band luminosities). Following Graham & Scott (2013), Scott et al. (2013) converted luminosities into stellar masses and found $M_{\text{BH}} \propto M_{*,\text{sph}}^{0.97 \pm 0.14}$ for core-Sérsic spheroids, and $M_{\text{BH}} \propto M_{*,\text{sph}}^{2.22 \pm 0.58}$ for Sérsic spheroids. More recently, Graham & Scott (2015) compiled a sample of ≈ 140 low-redshift ($z \leq 0.35$, with a median redshift $\langle z \rangle = 0.085$) bulges

hosting AGNs with virial black hole masses $10^5 \lesssim M_{\text{BH}}/\text{M}_{\odot} \lesssim 2 \times 10^6$ (Jiang et al., 2011), and showed that they roughly follow the near-quadratic $M_{\text{BH}} - M_{*,\text{sph}}$ relation defined by their Sérsic bulges.

The physical interpretation that Graham & Scott (2013) and Scott et al. (2013) attributed to the bent nature of the $M_{\text{BH}} - M_{*,\text{sph}}$ relation is the following. Core-Sérsic spheroids follow a near-linear $M_{\text{BH}} - M_{*,\text{sph}}$ relation because these high-mass systems grow mainly through non-dissipative (gas-poor) major merger events, where the progenitor black holes and galaxies are summed together in lock steps. Instead, the (two times) steeper relation for Sérsic galaxies implies that their central black hole must grow more rapidly than their host spheroid. Sérsic galaxies are intermediate-mass galaxies, thought to be built through wet-wet or wet-dry mergers as well as via gas accretion processes which enhance both star formation and AGN activity.

Many of the concepts treated in this and the previous Sections are extensively reviewed in Graham (2016a).

1.1.6 Sérsic and Core-Sérsic Spheroids

The nomenclature *Sérsic/core-Sérsic* was introduced as a consequence of an observed dichotomy in the nature of the central surface brightness profile of stellar spheroids (elliptical galaxies or the bulges of disc galaxies). The surface brightness profile of Sérsic spheroids is well described by the Sérsic (1963, 1968) model all over its radial extent, including the innermost central parsecs. Occasionally, the surface brightness profile of Sérsic spheroids can exhibit a nuclear light excess, due to the contribution of an additional stellar component (e.g. a nuclear star cluster) on top of the stellar spheroid itself. The surface brightness profile of core-Sérsic spheroids is characterised by the presence of a partially depleted core, i.e. a central deficit of stellar light not caused by dust obscuration. Beyond the region affected by the partially depleted core, the surface brightness profile of core-Sérsic spheroids is well approximated by the Sérsic (1963, 1968) model. The core-Sérsic model (Graham et al., 2003; Trujillo et al., 2004) provides an excellent description of the overall surface brightness profile of core-Sérsic spheroids. Core-Sérsic spheroids fall also into the category of “core galaxies”, as given by the Nuker definition (Lauer et al., 2007), although $\approx 20\%$ of “core galaxies” are not core-Sérsic galaxies (Dullo & Graham, 2014), i.e. they

do not have depleted cores. Figure 1.1 illustrates the dichotomy between a Sérsic and a core-Sérsic spheroid. The presence of a partially depleted core is detected in the surface brightness profile of NGC 3348, whereas the best-fit model for NGC 5831 is essentially a pure Sérsic model.

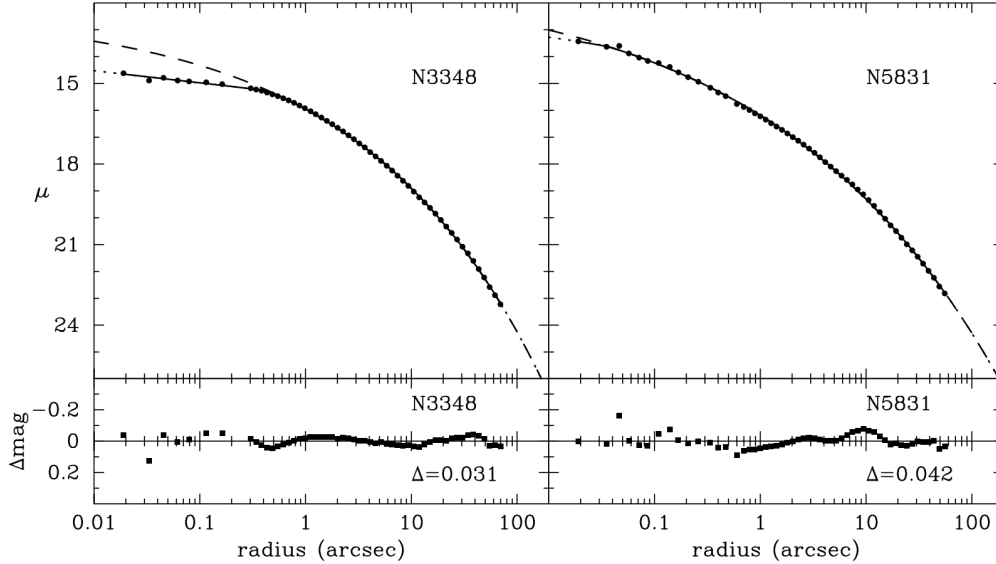


Figure 1.1: The observed major-axis surface brightness radial profiles (μ , in units of mag arcsec^{-2}) of the elliptical galaxies NGC 3348 and NGC 5831 are shown with the black points in the top left and right panels, respectively. The solid lines are fits using the empirical core-Sérsic model, and the dotted extensions are their inner and outer extrapolations. The long dashed lines indicate extrapolations of the outer Sérsic-like part of the core-Sérsic model. The residuals from the fits ($\Delta\mu = \text{data} - \text{model}$) are shown with black squares in the bottom panels, and the rms scatter Δ is given for each fit. This Figure was extracted from Graham et al. (2003).

Partially depleted cores are believed to form during dissipationless (“dry”, i.e. gas-poor) mergers (Begelman et al., 1980), where the progenitor black holes sink towards the centre of the remnant galaxy due to dynamical friction against stars, form a bound pair and further reduce their orbital separation by transferring their binding energy to the surrounding stars via a three-body scattering process also known as “gravitational slingshot” (Milosavljević & Merritt 2001; Merritt 2013b, and references therein). The scouring action of the black hole binary has the effect of lowering the galaxy’s stellar central density, in fact producing a partially depleted core (e.g. Merritt 2006a; Dotti et al. 2012; Colpi 2014). The lack of a significant amount of gas dur-

ing the merger is a necessary condition to guarantee the formation of a partially depleted core. Mayer (2009) and Colpi et al. (2009) followed the simulations of two merging Milky Way-like galaxies and reported that the time-scale for the formation of a close black hole binary system due to dynamical friction against gas is ≈ 100 times shorter than that due to dynamical friction against stars. Therefore, a black hole binary coalesces more quickly in a gas-rich (“wet”) merger than in a gas-poor (“dry”) merger, i.e. when gas is in play, the binary does not have enough time to form a partially depleted core. In addition, gas is likely to be funnelled towards the centre of the galaxy remnant, shock and induce star formation, which would act against the formation of a core by increasing the central stellar density.

1.1.7 Origin of Supermassive Black Holes

As of today, the formation of SMBHs is still an unsolved puzzle. The key astrophysical questions that pertain to this open debate are: (*i*) what are the initial seeds of SMBHs and when did they form? (*ii*) how were these seeds distributed in the early universe (i.e. what is their mass distribution function and space density)? and (*iii*) what is their accretion history throughout the Universe’s first few billion years? Volonteri & Bellovary (2012) review three possible pathways – not mutually exclusive – that have been proposed as viable mechanisms to SMBH seeds formation.

The first of these three theoretical scenarios states that SMBHs originated from the remnants of Population III stars. Population III stars are the (hypothetical) first generation of stars, which formed out of zero-metallicity pristine gas. The lack of metals implies inefficient cooling and inefficient fragmentation of the gas, making possible to produce very massive stars (with initial masses $\gtrsim 100 M_{\odot}$). The fate of Population III stars mainly depends on their initial mass (Heger et al., 2003). A low-metallicity star that initially weights $\approx 25 - 140 M_{\odot}$ is predicted to directly collapse into a black hole with about half of the mass of its progenitor star. Such black hole would not be heavy enough to be dragged by dynamical friction towards the host galaxy centre, therefore it would hardly contribute to the formation of a central SMBH. Between $\approx 140 - 260 M_{\odot}$, low-metallicity stars lie within the pair instability supernova regime, where the final nuclear-powered explosion completely disrupts the star and leaves no remnant. Above $\approx 260 M_{\odot}$, the nucleus of a low-metallicity star is highly unstable and quickly (≈ 2 Myr)

collapses into a black hole that retains at least half of the initial stellar mass. For many years, these high-mass stellar black holes have been considered the most promising SMBH seeds candidates. However, as recent numerical simulations were improved thanks to the achievement of better resolution and the inclusion of more complex physics (e.g. Turk et al. 2009; Greif et al. 2011; Clark et al. 2011; Stacy et al. 2012), it became clear that fragmentation played a more important role in the formation of Population III stars, which turned into less attractive candidates for the origin of SMBHs.

A second possibility for the genesis of SMBH seeds is the formation of a supermassive star (up to $\approx 10^6 M_\odot$) at the centre of a primordial galaxy. In this scenario, low-metallicity, low-angular momentum gas infalls towards the bottom of the potential well of a dark matter halo and, due to gravitational instabilities, does not settle into a rotationally supported disc, but accumulates into a very massive star, whose core rapidly (≈ 1 Myr) collapses into a black hole and swallows the surrounding gas envelope, giving birth to a $\approx 10^3 - 10^6 M_\odot$ SMBH seed.

According to the third theoretical scenario, gas infalls towards the centre of a dark matter halo and fragments into several stars that form a dense stellar cluster. Before the first supernova explosions can occur, small stars collide with each other within the cluster and merge into a massive ($\approx 10^3 M_\odot$) star which eventually collapses into a black hole with similar mass.

The discovery of ultraluminous quasars at $z > 6$ has accentuated the urge to create very massive black hole seeds in a relatively short time (e.g. Alexander & Natarajan 2014; Madau et al. 2014; Lupi et al. 2016). To date, there have been nearly 50 claims of $z > 6$ quasars hosting $\gtrsim 10^9 M_\odot$ black holes (e.g. Fan et al. 2003; Jiang et al. 2007; Mortlock et al. 2011; Bañados et al. 2014; Trakhtenbrot et al. 2015; Wu et al. 2015). Within a Λ CDM cosmology, such early giant monsters could not have formed so quickly without the creation of anomalously massive seeds or incredibly high accretion rates, i.e. exceeding the Eddington limit (but see Melia & McClintonck 2015 for an alternative explanation). However, it is worth noting that these black hole masses are calculated with the reverberation mapping method, assuming that M_{BH} is directly proportional to the virial factor f , which is calibrated on the normalisation of the $z = 0$ observed $M_{\text{BH}} - \sigma_*$ correlation. The existence of (unknown) selection biases in the local sample of directly measured black hole masses would imply a systematic overestimation of the virial factor

and, consequently, of the black hole masses estimated with the reverberation mapping technique.

1.1.8 Monster Black Holes

Over the last five years, several claims of detections of *over-massive* black holes accumulated in the literature. Over-massive black holes are black holes whose mass is significantly larger than what is expected from the galaxy's spheroid stellar velocity dispersion or stellar mass, i.e. they are positive outliers in the $M_{\text{BH}} - \sigma_*$ or $M_{\text{BH}} - M_{*,\text{sph}}$ diagrams.

Using integral-field spectrographs at the Gemini North and Keck 2 telescopes, McConnell et al. (2011) targeted the BCGs (NGC 3842 and NGC 4889) of two massive galaxy clusters, the Leo and Coma clusters (Abell 1367 and Abell 1656, respectively), and reported the direct detection of the two most massive black holes ever found at that time. They claimed that these two black holes are significantly more massive than predicted by the popular $M_{\text{BH}} - \sigma_*$ and $M_{\text{BH}} - L_{\text{sph}}$ correlations, and speculated that the growth of the largest galaxies and their black holes happens by means of evolutionary processes different from what is commonly assumed for less massive elliptical galaxies.

Rusli et al. (2011) obtained SINFONI integral-field unit observations of the nuclear region of the galaxy NGC 1332 and measured a one billion solar masses black hole, consistent with the galaxy's stellar velocity dispersion, but offset from the $M_{\text{BH}} - L_{\text{sph}}$ relation by a full order of magnitude.

van den Bosch et al. (2012) combined archival Hubble Space Telescope (*HST*) high-resolution imaging and long-slit spectroscopy (obtained with the Marcario Low Resolution Spectrograph on the Hobby-Eberly Telescope, Texas) of the nuclear region of the galaxy NGC 1277, and directly measured the central black hole mass by fitting self-consistent Schwarzschild models to the integrated stellar kinematics. They found a twenty billion solar masses black hole, which they estimated to weight 59% of the host spheroid's mass (or 14% of the galaxy's total stellar mass). According to their measurement, the black hole of NGC 1277 was an order of magnitude more massive than what expected from the host spheroid's stellar velocity dispersion and two

orders of magnitude more massive than what expected from the host spheroid's stellar mass. Emsellem (2013) re-analysed van den Bosch et al.'s data and showed that their observations were consistent with a black hole mass up to an order of magnitude smaller than the extraordinary value previously reported. However, Yıldırım et al. (2015) and Scharwächter et al. (2016) confirmed van den Bosch et al.'s measurement.

Bogdán et al. (2012) reported on the unusually high $M_{\text{BH}}/M_{*,\text{sph}}$ ratio for the galaxies NGC 4342 and NGC 4291 and concluded that no co-evolution subsisted between these two galaxies and their black holes. Other reportedly over-massive black holes belong to the galaxies NGC 1271 (Walsh et al., 2015) and Mrk 1216 (Yıldırım et al., 2015).

On the basis of these claims, Ferré-Mateu et al. (2015) theorised that, while most today's massive early-type galaxies have completed their two-phase growth path ("in-situ" and "ex-situ"), the over-massive black holes hosts skipped the second ("ex-situ") phase and therefore represent an exception.

1.2 Galaxy Decomposition

Galaxy decomposition is a parametric analysis that allows one to fit the surface brightness distribution of galaxies using a combination of analytic functions (usually one function per galaxy component, such as spheroid, disc, bar, nucleus, etc.). The 1D (one-dimensional) technique begins with fitting isophotes to the galaxy image. Isophotes are curves along which the intensity of light is constant and they are typically described with concentric ellipses. The 1D surface brightness radial profile is then extracted and modelled with a combination of 1D analytic functions. With the 2D (two-dimensional) technique one fits 2D analytic functions directly to digital images. Galaxy decomposition is useful to perform structural analysis of galaxies and obtain the best-fit parameters of the spheroidal component, such as the luminosity, the half-light radius and the central radial concentration of stars.

Pioneer studies that performed 1D bulge/disc decompositions of galaxies (e.g. Simien & de

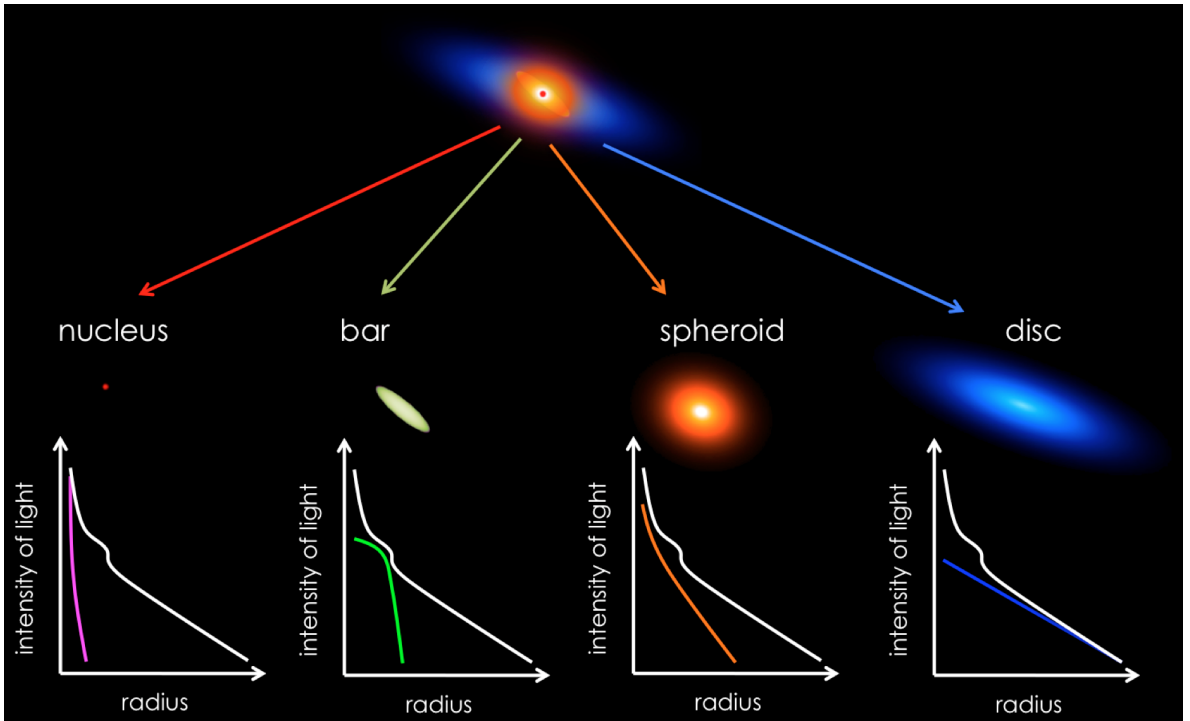


Figure 1.2: Schematic representation of one-dimensional galaxy decomposition. The mock galaxy at the top is composed of a spheroid (orange), a large-scale disc (blue), a bar (green), and a nuclear source (red). The observed surface brightness profile of the galaxy (intensity of light as a function of galactocentric radius) is the white curve. The contribution of each galaxy component to the total surface brightness profile is modelled with one analytic function, illustrated with a solid line of the same colour as the corresponding component. The sum of all analytic functions gives the total galaxy model, which is matched to the observed surface brightness profile.

Vaucouleurs 1986) described the bulge component with a de Vaucouleurs (1948) $R^{1/4}$ profile:

$$\mu_{\text{deVaucouleurs}}(\mu_e, R_e; R) = \mu_e + 8.32678 \left[\left(\frac{R}{R_e} \right)^{1/4} - 1 \right], \quad (1.2)$$

and the disc component with an exponential profile:

$$\mu_{\text{exponential}}(\mu_0, h; R) = \mu_0 + \frac{2.5}{\ln(10)} \left(\frac{R}{h} \right). \quad (1.3)$$

Here μ is the surface brightness profile, R is the projected galactic radius, i.e. the distance of the isophotes from the galaxy centre, R_e is the bulge effective radius (or half-light radius) that encloses half of the total light from the model, μ_e is the bulge surface brightness at the effective

radius, μ_0 is the disc central surface brightness, and h is the disc scale length.

However, it soon became clear to some that the fixed curvature of the two-parameter de Vaucouleurs $R^{1/4}$ law was not adequate to accommodate the variety of shapes observed in the light profiles of stellar spheroidal systems. A more ductile mathematical function was needed such as the three-parameter Sérsic (1963, 1968) $R^{1/n}$ model:

$$\mu_{\text{Sérsic}}(\mu_e, R_e, n; R) = \mu_e + \frac{2.5 b_n}{\ln(10)} \left[\left(\frac{R}{R_e} \right)^{1/n} - 1 \right], \quad (1.4)$$

where the Sérsic index n is the parameter that measures the curvature of the radial light profile, and b_n is a scalar value defined in terms of the Sérsic index (see Graham & Driver 2005 for a valuable compendium). After Caon et al. (1993) and D’Onofrio et al. (1994) demonstrated the superiority of the Sérsic model over the de Vaucouleurs law in describing the spatial distribution of light of early-type galaxies, the varying curvature of the Sérsic model became a necessity also for rendering the light profiles of the bulges of spiral galaxies (Andredakis et al., 1995; Moriondo et al., 1998; Graham & Prieto, 1999; Khosroshahi et al., 2000; Graham et al., 2001).

Thanks to the improved computational speed of machines, 2D fitting algorithms have become more and more popular over the last two decades. de Jong (1996) presented a 2D decomposition technique which allowed one to model the surface photometry of a galaxy using an exponential light profile for both the bulge and the disc. Simard (1998) developed the IRAF⁴ package GIM2D, a 2D decomposition code aimed at distant galaxies. GIM2D takes an input image and simultaneously decomposes all the objects as the sum of a Sérsic and an exponential profile.

A major breakthrough came with GALFIT, a 2D fitting algorithm released by Peng et al. (2002; the nowadays popular GALFIT3, an improved version of the original algorithm, was presented by Peng et al. 2010), which marked an important turning point for the quantitative morphological analysis of galaxies. Thanks to its capability of fitting a galaxy with an arbitrary number of components – chosen from a wide variety of analytical functions such as the Sérsic and the “Nuker” models, or the exponential, Gaussian, and Moffat profiles – and to its optimi-

⁴IRAF is the Image Reduction and Analysis Facility, distributed by the National Optical Astronomy Observatory, which is operated by the Association of Universities for Research in Astronomy (AURA) under cooperative agreement with the National Science Foundation.

sation in computational speed, GALFIT was specifically conceived for modelling large images of spatially well-resolved, nearby galaxies observed with the Hubble Space Telescope.

de Souza et al. (2004) developed BUDDA (Bulge/disc Decomposition Analysis), a code to perform 2D decomposition of galaxies using a two-component Sérsic+exponential model. The number of fitted components was intentionally limited to two (bulge+disc), with the purpose of using the residual images to study the additional substructures such as bars, lenses, rings, and inner discs.

Laurikainen et al. (2005) opted for a hybrid approach, combining the advantages of a 2D decomposition technique with the insight gained from a 1D isophotal analysis. In this exemplary study, the authors modelled the images of 24 early-type disc galaxies (S0/S0a) accounting for bulge, disc, bars, ovals/lenses⁵, and inner discs. Their decomposition method was assessed on synthetic images of galaxies composed of a bulge, a large-scale disc, and a bar. They tested the effects of the omission of the bar component from the galaxy model. While a three-component (bulge+disc+bar) model was correctly recovering the real bulge parameters, a two-component (bulge+disc) model was overestimating the bulge luminosity by up to 40% because the Sérsic model for the bulge was somehow “forced” to account also for the bar. They also experimented with a large number of different weighting maps, and concluded that the results from the fit were not significantly dependent on the choice of the weighting function, unless the signal-to-noise of the galaxy image was extremely low, or a prominent component was not included in the model. In addition, they pointed out that a fit lacking seeing correction resulted in notably biased bulge parameters. Laurikainen et al. (2005) stressed an important point about galaxy decomposition: in order to have control of the physical meaning of the different components in a galaxy, *a priori* evaluation of the existence of such components is required. This concept is opposed to the (nowadays popular) approach of repeating the fit of a galaxy by continuously increasing the number of model components until all residual structures are eliminated from the residual image. Laurikainen et al. (2005) used three different methods to identify the structural

⁵According to their nomenclature, an egg-shaped structure (with axis ratio $b/a \gtrsim 0.85$) embedded within the large-scale disc of a galaxy is dubbed lens or oval in case of a lenticular or spiral galaxy, respectively. Lenses/ovals and pseudobulges might have similar ellipticities, but the former typically have lower surface brightness and sharper outer edges than the latter (Kormendy & Kennicutt, 2004).

components of a galaxy: they inspected (*i*) the radial profiles of ellipticity and position angle of the galaxy's isophotes, whose bumps often correspond to bars, ovals/lenses, and inner discs when these components are sufficiently bright compared to the large-scale disc, (*ii*) the radial profiles of low azimuthal wavenumber Fourier amplitudes and phases, sensitive to weak bars and ovals/lenses, and (*iii*) the unsharp masks⁶, useful to reveal the innermost structures. Upon comparing the results from their three-component decompositions with those obtained from the two-component decompositions of Simien & de Vaucouleurs (1986) in the B-band and de Souza et al. (2004) in the K_S-band, Laurikainen et al. (2005) noted that their bulge-to-total ratios were considerably smaller for all Hubble types. This large discrepancy was not due to the wavelength used, but to the fact that, when a galaxy model does not account for a bar, a large fraction of the bar light erroneously goes into the bulge model, artificially increasing the bulge-to-total ratio. This sophisticated decomposition method was applied to the analysis of 175 early-type disc galaxies using deep near-infrared imaging (Laurikainen et al., 2007, 2010), and the results from these decompositions were used for a detailed study of bars, ovals/lenses and bulges. They found ovals/lenses in 70% of the S0/S0a galaxy sample, and nuclear components (bars/rings/discs) in 50% of them.

1.2.1 Photometry and Kinematics

Early-type galaxies can exhibit a wide variety of kinematic features, going from the fainter rotationally-supported systems to the brighter dispersion-dominated ones (e.g. Davies et al. 1983). While the identification of stellar discs in images of spiral galaxies is generally trivial thanks to the presence of spiral arms, featureless discs in bright, early-type galaxies can be particularly hard to recognise by looking at the photometry alone, due to well-known inclination effects (e.g. Rix & White 1990; Gerhard & Binney 1996). However, this problem can be alleviated with the use of kinematic information (e.g. Carter 1987; Franx et al. 1989; Nieto et al. 1991; Rix & White 1992; Cinzano & van der Marel 1993; D'Onofrio et al. 1995; Graham et al. 1998). In particular, our understanding of the internal structure of early-type galaxies has undoubtedly improved over the past decade thanks to the introduction of integral-field spectrographs and the analysis of two-dimensional kinematic maps (e.g. the ATLAS^{3D} survey, Cappellari et al. 2011).

⁶Unsharp masks are obtained from the original images with a mathematical operation of convolution. By suppressing large-scale, low-frequency variations in the images, they act as a filter and reveal faint asymmetric structures within the galaxies (Malin & Zealey, 1979; Erwin & Sparke, 2003).

Emsellem et al. (2007) used the specific angular momentum within one effective radius ($\lambda_R = \langle R|V| \rangle / (R\sqrt{V^2 + \sigma^2})$, where R is the semimajor-axis radius, V is the mean velocity and σ is the velocity dispersion) and the ellipticity at one effective radius ($\epsilon = 1 - (b/a)$, where (b/a) is the ratio of minor-to-major axis length) to classify early-type galaxies into fast rotators and slow rotators, based on the empirical divide $\lambda_R = 0.31\sqrt{\epsilon}$.

Krajnović et al. (2006) developed “kinemetry”, a method that combines surface photometry and kinematics to recognise less obvious structures in galaxies, such as embedded discs and kinematic subcomponents. Using kinemetry, Krajnović et al. (2011) measured the regularity of velocity maps and demonstrated that fast rotators are typically nearly axisymmetric systems, whereas most slow rotators are triaxial systems. At present, the joint effort of imaging and integral-field spectroscopy is undeniably our best chance to disclose the internal structure of galaxies (e.g. Krajnović 2015).

Putting this paradigm into practice, Krajnović et al. (2013) compared photometric signatures and kinematic properties of stellar discs for the 180 unbarred early-type galaxies of the ATLAS^{3D} sample. For each galaxy, they fit the light distribution using a single bulge (Sérsic, 1963, 1968) and a bulge+disc (Sérsic+exponential) model, preferring the latter when the improvement over the single bulge model was substantial and no correlation within the residuals was observed. They found that exponential sub-components in fast rotators correspond to a genuine family of rotationally-supported discs or disc-like structures, which were identified in 83% of the unbarred early-type subsample, contributing to 40% of the total stellar mass and covering a full range of disc-to-total flux ratios. From their analysis, Krajnović et al. (2013) concluded that, when using photometry only, inclination effects do not particularly affect the identification of dominant discs, but they become much more disruptive when dealing with low-inclination, medium size discs. The use of kinematics is therefore the best approach to mitigate inclination effects. One of the key results obtained by the ATLAS^{3D} Collaboration is that the majority of early-type galaxies contain stellar discs with an essentially continuous distribution of disc-to-total flux ratios, which led Cappellari et al. (2011) to the introduction of a new classification scheme aimed at replacing the classical Hubble diagram.

1.2.2 A Compendium of the Previous Literature

Over the past nine years, five independent studies (Graham & Driver, 2007a; Sani et al., 2011; Vika et al., 2012; Beifiori et al., 2012; Läsker et al., 2014a,b) have attempted galaxy decomposition for samples of galaxies with a direct measure of the black hole mass. The main aim of each study was to derive the parameters of the spheroidal components of their galaxies and explore correlation with the black hole mass. Table 1.1 summarises the main characteristics and findings of each work.

| | GD07 | S+11 | V+12 | B+12 | L+14 |
|---|-------------|-------------------|-------------|----------------|-------------|
| Galaxies | 27 | 57 | 25 | 19 | 35 |
| Wavelength | R-band | $3.6 \mu\text{m}$ | K-band | <i>i</i> -band | K-band |
| Decomposition | 1D | 2D | 2D | 2D | 2D |
| Nuclei | masked | modelled | modelled | not treated | modelled |
| Cores | masked | masked | masked | not treated | masked |
| Bars | excluded | modelled | modelled | excluded | modelled |
| Other components | no | no | no | no | yes |
| Kinematics | no | no | no | no | no |
| <i>Conclusions</i> | | | | | |
| $M_{\text{BH}} - n_{\text{sph}}$ | yes | no | no | no | - |
| $M_{\text{BH}} - L_{\text{sph}}$ | - | yes | yes | yes | fundamental |
| $M_{\text{BH}} - M_{\text{sph,dyn}}$ | - | yes | - | yes | - |
| $M_{\text{BH}} - M_{\text{sph,*}}$ | - | yes | - | - | - |
| $M_{\text{BH}} - R_e$ | - | secondary | - | - | - |
| $M_{\text{BH}} - \langle \mu_e \rangle$ | - | - | - | no | - |
| $M_{\text{BH}} - L_{\text{gal}}$ | - | - | - | secondary | fundamental |

Table 1.1: Main characteristics and findings of the latest five studies that have attempted galaxy decomposition to derive and explore black hole mass scaling relations. The number of galaxies accounts only for those with a direct measurement of the black hole mass (no upper limits are considered here). GD07 = Graham & Driver (2007a); S+11 = Sani et al. (2011); V+12 = Vika et al. (2012); B+12 = Beifiori et al. (2012); L+14 = Läsker et al. (2014a,b).

Sani et al. (2011) used galaxy images obtained with the *Spitzer* satellite in the $3.6 \mu\text{m}$ wavelength-band, which currently represents the best proxy for the stellar mass, even superior

to the K-band (Sheth et al. 2010, and references therein).

There has been an ongoing debate as to whether 2D galaxy decomposition techniques should be preferred over 1D techniques. The performance of each method can vary according to different technical factors (such as the signal-to-noise of the galaxy images, the accuracy of the description of the Point Spread Function, the gradient of ellipticity and position angle of the galaxy isophotes, the fitting weighting scheme, etc.), therefore advantages and disadvantages are not absolute and depend on the individual science case. To our best knowledge, no published study has ever been conducted on a systematic comparison between 1D and 2D galaxy decomposition techniques.

Previous works have demonstrated that, when studying galaxies with a complex morphology, the accuracy of the recovery of the bulge parameters increases when all galaxy components are taken into account by the model (Laurikainen et al., 2005; Gadotti, 2008; Salo et al., 2015). Läske et al. (2014a) identified and modelled more galaxy components than any other study, but no work did it with the assistance of kinematical information.

Interestingly, the past studies all used almost the same sample of galaxies (the number of directly measured black hole masses increased with time), but they claimed some contradictory conclusions. One study obtained a good $M_{\text{BH}} - n_{\text{sph}}$ correlation, whereas three did not. Läske et al. (2014b) elected the $M_{\text{BH}} - L_{\text{gal}}$ relation as the fundamental one (likewise the $M_{\text{BH}} - L_{\text{sph}}$), as opposed to Beifiori et al. (2012), who presented it as a secondary correlation. The past studies did not converge to the same conclusions because their best-fit models for the same galaxy were often significantly different and not consistent with each other in terms of fitted components. Moreover, none of these studies attempted an individual galaxy-by-galaxy comparison of their models with the previous literature.

1.3 Thesis Outline

The aim of this thesis is to refine and re-investigate several black hole mass scaling relations through the careful modelling of the spatial light distribution of a selected sample of 66 nearby galaxies. After obtaining robust structural parameters for the galaxies under study, I will explore

substructure in the correlations between these parameters and the black hole mass, and explain discrepancies in the results presented in the past literature.

In Chapter 2 (Savorgnan et al., 2013), we tackle the issue of the $M_{\text{BH}} - n_{\text{sph}}$ correlation using literature data. Four studies independently carried out photometric decompositions for similar samples of galaxies, but only one of them obtained a statistically significant $M_{\text{BH}} - n_{\text{sph}}$ relation. For each galaxy analysed by two or more studies, we compared the models used to fit the galaxy's spatial distribution of light, and found that the same galaxy was often described with remarkably different models in terms of number and type of sub-components. This was obviously resulting in significantly different best-fit parameters. We then collected the Sérsic index measurements obtained by the four studies for 54 common galaxies with a direct measure of their black hole mass, rejected the most discrepant values, and used the remaining measurements to populate the $M_{\text{BH}} - n_{\text{sph}}$ diagram. Besides recovering a statistically significant $M_{\text{BH}} - n_{\text{sph}}$ relation for all galaxies, we also explored substructure for different galaxy morphological types (elliptical galaxies versus bulges of disc galaxies) and nature of the nuclear light profile (Sérsic versus core-Sérsic).

In Chapter 3 (Savorgnan & Graham, 2016b), we present the 1D decompositions carried out by us for 66 local galaxies with a direct measure of their black hole mass. We describe the careful data reduction process through which we created the image-mosaics for these galaxies, using archival observations at $3.6 \mu\text{m}$ obtained with *Spitzer*. We detail our 1D galaxy decomposition technique and our method to estimate the uncertainties associated with the spheroid's best-fit parameters. Upon comparing the results obtained from our 1D and 2D galaxy models, we comment on the advantages and disadvantages connected with 1D and 2D decomposition techniques. The individual 1D galaxy decompositions are illustrated, along with a thorough analysis of each galaxy's structure and a scrupulous comparison with several past decompositions.

In Chapter 4 (Savorgnan et al., 2016), we use the results from our 1D galaxy decompositions to explore substructure in the $M_{\text{BH}} - L_{\text{gal}}$ and $M_{\text{BH}} - L_{\text{sph}}$ (or $M_{\text{BH}} - M_{*,\text{sph}}$) diagrams for different galaxy morphological types and nature of the nuclear light profile. Upon performing a detailed linear regression analysis using three different routines, we concluded that early-type (elliptical+lenticular) and late-type (spiral) galaxies follow two separate correlations in the $M_{\text{BH}} - L_{\text{sph}}$ (or $M_{\text{BH}} - M_{*,\text{sph}}$) diagram. In addition, we compared the level of intrinsic scatter

in the $M_{\text{BH}} - L_{\text{gal}}$ and $M_{\text{BH}} - L_{\text{sph}}$ diagrams to address the question of whether or not the $M_{\text{BH}} - L_{\text{sph}}$ correlation is more fundamental than the $M_{\text{BH}} - L_{\text{gal}}$ correlation.

In Chapter 5 (Savorgnan, 2016), we use the results from our 1D galaxy decompositions to populate the $L_{\text{sph}} - n_{\text{sph}}$ and $M_{\text{BH}} - n_{\text{sph}}$ diagrams. The analysis that we performed here is essentially analogous to that presented in Chapter 4. We did not observe any significant substructure in the $M_{\text{BH}} - n_{\text{sph}}$ diagram, where all galaxies, irrespective of their morphological type, define a single tight correlation. Consistency between the $M_{\text{BH}} - n_{\text{sph}}$ and other galaxy scaling relations is discussed here.

In Chapter 6 (Savorgnan & Graham, 2015), we concentrate on the $M_{\text{BH}} - \sigma_*$ scaling relation and the presence of some outlying, “overmassive” black holes at the high-mass end of this correlation. Volonteri & Ciotti (2013) proposed a theoretical interpretation to explain why central cluster galaxies tend to appear as positive outliers in the $M_{\text{BH}} - \sigma_*$ diagram, lying above the observed $z = 0$ correlation. According to the results from their semi-analytical models, central cluster galaxies experienced more dry mergers than the “average” population of massive early-type galaxies. Dry mergers are expected to increase the black hole mass, while leaving almost unchanged the stellar velocity dispersion. We tested the interpretation offered by Volonteri & Ciotti (2013) using the latest observational data. First, we updated the $M_{\text{BH}} - \sigma_*$ diagram with a total of 89 galaxies and performed a linear regression analysis of it. Then, for each galaxy with a partially depleted core we measured the extent of dry mergers experienced by the galaxy by means of the ratio between the central stellar mass deficit and the black hole mass. We showed that no positive trend is observed between the number of dry mergers and the positive vertical offset from the $M_{\text{BH}} - \sigma_*$ correlation. A similar test using the kinematics of galaxies gave consistent results, disproving the scenario advocated by Volonteri & Ciotti (2013).

In Chapter 7 (Savorgnan & Graham, 2016a), we tackle the issue of the “overmassive” black holes in the $M_{\text{BH}} - M_{*,\text{sph}}$ diagram. Due to inaccurate decompositions that failed to take into account the correct size of the main disc component, a number of galaxies (Mrk 1216, NGC 1271, NGC 1277, and NGC 1332) had their spheroid luminosity underestimated, which made them appear as positive outliers above the $M_{\text{BH}} - M_{*,\text{sph}}$ correlation. With the aid of photometric and kinematic information, we identified the radial extent of the main disc component, and built

a galaxy model accordingly. We showed that when these galaxies are correctly modelled, they lie well within the scatter of the observed $M_{\text{BH}} - M_{*,\text{sph}}$ correlation.

Finally, Chapter 8 contains a summary of my principal findings, conclusions, and some promising directions for future research.

The Recovery of the $M_{\text{BH}} - n_{\text{sph}}$ Relation

Graham et al. (2001) demonstrated that the mass of SMBHs is correlated with the stellar light concentration of their host spheroid. Six years later, Graham & Driver (2007a) expanded the galaxy sample of Graham et al. (2001) and carried out 1D bulge/disc decompositions. They described the 1D surface brightness profile of spheroids with the Sérsic model, and obtained a direct measure of the central radial concentration of stars by means of the Sérsic index. Graham & Driver (2007a) confirmed the early findings of Graham et al. (2001), presenting a strong correlation between the black hole mass and the spheroid Sérsic index ($M_{\text{BH}} - n_{\text{sph}}$). They measured a small level of scatter, which made the $M_{\text{BH}} - n_{\text{sph}}$ and $M_{\text{BH}} - \sigma_*$ correlations evenly competing for the title of fundamental black hole mass scaling relation.

As the number of directly measured black hole masses increased with time and the constantly improving technology of machines allowed shorter computational times for 2D decomposition codes, more studies were dedicated to the analysis of various black hole mass scaling relations. Sani et al. (2011), Vika et al. (2012), and Beifiori et al. (2012) attempted 2D decompositions of their samples of galaxies with a direct measure of the black hole mass. Sani et al. and Vika et al. included more than two components in their galaxy models such as bars and nuclear sources, whereas Beifiori et al. excluded barred galaxies from their analysis and used simple bulge+disc models. From these decompositions, they derived and analysed several correlations. However, none of these three studies was able to obtain a strong $M_{\text{BH}} - n_{\text{sph}}$ relation from their data. This raised an obvious question: what prevented Sani et al., Vika et al., and Beifiori et al. from the recovery of a tight $M_{\text{BH}} - n_{\text{sph}}$ correlation? Imputable factors could be the decomposition technique (1D versus 2D), the use of more sophisticated models featuring a larger number

of components, the use of different wavelengths, or possibly the accuracy of the decompositions.

These circumstances motivated us to engage a preliminary study in 2012, aiming at explaining the lack of an $M_{\text{BH}} - n_{\text{sph}}$ correlation in the data of Sani et al., Vika et al., and Beifiori et al. After collecting and comparing the results from the galaxy decompositions of the aforementioned four studies (Graham & Driver, Sani et al., Vika et al., and Beifiori et al.), we immediately noticed that some galaxies had been described by these authors with significantly different models (e.g. the galaxy M60, treated as a discless elliptical galaxy by two studies, and as a lenticular galaxy by the other two studies). Different galaxy models (for the same galaxy) evidently resulted in different best-fit parameters. Not only this, but some studies obtained largely discrepant best-fit parameters for the same galaxy even when they used the same choice of decomposition (e.g. two studies described the galaxy NGC 3115 with a Sérsic-bulge + exponential-disc model, but obtained a bulge Sérsic index of 3 and 13, respectively). This confirmed our doubts about the accuracy of some decompositions.

For each galaxy, we averaged the available Sérsic index measurements and used these average values to populate the $M_{\text{BH}} - n_{\text{sph}}$ diagram. We noticed that a clear correlation was emerging from the data, although with a significant amount of scatter. We attributed the large amount of scatter to “bad” decompositions, and decided to develop a method for an impartial identification of the “bad” Sérsic index measurements. After estimating a maximum tolerable disagreement between the Sérsic index measurements of the same galaxy by taking into account the use of different decomposition methods and wavelengths, we excluded the most discrepant measurements and averaged the remaining ones. This resulted in a dramatic reduction of scatter and the recovery of a strong $M_{\text{BH}} - n_{\text{sph}}$ correlation. Finally, we explored substructure in the $M_{\text{BH}} - n_{\text{sph}}$ diagram expected for consistency with other known scaling relations.

The remainder of this Chapter comprises the published version of the paper “The supermassive black hole mass – Sérsic index relations for bulges and elliptical galaxies” by G. A. D. Savorgnan et al., as it appears in Volume 434 of *Monthly Notices of the Royal Astronomical Society*.



The supermassive black hole mass–Sérsic index relations for bulges and elliptical galaxies

G. Savorgnan,¹★ A. W. Graham,¹ A. Marconi,² E. Sani,³ L. K. Hunt,³ M. Vika⁴ and S. P. Driver^{5,6}

¹Centre for Astrophysics and Supercomputing, Swinburne University of Technology, Hawthorn, Victoria 3122, Australia

²Dipartimento di Fisica e Astronomia, Università di Firenze, via G. Sansone 1, I-50019 Sesto Fiorentino, Firenze, Italy

³INAF - Osservatorio Astrofisico di Arcetri, Largo E. Fermi 5, I-50125 Firenze, Italy

⁴Carnegie Mellon University in Qatar, Education City, PO Box 24866, Doha, Qatar

⁵ICRAR - The University of Western Australia, 35 Stirling Highway, Crawley, WA 6009, Australia

⁶SUPA - School of Physics and Astronomy, University of St Andrews, North Haugh, St Andrews KY16 9SS, UK

Accepted 2013 June 6. Received 2013 April 22

ABSTRACT

Scaling relations between supermassive black hole mass, M_{BH} , and host galaxy properties are a powerful instrument for studying their co-evolution. A complete picture involving *all* of the black hole scaling relations, in which each relation is consistent with the others, is necessary to fully understand the black hole–galaxy connection. The relation between M_{BH} and the central light concentration of the surrounding bulge, quantified by the Sérsic index n , may be one of the simplest and strongest such relations, requiring only uncalibrated galaxy images. We have conducted a census of literature Sérsic index measurements for a sample of 54 local galaxies with directly measured M_{BH} values. We find a clear $M_{\text{BH}}-n$ relation, despite an appreciable level of scatter due to the heterogeneity of the data. Given the current $M_{\text{BH}}-L_{\text{sph}}$ and the $L_{\text{sph}}-n$ relations, we have additionally derived the *expected* $M_{\text{BH}}-n$ relations, which are marginally consistent at the 2σ level with the *observed* relations. Elliptical galaxies and the bulges of disc galaxies are each expected to follow two distinct *bent* $M_{\text{BH}}-n$ relations due to the Sérsic/core-Sérsic divide. For the same central light concentration, we predict that M_{BH} in the Sérsic bulges of disc galaxies are an order magnitude higher than in Sérsic elliptical galaxies if they follow the same $M_{\text{BH}}-L_{\text{sph}}$ relation.

Key words: black hole physics – galaxies: bulges – galaxies: fundamental parameters – galaxies: structure.

1 INTRODUCTION

Observations over the past decade have suggested a strong connection between supermassive black holes (SMBHs) and their host galaxies, or rather spheroids, in spite of the huge difference between their respective sizes. While it is clear that the stories of these two objects – the black hole and the galaxy – are tightly interwoven, the origin and nature of their link are still a subject of debate. The scaling relations between the SMBH mass, M_{BH} , and the host spheroid properties make the study of black hole growth an indispensable ingredient to understand the more general framework of galaxy formation and evolution. Beyond the well-known relation with the velocity dispersion σ (Ferrarese & Merritt 2000; Gebhardt et al. 2000; Graham et al. 2011), the masses of SMBHs have been shown to correlate with a wide series of properties belonging

to the spheroidal component of the host galaxy, such as the spheroid luminosity (Kormendy & Richstone 1995; McLure & Dunlop 2002; Marconi & Hunt 2003; Graham & Scott 2013) and stellar mass (Laor 2001; Scott, Graham & Schombert 2013), the spheroid dynamical mass (Magorrian et al. 1998; Marconi & Hunt 2003; Häring & Rix 2004; Scott et al. 2013) and the central stellar concentration of the spheroid (Graham et al. 2001). The connection between bulge mass and disc galaxy morphological type means that the pitch angle of a disc galaxy’s spiral arms is also related to the black hole mass (e.g. Berrier et al. 2013; Davis et al. 2013, and references therein). The old $M_{\text{BH}} \propto \sigma^4$ and $M_{\text{BH}} \propto L^{1.4}$ relations were actually inconsistent with each other (e.g. Lauer et al. 2007), and inconsistent with the curved $M_{\text{BH}}-n$ relation (Graham & Driver 2007b) given the existence of a linear $L-n$ relation (see Section 4). The first of these inconsistencies was addressed in Graham (2012; see also section 6 of Graham 2008), and we tackle the second here. The astrophysical interest in all of these empirical relations resides partly in the fact that they must *all* be taken into account by any complete theory

* E-mail: gsavorgn@astro.swin.edu.au

or model describing the co-evolution of galaxies and SMBHs, and also in their employment to predict the masses of SMBHs in other galaxies.

A decade ago Graham et al. (2001) presented evidence for a strong correlation between the stellar light concentration $C_{\text{re}}(1/3)$ of spheroids and their SMBH mass, showing that more centrally concentrated spheroids have more massive black holes. Graham & Driver (2007b) re-investigated the same relation, directly using the Sérsic (1963, 1968) index n as a measure of the radial concentration of the stars. In addition to a log-linear relation, Graham & Driver (2007b) fit a log-quadratic regression, finding that the $M_{\text{BH}} - n$ relation changed slopes at the low- and high-mass end, and had a level of scatter equivalent to the $M_{\text{BH}} - \sigma$ relation at that time (~ 0.3 dex). The advantages of using the $M_{\text{BH}} - n$ relation to predict the mass of SMBHs are several: as noted by Graham & Driver (2007b), the measurement of n requires only images (even photometrically uncalibrated); it is not heavily affected by possible kinematic substructure at the centre of a galaxy, nor by rotational velocity or the vertical velocity dispersion of an underlying disc, nor by aperture corrections; it is cheap to acquire in terms of telescope time; and it does not depend on galaxy distances.

Pastrav et al. (2013) have recently pointed out that the recent deep, wide-field photometric surveys of galaxies – e.g. the Sloan Digital Sky Survey (SDSS, York et al. 2000) and the Galaxy And Mass Assembly (GAMA, Driver et al. 2011) – are providing us with large statistically useful samples of galaxies whose major morphological components can be resolved out to $z \simeq 0.1$. Furthermore, automatic image analysis routines, such as GIM2D (Simard et al. 2002), GALFIT (Peng et al. 2002, 2010), BUDDA (Gadotti 2008) and GALPHAT (Yoon, Weinberg & Katz, in preparation), can be used to model the surface brightness distribution of the stellar components of these galaxies (e.g. Allen et al. 2006; Simard et al. 2011; Kelvin et al. 2012). A bulge/disc decomposition, along with adequate corrections to account for dust and inclination effects as provided by Pastrav et al. (2013), can provide the Sérsic index of the spheroid component of both elliptical and disc galaxies. This can then be used to predict black hole masses in large samples of galaxies to derive the local black hole mass function (e.g. Graham et al. 2007) and space density (Graham & Driver 2007a, and references therein), if a well calibrated $M_{\text{BH}} - n$ relation exists. However, in the past two years Sani et al. (2011), Vika et al. (2012) and Beifiori et al. (2012) have failed to recover a strong $M_{\text{BH}} - n$ relation.

Due to the existence of the luminosity– n relation (e.g. Young & Currie 1994; Jerjen, Binggeli & Freeman 2000; Graham 2013, and references therein) and the M_{BH} –luminosity relation (e.g. Magorrian et al. 1998), an $M_{\text{BH}} - n$ relation must exist.¹ It is important to investigate why the $M_{\text{BH}} - n$ relation may not have been recovered in the above studies. It is also important to know how it fits in with, and is consistent with, the other scaling relations. Not only does a proper and complete understanding of the SMBH–galaxy connection require this, but the central concentration of stars, reflecting the inner gradient of the gravitational potential, should be intimately related to the black hole mass. A well-determined $M_{\text{BH}} - n$ relation may also provide an easy and accurate means to predict black hole masses in other galaxies. Eventually, semi-analytic models of galaxy formation and simulations should include in their recipes *all* of the black hole mass scaling relations.

In this work, we present a census of literature Sérsic index measurements for local galaxies with directly measured SMBH mass.

¹ It is not yet established which are the primary or secondary relations.

We re-investigate and recover the $M_{\text{BH}} - n$ relation using the combined data from four past independent works. In Section 2, we describe our galaxy sample and in Section 3, we present the $M_{\text{BH}} - n$ scaling relation which is then discussed and compared with predictions in Section 4. Finally, we summarize our analysis in Section 5.

2 DATA

2.1 SMBH masses

Our SMBH galaxy sample comes from Graham & Scott (2013), who have built a catalogue of 80 galaxies with SMBH masses obtained from direct maser, stellar or gas kinematic measurements. Black hole masses for our final sample are listed in Table 1, along with their total galaxy B -band absolute magnitudes, M_{BT} , taken from the *Third Reference Catalogue of Bright Galaxies* (de Vaucouleurs et al. 1991, hereafter RC3) and also their morphological classification. The final sample consists of those galaxies for which Sérsic indices have been reported by at least one of the four studies mentioned below.

2.2 Collecting Sérsic indices

The radial light distribution of spheroidal systems (such as elliptical galaxies or the bulges of lenticular and spiral galaxies) is well described by the Sérsic (1963, 1968) $R^{1/n}$ model that parametrizes the intensity I as a function of the projected galactic radius R such that

$$I(R) = I_{\text{e}} \exp \left\{ -b_n \left[\left(\frac{R}{R_{\text{e}}} \right)^{1/n} - 1 \right] \right\}$$

(Caon, Capaccioli & D’Onofrio 1993; Andredakis et al. 1995; Graham & Driver 2005, and references therein). The quantity I_{e} is the intensity at the effective radius R_{e} that encloses half of the total light from the model, and b_n is a constant defined in terms of the Sérsic index n , which is the parameter that measures the curvature of the radial light profile.

We obtained Sérsic index measurements for our SMBH sample from the following four independent works.

(i) Graham & Driver (2007b, hereafter GD07) fit the radial light profiles from a sample of 27 elliptical and disc galaxies with SMBH masses derived from resolved dynamical studies. The light profiles they used were predominantly from Graham et al. (2001), who searched the various public archives for high-quality R -band images and fit ellipses to the isophotes with the *IRAF* task `ellipse`, allowing the position angle and ellipticity to vary with radius.² The resulting light profiles were then fit by GD07 with a seeing-convolved Sérsic $R^{1/n}$ model for elliptical galaxies, and with a combined (seeing-convolved) exponential disc and $R^{1/n}$ bulge for the disc galaxies, using the subroutine `UNCMND` from Kahaner et al. (1989). The inner couple of arcseconds of the profiles was in some instances excluded from the fit due to the potential presence of partially depleted cores or active galactic nuclei (AGNs), that would produce a biasing central deficit or excess of light relative to the inward extrapolation of their outer Sérsic profile.

(ii) Vika et al. (2012, hereafter V12) investigated the $M_{\text{BH}} - n$ and the $M_{\text{BH}} - L$ relations. They performed two-dimensional (2D) profiling with *GALFIT3* on near-IR images [from the UKIRT Infrared

² A discussion of the original galaxy light profiles can be found in Erwin, Graham & Caon (2004) and Trujillo et al. (2004).

Table 1. SMBH galaxy sample. Column (1): galaxy names; eight galaxies marked with an asterisk (*) have been excluded from the final analysis due to the large disagreement on their Sérsic index measurements, according to the criteria mentioned in Section 2.4. Column (2): morphological type as listed by Graham & Scott (2013), primarily from NED. Column (3): absolute total B -band magnitudes, from the RC3 catalogue using the galaxy distances published in Graham & Scott (2013). Column (4): black hole masses from Graham & Scott (2013). Column (5): presence of a partially depleted core as listed by Graham & Scott (2013) and such that the question mark is used when the classification has come from the velocity dispersion criteria mentioned in Section 3. Columns (6–9): galaxy decomposition performed by the four works described in Section 2.2; B = Sérsic profile, D = disc, g = Gaussian, m = central mask, b = bar, p = PSF. Columns (10–13): measured Sérsic index values.

| Galaxy (1) | Type (2) | M_{B_T} (mag) (3) | M_{BH} ($10^8 M_{\odot}$) (4) | Core (5) | Decomposition | | | | n (10) | $V12^b$ (11) | $S11^c$ (12) | $B12^d$ (13) | |
|----------------|-------------|----------------------------------|--|-------------|--------------------------|----------------|----------------|----------------|-------------|-----------------|-----------------|-----------------|------|
| | | | | | GD07 ^a (6) | $V12^b$ (7) | $S11^c$ (8) | $B12^d$ (9) | | | | | |
| Abell 1836-BCG | E1 | -21.43 | 39^{+4}_{-5} | y? | | | | BD | | | | | 2.73 |
| Circinus | Sb | -15.14 | $0.011^{+0.002}_{-0.002}$ | n? | | | | BD | | | | | 2.0 |
| IC 1459 | E | -21.30 | 24^{+10}_{-10} | y | | | | Bg | | | | | 6.0 |
| IC 2560 | SBb | -20.52 | $0.044^{+0.044}_{-0.022}$ | n? | | | | BDg | | | | | 2.0 |
| MESSIER 32 | S0? | -15.46 | $0.024^{+0.005}_{-0.005}$ | n | BD | BDm | BD | | 1.51 | 2.1 | 4.0 | | |
| MESSIER 59 | E | -20.68 | $3.9^{+0.4}_{-0.4}$ | n | | Bm | B | | | 5.7 | 5.0 | | |
| MESSIER 60 | E1 | -21.26 | 47^{+10}_{-10} | y | B | Bm | BD | BD | 6.04 | 3.6 | 3.0 | 1.63 | |
| MESSIER 64 | Sab | -19.96 | $0.016^{+0.004}_{-0.004}$ | n? | | | | BD | | | | | 1.49 |
| MESSIER 77 | SBb | -21.30 | $0.084^{+0.003}_{-0.003}$ | n | | BDbm | BDg | BD | | 0.8 | 1.0 | 1.27 | |
| MESSIER 81 | Sab | -20.01 | $0.74^{+0.21}_{-0.11}$ | n | BD | | BDg | BD | 3.26 | | 3.0 | 2.57 | |
| MESSIER 84 | E1 | -21.17 | $9^{+0.9}_{-0.8}$ | y | B | Bm | Bg | B | 5.60 | 3.5 | 7.0 | 4.10 | |
| MESSIER 87* | E0 | -21.38 | $58^{+3.5}_{-3.5}$ | y? | B | Bm | Bg | | 6.86 | 2.4 | 4.0 | | |
| MESSIER 89 | E | -20.14 | $4.7^{+0.5}_{-0.5}$ | y | | B | BDg | B | | 3.6 | 4.0 | 4.30 | |
| MESSIER 96 | SBab | -19.91 | $0.073^{+0.015}_{-0.015}$ | n | | | BDb | | | | | 1.0 | |
| MESSIER 104 | Sa | -20.91 | $6.4^{+0.4}_{-0.4}$ | y | | | BDbg | | | | | 1.5 | |
| MESSIER 105 | E1 | -19.82 | 4^{+1}_{-1} | y | B | | B | | 4.29 | | | 5.0 | |
| MESSIER 106 | SBbc | -20.19 | $0.39^{+0.01}_{-0.01}$ | n | BD | BDp | BDg | | 2.04 | 3.5 | 2.0 | | |
| Milky Way | SBbc | | $0.043^{+0.004}_{-0.004}$ | n | BD | | | | | 1.32 | | | |
| NGC 0524 | S0 | -20.54 | $8.3^{+2.7}_{-1.3}$ | y | | | BD | | | | | 3.0 | |
| NGC 0821 | E | -20.18 | $0.39^{+0.26}_{-0.09}$ | n | B | | B | B | 4.00 | | 7.0 | 7.70 | |
| NGC 1023 | SB0 | -19.88 | $0.42^{+0.04}_{-0.04}$ | n | BD | | BDb | | 2.01 | | | 3.0 | |
| NGC 1300 | SBbc | -20.47 | $0.73^{+0.69}_{-0.35}$ | n | | | BD | | | | | 3.0 | |
| NGC 1316 | SB0 | -21.93 | $1.5^{+0.75}_{-0.8}$ | y? | | | BDg | | | | | 5.0 | |
| NGC 1399 | E | -20.89 | $4.7^{+0.6}_{-0.6}$ | y | B | | | | 16.8 | | | | |
| NGC 2549 | SB0 | -18.26 | $0.14^{+0.02}_{-0.13}$ | n | | | BD | | | | | 7.0 | |
| NGC 2778 | SB0 | -18.39 | $0.15^{+0.09}_{-0.1}$ | n | BD | BD | BD | | 1.60 | 2.7 | 2.5 | | |
| NGC 2787* | SB0 | -17.50 | $0.4^{+0.04}_{-0.05}$ | n | BD | | BDbg | | 1.97 | | | 3.0 | |
| NGC 2960 | Sa? | -21.25 | $0.12^{+0.005}_{-0.005}$ | n? | | BD | | | | 4.0 | | | |
| NGC 2974 | E | -19.73 | $1.7^{+0.2}_{-0.2}$ | n | | | Bg | | | | | 3.0 | |
| NGC 3079 | SBc | -20.04 | $0.024^{+0.024}_{-0.012}$ | n? | | | BDbg | | | | | 2.0 | |
| NGC 3115* | S0 | -20.00 | $8.8^{+10}_{-2.7}$ | n | BD | | BD | | 13.0 | | | 3.0 | |
| NGC 3227 | SBa | -20.44 | $0.14^{+0.1}_{-0.06}$ | n | | | BD | | | | | 4.0 | |
| NGC 3245 | S0 | -19.84 | $2^{+0.5}_{-0.5}$ | n | BD | BD | BD | BD | 4.31 | 2.6 | 2.5 | 1.60 | |
| NGC 3377 | E5 | -18.95 | $0.77^{+0.04}_{-0.06}$ | n | B | | B | B | 3.04 | | 6.0 | 3.47 | |
| NGC 3384 | SB0 | -19.42 | $0.17^{+0.01}_{-0.02}$ | n | BD | | BDb | BD | 1.72 | | 2.5 | 2.33 | |
| NGC 3414 | S0 | -19.99 | $2.4^{+0.3}_{-0.3}$ | n | | | BDb | | | | | 5.0 | |
| NGC 3489 | SB0 | -19.22 | $0.058^{+0.008}_{-0.008}$ | n | | | BD | | | | | 1.5 | |
| NGC 3585 | S0 | -20.57 | $3.1^{+1.4}_{-0.6}$ | n | | | BD | | | | | 2.5 | |
| NGC 3607 | S0 | -20.91 | $1.3^{+0.5}_{-0.5}$ | n | | | Bg | B | | | | 5.0 | 4.70 |
| NGC 3608* | E2 | -20.04 | $2^{+1.1}_{-0.6}$ | y | | | B | B | | | | 6.0 | 9.03 |
| NGC 3998* | S0 | -19.07 | $8.1^{+2}_{-1.9}$ | y? | | | BDg | BD | | | | 1.5 | 2.29 |
| NGC 4026 | S0 | -18.93 | $1.8^{+0.6}_{-0.3}$ | n | | | BD | | | | | 3.5 | |
| NGC 4151 | SBab | -20.01 | $0.65^{+0.07}_{-0.07}$ | n | | | BDg | | | | | 3.5 | |
| NGC 4261 | E2 | -21.03 | 5^{+1}_{-1} | y | B | Bm | BDg | B | 7.30 | 3.5 | 4.0 | 4.31 | |

Table 1 – *continued*

| Galaxy | Type | M_{B_T} (mag) | M_{BH} ($10^8 M_{\odot}$) | Core | GD07 ^a | Decomposition | | | GD07 ^a | n | $V12^b$ | $S11^c$ | $B12^d$ |
|-----------|------|---------------------------|---|------|-------------------|---------------|---------|---------|-------------------|------|---------|---------|---------|
| | | | | | | $V12^b$ | $S11^c$ | $B12^d$ | | | | | |
| (1) | (2) | (3) | (4) | (5) | (6) | (7) | (8) | (9) | (10) | (11) | (12) | (13) | |
| NGC 4291 | E2 | -19.60 | $3.3^{+0.9}_{-2.5}$ | y | B | | | | | 4.02 | | | |
| NGC 4342* | S0 | -18.40 | $4.5^{+2.3}_{-1.5}$ | n | BD | BD | | | | 5.11 | 1.9 | | |
| NGC 4459* | S0 | -19.66 | $0.68^{+0.13}_{-0.13}$ | n | | B | BD | B | | 3.9 | 2.5 | 7.44 | |
| NGC 4473 | E5 | -19.76 | $1.2^{+0.4}_{-0.9}$ | n | B | Bm | B | BD | 2.73 | 4.3 | 7.0 | 2.23 | |
| NGC 4486A | E2 | -18.04 | $0.13^{+0.08}_{-0.08}$ | n | | Bm | B | | | 2.0 | 2.5 | | |
| NGC 4564 | S0 | -18.77 | $0.6^{+0.03}_{-0.09}$ | n | BD | BD | BD | | 3.15 | 3.7 | 7.0 | | |
| NGC 4596 | SB0 | -19.80 | $0.79^{+0.38}_{-0.33}$ | n | | BDb | BDb | BD | | 3.6 | 3.0 | 4.43 | |
| NGC 4697 | E4 | -20.14 | $1.8^{+0.2}_{-0.1}$ | n | B | B | B | B | 4.00 | 3.8 | 5.0 | 4.96 | |
| NGC 5077 | E3 | -20.69 | $7.4^{+4.7}_{-3}$ | y | | | Bg | | | | 6.0 | | |
| NGC 5128 | S0 | -20.06 | $0.45^{+0.17}_{-0.1}$ | n? | | | BDbg | | | | 3.5 | | |
| NGC 5252 | S0 | -21.03 | 11^{+16}_{-5} | n | | | | BD | | | | 4.82 | |
| NGC 5576 | E3 | -20.12 | $1.6^{+0.3}_{-0.4}$ | n | | Bm | B | B | | 5.1 | 7.0 | 8.71 | |
| NGC 5813 | E | -21.03 | $6.8^{+0.7}_{-0.7}$ | y | | Bm | B | | | 8.3 | 6.0 | | |
| NGC 5845 | E3 | -18.51 | $2.6^{+0.4}_{-1.5}$ | n | B | B | B | B | 3.22 | 2.6 | 3.0 | 3.45 | |
| NGC 5846 | E | -20.87 | 11^{+1}_{-1} | y | | Bm | B | | | 3.7 | 3.0 | | |
| NGC 6251* | E2 | -21.46 | 5.9^{+2}_{-2} | y? | B | | Bg | | | 11.8 | | 7.0 | |
| NGC 7052 | E | -20.71 | $3.7^{+2.6}_{-1.5}$ | y | B | BD | B | | 4.55 | 1.8 | 5.0 | | |
| NGC 7582 | SBab | -20.34 | $0.55^{+0.26}_{-0.19}$ | n | | | BDg | | | | 4.0 | | |

^a Graham & Driver (2007b). ^b Vika et al. (2012). ^c Sani et al. (2011). ^d Beifiori et al. (2012).

Deep Sky Survey Large Area Survey (UKIDSS-LAS); Lawrence et al. (2007)] of a sample of 25 galaxies. V12 fit the light distribution using a Sérsic function for the elliptical galaxies, the bulges and the bars of lenticular/spiral galaxies and an exponential function for the disc components. In the case of core-Sérsic galaxies with partially depleted cores, they implemented a mask for the inner region. Bright nuclei were additionally modelled as point sources using the point spread function (PSF). A relation between SMBH mass and the Sérsic index was not found by V12. They noticed that the Sérsic index can vary significantly from study to study and they suggested that such mismatch may be due to the different weighting of pixels during the fit that each study used and/or to a wavelength bias. The signal-to-noise-weighted fitting routines, such as GALFIT, can be highly sensitive to central dust obscuration, unaccounted for central excesses and deficits of light relative to the fitted model, and especially errors in the adopted PSF.

(iii) From their GALFIT3-derived 2D bulge-disc decompositions of *Spitzer*/IRAC 3.6 μm images of 57 galaxies, Sani et al. (2011, hereafter S11) investigated the scaling relations between SMBH mass and several other parameters of the host spheroids. The image decomposition was performed with a Sérsic model for the elliptical galaxies and with a Sérsic model plus an exponential model for the lenticular and spiral galaxies. A Gaussian component and a nuclear point source were added in the presence of a bar or an AGN, respectively. In an attempt to restrict the degeneracy between the effective radius and the Sérsic index, following Hunt, Pierini & Giovanardi (2004), S11 performed 2D fitting by fixing the Sérsic index to a set of constant values in the range between $n = 1$ and $n = 7$. They found tight correlations between the SMBH mass and the bulge luminosity and dynamical mass. However, the relation between the SMBH mass and the effective radius had a high intrinsic dispersion and no correlation with the Sérsic index was found.

(iv) Beifiori et al. (2012, hereafter B12) analysed SDSS *i*-band images and extracted photometric and structural parameters for a sample of 57 galaxies, for which 19 had an accurate M_{BH} measurement and the remaining 38 had only an upper limit which are not used here. They performed 2D decompositions with GASP2D (Méndez-Abreu et al. 2008), using a Sérsic profile to model the elliptical galaxies and a combination of a Sérsic plus an exponential model for the disc galaxies. Galaxies affected by poor decomposition due to either a central bar, a Freeman Type II disc profile (Freeman 1970), or just inadequately represented by the single or double component modelling were eliminated from their initial sample. Among their correlations involving the SMBH mass and the parameters of the host galaxy, the tightest was with the stellar velocity dispersion. Little or no correlation was found with the Sérsic index (see their fig. 7).

Table 1 reports the Sérsic index measurements from the above four works, along with the type of photometric decomposition performed. It comprises 62 galaxies. Each galaxy can have up to four Sérsic index estimates. 35 galaxies have multiple measurements of their Sérsic index. In the next two Sections we discuss how we compare and combine them.

2.3 Comparing Sérsic indices

There are three main points that distinguish each study: the first is the wavelength of the image.

The spatial distribution of the surface brightness of a galaxy, and hence its light profile, is a function of the observational bandpass. This means that the structural parameters, in general, may vary with wavelength due to stellar population gradients or dust obscuration. The central light concentration of a galaxy, described by the Sérsic index, is indeed a slight function of wavelength. Using reprocessed

Sloan Digital Sky Survey Data Release Seven (SDSS DR7, Abazajian et al. 2009) and UKIDSS-LAS (Lawrence et al. 2007) imaging data available from the GAMA data base, Kelvin et al. (2012) performed 2D model fits with GALFIT to $\sim 170\,000$ galaxies in the $ugrizYJHK$ bandpasses, using primarily a pure Sérsic profile, to quantify how photometric and structural parameters of a galaxy vary with wavelength. Their fig. 21 shows the mean Sérsic index as a function of the rest-frame wavelength for two subsamples: the disc-dominated and the spheroid-dominated systems. Kelvin et al. (2012) find that the spheroid-dominated population is characterized by mean Sérsic indices that remain relatively stable at all wavelengths, with n increasing by 30 per cent from g to K .

The second point is the model-fitting method: one-dimensional and two-dimensional photometric decomposition techniques, if performed on the same galaxy, can produce different values of the Sérsic index due to ellipticity gradients which the 2D models cannot accommodate. The parameters of the Sérsic model can vary if derived along the major or the minor axis, as first noted by Caon et al. (1993). Ferrari et al. (2004) quantified such discrepancy in terms of ellipticity gradients, i.e. the isophote eccentricity that varies with radius. The histogram in Fig. 1 has been created using data from Caon et al. (1993) and shows the distribution of the ratio between the ‘equivalent’ Sérsic index n_{eq} and that measured along the major axis, n_{maj} . The ‘equivalent’ axis is the geometric mean, \sqrt{ab} , of the major and the minor axis of the isophotal ellipses. The mean (and the standard deviation) of the whole sample is $\langle n_{\text{eq}}/n_{\text{maj}} \rangle = 1.10 \pm 0.27$. This tells us that the equivalent Sérsic index is on average 10 per cent higher than the major axis Sérsic index. From Fig. 1, their relative difference will be less than 40 per cent in 95 per cent of the time.

The third issue pertains to the weighting scheme used for the fits. The arrival of photons, which build up a galaxy image, is a Poissonian process ($\text{noise} \propto \sqrt{\text{signal}}$), which therefore advocates

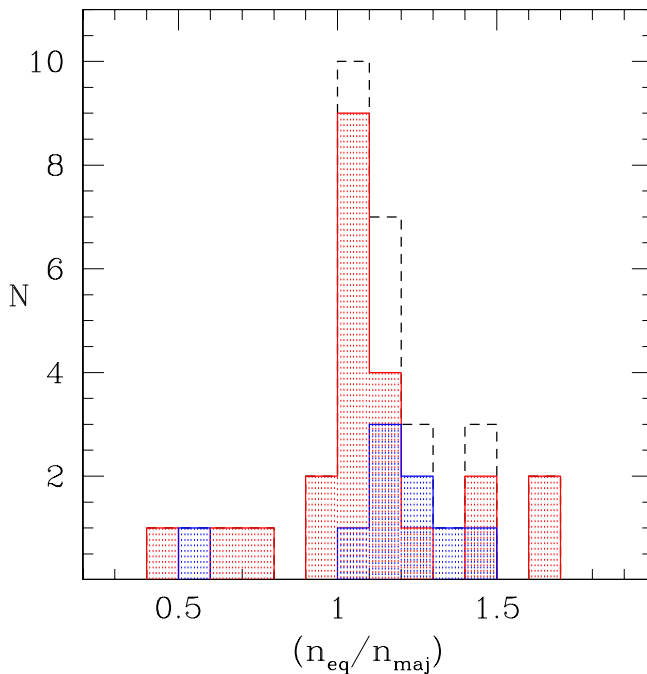


Figure 1. Distribution of the ratio between the “equivalent” Sérsic index n_{eq} and that measured along the major-axis n_{maj} . Data are taken from Caon et al. (1993). The red histogram is for elliptical galaxies, while the blue is for lenticular galaxies and the black dashed line represents the whole sample.

the need for a signal-to-noise-weighted fitting scheme. However, the presence of AGNs, nuclear star clusters, nuclear stellar discs, dust, partially depleted cores and an uncertain PSF make such a weighting prone to error unless all of these factors are taken into account.

Hence, what do we expect from our heterogeneous collection of data? First, the wavelength bias should produce a systematic effect in the Sérsic index measurements, i.e. we expect the measurements from GD07 (R band) and B12 (i band) to be slightly smaller than those from V12 (K band) and S11 (3.6 μm). Secondly, because the Sérsic index derived from a two-dimensional analysis can be approximated to the one-dimensional n_{eq} , one may expect the Sérsic index derived from one-dimensional decomposition along the major axis, as performed by GD07, to be slightly smaller than the Sérsic index derived from the two-dimensional modelling in V12, S11 and B12. However, when we compare different measurements of the Sérsic index (belonging to the same galaxy), we do not observe the previous systematic effects; moreover, for a non-negligible number of galaxies we find that multiple measurements have a relative difference³ greater than 50 per cent.

Many factors, if not properly taken into account, can affect the model fitting of the light distribution of a galaxy and hence the derivation of its structural parameters. These factors can include: additional nuclear components, the presence of a bar, a partially depleted core in high-resolution images, a bad sky subtraction, etc. Moreover, different choices of structural components for the same galaxy will produce contrasting Sérsic indices. Table 2 reports a few examples of discrepant measurements. For the first five galaxies, each study used the same type of decomposition (Sérsic or Sérsic+exponential). For the last three galaxies, each study performed a different image decomposition. M60 was modelled with a pure Sérsic profile by GD07 and V12, while S11 and B12 used an additional disc component. NGC 4459 has a bulge+disc profile according to S11, while V12 and B12 agreed in modelling the galaxy with a pure Sérsic profile. GD07 and S11 fit NGC 7052 with a pure Sérsic profile, whereas V12 chose a bulge+disc model. An exhaustive analysis of why the individual Sérsic indices differ from author to author is however beyond the scope of this work.

2.4 Combining Sérsic indices

To combine the results of these four heterogeneous works, we decided to use a method that was as simple as possible and that involved the least manipulation of the data. Our strategy consisted of looking at galaxies with multiple measurements, comparing the different Sérsic indices and excluding the most contrasting measurements before then averaging the remaining Sérsic indices.

The exclusion algorithm is the following: given a galaxy A that has been analysed by more than one study, we take each measurement n_i^A and we look for the closest one n_j^A . If the absolute difference $|\Delta n_{ij}^A| = |n_i^A - n_j^A|$ is more than 50 per cent of the minimum among the two measurements, we exclude n_i^A . Obviously, if a galaxy has only two measurements, we exclude both of them. After applying the exclusion algorithm, we compute the average logarithmic value of the remaining measurements to give us $\langle \log(n^A) \rangle$.

Figs 2 and 3 are helpful to visualize our approach. Fig. 3 is a ‘zoom’ of Fig. 2 and they both show the absolute total B -band magnitude M_{B_T} of elliptical galaxies plotted against their Sérsic

³ Given two measurements n_1 and n_2 , with $n_1 < n_2$, we define the *relative difference* as $(n_2 - n_1)/n_1$.

Table 2. Examples of outlying measurements, used to explain the crossed out data in Fig. 3. Column (1): galaxy names. Columns (2,4,6,8): literature Sérsic index measurements in ascending order; the reference is given in the superscript. Columns (3,5,7): relative differences; bold type is used for values greater than 50 per cent.

| Galaxy (1) | n_1 (2) | $\frac{n_2-n_1}{n_1}$ (3) | n_2 (4) | $\frac{n_3-n_2}{n_2}$ (5) | n_3 (6) | $\frac{n_4-n_3}{n_3}$ (7) | n_4 (8) |
|--|----------------------|------------------------------|----------------------|------------------------------|----------------------|------------------------------|----------------------|
| Galaxies with same choice of decomposition | | | | | | | |
| M87 | 2.4 ^{V12} | 0.67 | 4.0 ^{S11} | 0.72 | 6.86 ^{GD07} | | |
| NGC 0821 | 4.0 ^{GD07} | 0.75 | 7.0 ^{S11} | 0.10 | 7.70 ^{B12} | | |
| NGC 3115 | 3.0 ^{S11} | 3.33 | 13.0 ^{GD07} | | | | |
| NGC 4342 | 1.9 ^{V12} | 1.69 | 5.11 ^{GD07} | | | | |
| NGC 4564 | 3.15 ^{GD07} | 0.17 | 3.7 ^{V12} | 0.89 | 7.0 ^{S11} | | |
| NGC 6251 | 7.0 ^{S11} | 0.69 | 11.8 ^{GD07} | | | | |
| Galaxies with different choices of decomposition | | | | | | | |
| M60 | 1.63 ^{B12} | 0.84 | 3.0 ^{S11} | 0.20 | 3.6 ^{V12} | 0.68 | 6.04 ^{GD07} |
| NGC 4459 | 2.5 ^{S11} | 0.56 | 3.9 ^{V12} | 0.91 | 7.44 ^{B12} | | |
| NGC 7052 | 1.8 ^{V12} | 1.53 | 4.55 ^{GD07} | 0.10 | 5.0 ^{S11} | | |

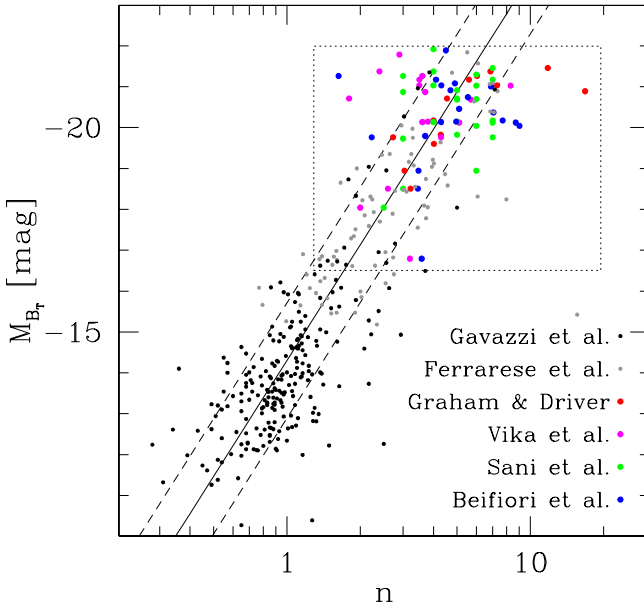


Figure 2. Absolute B -band magnitude versus Sérsic index of elliptical galaxies. Black points are measurements from Gavazzi et al. (2005); grey points are from Ferrarese et al. (2006); red points are from GD07; pink points are from V12; green points are from S11; blue points are from B12. The black points from Gavazzi et al. (2005) and the grey points from Ferrarese et al. (2006) have been plotted just for illustrative purposes, but they will be ignored in the following analysis because they are not from a black hole sample. Each galaxy can have more than one Sérsic measurement and hence may be represented more than once along the horizontal axis (with different colours). The black solid line shows the elliptical galaxy $M_{\mathrm{B}_T} - n$ relation from Graham & Guzmán (2003), while the dashed lines are a rough ‘by eye’ estimate of the scatter from their diagram. The dotted box marks the region that is shown in Fig. 3.

index. The black solid line shows the $M_{\mathrm{B}_T} - n$ relation from Graham & Guzmán (2003) such that $M_{\mathrm{B}_T} = -9.4 \log(n) - 14.3$, while the dashed lines are a rough ‘by eye’ estimate of its scatter.

The horizontal solid lines in Fig. 3 connect the different Sérsic index measurements of the same galaxy. If a galaxy’s Sérsic index has been measured by more than one study, it is represented with a bigger dot. Thus, small dots refer to galaxies that have been measured by only one study. A black cross on a dot means that

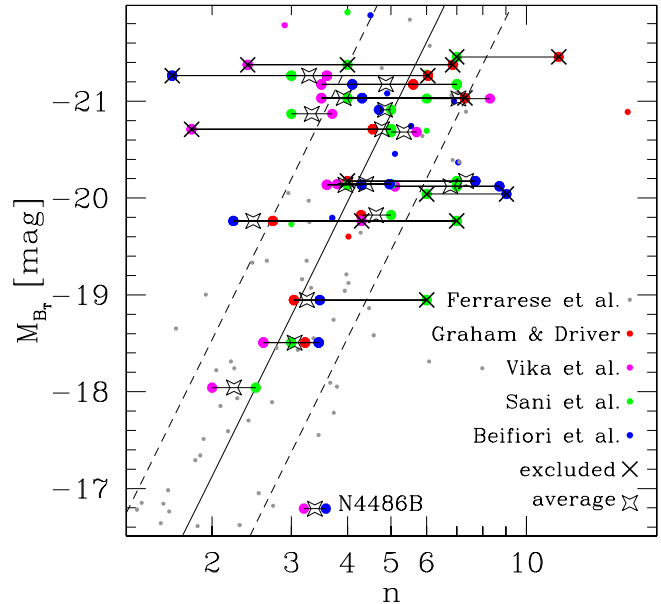


Figure 3. Absolute B -band magnitude versus Sérsic index of elliptical galaxies. This figure is a ‘zoom’ of the dotted box in Fig. 2 and it uses the same colour coding (see the previous caption). The black solid line and the dashed lines are again the $M_{\mathrm{B}_T} - n$ relation from Graham & Guzmán (2003) and a rough ‘by eye’ estimate of the scatter in their diagram. The grey points are excluded from the following description. Horizontal solid lines connect different Sérsic measurements of the same galaxy. Bigger dots refer to galaxies with multiple measurements, while smaller dots show galaxies with only one measurement. The black crosses mark the excluded measurements, according to the algorithm described in Section 2.4 and illustrated in Table 2. Big empty stars indicate the average $(\log(n^A))$ of the logarithmic values of the remaining measurements is denoted by an empty star.

we intend to exclude that particular measurement because it is in strong disagreement (>50 per cent) with the other points according to our exclusion algorithm. The average $(\log(n^A))$ of the logarithmic values of the remaining measurements is denoted by an empty star.

We apply the same procedure to the bulges of the lenticular and spiral galaxies, which are not shown in the $M_{\mathrm{B}_T} - n$ plots (Figs 2 and 3), but are included in the following analysis. Our final sample consists of 54 galaxies with directly measured SMBH mass and at least one measurement of the Sérsic index; among these, 27 galaxies

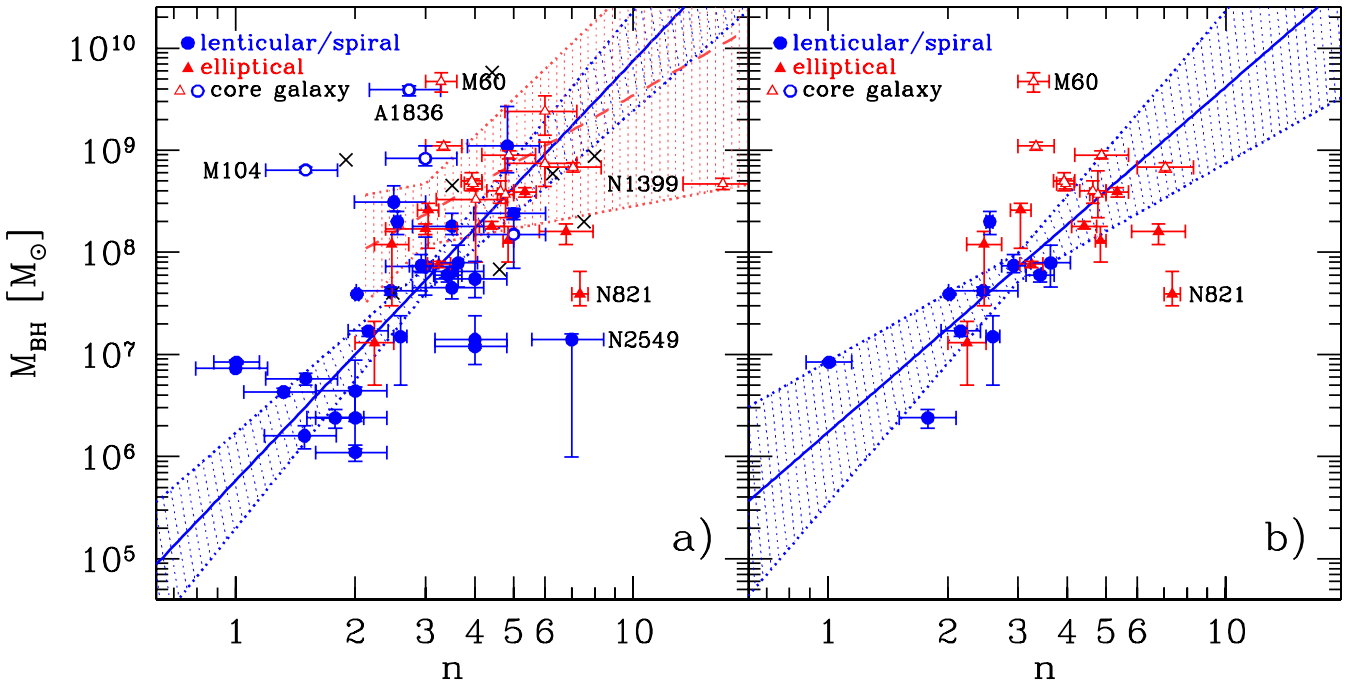


Figure 4. Black hole mass versus Sérsic index. Fig. 4(a): all galaxies with at least one measurement from GD07, V12, S11 and B12; if a galaxy has been measured by more than one study, we plot the average value of its Sérsic index as obtained in Section 2.4. The black crosses are used to show the location of the eight galaxies excluded from the initial sample of 62, due to widely varying Sérsic indices (we plot their mean Sérsic index). Fig. 4(b): only the 27 galaxies with multiple Sérsic measurements. Open symbols are used for core-Sérsic galaxies, rather than filled symbols that denote Sérsic galaxies. The solid blue line (and the blue dotted lines) shows the symmetrical bisector regression (with errors) for the Sérsic bulges of disc galaxies. The dashed red line (and the red dotted lines) shows the symmetrical bisector regression (with errors) for core-Sérsic elliptical galaxies (not shown in Fig. 4(b) due to the low number statistics). The labelled galaxies designate outliers that were excluded from the regressions.

have indices measured by more than one study. The eight galaxies excluded from the initial sample of 62 objects, due to widely varying Sérsic indices, are marked with a star in Table 1.

3 ANALYSIS

After taking galaxies with multiple Sérsic index measurements, rejecting the outlying values and averaging the remaining ones, according to the strategy discussed in Section 2.4, we build the $M_{\text{BH}}-n$ diagram. For galaxies with multiple measurements, we calculated the error on their mean Sérsic index, whereas for single-measured objects we assumed an error⁴ of 20 per cent. Fig. 4(a) includes galaxies with single and averaged-multiple Sérsic indices, whereas Fig. 4(b) only shows those with an averaged-multiple measurement and is thus more reliable.

Despite the higher level of scatter in Fig. 4(a), both diagrams display an appreciable correlation between the SMBH mass and the spheroid light concentration. That is, after excluding the discrepant Sérsic indices according to the process in Section 2.4, presumably from poor fits, we recover a clear trend between black hole mass and Sérsic index. We have visually identified six⁵ outliers in Fig. 4(a) and two⁶ outliers in Fig. 4(b); these objects are labelled in both

Table 3. Spearman's correlation coefficients $r_s(N - 2)$ and likelihood of the correlation occurring by chance P . $N - 2$ are the degrees of freedom.

| | | |
|------------------------------|------------------|--------------------|
| Fig. 4(a) excluding outliers | $r_s(46) = 0.72$ | $P < 0.1$ per cent |
| Fig. 4(a) including outliers | $r_s(52) = 0.53$ | $P < 0.1$ per cent |
| Fig. 4(b) excluding outliers | $r_s(23) = 0.76$ | $P < 0.1$ per cent |
| Fig. 4(b) including outliers | $r_s(25) = 0.60$ | $P < 1$ per cent |

diagrams and were excluded from the following regression analysis. The Spearman's correlation coefficients r_s and the likelihood of the correlation occurring by chance P are given in Table 3. In both panels, we have performed a symmetrical linear bisector regression using the BCES routine from Akritas & Bershady (1996), which was checked using the Bayesian linear regression code LINMIX_ERR (Kelly 2007). However, we have not lumped all the galaxy data together, as there is good reason not to do this.

Among our galaxy sample with direct M_{BH} measurements, Graham & Scott (2013) identified 'core-Sérsic' galaxies that display a central deficit of light relative to the inward extrapolation of their outer Sérsic light profile, and 'Sérsic' galaxies that do not (Graham & Guzmán 2003; Graham et al. 2003; Trujillo et al. 2004). 'Core-Sérsic' galaxies are thought to have formed from dry merger events, whereas 'Sérsic' galaxies are the result of gaseous processes. Their classification (Column 5 of Table 1) has primarily come from the inspection of high-resolution images. When no core designation was available or possible from the literature, Graham & Scott (2013) used a criteria based on the velocity dispersion σ , such that galaxies with $\sigma > 270 \text{ km s}^{-1}$ are considered likely to possess a partially depleted core, while galaxies with $\sigma < 165 \text{ km s}^{-1}$ are

⁴ The error of single-measured objects was estimated as follows. Using the 35 galaxies with multiple measurements of their Sérsic indices, we first computed the average $\langle \log(n) \rangle$ of each galaxy without applying the exclusion algorithm (see Section 2.4) and its error $\sigma_{\langle \log(n) \rangle}$; we then calculated the median value of the errors $\langle \sigma_{\langle \log(n) \rangle} \rangle = 0.08$ (20 per cent).

⁵ Abell 1836-BCG, M60, M104, NGC 1399, NGC 821, NGC 2549.

⁶ M60, NGC 821.

Table 4. Observed $M_{\text{BH}} - n$ scaling relations. M_{BH} = black hole mass, n = Sérsic index. A symmetrical bisector regression (BCES routine from Akritas & Bershady 1996) was used. The quantity n is normalized to the round median value of the distribution of the Sérsic indices for the SMBH galaxy sample ($\langle n \rangle = 3$). The total rms scatter in the $\log(M_{\text{BH}})$ direction is denoted by Δ .

| Number | Type | α | β | Δdex |
|--|---------------------------------|-----------------|-----------------|---------------------|
| Fig. 4(a) $\log(M_{\text{BH}}/\text{M}_{\odot}) = \alpha + \beta \log(n/3)$ | | | | |
| 9 Sérsic elliptical galaxies 27 Sérsic bulges 10 Core-Sérsic elliptical galaxies 2 Core-Sérsic bulges | | | | |
| 9 | Sérsic elliptical galaxies | — | — | — |
| 27 | Sérsic bulges | 7.73 ± 0.12 | 4.11 ± 0.72 | 0.62 |
| 10 | Core-Sérsic elliptical galaxies | 8.37 ± 0.30 | 2.23 ± 1.50 | 0.27 |
| 2 | Core-Sérsic bulges | — | — | — |
| Fig. 4(b) $\log(M_{\text{BH}}/\text{M}_{\odot}) = \alpha + \beta \log(n/3)$ | | | | |
| 8 Sérsic elliptical galaxies 10 Sérsic bulges 7 Core-Sérsic elliptical galaxies 0 Core-Sérsic bulges | | | | |
| 8 | Sérsic elliptical galaxies | — | — | — |
| 10 | Sérsic bulges | 7.85 ± 0.14 | 3.38 ± 1.16 | 0.44 |
| 7 | Core-Sérsic elliptical galaxies | — | — | — |
| 0 | Core-Sérsic bulges | — | — | — |

not. For reasons discussed in Section 4, we divided our sample into four subsamples:

- (i) the Sérsic bulges of disc galaxies;
- (ii) Sérsic elliptical galaxies;
- (iii) the core-Sérsic bulges of disc galaxies;
- (iv) core-Sérsic elliptical galaxies.

We expect a different $M_{\text{BH}} - n$ relation for each of the previous subsamples, and hence we elect not to perform a single linear regression to all the data shown in Figs 4(a) and 4(b). Our symmetrical regressions have been performed for the Sérsic bulges of disc galaxies in Figs 4(a) and 4(b) and for core-Sérsic elliptical galaxies in Fig. 4(a). Due to small numbers, the statistics were not able to provide reliable regressions for core-Sérsic elliptical galaxies in Fig. 4(b), nor for Sérsic elliptical galaxies and core-Sérsic bulges in either Figs 4(a) and 4(b). Table 4 contains the results from the symmetrical regressions. All of the outliers reside more than 3σ from the linear regressions.

4 PREDICTIONS AND DISCUSSION

The $M_{\text{BH}} - n$ relation can be predicted from two other important scaling relations: the $M_{\text{BH}} - L_{\text{sph}}$ and the $L_{\text{sph}} - n$ relations, where L_{sph} is the luminosity of the galaxy's spheroidal component.

Since at least Graham (2001, his fig. 14), we have known that the $L_{\text{sph}} - n$ relation is different for elliptical galaxies and the bulges of disc galaxies. fig. 10 from Graham & Guzmán (2003) and fig. 11 from Graham (2013) display the $L_{\text{sph}} - n$ relation for elliptical galaxies (in the B -band) and for the bulges of disc galaxies (in the K_s band), respectively. In both figures, the linear regressions had been estimated ‘by eye’. We re-analysed the data from their figures and performed a symmetrical linear bisector regression analysis using the BCES routine from Akritas & Bershady (1996).

We obtained

$$M_{B,\text{sph}} = (-18.25 \pm 0.18) + (-9.01 \pm 0.47) \log(n/3)$$

for the elliptical galaxies, and

$$M_{K_s,\text{sph}} = (-23.01 \pm 0.15) + (-5.55 \pm 0.47) \log(n/3)$$

for the bulges of the disc galaxies. Here, $M_{B,\text{sph}}$ indicates the absolute B -band magnitude of elliptical galaxies and $M_{K_s,\text{sph}}$ indicates

the dust-corrected, absolute K_s -band magnitude of the bulges of disc galaxies.

We have used the $M_{\text{BH}} - L_{\text{sph}}$ relation from Graham & Scott (2013) who derived B -band and K_s -band bulge magnitudes, from the total luminosity of lenticular and spiral galaxies, through a statistical correction that takes into account inclination effects and dust absorption. Following Graham (2012), Graham & Scott (2013) derived the $M_{\text{BH}} - L_{\text{sph}}$ relation separately for core-Sérsic and Sérsic spheroids. They observed a near-linear $M_{\text{BH}} - L_{\text{sph}}$ relation for the core-Sérsic spheroids, thought to be built in additive dry merger events, and a notably (2.5 times) steeper $M_{\text{BH}} - L_{\text{sph}}$ relation for the Sérsic spheroids considered to be products of gas-rich processes. They reported

$$\log(M_{\text{BH}}) = (9.03 \pm 0.09) + (-0.54 \pm 0.12)(M_{B,\text{sph}} + 21)$$

and

$$\log(M_{\text{BH}}) = (9.05 \pm 0.09) + (-0.44 \pm 0.08)(M_{K_s,\text{sph}} + 25)$$

for their core-Sérsic subsample, whereas

$$\log(M_{\text{BH}}) = (7.37 \pm 0.15) + (-0.94 \pm 0.16)(M_{B,\text{sph}} + 19)$$

and

$$\log(M_{\text{BH}}) = (7.39 \pm 0.14) + (-1.09 \pm 0.22)(M_{K_s,\text{sph}} + 22.5)$$

for their Sérsic galaxies.

The *bent* nature of the above $M_{\text{BH}} - L_{\text{sph}}$ relations and the *linear* nature of the two distinct $L_{\text{sph}} - n$ relations for elliptical galaxies and bulges requires that there be two distinct *bent* $M_{\text{BH}} - n$ relations for elliptical galaxies and bulges. This explains the *curved* nature of the $M_{\text{BH}} - n$ relation reported by GD07. The *predicted* $M_{\text{BH}} - n$ relations, derived from the above six equations, are reported in Table 5 and shown in Fig. 5.

The expected $M_{\text{BH}} - n$ relations for the Sérsic bulges of disc galaxies and for core-Sérsic elliptical galaxies (Table 5) are marginally consistent at the 2σ level with the results from the linear regression analysis performed in Fig. 4 (Table 4). More quality data and a wider range of Sérsic indices would be beneficial to confirm the predicted relations.

For comparison, in Fig. 5 we plot 10 additional galaxies with $M_{\text{BH}} < 10^7 \text{ M}_{\odot}$ taken from the sample of Greene et al. (2008). The horizontal offset that separates the bulges of their four disc galaxies

Table 5. Predicted $M_{\text{BH}}-n$ relations.

| Type | Prediction |
|---------------------------------|---|
| Sérsic elliptical galaxies | $\log(M_{\text{BH}}) = (6.66 \pm 0.26) + (8.47 \pm 1.51) \log(n/3)$ |
| Sérsic bulges | $\log(M_{\text{BH}}) = (7.95 \pm 0.24) + (6.05 \pm 1.32) \log(n/3)$ |
| Core-Sérsic elliptical galaxies | $\log(M_{\text{BH}}) = (7.54 \pm 0.35) + (4.87 \pm 1.11) \log(n/3)$ |
| Core-Sérsic bulges | $\log(M_{\text{BH}}) = (8.17 \pm 0.19) + (2.44 \pm 0.49) \log(n/3)$ |

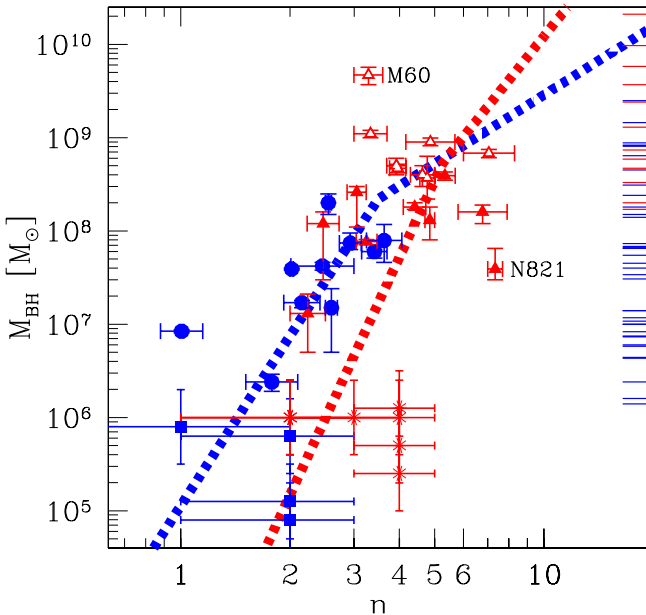


Figure 5. Same data as Fig. 4(b). For comparison, we plot four additional bulges of disc galaxies (blue squares) and six additional elliptical galaxies (red asterisks) taken from the sample of Greene, Ho & Barth (2008). The dashed lines show the predicted $M_{\text{BH}}-n$ relations for elliptical galaxies in red and for the bulges of disc galaxies in blue, given the observed $M_{\text{BH}}-L_{\text{sph}}$ and the $L_{\text{sph}}-n$ relations in the literature. The ticks on the right-hand axis indicate the black hole masses of 14 elliptical galaxies (in red) and 37 disc galaxies (in blue) that belong to the sample of Graham & Scott (2013) (and hence have a secure M_{BH} detection) but do not have multiple Sérsic index measurements.

from their six elliptical galaxies supports our predicted gap between the $M_{\text{BH}}-n$ relations for elliptical galaxies and bulges at the low-mass end of this diagram. If the bent $M_{\text{BH}}-L_{\text{sph}}$ relation is the same for all galaxies – irrespective of their morphology – this gap occurs because elliptical galaxies and the bulges of disc galaxies inhabit different regions of the $L_{\text{sph}}-n$ diagram (see fig. 14 in Graham 2001). That is, for a given light profile shape (i.e. Sérsic index n) the bulges of disc galaxies are brighter than elliptical galaxies. Fig. 5 allows one to predict that an order of magnitude gap is expected between the SMBH masses of Sérsic elliptical galaxies and the Sérsic bulges of disc galaxies having the same n .

In Fig. 5, we also show the black hole masses of 51 galaxies that belong to the sample of Graham & Scott (2013) but do not have multiple Sérsic index measurements. Among them, 13 are core-Sérsic elliptical galaxies, 5 are core-Sérsic bulges of disc galaxies, 1 is a Sérsic elliptical galaxy and 32 are Sérsic bulges of disc galaxies. We point out that measuring the Sérsic indices of these galaxies could add many useful points to the $M_{\text{BH}}-n$ diagram. In particular, the 13 extra core-Sérsic elliptical galaxies would allow one to better explore the $M_{\text{BH}}-n$ diagram in the high- M_{BH} end, between 10^8 and $10^{10} M_{\odot}$, where most galaxies are thought to

have formed from a different process, namely dry major mergers. Similarly, there are an additional 10 Sérsic bulges of disc galaxies with $M_{\text{BH}} < 10^7 M_{\odot}$ that could extend the low- M_{BH} end of the correlation.

The Sérsic index is a slight function of the observational bandpass. This dependence of galaxy structural parameters with wavelength arises due to radial gradients in the stellar population gradients and/or dust obscuration (Kelvin et al. 2012). We therefore plan to perform accurate galaxy image decompositions for all the galaxies belonging to the sample of Graham & Scott (2013) – with a directly measured SMBH mass – to explore the $M_{\text{BH}}-n$ relation and other black hole mass scaling relations in a homogeneous analysis (same observational bandpass and same light profile decomposition method).

Finally, we compare the results from this work with those from GD07, highlighting two main points. First, and similar to our sample, the galaxy sample used by GD07 was dominated (~ 80 per cent) by disc galaxies in the low-mass end ($M_{\text{BH}} < 10^8 M_{\odot}$) and by elliptical galaxies (~ 80 per cent) in the high-mass end ($M_{\text{BH}} > 10^8 M_{\odot}$). Secondly, GDO7 measured a Sérsic index greater than 10 for three spheroids with $M_{\text{BH}} \sim 10^9 M_{\odot}$, which are absent in Fig. 4(b). Combining the different galaxy types and fitting a single relation, it is easy to understand why a quadratic relation would be more appropriate than a single log-linear relation to describe their data. At $n = 3$ ($M_{\text{BH}} \sim 10^8 M_{\odot}$), their quadratic relation has a slope of 3.70 ± 0.46 , similar to that observed for our Sérsic bulges.

5 SUMMARY AND CONCLUSIONS

The $M_{\text{BH}}-n$ relation (GD07) is important for any complete theory or model to describe the co-evolution of galaxies and SMBHs. It also provides a means to estimate black hole masses in galaxies and may prove fruitful for recent and future deep, wide-field photometric surveys of galaxies which can statistically estimate the black hole masses in a large sample of galaxies up to $z \sim 0.1$. The main motivation of this work was to re-investigate the $M_{\text{BH}}-n$ relation, given a recent spate of papers which did not detect it. We have gone beyond the simple recovery of the $M_{\text{BH}}-n$ relation, and explored potential substructures in this diagram in terms of distinct relations for Sérsic and core-Sérsic galaxies, and for bulges and elliptical galaxies.

We compiled a large collection of literature Sérsic index measurements GD07, S11, V12, B12 for a sample of 62 galaxies with directly measured SMBH masses. We compared multiple Sérsic index measurements which existed for 35 galaxies, and found relative differences greater than 50 per cent in many instances. This is more than expected from a systematic bias produced by different types of light profile modelling (1D or 2D) or different observational bandpasses. We therefore excluded the outlying Sérsic indices and averaged the remaining values. This exclusion resulted in the removal of eight galaxies. Our final sample therefore consists of 54 galaxies: among them, 27 had Sérsic indices measured only by one

study and the remaining 27 have an averaged Sérsic index measurement.

Our principal conclusions are as follows.

(i) The $M_{\text{BH}} - n$ diagram (Fig. 4) displays an appreciable correlation.

(ii) The results from the symmetrical linear regressions (Fig. 4) are consistent at the 2σ level with predictions (Fig. 5) obtained by combining the $M_{\text{BH}} - L_{\text{sph}}$ relations for core-Sérsic and Sérsic galaxies with the $L_{\text{sph}} - n$ relations for elliptical galaxies and the bulges of disc galaxies.

(iii) If Sérsic bulges and Sérsic elliptical galaxies follow the same $M_{\text{BH}} - L_{\text{sph}}$ relation, then an order of magnitude gap is expected between the SMBH masses of Sérsic elliptical galaxies and the Sérsic bulges of disc galaxies having the same n .

A wider range of Sérsic indices would be beneficial to put tighter constraints on the observed slopes of the correlations. The catalogue of 80 directly measured SMBH masses compiled by Graham & Scott (2013) allows one to explore the $M_{\text{BH}} - n$ diagram in the low- and high-mass end. We recognize the need for a well-calibrated $M_{\text{BH}} - n$ relation and plan to perform accurate galaxy light profile decompositions to refine the black hole mass scaling relations.

ACKNOWLEDGEMENTS

GS thanks Dr Nicholas Scott for useful discussions. This research was supported by Australian Research Council funding through grants DP110103509 and FT110100263. AM, LKH, ES acknowledge support from grants PRIN-MIUR 2010-2011 ‘The dark Universe and the cosmic evolution of baryons: from current surveys to Euclid’ and PRIN-INAF 2011 ‘Black hole growth and AGN feedback through the cosmic time’. This research has made use of the GOLDMine data base (Gavazzi et al. 2003) and the NASA/IPAC Extragalactic Database (NED) which is operated by the Jet Propulsion Laboratory, California Institute of Technology, under contract with the National Aeronautics and Space Administration.

REFERENCES

- Abazajian K. N. et al., 2009, *ApJS*, 182, 543
 Akritas M. G., Bershady M. A., 1996, *ApJ*, 470, 706
 Allen P. D., Driver S. P., Graham A. W., Cameron E., Liske J., de Propris R., 2006, *MNRAS*, 371, 2
 Andredakis Y. C., Peletier R. F., Balcells M., 1995, *MNRAS*, 275, 874
 Beifiori A., Courteau S., Corsini E. M., Zhu Y., 2012, *MNRAS*, 419, 2497 (B12)
 Berrier J. C. et al., 2013, *ApJ*, 769, 2
 Caon N., Capaccioli M., D’Onofrio M., 1993, *MNRAS*, 265, 1013
 Davis B. L., Berrier J. C., Shields D. W., Kennefick J., Kennefick D., Seigar M. S., Lacy C. H. S., Puerari I., 2013, *ApJS*, 199, 33
 de Vaucouleurs G., de Vaucouleurs A., Corwin H. G., Jr, Buta R. J., Paturel G., Fouqué P., 1991, *Third Reference Catalogue of Bright Galaxies*. Springer, New York (RC3)
 Driver S. P. et al., 2011, *MNRAS*, 413, 971
 Erwin P., Graham A. W., Caon N., 2004, *Coevolution of Black Holes and Galaxies*, Cambridge Univ. Press, Cambridge
 Ferrarese L., Merritt D., 2000, *ApJ*, 539, L9
 Ferrarese L. et al., 2006, *ApJS*, 164, 334
 Ferrari F., Dotti H., Caon N., Nobrega A., Pavani D. B., 2004, *MNRAS*, 347, 824
 Freeman K. C., 1970, *ApJ*, 160, 811
 Gadotti D. A., 2008, *MNRAS*, 384, 420
 Gavazzi G., Boselli A., Donati A., Franzetti P., Scodellaggio M., 2003, *A&A*, 400, 451
 Gavazzi G., Donati A., Cucciati O., Sabatini S., Boselli A., Davies J., Zibetti S., 2005, *A&A*, 430, 411
 Gebhardt K. et al., 2000, *ApJ*, 539, L13
 Graham A. W., 2013, in Oswalt T. D., Keel W. C., eds, *Planets, Stars and Stellar Systems*, Volume 6. Springer, Berlin, p. 91
 Graham A. W., 2001, *AJ*, 121, 820
 Graham A. W., 2008, *ApJ*, 680, 143
 Graham A. W., 2012, *ApJ*, 746, 113
 Graham A. W., Driver S. P., 2005, *PASA*, 22, 118
 Graham A. W., Driver S. P., 2007a, *MNRAS*, 380, L15
 Graham A. W., Driver S. P., 2007b, *ApJ*, 655, 77 (GD07)
 Graham A. W., Guzmán R., 2003, *AJ*, 125, 2936
 Graham A. W., Scott N., 2013, *ApJ*, 764, 151
 Graham A. W., Erwin P., Caon N., Trujillo I., 2001, *ApJ*, 563, L11
 Graham A. W., Erwin P., Trujillo I., Asensio Ramos A., 2003, *AJ*, 125, 2951
 Graham A. W., Driver S. P., Allen P. D., Liske J., 2007, *MNRAS*, 378, 198
 Graham A. W., Onken C. A., Athanassoula E., Combes F., 2011, *MNRAS*, 412, 2211
 Greene J. E., Ho L. C., Barth A. J., 2008, *ApJ*, 688, 159
 Häring N., Rix H.-W., 2004, *ApJ*, 604, L89
 Hunt L. K., Pierini D., Giovanardi C., 2004, *A&A*, 414, 905
 Jerjen H., Binggeli B., Freeman K. C., 2000, *AJ*, 119, 593
 Kahane D., Moler C., Nash S., 1989, *Numerical Methods and Software*. Englewood Cliffs: Prentice Hall
 Kelly B. C., 2007, *ApJ*, 665, 1489
 Kelvin L. S. et al., 2012, *MNRAS*, 421, 1007
 Kormendy J., Richstone D., 1995, *ARA&A*, 33, 581
 Laor A., 2001, *ApJ*, 553, 677
 Lauer T. R., Tremaine S., Richstone D., Faber S. M., 2007, *ApJ*, 670, 249
 Lawrence A. et al., 2007, *MNRAS*, 379, 1599
 Magorrian J. et al., 1998, *AJ*, 115, 2285
 Marconi A., Hunt L. K., 2003, *ApJ*, 589, L21
 McLure R. J., Dunlop J. S., 2002, *MNRAS*, 331, 795
 Méndez-Abreu J., Aguerri J. A. L., Corsini E. M., Simonneau E., 2008, *A&A*, 478, 353
 Pastrav B. A., Popescu C. C., Tuffs R. J., Sansom A. E., 2013, *A&A*, 553, A80
 Peng C. Y., Ho L. C., Impey C. D., Rix H.-W., 2002, *AJ*, 124, 266
 Peng C. Y., Ho L. C., Impey C. D., Rix H.-W., 2010, *AJ*, 139, 2097
 Sani E., Marconi A., Hunt L. K., Risaliti G., 2011, *MNRAS*, 413, 1479 (S11)
 Scott N., Graham A. W., Schombert J., 2013, *ApJ*, 768, 76
 Sérsic J.-L., 1963, *Boletin de la Asociacion Argentina de Astronomia La Plata Argentina*, 6, 41
 Sérsic J.-L., 1968, *Atlas de Galaxias Australes*. Observatorio Astronomico. Cordoba
 Simard L. et al., 2002, *ApJS*, 142, 1
 Simard L., Mendel J. T., Patton D. R., Ellison S. L., McConnachie A. W., 2011, *ApJS*, 196, 11
 Trujillo I., Erwin P., Asensio Ramos A., Graham A. W., 2004, *AJ*, 127, 1917
 Vika M., Driver S. P., Cameron E., Kelvin L., Robotham A., 2012, *MNRAS*, 419, 2264 (V12)
 York D. G. et al., 2000, *AJ*, 120, 1579
 Young C. K., Currie M. J., 1994, *MNRAS*, 268, L11

APPENDIX A

Section 2.4 illustrates the method we used to combine multiple Sérsic index measurements of the same galaxy. These came from four different studies among which only one (GD07) reported a strong $M_{\text{BH}} - n$ relation.

To check the consistency and the robustness of our results, here we repeat the analysis excluding all the GD07 measurements. Fig. A1(a), which can be compared to Fig. 4(a), still displays a correlation, although it is more noisy at the high-mass end

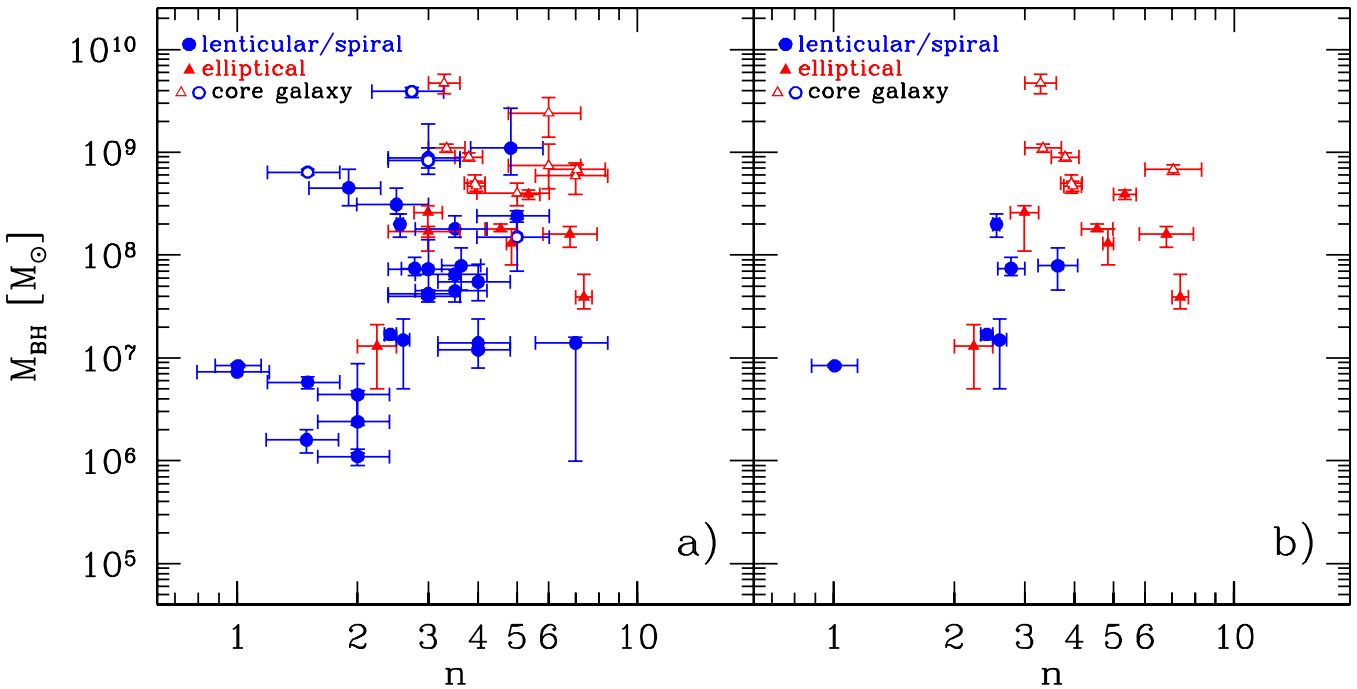


Figure A1. Same as Fig. 4 but excluding all the GD07 measurements.

(Spearman's correlation coefficient $r_s(47) = 0.38$, likelihood of the correlation occurring by chance $P < 1$ per cent). Hence, we conclude that the inclusion of the GD07 data did not force the recovery of the $M_{\text{BH}} - n$ relation(s). However, the two galaxies previously identified as outliers in Fig. 4(b) reduce the strength of the correlation vsp

in Fig. A1(b) to a likelihood of the correlation occurring by chance to $P < 5$ per cent.

This paper has been typeset from a TeX/LaTeX file prepared by the author.

3

Galaxy Vivisection

The preliminary investigation presented in Chapter 2 (Savorgnan et al., 2013) demonstrated the need for a new, systematic and homogeneous study aimed at obtaining more accurate galaxy decompositions and refining our knowledge about black hole mass scaling relations. In 2013, I visited A. Marconi, E. Sani, and L. K. Hunt (co-authors of the paper Sani et al. 2011) in Arcetri (Florence) for a short collaboration, during which I was shown their 2D galaxy decomposition method using GALFIT3 (Peng et al., 2010). This helped set the basis for the development of my own galaxy decomposition strategy, which is detailed in this Chapter.

Building on the catalog of Graham & Scott (2013) with the addition of some new black hole mass measurements later published by Rusli et al. (2013), I assembled my initial sample of 75 galaxies. For the imaging data, I chose to use *Spitzer* archival observations at $3.6\text{ }\mu\text{m}$ for three main reasons: (*i*) the $3.6\text{ }\mu\text{m}$ passband is currently the best proxy for the stellar mass (Sheth et al. 2010, and references therein); (*ii*) archival observations were publicly available for the majority of the galaxies in my initial sample; and (*iii*) within a *Spitzer* observation set of a galaxy, roughly half of the telescope pointings are dedicated to the imaging of the surrounding sky, ensuring a robust background determination during the data reduction process¹. While for each galaxy Sani et al. (2011) used only one set of *Spitzer* astronomical observations, I downloaded all the publicly available observation sets and merged them into a single mosaic with higher signal-to-noise. I paid particular attention to (and invested a consistent amount of time into) the characterisation of the 2D Point Spread Function (PSF), following the expert advice

¹These three points put together led me to prefer *Spitzer* rather than *HST* observations, albeit the lower spatial resolution.

of C. Peng.

Being aware of the importance of choosing the correct galaxy model in order to obtain reliable and meaningful structural parameters, I embraced the approach of Laurikainen et al. (2005) and planned *a priori* identification of the number and nature of the structural components in each galaxy. Given the lack of reference literature about advantages and disadvantages related to 1D and 2D decomposition techniques, I decided to experiment with both.

I wrote substantial software to perform 1D decomposition of surface brightness profiles. This code is written in Python and is based on the Levenberg-Marquardt minimisation routine of the `scipy.optimize` module. This software allows the user to build a galaxy model with any arbitrary number of analytical functions (Sérsic, exponential, Gaussian, Ferrer, etc.). Because the code is written in an object-oriented fashion, it is particularly easy to implement any new analytical function into it.

For the 2D analysis, I experimented with the codes GALFIT3 (Peng et al., 2010) and Imfit (Erwin, 2015). After checking that both codes give consistent results, I preferred the more script-oriented Imfit over GALFIT3.

The NASA/IPAC Extragalactic Database (NED) has been an invaluable resource for the structural analysis of galaxies. NED lists all the literature references contained in the SAO/NASA Astrophysics Data System (ADS) which mentioned a particular galaxy. Thanks to this functionality, I was able to search for previous photometric and kinematic analyses, structural decompositions, information about the nuclear activity, presence of dust or peculiar features, and any other detail that could be useful to the analysis of my galaxies.

The remainder of this Chapter comprises the published version of the paper “Supermassive Black Holes and Their Host Spheroids. I. Disassembling Galaxies” by G. A. D. Savorgnan & A. W. Graham, as it appears in Volume 222 of the *The Astrophysical Journal Supplement Series*.



SUPERMASSIVE BLACK HOLES AND THEIR HOST SPHEROIDS. I. DISASSEMBLING GALAXIES

G. A. D. SAVORGNA AND A. W. GRAHAM

Centre for Astrophysics and Supercomputing, Swinburne University of Technology, Hawthorn, Victoria 3122, Australia; gsavorgn@astro.swin.edu.au

Received 2015 July 16; accepted 2015 November 19; published 2016 January 19

ABSTRACT

Several recent studies have performed galaxy decompositions to investigate correlations between the black hole mass and various properties of the host spheroid, but they have not converged on the same conclusions. This is because their models for the same galaxy were often significantly different and not consistent with each other in terms of fitted components. Using $3.6\text{ }\mu\text{m}$ *Spitzer* imagery, which is a superb tracer of the stellar mass (superior to the K band), we have performed state-of-the-art multicomponent decompositions for 66 galaxies with directly measured black hole masses. Our sample is the largest to date and, unlike previous studies, contains a large number (17) of spiral galaxies with low black hole masses. We paid careful attention to the image mosaicking, sky subtraction, and masking of contaminating sources. After a scrupulous inspection of the galaxy photometry (through isophotal analysis and unsharp masking) and—for the first time—2D kinematics, we were able to account for spheroids; large-scale, intermediate-scale, and nuclear disks; bars; rings; spiral arms; halos; extended or unresolved nuclear sources; and partially depleted cores. For each individual galaxy, we compared our best-fit model with previous studies, explained the discrepancies, and identified the optimal decomposition. Moreover, we have independently performed one-dimensional (1D) and two-dimensional (2D) decompositions and concluded that, at least when modeling large, nearby galaxies, 1D techniques have more advantages than 2D techniques. Finally, we developed a prescription to estimate the uncertainties on the 1D best-fit parameters for the 66 spheroids that takes into account systematic errors, unlike popular 2D codes that only consider statistical errors.

Key words: black hole physics – galaxies: bulges – galaxies: elliptical and lenticular, cD – galaxies: evolution – galaxies: structure

1. INTRODUCTION

Supermassive black holes and their host spheroids¹ have very different sizes. If the event horizon of the Galactic supermassive black hole was as big as a grain of sand in the Sahara Desert, then the black hole’s gravitational sphere of influence would be as big as the international airport of Cairo, and the Galactic bulge would be as big as the Sahara Desert itself. It is thus surprising that the masses of supermassive black holes (M_{BH}) scale with a number of properties of their host spheroid, indicating the nongravitational origin of these correlations (e.g., Dressler 1989; Yee 1992; Kormendy & Richstone 1995; Laor et al. 1997; Magorrian et al. 1998; Ferrarese & Merritt 2000; Gebhardt et al. 2000; Graham et al. 2001; Marconi & Hunt 2003; Häring & Rix 2004; Graham & Scott 2015).

The tightness of (i.e., the small scatter about) the above observed black hole mass correlations has led to the idea that black holes and host spheroids have coevolved with some sort of self-regulated growth. Exploring the evolution of this growth with cosmic time could help identify the driving mechanisms of the black hole–spheroid coevolution. Observations at $z = 0$ set the local benchmark from which to measure this evolution. Any complete theory or model describing the coevolution of spheroids and black holes must incorporate all of the observed scaling relations, which also have to be consistent with each other. Modern hydrodynamical simulations, such as EAGLE (Schaye et al. 2015), calibrate the feedback efficiencies to match the $z = 0$ black hole mass–galaxy mass relation. The observed scaling relations can also be employed to predict the

masses of black holes in other galaxies, where a direct measure of M_{BH} would be extremely time-consuming or simply impossible owing to technological limitations. Moreover, many accurate M_{BH} predictions enable one to derive the local black hole mass function (e.g., Salucci et al. 1999; Graham et al. 2007; Shankar 2009, 2013; Fontanot et al. 2015) and space density (e.g., Graham & Driver 2007b; Comastri et al. 2015). All of these examples depend on the $z = 0$ relations, and as such the recalibration of the black hole mass–spheroid stellar mass ratio ($M_{\text{BH}}/M_{*,\text{sph}}$) in large spheroids, from 0.1% to 0.2% (e.g., Marconi & Hunt 2003; Häring & Rix 2004) to 0.49% (Graham & Scott 2015), has many substantial implications.

Since the early stellar dynamical detections of black holes were carried out in the 1980s (see the references in the reviews by Kormendy & Richstone 1995; Richstone et al. 1998; Graham 2015 for pioneering papers), the number of (direct) black hole mass measurements has increased with time and it has recently become a statistically meaningful sample with which one can study SMBH demographics. It is now generally accepted that supermassive black holes reside at the center of most, if not all, massive spheroids, either quiescent or active.

Massive, early-type (E, E/S0, S0) galaxies are often composite systems. The knowledge that many “elliptical” (E) galaxies were misclassified and actually contain embedded stellar disks dates back at least three decades (Capaccioli 1987; Carter 1987; Bender 1990; Rix & White 1990, 1992; Scorz & Bender 1990, 1995; Nieto et al. 1991). After examining long-slit and integral field unit spectroscopic observations of morphologically classified elliptical galaxies in the Fornax Cluster, D’Onofrio et al. (1995), Graham et al. (1998), and Scott et al. (2014) concluded that only three bright galaxies do not harbor a disk-like component. Larger surveys with integral

¹ By the term “spheroid” we mean either an elliptical galaxy or the bulge component of a disk galaxy, with no attempt at distinguishing between classical bulges and disk-like pseudobulges.

field spectrographs of early-type galaxies, such as the ATLAS^{3D} Project (Cappellari et al. 2011), have further advanced this view of “elliptical” galaxies being all but simple and featureless pressure-supported systems. Most of the morphologically classified elliptical galaxies in the ATLAS^{3D} sample are fast rotators (Emsellem et al. 2011). Krajnović et al. (2013) showed that “fast rotators” as a class are disk galaxies or at least disk-like galaxies. In their magnitude-limited survey, systems without any signature of disk-like components (neither in the kinematics nor in the photometry) dominate only the most massive end (with stellar masses beyond $10^{11.5} M_{\odot}$) of the distribution. Given the prevalence of disks, it is clearly important to perform spheroid/disk decompositions, if one is to properly explore the black hole–spheroid connection. Indeed, separating the disk light from that of the bulge has led to the discovery of the missing population of compact, massive spheroids in the local universe (Graham et al. 2015). If we are to properly understand the evolution of galaxies, we need to understand their components.

Measuring the photometric and structural properties of a galaxy’s spheroidal component requires the ability to separate it from the rest of the galaxy. Such galaxy decomposition involves a parametric analysis that allows one to fit the surface brightness distribution of galaxies using a combination of analytic functions (usually one function per galaxy component, such as spheroids, disks, bars, nuclei, etc.). The one-dimensional (1D) technique involves fitting isophotes to the galaxy image, extracting the (1D) surface brightness radial profile, and modeling it with a combination of analytic functions. With the two-dimensional (2D) technique, one fits analytic functions directly to the 2D images.

Over the past 8 yr, five independent studies (Graham & Driver 2007a; Sani et al. 2011; Beifiori et al. 2012; Vika et al. 2012; Läsker et al. 2014a, 2014b) have attempted galaxy decomposition in order to derive the spheroid parameters and explore their relation with the black hole masses. Interestingly, the past studies used almost the same sample of galaxies, yet they claimed some contradictory conclusions. For example, one study (Graham & Driver 2007a) obtained a good $M_{\text{BH}} - n_{\text{sph}}$ correlation (the spheroid Sérsic index n_{sph} is a measure of the central radial concentration of stars; Trujillo et al. 2001), whereas the remaining four did not.² In addition, Läsker et al. (2014b) declared that M_{BH} correlates equally well with the total galaxy luminosity as it does with the spheroid luminosity, as opposed to Beifiori et al. (2012), who claimed that the spheroid mass is a better tracer of M_{BH} than the galaxy mass (see also Kormendy & Gebhardt 2001; Erwin & Gadotti 2012). The past studies did not converge to the same conclusions because their best-fit models for the same galaxy were often significantly different and not consistent with each other in terms of fitted components. Moreover, none of these studies attempted an individual galaxy-by-galaxy comparison of their models with the previous literature. We have now made this comparison and performed the optimal decompositions, using 3.6 μm *Spitzer* satellite imagery, which is an excellent proxy for the stellar mass, superior to the K band (Jun & Im 2008; Sheth et al. 2010). We will use these in a series of forthcoming papers to obtain improved black hole mass scaling relations

² Savorgnan et al. (2013) showed that, by rejecting the most discrepant Sérsic index measurements and averaging the remaining ones, a strong $M_{\text{BH}} - n_{\text{sph}}$ correlation was recovered.

using the largest sample (66) of galaxies to date with accurate spheroid properties.

This paper is structured as follows. Section 2 presents the galaxy sample and imaging data set used to conduct this study. Section 3 describes how we performed the galaxy decompositions, i.e., how we identified and modeled the subcomponents that constitute our galaxies. In Section 4 we outline the results from our analysis and discuss the error analysis. Section 5 summarizes our main conclusions. The individual galaxy decompositions are made available in the electronic version of this manuscript.

2. DATA

Our initial galaxy sample (see Table 1) consists of 75 objects for which a dynamical detection of the black hole mass had been reported in the literature at the time we started this project, and for which at least one 3.6 μm *Spitzer*/IRAC³ observation was publicly available. Black hole masses were drawn from the catalog of Graham & Scott (2013) for 70 galaxies, from Rusli et al. (2013b) for four galaxies, and from Greenhill et al. (2003) for one galaxy. As explained in Section 4, this initial sample was ultimately reduced to 66 galaxies for which useful spheroid parameters could be obtained.

2.1. Spitzer/IRAC Observations

2.1.1. Data Acquisition

For each of our 75 galaxies, we downloaded from the Spitzer Heritage Archive⁴ all the available 3.6 μm IRAC Astronomical Observation Requests (AORs). Each AOR is an individual *Spitzer* observation sequence and includes a number of data frames (the individual exposures) and the calibration data. The data frames were selected to be corrected basic calibrated data (cBCD), produced by the IRAC Level 1 pipeline. This automatic pipeline takes a single “raw” image, removes the scattered light, and performs dark subtraction, flat-fielding correction, and flux calibration (into units of MJy sr⁻¹). The final product (the BCD) is a flux-calibrated image that has had all the well-understood instrumental signatures removed. BCD frames are further processed through an “artifact correction” pipeline that mitigates the commonly found artifacts of stray light, saturation, “muxbleed,” and column pulldown.⁵ After the artifact correction has been applied, the BCD becomes a cBCD.

2.1.2. Mosaicking

We performed image mosaicking using the MOPEX package (Makovoz & Marleau 2005). This enabled the production of suitably wide field-of-view images for accurate sky background subtraction. Individual cBCD frames with exposure time of 1 s were rejected. Permanent or semipermanent bad pixels, contained in a semistatic mask (the “pmask”), were ignored. Each AOR is associated with a specific pmask. Therefore, when multiple AORs were available for the same

³ IRAC is the InfraRed Array Camera on board the *Spitzer Space Telescope*.

⁴ <http://irsa.ipac.caltech.edu/applications/Spitzer/SHA/>

⁵ Stray light includes scattered light from stars outside the array location, as well as filter ghosts from bright stars. Multiplexer bleed, or “muxbleed,” can be generated by stars, hot pixels, and particle hits. It appears as a decaying trail of pixels, repeating every fourth column. “Column pulldown” is caused by a bright pixel that triggers a bias shift within its respective column, creating a lower background value throughout the entire column than in the surrounding columns.

Table 1
Galaxy Sample

| Galaxy | Distance (Mpc) | M_{BH} ($10^8 M_{\odot}$) | Ref. | Core (arcsec) | Ref. | Rot. | Vel. Map | 1D Fit | 2D Fit |
|----------|-------------------|---|-------|------------------|-------------|------|----------|--------|--------|
| (1) | (2) | (3) | (4) | (5) | (6) | (7) | (8) | (9) | (10) |
| Circinus | 4.0 | $0.017^{+0.004}_{-0.003}$ | G+03 | no? | ... | ... | ... | no | no |
| IC 1459 | 28.4 | 24^{+10}_{-10} | GS13 | yes (0.7) | R+13a | ... | ... | yes | yes |
| IC 2560 | 40.7 | $0.044^{+0.044}_{-0.022}$ | GS13 | no? | ... | ... | ... | yes | no |
| IC 4296 | 40.7 | 11^{+2}_{-2} | GS13 | yes? | ... | ... | ... | yes | yes |
| M31 | 0.7 | $1.4^{+0.9}_{-0.3}$ | GS13 | no | ... | ... | ... | yes | no |
| M32 | 0.8 | $0.024^{+0.005}_{-0.005}$ | GS13 | no | ... | ... | ... | no | no |
| M49 | 17.1 | 25^{+3}_{-1} | R+13b | yes (1.5) | DG13, R+13a | SLOW | A | yes | yes |
| M59 | 17.8 | $3.9^{+0.4}_{-0.4}$ | GS13 | no | ... | FAST | A | yes | no |
| M60 | 16.4 | 47^{+10}_{-10} | GS13 | yes (2.7) | DG13, R+13a | FAST | A, S | no | no |
| M64 | 7.3 | $0.016^{+0.004}_{-0.004}$ | GS13 | no? | ... | ... | ... | yes | no |
| M77 | 15.2 | $0.084^{+0.003}_{-0.003}$ | GS13 | no | ... | ... | ... | no | no |
| M81 | 3.8 | $0.74^{+0.21}_{-0.11}$ | GS13 | no | ... | ... | ... | yes | no |
| M84 | 17.9 | $9.0^{+0.9}_{-0.8}$ | GS13 | yes (1.9) | F+06 | SLOW | A, S | yes | yes |
| M87 | 15.6 | $58.0^{+3.5}_{-3.5}$ | GS13 | yes (7.2) | F+06 | SLOW | A, S | yes | yes |
| M89 | 14.9 | $4.7^{+0.5}_{-0.5}$ | GS13 | yes (0.4) | DG13, R+13a | SLOW | A | yes | no |
| M94 | 4.4 | $0.060^{+0.014}_{-0.014}$ | GS13 | no? | ... | ... | ... | yes | no |
| M96 | 10.1 | $0.073^{+0.015}_{-0.015}$ | GS13 | no | ... | ... | ... | yes | yes |
| M104 | 9.5 | $6.4^{+0.4}_{-0.4}$ | GS13 | yes | J+11 | ... | ... | yes | no |
| M105 | 10.3 | 4^{+1}_{-1} | GS13 | yes (1.1) | DG13, R+13a | FAST | A | yes | yes |
| M106 | 7.2 | $0.39^{+0.01}_{-0.01}$ | GS13 | no | ... | ... | ... | yes | no |
| NGC 0253 | 3.5 | $0.10^{+0.10}_{-0.05}$ | GS13 | no | ... | ... | ... | no | no |
| NGC 0524 | 23.3 | $8.3^{+2.7}_{-1.3}$ | GS13 | yes (0.2) | R+11 | FAST | A | yes | no |
| NGC 0821 | 23.4 | $0.39^{+0.26}_{-0.09}$ | GS13 | no | ... | FAST | A, S | yes | yes |
| NGC 1023 | 11.1 | $0.42^{+0.04}_{-0.04}$ | GS13 | no | ... | FAST | A, S | yes | yes |
| NGC 1300 | 20.7 | $0.73^{+0.69}_{-0.35}$ | GS13 | no | ... | ... | ... | yes | no |
| NGC 1316 | 18.6 | $1.50^{+0.75}_{-0.80}$ | GS13 | no | ... | FAST | ... | yes | no |
| NGC 1332 | 22.3 | 14^{+2}_{-2} | GS13 | no | ... | ... | ... | yes | no |
| NGC 1374 | 19.2 | $5.8^{+0.5}_{-0.5}$ | R+13b | no? | ... | FAST | A | yes | yes |
| NGC 1399 | 19.4 | $4.7^{+0.6}_{-0.6}$ | GS13 | yes (2.4) | DG13, R+13a | SLOW | A | yes | no |
| NGC 2273 | 28.5 | $0.083^{+0.004}_{-0.004}$ | GS13 | no | ... | ... | ... | yes | no |
| NGC 2549 | 12.3 | $0.14^{+0.02}_{-0.13}$ | GS13 | no | ... | FAST | A | yes | yes |
| NGC 2778 | 22.3 | $0.15^{+0.09}_{-0.10}$ | GS13 | no | ... | FAST | A | yes | no |
| NGC 2787 | 7.3 | $0.40^{+0.04}_{-0.05}$ | GS13 | no | ... | ... | ... | yes | no |
| NGC 2974 | 20.9 | $1.7^{+0.2}_{-0.2}$ | GS13 | no | ... | FAST | A, S | yes | yes |
| NGC 3079 | 20.7 | $0.024^{+0.024}_{-0.012}$ | GS13 | no? | ... | ... | ... | yes | no |
| NGC 3091 | 51.2 | 36^{+1}_{-2} | R+13b | yes (0.6) | R+13a | ... | ... | yes | yes |
| NGC 3115 | 9.4 | $8.8^{+10.0}_{-2.7}$ | GS13 | no | ... | ... | S | yes | no |
| NGC 3227 | 20.3 | $0.14^{+0.10}_{-0.06}$ | GS13 | no | ... | ... | ... | yes | no |
| NGC 3245 | 20.3 | $2.0^{+0.5}_{-0.5}$ | GS13 | no | ... | FAST | A | yes | yes |
| NGC 3377 | 10.9 | $0.77^{+0.04}_{-0.06}$ | GS13 | no | ... | FAST | A, S | yes | yes |
| NGC 3384 | 11.3 | $0.17^{+0.01}_{-0.02}$ | GS13 | no | ... | FAST | A | yes | no |
| NGC 3393 | 55.2 | $0.34^{+0.02}_{-0.02}$ | GS13 | no | ... | ... | ... | yes | yes |
| NGC 3414 | 24.5 | $2.4^{+0.3}_{-0.3}$ | GS13 | no | ... | SLOW | A | yes | no |
| NGC 3489 | 11.7 | $0.058^{+0.008}_{-0.008}$ | GS13 | no | ... | FAST | A | yes | yes |
| NGC 3585 | 19.5 | $3.1^{+1.4}_{-0.6}$ | GS13 | no | ... | ... | ... | yes | no |
| NGC 3607 | 22.2 | $1.3^{+0.5}_{-0.5}$ | GS13 | no | ... | FAST | A | yes | yes |
| NGC 3608 | 22.3 | $2.0^{+1.1}_{-0.6}$ | GS13 | yes (0.2) | DG13, R+13a | SLOW | A, S | yes | yes |
| NGC 3842 | 98.4 | 97^{+30}_{-26} | GS13 | yes (0.7) | DG13, R+13a | ... | ... | yes | no |
| NGC 3998 | 13.7 | $8.1^{+2.0}_{-1.9}$ | GS13 | no | ... | FAST | A | yes | no |
| NGC 4026 | 13.2 | $1.8^{+0.6}_{-0.3}$ | GS13 | no | ... | FAST | A | yes | no |
| NGC 4151 | 20.0 | $0.65^{+0.07}_{-0.07}$ | GS13 | no | ... | ... | ... | yes | no |
| NGC 4261 | 30.8 | 5^{+1}_{-1} | GS13 | yes (1.6) | R+11 | SLOW | A | yes | yes |
| NGC 4291 | 25.5 | $3.3^{+0.9}_{-2.5}$ | GS13 | yes (0.3) | DG13, R+13a | ... | ... | yes | yes |
| NGC 4342 | 23.0 | $4.5^{+2.3}_{-1.5}$ | GS13 | no | ... | FAST | A | no | no |
| NGC 4388 | 17.0 | $0.075^{+0.002}_{-0.002}$ | GS13 | no? | ... | ... | ... | yes | no |
| NGC 4459 | 15.7 | $0.68^{+0.13}_{-0.13}$ | GS13 | no | ... | FAST | A | yes | no |

Table 1
(Continued)

| Galaxy | Distance (Mpc) | M_{BH} ($10^8 M_{\odot}$) | Ref. | Core (arcsec) | Ref. | Rot. | Vel. Map | 1D Fit | 2D Fit |
|-----------|-------------------|---|-------|------------------------|-------------|------|----------|--------|--------|
| (1) | (2) | (3) | (4) | (5) | (6) | (7) | (8) | (9) | (10) |
| NGC 4473 | 15.3 | $1.2^{+0.4}_{-0.9}$ | GS13 | no | ... | FAST | A, S | yes | yes |
| NGC 4486A | 17.0 | $0.13^{+0.08}_{-0.08}$ | GS13 | no | ... | FAST | A | no | no |
| NGC 4564 | 14.6 | $0.60^{+0.03}_{-0.09}$ | GS13 | no | ... | FAST | A | yes | no |
| NGC 4596 | 17.0 | $0.79^{+0.38}_{-0.33}$ | GS13 | no | ... | FAST | A | yes | no |
| NGC 4697 | 11.4 | $1.8^{+0.2}_{-0.1}$ | GS13 | no | ... | FAST | A, S | yes | yes |
| NGC 4889 | 103.2 | 210^{+160}_{-160} | GS13 | yes (1.7) | F+97 | ... | ... | yes | yes |
| NGC 4945 | 3.8 | $0.014^{+0.014}_{-0.007}$ | GS13 | no? | ... | ... | ... | yes | yes |
| NGC 5077 | 41.2 | $7.4^{+4.7}_{-3.0}$ | GS13 | yes (0.3) | T+04 | ... | ... | yes | yes |
| NGC 5128 | 3.8 | $0.45^{+0.17}_{-0.10}$ | GS13 | no? | ... | ... | ... | yes | no |
| NGC 5576 | 24.8 | $1.6^{+0.3}_{-0.4}$ | GS13 | no | ... | SLOW | A | yes | yes |
| NGC 5813 | 31.3 | $6.8^{+0.7}_{-0.7}$ | GS13 | yes (0.4) | DG13, R+13a | SLOW | A | no | no |
| NGC 5845 | 25.2 | $2.6^{+0.4}_{-1.5}$ | GS13 | no | ... | FAST | A | yes | yes |
| NGC 5846 | 24.2 | 11^{+1}_{-1} | GS13 | yes | F+97 | SLOW | A, S | yes | yes |
| NGC 6251 | 104.6 | 5^{+2}_{-2} | GS13 | yes? | ... | ... | ... | yes | yes |
| NGC 7052 | 66.4 | $3.7^{+2.6}_{-1.5}$ | GS13 | yes (0.8) | Q+00 | ... | ... | yes | yes |
| NGC 7582 | 22.0 | $0.55^{+0.26}_{-0.19}$ | GS13 | no | ... | ... | ... | no | no |
| NGC 7619 | 51.5 | 25^{+8}_{-3} | R+13b | yes ^a (0.5) | DG13, R+13a | ... | ... | yes | no |
| NGC 7768 | 112.8 | 13^{+5}_{-4} | GS13 | yes | G+94 | ... | ... | yes | no |
| UGC 03789 | 48.4 | $0.108^{+0.005}_{-0.005}$ | GS13 | no? | ... | ... | ... | yes | no |

Notes. Column (1): galaxy name. Column (2): distance. Column (3): black hole mass. Column (4): reference of the black hole mass reported here (G+03—Greenhill et al. 2003; GS13—Graham & Scott 2013; R+13b—Rusli et al. 2013b). Column (5): presence of a partially depleted core. The question mark is used when the classification has come from the velocity dispersion criteria mentioned in Section 2.2.3. The value of the core break radius is reported in parentheses when available. Column (6): reference of the identification of a partially depleted core (G+94—Grillmair et al. 1994; F+97—Forbes et al. 1997; Q+00—Quillen et al. 2000; T+04—Trujillo et al. 2004; F+06—Ferrarese et al. 2006; J+11—Jardel et al. 2011; R+11—Richings et al. 2011; DG13—Dullo & Graham 2013; R+13a—Rusli et al. 2013a). Column (7): kinematical classification (fast/slow rotator). Column (8): availability of velocity map (A—ATLAS^{3D}; S—SLUGGS). Column (9): completion of 1D fit. Column (10): completion of 2D fit.

^a NGC 7619 may contain an embedded disk, rather than possessing a partially depleted core (see Figure 77).

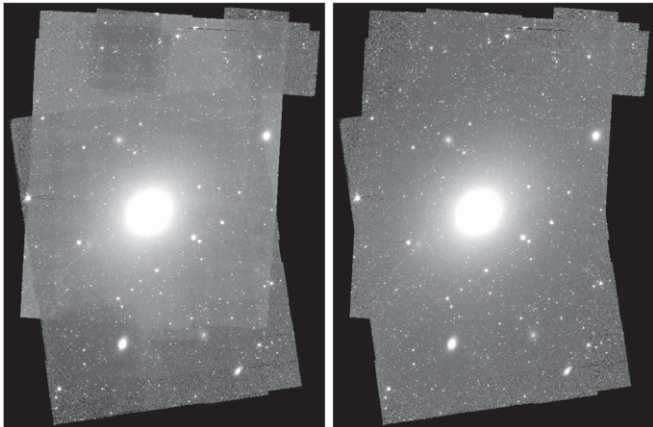


Figure 1. Example of the *overlap* correction. The image mosaic of the galaxy M49 was obtained by co-adding frames coming from eight different AORs. The evident patchiness (left image) was removed (right image) using the *overlap* module.

galaxy, we merged the different pmasks. Cosmic-ray rejection was performed with the dual outlier and multiframe techniques. The pixel size of the mosaic was set to be the same as the input cBCD frames ($1.^{\prime\prime}22 \times 1.^{\prime\prime}22$). For $3.6 \mu\text{m}$ observations with this pixel scale, the photometric zero-point magnitude is $m_{\text{zp}} = 17.26$ mag. The orientation of the mosaic was set to the average rotation angle of the input cBCD frames. Individual cBCD frames were combined together into a single mosaic with the default linear interpolation algorithm.

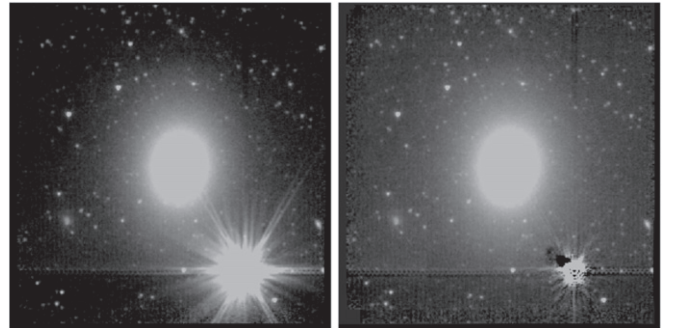


Figure 2. Example of aesthetic correction. The images show the mosaic of the galaxy NGC 4459 before (left) and after (right) the partial removal of a bright saturated star.

2.1.3. Overlap Correction

Before generating a mosaic, MOPEX can perform background matching among the individual frames by using the *overlap* module. This module calculates and applies an additive correction to the individual frames, producing a consistent background across the mosaicked image. According to the *Spitzer Data Analysis Cookbook*,⁶ the use of the *overlap* module is not particularly recommended for $3.6 \mu\text{m}$ observations. However, after a visual inspection of the mosaics

⁶ http://irsa.ipac.caltech.edu/data/SPITZER/docs/dataanalysistools/cookbook/Spitzer_Data_Cookbook.pdf

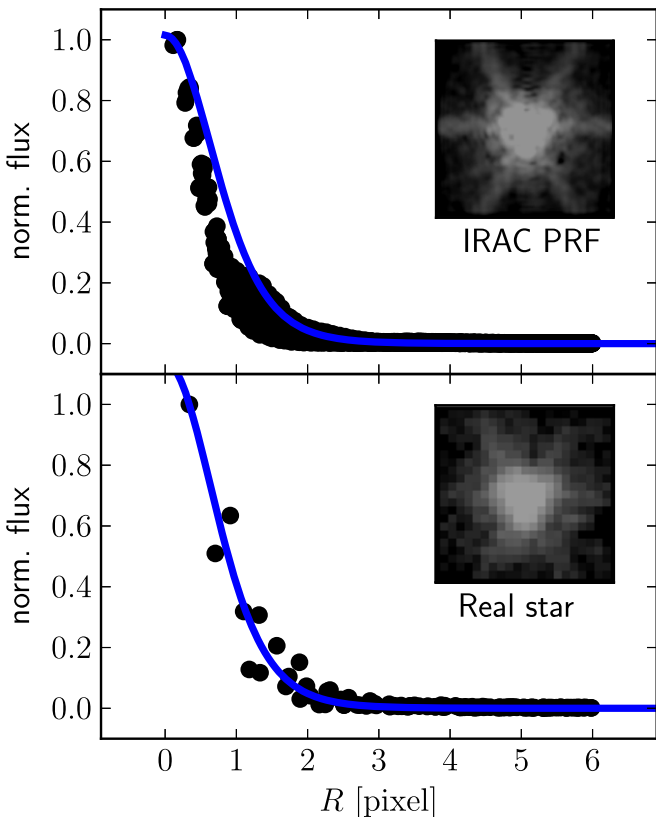


Figure 3. Normalized flux vs. radial distance from the image centroid of an observed point source (bottom panel) and of the IRAC instrument PRF (top panel). The normalized flux is given in arbitrary units, and the radial distance is in units of pixel size of the IRAC detector (1 pixel = 1''.22). The blue solid line shows our 1D Moffat PSF model, which has been normalized to intersect the data point with the largest flux. The FWHM of the IRAC PRF is clearly smaller than that of a “real” star. The inserts display the images of the observed point source and the IRAC PRF.

obtained without activating the *overlap* module, we found that all the mosaics obtained from multiple AORs were affected by patchiness, owing to bias fluctuations in the CCD array. For this reason, we regenerated the multiple-AOR mosaics by activating the *overlap* correction, which successfully removed the “chessboard” pattern (see Figure 1 for an example).

2.1.4. Sigma Mosaics

For each individual cBCD frame, the IRAC Level 1 pipeline calculates the uncertainty associated with each pixel and produces an uncertainty frame (or sigma frame). The initial uncertainty is estimated as the Poisson noise in electrons plus the readout noise added in quadrature ($\sigma^2 = \sigma_{\text{readoutnoise}}^2 + \sigma_{\text{Poisson}}^2$). This initial sigma frame is carried through the pipeline, and additional uncertainties (e.g., dark current and flat field uncertainties) are added in quadrature when appropriate. When MOPEX generates an image mosaic, it also produces the associated sigma mosaic by interpolating the individual uncertainty frames and co-adding them, following the standard assumption of additive variances.

⁷ IRAF is the Image Reduction and Analysis Facility, distributed by the National Optical Astronomy Observatory, which is operated by the Association of Universities for Research in Astronomy (AURA) under cooperative agreement with the National Science Foundation.

2.1.5. Sky Subtraction

Sky subtraction was performed manually on the image mosaics using the tasks `marksky` and `skyfit` of the IRAF⁷ package GALPHOT.⁸ The task `skyfit` also provided an estimate of the sky rms (rms_{sky}).

2.1.6. Additional Aesthetic Corrections

The image mosaics of four galaxies (NGC 0821, NGC 2974, NGC 4291, NGC 4459) were found to be affected by bright, highly saturated stars lying close to the target galaxies. These stars were modeled and subtracted using the software Galfit (Peng et al. 2010) and the extended IRAC point response function (PRF) image at 3.6 μm . This helped remove the extended wings and spikes of the saturated stars (see Figure 2 for an example).

2.1.7. Image Masking

Galactic stars and any other objects different from the target galaxy were masked through a two-step procedure. First, we created an initial mask using the IRAF task `objmasks` that identifies objects by threshold sigma detection. Then, we refined each mask by hand, using the software SAOImage DS9⁹ in conjunction with the IRAF task `mskregions`. We identified and carefully masked not only contaminating sources located in the field of the image mosaic but also objects overlapping with the target galaxy, such as foreground stars, background galaxies, globular clusters, and red giant stars.

2.1.8. 1D Point-spread Function (PSF)

A universal,¹⁰ average, 1D PSF was characterized using the IRAF task `imexamine`. A nonlinear least-squares Moffat (1969)¹¹ profile of fixed center and zero background was fit to the (background-subtracted) pixels of 20 bright stars, belonging to different image mosaics. The best-fit parameters of the 20 stars were then averaged together. Doing so, we obtained $(\alpha, \beta) = (2''.38, 4.39)$.

2.1.9. 2D PSF

The IRAC support team provides users with a 2D instrument PRF at 3.6 μm . However, while this helped remove the extended wings of saturated stars (see Section 2.1.6), we found

⁸ GALPHOT was developed in the IRAF—STSDAS environment mainly by W. Freudling, J. Salzer, and M. P. Haynes (Haynes et al. 1999).

⁹ SAOImage DS9 development has been made possible by funding from the Chandra X-ray Science Center (CXC) and the High Energy Astrophysics Science Archive Center (HEASARC).

¹⁰ Across all mosaics, the variation of the Moffat FWHM is $\pm 0''.1$, and the variation of the Moffat β is ± 2.0 . The use of a universal PSF is justified for the following reasons: (i) the PSF convolution is more sensitive to the value of the FWHM than β , i.e., having a 50% variation in β is not an issue as long as the variation in FWHM is small; (ii) the use of a non-signal-to-noise-weighted fitting scheme minimizes biases from a nonaccurate PSF description; (iii) not all mosaics have enough stars suitable for the PSF characterization: rather than having an individual PSF for each mosaic (which would have been based on only one to two stars for some mosaics), we preferred the use of a universal PSF.

¹¹ The Moffat (1969) profile has the following form:

$$\mu = \mu_0 - 2.5 \log \left[1 + \left(\frac{R}{\alpha} \right)^2 \right]^{-\beta}, \quad (1)$$

where R is the projected radius, μ_0 is the central surface brightness, and α and β regulate the width and the shape of the profile.

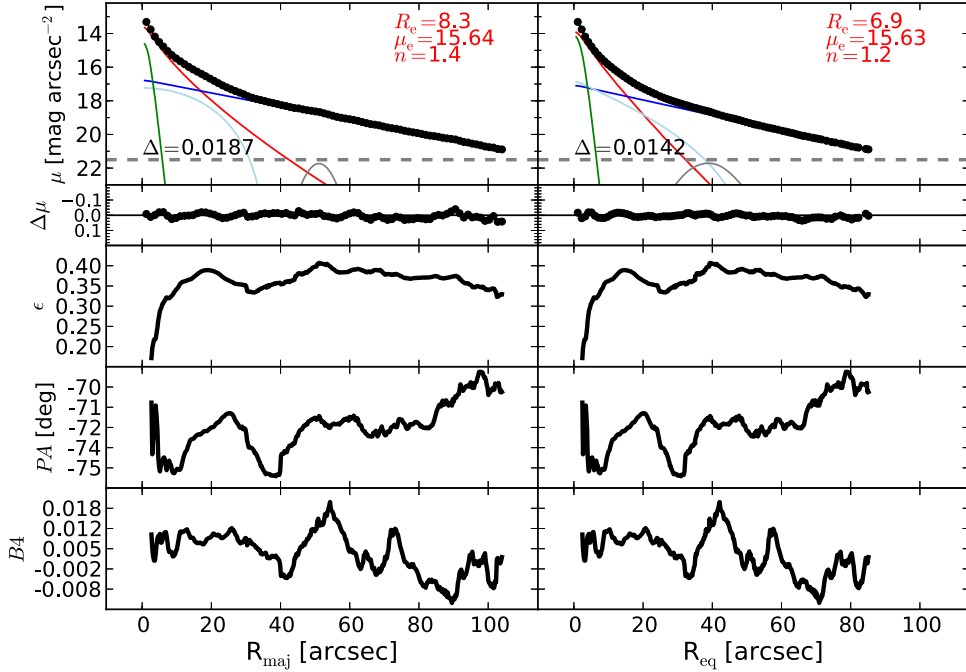


Figure 4. Best-fit model and isophotal parameters for the galaxy NGC 2974. The left panels refer to the major-axis R_{maj} , while the right panels refer to the equivalent-axis R_{eq} , i.e., the geometric mean of the major (a) and minor (b) axis ($R_{\text{eq}} = \sqrt{ab}$). The top panels display the galaxy surface brightness radial profiles obtained with a linear sampling. The black points are the observed data. The colored lines represent the individual (PSF-convolved) model components: red = Sérsic (bulge), dark blue = exponential (disk), green = Gaussian (AGN), cyan = Ferrer (bar), gray = Gaussian ring (ring). The best-fit parameters for the Sérsic bulge model are inset. The total (PSF-convolved) model is shown with a black dashed line, but it is hard to distinguish because it almost perfectly matches the data, hence the residual profile is additionally shown as $\Delta\mu$ in the second row. The horizontal gray dashed line corresponds to an intensity equal to three times the rms of the sky background fluctuations ($3 \times \text{rms}_{\text{sky}}$). Δ denotes the rms scatter of the fit in units of mag arcsec $^{-2}$. The lower six panels show the ellipticity (ϵ), position angle (PA), and fourth harmonic (B_4) radial profiles. Such profiles are available online for all other galaxies successfully modeled in 1D (see Table 2).

this PRF to be inadequate for the purposes of our modeling. In fact, the FWHM of the IRAC instrument PRF ($\sim 1.^{\circ}8$), as measured by the IRAF task `imexamine`, is systematically smaller than the average FWHM of “real” stars ($\sim 2.^{\circ}0$). Figure 3 illustrates this issue. We also tested the IRAC PRF by providing it as the input PSF for Galfit and fitting a number of stars in different image mosaics. A visual inspection of the fit residuals confirmed that the IRAC instrument PRF is narrower than “real” point sources. For this reason, we constructed our 2D PSF according to the following method (as directed by C. Peng 2013, private communication).

We provided the IRAC instrument PRF as the input PSF for Galfit and simultaneously fit seven bright stars (belonging to different mosaics), modeling the stars with Moffat profiles and constraining all the profiles to have the same (α, β), position angle, and axis ratio. The 2D PSF image was then obtained by taking the best-fit Moffat model—the same best-fit model for all seven stars, by construction—and convolving it with the IRAC instrument PRF. The advantage of this method is to obtain a 2D PSF that is wider than the instrument PRF but maintains the asymmetric features of the instrument PRF (e.g., wings and spikes). We then tested this 2D PSF on a number of stars (these stars were different from the seven stars employed to build the 2D PSF image) and verified that it correctly reproduces the shape of “real” point sources.

2.2. Additional Data

2.2.1. Kinematics

A kinematical classification (slow/fast rotator) is available for 34 of our 75 galaxies from the ATLAS^{3D} survey (Emsellem

et al. 2011) and for three additional galaxies from Scott et al. (2014). This classification (Table 1, column (7)) concerns the kinematic properties of galaxies within the spectroscopic instrument’s field of view, but does not contain additional information—crucial for our analysis—about kinematic substructures, such as embedded disks or kinematically decoupled components, which can require separate modeling. For this reason, we also visually inspected the velocity fields of our galaxies, when available from the literature. Velocity maps were taken from the ATLAS^{3D} survey for 34 galaxies (observed with SAURON by Krajnović et al. 2011), from Scott et al. (2014) for 2 galaxies (observed with WiFeS), and from the SLUGGS survey for 12 galaxies (observed with DEIMOS by Arnold et al. 2014). While the fields of view of SAURON ($33'' \times 41''$) and WiFeS ($25'' \times 38''$) reach to about one galaxy effective radius (for our local galaxies), observations taken with DEIMOS can probe the galaxy kinematics well beyond two effective radii.

2.2.2. Active Galactic Nuclei (AGNs) and Nuclear Dust

The X-ray, UV, and optical radiation emitted by the accretion disks of AGNs can stimulate infrared thermal emission from circumnuclear dust, if present. This means that if a galaxy hosts an optical AGN and a certain amount of nuclear dust, we may detect some nonstellar nuclear emission at $3.6 \mu\text{m}$. It is therefore important to identify which of our galaxies have both an optical AGN and circumnuclear dust. To help with this task, we searched NED¹² for the individual

¹² NED is the NASA/IPAC Extragalactic Database.

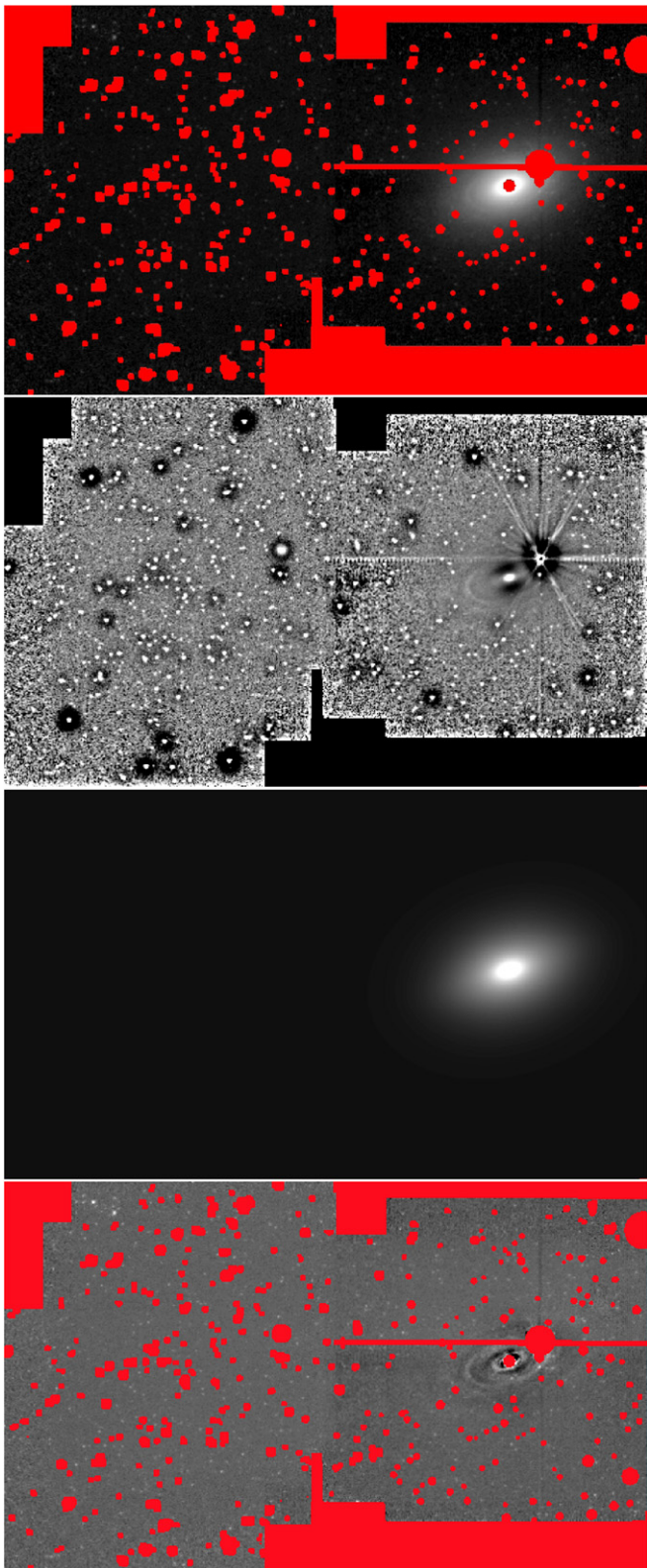


Figure 5. Image of the galaxy NGC 2974 with its mask (top panel, on a logarithmic scale), unsharp mask (second panel, on a linear scale), best-fit 2D model (third panel, on a logarithmic scale), and residual image after the subtraction of the 2D model (bottom panel, on a linear scale; the residual patterns correspond to differences between the data and the model of less than 6%). The left-hand side of the mosaic allowed an accurate determination of the sky background level.

galaxies and their associated literature. Unsurprisingly, dusty AGNs were more frequently found in late-type spiral galaxies and modeled by us with either a point source or a PSF-convolved Gaussian.

2.2.3. Sérsic/Core-Sérsic Classification

Core-Sérsic galaxies (Graham and Guzmán 2003; Graham et al. 2003; Trujillo et al. 2004) are galaxies (or spheroids) with partially depleted cores, i.e., a central deficit of light relative to the inward extrapolation of their outer Sérsic light profile. Such deficits were first noted and researched by King & Minkowski (1966). Sérsic galaxies, instead, do not exhibit such central stellar deficits. Partially depleted cores, as measured from high-resolution observations, have typical sizes of a few tens of parsecs (Rusli et al. 2013a; Dullo & Graham 2014). The majority are thus unresolved in our image mosaics. We masked these unresolved cores (identified in high-resolution images; - see Table 1) by excluding the surface brightness profile within 3 PSF's FWHM from the galaxy center. In the case of cores with sizes exceeding the PSF's FWHM, we excluded the data points within the size of the core plus 3 PSF's FWHM. The Sérsic/core-Sérsic classification presented in this work (Table 1, column (5)) comes from the compilation of Savorgnan & Graham (2015b), who identified partially depleted cores according to the same criteria used by Graham & Scott (2013). When no high-resolution image analysis was available from the literature, they inferred the presence of a partially depleted core based on the stellar velocity dispersion, σ : a galaxy is classified as core-Sérsic if $\sigma > 270 \text{ km s}^{-1}$, or as Sérsic if $\sigma < 166 \text{ km s}^{-1}$. This resulted in us assigning cores to just two galaxies using this alternative method when no high-resolution image was available.

3. ANALYSIS

3.1. Isophotal Analysis

We performed an isophotal analysis of our galaxies using the IRAF task `ellipse` (Jedrzejewski 1987), which fits elliptical isophotes to galaxy images. The center of the isophotes was held fixed, while the ellipticity (ϵ), the position angle (P.A.), and the amplitude of the fourth harmonic¹³ (B_4) were allowed to vary with radius. The step in semimajor axis length between successive ellipses was first set to increase linearly, and then geometrically in our second run.¹⁴ As a result, for each galaxy we produced respectively a “linearly sampled” and a “logarithmically sampled” surface brightness profile along the major axis. Major-axis surface brightness profiles were additionally converted into the equivalent axis, i.e., the geometric mean of the major (a) and minor (b) axis ($R_{\text{eq}} = \sqrt{ab}$), equivalent to the circularized radius. This resulted in four profiles per galaxy. Isophotes corresponding to an intensity less than three times the rms of the sky background fluctuations ($3 \times \text{rms}_{\text{sky}}$) were ignored. Some surface brightness profiles were truncated at our discretion before the $3 \times \text{rms}_{\text{sky}}$ limit, according to specific technical reasons (e.g., contamination from light of a neighboring galaxy, disturbed morphology in

¹³ The amplitude of the fourth harmonic deviations from perfect ellipses (B_4) parameterizes the diskyness ($B_4 > 0$) or boxyness ($B_4 < 0$) of the isophotes.

¹⁴ In the case of linear steps, the semimajor axis length for the next ellipse was calculated by adding 1 pixel to the current length. In the case of geometric steps, the semimajor axis length for the next ellipse was calculated as 1.1 times the current length.

Table 2
Results of Galaxy Decompositions

| Galaxy (1) | 1D Major Axis | | | 1D Equivalent Axis | | | | 2D | | | | |
|---------------|---------------|----------------|------------|--------------------|----------------|------------|-------------------------|-------------------------|--------------|---------------|-------------|--------------------------|
| | R_e (2) | μ_e (3) | n (4) | R_e (5) | μ_e (6) | n (7) | m_{sph} (8) | m_{gal} (9) | Q.F. (10) | R_e (11) | n (12) | m_{sph} (13) |
| Circinus | ... | ... | ... | ... | ... | ... | ... | ... | ... | ... | ... | ... |
| IC 1459 | 63.1 | 18.49 | 6.6 | 57.3 | 18.59 | 7.0 | 6.11 | 6.11 | 1 | 87.5 | 8.3 | 6.04 |
| IC 2560 | 6.1 | 16.58 | 0.8 | 4.5 | 16.48 | 0.6 | 10.77 | 8.29 | 2 | ... | ... | ... |
| IC 4296 | 65.9 | 19.32 | 5.8 | 68.1 | 19.48 | 6.2 | 6.70 | 6.70 | 1 | 82.3 | 6.6 | 6.66 |
| M104 | 11.0 | 14.63 | 5.8 | 19.6 | 15.78 | 3.7 | 5.98 | 4.68 | 2 | ... | ... | ... |
| M105 | 57.2 | 17.93 | 5.2 | 50.9 | 17.84 | 5.3 | 5.77 | 5.77 | 2 | 73.6 | 7.0 | 5.62 |
| M106 | 15.3 | 16.11 | 2.0 | 8.3 | 15.57 | 1.2 | 8.18 | 5.24 | 1 | ... | ... | ... |
| M31 | 418.6 | 16.80 | 2.2 | 173.6 | 15.63 | 1.3 | 1.61 | -0.33 | 1 | ... | ... | ... |
| M32 | ... | ... | ... | ... | ... | ... | ... | ... | ... | ... | ... | ... |
| M49 | 190.2 | 19.33 | 6.6 | 135.3 | 18.83 | 5.4 | 4.63 | 4.63 | 1 | 151.9 | 5.5 | 4.64 |
| M59 | 48.0 | 18.02 | 5.5 | 90.9 | 19.67 | 8.8 | 6.07 | 5.98 | 1 | ... | ... | ... |
| M60 | ... | ... | ... | ... | ... | ... | ... | ... | ... | ... | ... | ... |
| M64 | 3.8 | 13.38 | 0.8 | 4.3 | 13.78 | 1.4 | 7.78 | 5.08 | 1 | ... | ... | ... |
| M77 | ... | ... | ... | ... | ... | ... | ... | ... | ... | ... | ... | ... |
| M81 | 31.0 | 15.22 | 1.7 | 33.2 | 15.55 | 2.1 | 4.89 | 3.47 | 3 | ... | ... | ... |
| M84 | 101.6 | 19.01 | 7.8 | 129.8 | 19.57 | 7.9 | 5.25 | 5.25 | 2 | 181.8 | 8.4 | 5.20 |
| M87 | 203.0 | 19.87 | 10.0 | 87.1 | 18.26 | 5.9 | 4.97 | 4.97 | 2 | 88.3 | 4.3 | 5.11 |
| M89 | 29.0 | 17.14 | 4.6 | 28.2 | 17.15 | 5.1 | 6.38 | 6.12 | 2 | ... | ... | ... |
| M94 | 11.4 | 13.73 | 0.9 | 8.4 | 13.50 | 1.1 | 6.14 | 4.86 | 1 | ... | ... | ... |
| M96 | 7.5 | 14.63 | 1.5 | 5.3 | 14.28 | 1.3 | 7.87 | 5.82 | 1 | 8.3 | 2.0 | 7.36 |
| NGC 0253 | ... | ... | ... | ... | ... | ... | ... | ... | ... | ... | ... | ... |
| NGC 0524 | 6.0 | 15.24 | 1.1 | 5.8 | 15.21 | 1.1 | 8.65 | 6.91 | 1 | ... | ... | ... |
| NGC 0821 | 36.5 | 18.40 | 5.3 | 18.9 | 17.83 | 6.1 | 7.85 | 7.59 | 3 | 33.8 | 2.5 | 7.78 |
| NGC 1023 | 9.2 | 14.96 | 2.1 | 7.4 | 14.79 | 2.0 | 7.41 | 6.03 | 1 | 6.6 | 2.3 | 7.49 |
| NGC 1300 | 9.9 | 17.62 | 3.8 | 8.1 | 17.41 | 3.6 | 9.52 | 7.42 | 2 | ... | ... | ... |
| NGC 1316 | 21.5 | 15.55 | 2.0 | 15.9 | 15.43 | 1.8 | 6.46 | 4.87 | 2 | ... | ... | ... |
| NGC 1332 | 34.7 | 17.44 | 5.1 | 18.0 | 16.47 | 3.7 | 6.85 | 6.79 | 3 | ... | ... | ... |
| NGC 1374 | 25.6 | 18.06 | 3.7 | 24.8 | 18.11 | 4.1 | 7.74 | 7.72 | 1 | 25.2 | 3.7 | 7.81 |
| NGC 1399 | 405.2 | 21.80 | 10.0 | 338.1 | 21.53 | 10.0 | 5.01 | 4.98 | 1 | ... | ... | ... |
| NGC 2273 | 1.6 | 13.36 | 2.1 | 1.9 | 13.83 | 2.7 | 9.27 | 8.06 | 2 | ... | ... | ... |
| NGC 2549 | 6.1 | 15.57 | 2.3 | 3.1 | 14.54 | 1.5 | 9.20 | 7.85 | 1 | 5.6 | 2.1 | 8.76 |
| NGC 2778 | 2.3 | 15.61 | 1.3 | 2.2 | 15.46 | 1.2 | 10.94 | 9.30 | 2 | ... | ... | ... |
| NGC 2787 | 4.8 | 14.86 | 1.1 | 3.3 | 14.62 | 1.3 | 9.21 | 7.04 | 2 | ... | ... | ... |
| NGC 2974 | 8.3 | 15.64 | 1.4 | 6.9 | 15.63 | 1.2 | 8.65 | 7.44 | 2 | 10.6 | 1.3 | 8.39 |
| NGC 3079 | 6.8 | 14.47 | 1.3 | 4.3 | 14.48 | 1.1 | 8.57 | 7.13 | 2 | ... | ... | ... |
| NGC 3091 | 100.5 | 20.43 | 7.6 | 51.2 | 19.47 | 6.6 | 7.27 | 7.27 | 1 | 67.1 | 6.7 | 7.26 |
| NGC 3115 | 43.6 | 16.67 | 4.4 | 34.4 | 16.85 | 5.1 | 5.65 | 5.47 | 1 | ... | ... | ... |
| NGC 3227 | 8.1 | 16.56 | 1.7 | 4.6 | 15.83 | 1.1 | 9.77 | 7.28 | 2 | ... | ... | ... |
| NGC 3245 | 4.4 | 14.96 | 2.9 | 2.4 | 14.00 | 1.7 | 9.11 | 7.66 | 1 | 1.9 | 1.8 | 9.19 |
| NGC 3377 | 61.8 | 19.16 | 7.7 | 91.7 | 20.33 | 9.2 | 6.69 | 6.62 | 2 | 71.8 | 3.7 | 7.21 |
| NGC 3384 | 5.5 | 14.21 | 1.6 | 5.6 | 14.56 | 1.8 | 7.83 | 6.52 | 1 | ... | ... | ... |
| NGC 3393 | 1.4 | 14.03 | 3.4 | 1.4 | 14.15 | 2.6 | 10.23 | 8.42 | 2 | 1.2 | 1.9 | 10.45 |
| NGC 3414 | 28.0 | 18.10 | 4.8 | 25.5 | 18.08 | 4.5 | 7.60 | 7.53 | 1 | ... | ... | ... |
| NGC 3489 | 2.2 | 13.47 | 1.5 | 1.7 | 13.25 | 1.3 | 9.21 | 7.27 | 2 | 1.7 | 2.1 | 9.04 |
| NGC 3585 | 105.0 | 19.13 | 5.2 | 86.3 | 19.24 | 6.3 | 5.93 | 5.90 | 2 | ... | ... | ... |
| NGC 3607 | 69.3 | 19.00 | 5.5 | 65.5 | 19.01 | 5.6 | 6.37 | 6.29 | 2 | 60.0 | 5.3 | 6.40 |
| NGC 3608 | 47.5 | 18.93 | 5.2 | 43.4 | 19.00 | 5.7 | 7.25 | 7.25 | 2 | 62.0 | 7.0 | 7.15 |
| NGC 3842 | 100.7 | 21.43 | 8.1 | 73.6 | 21.07 | 8.2 | 7.97 | 7.92 | 1 | ... | ... | ... |
| NGC 3998 | 5.8 | 15.15 | 1.2 | 4.8 | 14.63 | 1.3 | 8.37 | 7.15 | 3 | ... | ... | ... |
| NGC 4026 | 3.4 | 15.52 | 2.4 | 6.3 | 16.09 | 2.1 | 9.02 | 7.44 | 3 | ... | ... | ... |
| NGC 4151 | 7.6 | 15.50 | 1.4 | 6.8 | 15.26 | 1.9 | 8.10 | 7.06 | 2 | ... | ... | ... |
| NGC 4261 | 52.6 | 18.58 | 4.7 | 47.3 | 18.53 | 4.3 | 6.72 | 6.68 | 2 | 50.4 | 4.4 | 6.73 |
| NGC 4291 | 15.0 | 17.14 | 4.2 | 15.4 | 17.51 | 5.9 | 7.99 | 7.99 | 2 | 20.8 | 7.7 | 7.91 |
| NGC 4342 | ... | ... | ... | ... | ... | ... | ... | ... | ... | ... | ... | ... |
| NGC 4388 | 4.6 | 15.89 | 0.6 | 4.2 | 15.86 | 1.3 | 9.89 | 7.66 | 3 | ... | ... | ... |
| NGC 4459 | 18.4 | 16.69 | 3.1 | 13.0 | 16.23 | 2.6 | 7.50 | 6.97 | 2 | ... | ... | ... |
| NGC 4473 | 45.9 | 17.93 | 2.3 | 36.9 | 18.10 | 2.9 | 7.04 | 6.82 | 2 | 49.8 | 3.0 | 7.03 |
| NGC 4486A | ... | ... | ... | ... | ... | ... | ... | ... | ... | ... | ... | ... |
| NGC 4564 | 5.0 | 15.23 | 2.6 | 6.0 | 15.65 | 3.0 | 8.52 | 7.83 | 1 | ... | ... | ... |
| NGC 4596 | 6.6 | 15.93 | 2.7 | 9.0 | 16.44 | 3.0 | 8.43 | 6.98 | 1 | ... | ... | ... |
| NGC 4697 | 239.3 | 20.62 | 7.2 | 226.4 | 20.90 | 6.7 | 5.47 | 5.34 | 3 | 121.4 | 5.0 | 5.72 |
| NGC 4889 | 119.7 | 21.01 | 8.1 | 60.8 | 20.11 | 6.8 | 7.53 | 7.53 | 1 | 104.3 | 7.8 | 7.43 |

Table 2
(Continued)

| Galaxy (1) | 1D Major Axis | | | 1D Equivalent Axis | | | | 2D | | | | |
|---------------|---------------|----------------|------------|--------------------|----------------|------------|-------------------------|-------------------------|--------------|---------------|-------------|--------------------------|
| | R_e (2) | μ_e (3) | n (4) | R_e (5) | μ_e (6) | n (7) | m_{sph} (8) | m_{gal} (9) | Q.F. (10) | R_e (11) | n (12) | m_{sph} (13) |
| NGC 4945 | 13.9 | 14.95 | 1.4 | 9.5 | 14.78 | 1.7 | 6.94 | 4.11 | 2 | 16.2 | 0.8 | 7.07 |
| NGC 5077 | 23.5 | 17.67 | 4.2 | 23.0 | 18.01 | 5.7 | 7.62 | 7.62 | 1 | 30.5 | 6.8 | 7.57 |
| NGC 5128 | 61.3 | 15.73 | 1.2 | 60.8 | 16.01 | 2.2 | 4.01 | 2.93 | 3 | ... | ... | ... |
| NGC 5576 | 61.5 | 19.41 | 3.3 | 49.3 | 19.34 | 3.7 | 7.53 | 7.53 | 1 | 45.9 | 8.3 | 7.19 |
| NGC 5813 | ... | ... | ... | ... | ... | ... | ... | ... | ... | ... | ... | ... |
| NGC 5845 | 3.6 | 14.79 | 2.5 | 3.1 | 14.64 | 2.3 | 9.05 | 8.91 | 3 | 2.8 | 2.4 | 9.09 |
| NGC 5846 | 105.1 | 19.67 | 6.4 | 83.4 | 19.28 | 5.7 | 6.10 | 6.10 | 2 | 85.1 | 5.2 | 6.14 |
| NGC 6251 | 41.7 | 19.82 | 6.8 | 30.1 | 19.31 | 5.6 | 8.35 | 8.35 | 1 | 39.3 | 7.1 | 8.27 |
| NGC 7052 | 59.4 | 19.38 | 4.2 | 37.0 | 19.19 | 5.6 | 7.79 | 7.79 | 1 | 36.2 | 4.0 | 8.09 |
| NGC 7582 | ... | ... | ... | ... | ... | ... | ... | ... | ... | ... | ... | ... |
| NGC 7619 | 63.2 | 19.53 | 5.3 | 58.0 | 19.55 | 5.2 | 7.21 | 7.15 | 2 | ... | ... | ... |
| NGC 7768 | 92.9 | 21.37 | 8.4 | 42.1 | 20.15 | 6.7 | 8.36 | 8.36 | 2 | ... | ... | ... |
| UGC 03789 | 1.8 | 15.26 | 1.9 | 2.4 | 15.39 | 1.4 | 10.65 | 9.22 | 3 | ... | ... | - |

Note. Column (1): galaxy name. Columns (2)–(4): effective radius (in units of arcsec), surface brightness at the effective radius (in units of mag arcsec $^{-2}$), and Sérsic index for 1D fits along the major axis. Columns (5)–(9): effective radius (in units of arcsec), surface brightness at the effective radius (in units of mag arcsec $^{-2}$), Sérsic index, spheroid apparent magnitude (in units of mag, Vega system), and galaxy apparent magnitude (in units of mag, Vega system) for 1D fits along the equivalent axis. Column (10): quality flag of the 1D fits (see Section 4.2). Columns (11)–(13): effective radius (in units of arcsec), Sérsic index, and spheroid apparent magnitude (in units of mag, Vega system) for 2D fits.

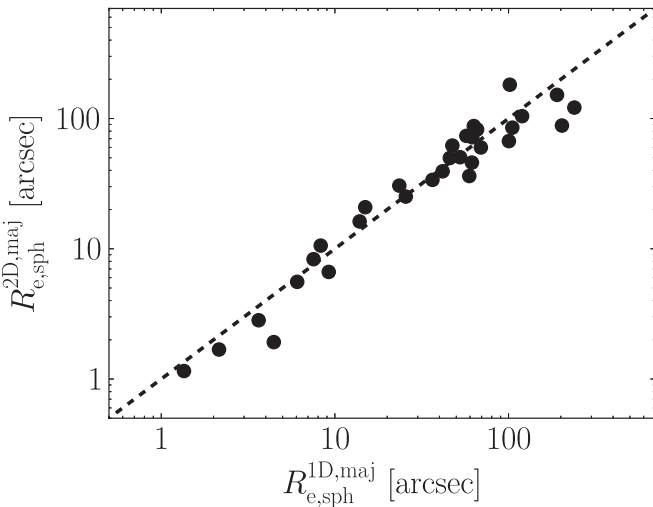


Figure 6. 2D vs. 1D major-axis measurements of the spheroid effective radii. The dashed line displays the 1:1 relation.

the galaxy outskirts, etc.). In particular, we did not attempt to fit bends or truncations of large-scale disks (e.g., Erwin et al. 2005, 2008, 2012; Gutiérrez et al. 2011; Comerón et al. 2012; Muñoz-Mateos et al. 2013; Kim et al. 2014), but instead truncated the surface brightness profiles before the occurrence of such features. Individual cases are discussed in Section 5.1.

3.2. Unsharp Masking

Unsharp masking is an image-sharpening technique that is useful to reveal asymmetric structures in galaxies, such as bars or (inclined) embedded disks. First, the original galaxy image was smoothed with a Gaussian filter. Then, the original image was divided by the smoothed one. The result of such an operation is the “unsharp mask.” The asymmetric features revealed by this technique have sizes comparable to the FWHM of the Gaussian kernel used for the smoothing. Therefore, for each galaxy, we produced a set of different

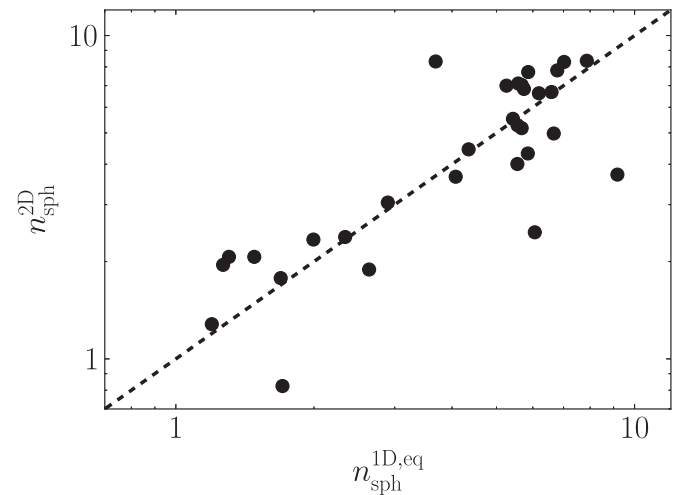


Figure 7. 2D measurements of the spheroid Sérsic indices roughly approximate the 1D equivalent-axis measurements. The dashed line displays the 1:1 relation. The four most obvious outliers are NGC 821, NGC 3377, NGC 4945, and NGC 5576. Their individual cases are discussed in the Appendix.

unsharp masks by varying the FWHM of the filter, to identify all the asymmetric features that could bias the fitting process and may therefore need to be considered during the galaxy modeling phase. This information was used in combination with kinematic and AGN information discussed in Section 2.2.

3.3. 1D Fitting Routine

The decomposition of the surface brightness profiles was performed with software written by G. Savorgnan. This software can fit an observed surface brightness profile with any linear combination of a set of analytical functions (Sérsic, exponential, Gaussian, Moffat, Ferrer, symmetric Gaussian ring, etc.; see the Appendix for a description of the analytical form of these profiles). At each iteration, the model is numerically convolved with a Moffat filter, to account for PSF effects, and then matched to the data. The minimization

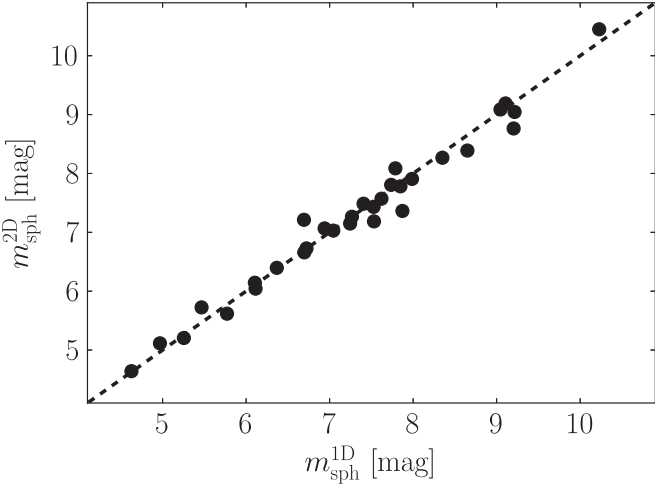


Figure 8. 2D vs. 1D measurements of the $3.6\ \mu\text{m}$ spheroid magnitudes. The dashed line displays the 1:1 relation.

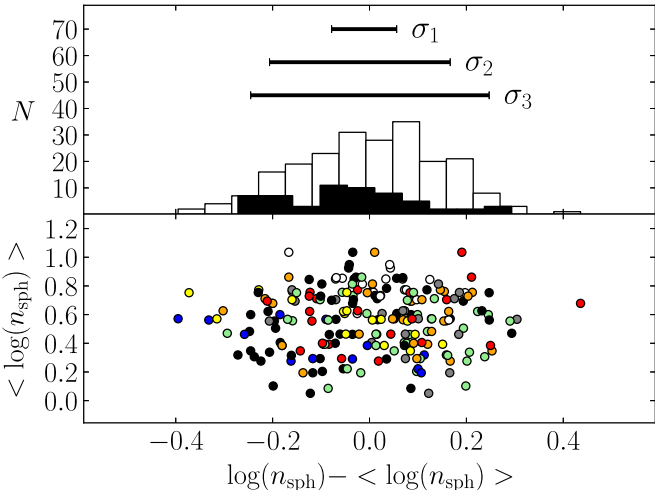


Figure 9. Bottom panel: 58 galaxies for which at least one measurement of the spheroid Sérsic index n_{sph} is available from the literature (Table 3), in addition to that measured by us. The average (logarithmic) value ($\langle \log(n_{\text{sph}}) \rangle$) is plotted against the difference between (the logarithm of) the individual measurements of a galaxy and the average (logarithmic) value for that same galaxy. Each data point corresponds to an individual measurement from Graham & Driver (2007a; red points), Laurikainen et al. (2010; blue points), Sani et al. (2011; green points), Vika et al. (2012; yellow points), Beifiori et al. (2012; gray points), Rusli (2013a; white points), and Läsker et al. (2014a; orange points). Black points are measurements obtained from the 1D fits presented in this work (using linearly sampled surface brightness profiles, along the major axis). In the top panel, the white histogram shows the distribution of $\log(n_{\text{sph}}) - \langle \log(n_{\text{sph}}) \rangle$ for all measurements, whereas the black histogram refers only to the measurements obtained by us. The (asymmetric) error bars σ_1 , σ_2 , and σ_3 enclose 38%, 78%, and 92% of the black histogram, respectively, corresponding to our quality flags 1, 2, and 3 given in Table 2 (see Section 4.2 for details). We consider these to be absolute upper limits to the uncertainty on our parameters given the care we have taken to minimize sources of systematic errors.

routine is based on the Levenberg–Marquardt algorithm. During the fit, we deliberately did not make use of any weighting scheme on the data points that constitute the surface brightness profile, although the use of a linearly and logarithmically sampled profile effectively represents a different weighting scheme. The all too often overlooked flaw with signal-to-noise ratio (S/N) based weighting schemes is that they immediately become biased weighting schemes when

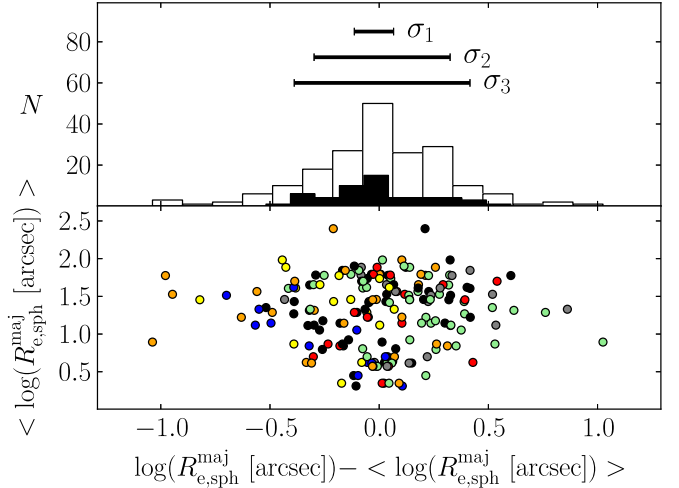


Figure 10. Bottom panel: 52 galaxies for which at least one measurement of the spheroid major-axis effective radius $R_{\text{e}}^{\text{maj}}$ is available from the literature (Table 3), in addition to that measured by us. The average (logarithmic) value ($\langle \log(R_{\text{e}}^{\text{maj}}) \rangle$) is plotted against the difference between (the logarithm of) the individual measurements of a galaxy and the average (logarithmic) value for that same galaxy. See Figure 9 for color description and explanation of the top panel.

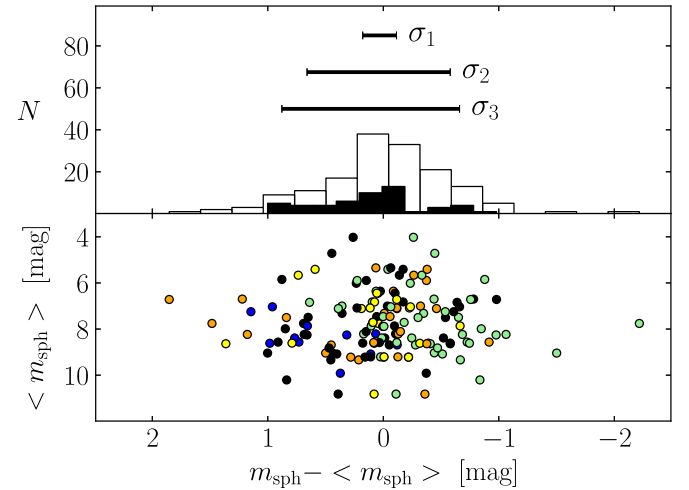


Figure 11. Bottom panel: 51 galaxies for which at least one measurement of the spheroid apparent magnitude m_{sph} —either in the K band or at $3.6\ \mu\text{m}$ —is available from the literature (Table 3), in addition to that measured by us. The $3.6\ \mu\text{m}$ magnitudes were converted into K -band magnitudes (see Section 4.2 for details). The average value ($\langle m_{\text{sph}} \rangle$) is plotted against the difference between the individual measurements of a galaxy and the average value for that same galaxy. See Figure 9 for color description and explanation of the top panel.

additional components are present but not modeled. For example, fitting only a Sérsic model to what is actually a nucleated elliptical galaxy immediately voids a S/N-based weighting scheme and results in Sérsic parameters that describe the spheroid less accurately than had no S/N-based weighting been used. While we have paid careful attention to the components in each galaxy, this is an issue that warrants the nonapplication of S/N-based weighting schemes. Overlooked partially depleted cores, or an incorrect PSF, can of course also result in S/N-weighted fitting schemes performing poorly because of the emphasis they place on matching the model to the inner data.

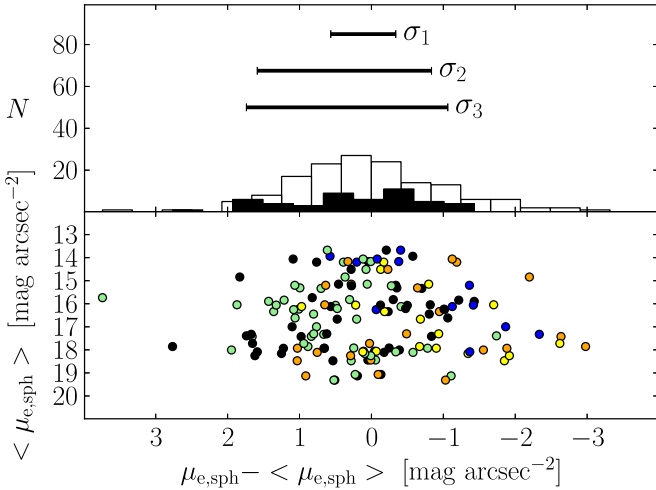


Figure 12. Bottom panel: 49 galaxies for which at least one measurement of the spheroid effective surface brightness $\mu_{e,\text{sph}}$ —either in the K band or at $3.6 \mu\text{m}$ —is available from the literature (Table 3), in addition to that measured by us. The K -band magnitudes were converted into $3.6 \mu\text{m}$ magnitudes (see Section 4.2 for details). The average value $\langle \mu_{e,\text{sph}} \rangle$ from all fits to a galaxy, not to be confused with the mean effective surface brightness within $R_{e,\text{sph}}$, is plotted against the difference between the individual measurements of a galaxy and the average value for that same galaxy. See Figure 9 for color description and explanation of the top panel.

| Table 3 Summary of Previous Investigations of Black Hole Mass Scaling Relations | | | | | |
|--|-----------|-------------------|-----------|-------------|-----------|
| | GD07 | S+11 | V+12 | B+12 | L+14 |
| Galaxies with successful fit | 27 | 57 | 25 | 19 | 35 |
| Wavelength | R -band | $3.6 \mu\text{m}$ | K -band | i -band | K -band |
| Decomposition | 1D | 2D | 2D | 2D | 2D |
| Nuclear components | masked | modeled | modeled | not treated | modeled |
| Partially depleted cores | masked | masked | masked | not treated | masked |
| Bars | excluded | modeled | modeled | excluded | modeled |
| Other components | no | no | no | no | yes |
| Kinematics | no | no | no | no | no |

Note. GD07—Graham & Driver (2007a); S+11—Sani et al. (2011); V+12—Vika et al. (2012); B+12—Beifiori et al. (2012); L+14—Läsker et al. (2014a).

Table 4
Best-fit Parameters for the Spheroidal Component of IC 1459

| Work | Model | $R_{e,\text{sph}}$ (arcsec) | n_{sph} |
|-------------|-------------|--------------------------------|------------------|
| 1D maj. | S-bul + m-c | 63.1 | 6.6 |
| 1D eq. | S-bul + m-c | 57.3 | 7.0 |
| 2D | S-bul + m-c | 87.5 | 8.3 |
| S+11 2D | S-bul + G-n | 61.1 | 6.0 |
| R+13 1D eq. | core-Sérsic | 45.4 | 7.6 |
| L+14 2D | S-bul + m-c | 62.4 | 8.3 |

Note. Our results are shown in the upper portion of the table. See Section 5.1 for the legend key to the other authors listed in the lower portion of the table. See Table 2 for our associated surface brightnesses and magnitudes.

3.4. Smoothing Technique

Some nearby galaxies in our sample have very large apparent sizes, and for them we obtained surface brightness profiles more extended than 8 arcmin. This means that their outermost (significant) isophote corresponds to a projected galactic radius R of more than 240 times the FWHM of the instrumental PSF. Such a level of spatial resolution is

Table 5
Best-fit Parameters for the Spheroidal Component of IC 2560

| Work | Model | $R_{e,\text{sph}}$ (arcsec) | n_{sph} |
|---------|---------------------------|--------------------------------|------------------|
| 1D maj. | S-bul + e-d + F-bar + G-n | 6.1 | 0.8 |
| 1D eq. | S-bul + e-d + F-bar + G-n | 4.5 | 0.6 |
| S+11 2D | S-bul + e-d + G-n | 27.5 | 2.0 |

Note. In their model, S+11 did not account for the bar component and thus overestimated the effective radius and the Sérsic index of the bulge.

Table 6
Best-fit Parameters for the Spheroidal Component of IC 4296

| Work | Model | $R_{e,\text{sph}}$ (arcsec) | n_{sph} |
|---------|-------------|--------------------------------|------------------|
| 1D maj. | S-bul + m-c | 65.9 | 5.8 |
| 1D eq. | S-bul + m-c | 68.1 | 6.2 |
| 2D | S-bul + m-c | 82.3 | 6.6 |
| S+11 2D | S-bul + G-n | 33.6 | 4.0 |
| L+14 2D | S-bul + m-c | 97.8 | 8.2 |

Note. S+11 obtained a small effective radius and Sérsic index because they fit a nuclear component rather than masking the core.

Table 7
Best-fit Parameters for the Spheroidal Component of M31

| Work | Model | $R_{e,\text{sph}}$ (arcsec) | n_{sph} |
|---------|---------------------|--------------------------------|------------------|
| 1D maj. | S-bul + e-d + F-bar | 418.6 | 2.2 |
| 1D eq. | S-bul + e-d + F-bar | 173.6 | 1.3 |

Table 8
Best-fit Parameters for the Spheroidal Component of M49

| Work | Model | $R_{e,\text{sph}}$ (arcsec) | n_{sph} |
|-------------|-------------|--------------------------------|------------------|
| 1D maj. | S-bul + m-c | 190.2 | 6.6 |
| 1D eq. | S-bul + m-c | 135.3 | 5.4 |
| 2D | S-bul + m-c | 151.9 | 5.5 |
| R+13 1D eq. | core-Sérsic | 199.0 | 5.6 |

Note. The equivalent-axis effective radius estimated by R+13 is larger than that measured by us. Since their circularized light profile is almost three times more extended than ours, it is possible that their best-fit model required a larger R_e to account for the galaxy intracluster halo light.

Table 9
Best-fit Parameters for the Spheroidal Component of M59

| Work | Model | $R_{\text{e,sph}}$ (arcsec) | n_{sph} |
|---------|--------------------|--------------------------------|------------------|
| 1D maj. | S-bul + m-n + e-id | 48.0 | 5.5 |
| 1D eq. | S-bul + m-n + e-id | 90.9 | 8.8 |
| S+11 2D | S-bul | 70.1 | 5.0 |
| V+12 2D | S-bul + m-c | 54.7 | 5.7 |

Table 10
Best-fit Parameters for the Spheroidal Component of M64

| Work | Model | $R_{\text{e,sph}}$ (arcsec) | n_{sph} |
|---------|----------------------------|--------------------------------|------------------|
| 1D maj. | S-bul + e-d + F-bar + S-id | 3.8 | 0.8 |
| 1D eq. | S-bul + e-d + F-bar + S-id | 4.3 | 1.4 |
| B+12 2D | S-bul + e-d | 5.0 | 1.5 |

Table 11
Best-fit Parameters for the Spheroidal Component of M81

| Work | Model | $R_{\text{e,sph}}$ (arcsec) | n_{sph} |
|--------------|-------------------|--------------------------------|------------------|
| 1D maj. | S-bul + e-d | 31.0 | 1.7 |
| 1D eq. | S-bul + e-d | 33.2 | 2.1 |
| GD07 1D maj. | S-bul + e-d | 68.1 | 3.3 |
| S+11 2D | S-bul + e-d + G-n | 127.3 | 3.0 |
| B+12 2D | S-bul + e-d | 50.0 | 2.6 |

Note. GD07 and B+12 obtained estimates of the effective radius larger than ours by a factor of two. This is not particularly surprising, given the complicated surface brightness distribution of this galaxy. The large measurement of the effective radius reported by S+11 is the most discrepant, but the reasons for this are unclear.

Table 12
Best-fit Parameters for the Spheroidal Component of M84

| Work | Model | $R_{\text{e,sph}}$ (arcsec) | n_{sph} |
|--------------|-------------|--------------------------------|------------------|
| 1D maj. | S-bul + m-c | 101.6 | 7.8 |
| 1D eq. | S-bul + m-c | 129.8 | 7.9 |
| 2D | S-bul + m-c | 181.8 | 8.4 |
| GD07 1D maj. | S-bul | 75.1 | 5.6 |
| S+11 2D | S-bul + G-n | 105.9 | 7.0 |
| V+12 2D | S-bul + m-c | 28.7 | 3.5 |
| B+12 2D | S-bul | 63.6 | 4.1 |
| R+13 1D eq. | core-Sérsic | 126.2 | 7.1 |
| L+14 2D | S-bul + m-c | 139.0 | 8.3 |

Note. B+12 did not mask the core and thus underestimated the effective radius and the Sérsic index. V+12 used the same model as R+13, L+14, and us, but the smaller radial extent of their data led them to underestimate the effective radius and the Sérsic index.

unnecessary for the purposes of our analysis, and, especially in the case of a clumpy star-forming galaxy, it results in a “noisy” surface brightness profile. Moreover, in the case of a linearly sampled light profile, it significantly prolongs the computational time of the fitting routine (because, at each iteration, the PSF convolution is performed numerically on a large array). To overcome this problem, we introduced a method to which we refer as the “smoothing technique.” This method was applied to the galaxies M31, M81, NGC 4945, and NGC 5128. For each

Table 13
Best-fit Parameters for the Spheroidal Component of M87

| Work | Model | $R_{\text{e,sph}}$ (arcsec) | n_{sph} |
|--------------|-------------|--------------------------------|------------------|
| 1D maj. | S-bul + m-c | 203.9 | 10.0 |
| 1D eq. | S-bul + m-c | 87.1 | 5.9 |
| 2D | S-bul + m-c | 88.3 | 4.3 |
| GD07 1D maj. | S-bul | ... | 6.9 |
| S+11 2D | S-bul + G-n | 99.5 | 4.0 |
| V+12 2D | S-bul + m-c | 34.6 | 2.4 |
| R+13 1D eq. | core-Sérsic | 180.9 | 8.9 |
| L+14 2D | S-bul + m-c | 122.0 | 5.6 |

Note. The equivalent-axis fit of R+13 returns the largest values for $R_{\text{e,sph}}$ and n_{sph} . As in the case of M49, since their circularized light profile is almost three times more extended than ours, it is possible that their best-fit model required a larger R_{e} to account for the extra intracluster halo light. V+12 obtained the smallest estimates of $R_{\text{e,sph}}$ and n_{sph} because of the small radial extent of their data.

Table 14
Best-fit Parameters for the Spheroidal Component of M89

| Work | Model | $R_{\text{e,sph}}$ (arcsec) | n_{sph} |
|-------------|----------------|--------------------------------|------------------|
| 1D maj. | S-bul + e-halo | 29.0 | 4.6 |
| 1D eq. | S-bul + e-halo | 28.2 | 5.1 |
| S+11 2D | S-bul + e-d | 24.3 | 4.0 |
| V+12 2D | S-bul | 16.7 | 3.6 |
| B+12 2D | S-bul | 45.2 | 4.3 |
| R+13 1D eq. | S-bul + S-halo | 19.8 | 3.8 |

Table 15
Best-fit Parameters for the Spheroidal Component of M94

| Work | Model | $R_{\text{e,sph}}$ (arcsec) | n_{sph} |
|---------|---------------------|--------------------------------|------------------|
| 1D maj. | S-bul + e-d + F-bar | 11.4 | 0.9 |
| 1D eq. | S-bul + e-d + F-bar | 8.4 | 1.1 |

Table 16
Best-fit Parameters for the Spheroidal Component of M96

| Work | Model | $R_{\text{e,sph}}$ (arcsec) | n_{sph} |
|---------|----------------------------|--------------------------------|------------------|
| 1D maj. | S-bul + e-d + F-bar + S-id | 7.5 | 1.5 |
| 1D eq. | S-bul + e-d + F-bar + S-id | 5.3 | 1.3 |
| 2D | S-bul + e-d + G-bar + G-id | 8.3 | 2.0 |
| S+11 2D | S-bul + e-d + G-bar | 45.6 | 1.0 |

Note. The bulge effective radius obtained by S+11 largely exceeds our estimates because their galaxy decomposition does not account for the inner component embedded in the bulge ($R_{\text{maj}} \lesssim 25''$).

of these galaxies, we took the image mosaic and convolved it with a Gaussian filter whose FWHM was larger than the FWHM of the instrumental PSF. We then ran `ellipse` on the convolved image and extracted “linearly sampled” and “logarithmically sampled” surface brightness profiles. For the “linearly sampled” profiles, we set the radial step between contiguous isophotes to be comparable to the FWHM of the smoothing Gaussian filter. Doing so, we reduced the number of fitted isophotes and also produced smoother surface brightness

Table 17
Best-fit Parameters for the Spheroidal Component of M104

| Work | Model | $R_{\text{e,sph}}$ (arcsec) | n_{sph} |
|---------|---------------------------|--------------------------------|------------------|
| 1D maj. | S-bul + e-d + F-bar + m-c | 11.0 | 5.8 |
| 1D eq. | S-bul + e-d + F-bar + m-c | 19.6 | 3.7 |
| S+11 2D | S-bul + e-d + G-bar + G-n | 66.1 | 1.5 |

Note. The bulge Sérsic index obtained by S+11 is smaller than our estimates because they fit an additional nuclear component.

Table 18
Best-fit Parameters for the Spheroidal Component of M105

| Work | Model | $R_{\text{e,sph}}$ (arcsec) | n_{sph} |
|--------------|-------------|--------------------------------|------------------|
| 1D maj. | S-bul + m-c | 57.2 | 5.2 |
| 1D eq. | S-bul + m-c | 50.9 | 5.3 |
| 2D | S-bul + m-c | 73.6 | 7.0 |
| GD07 1D maj. | S-bul | 58.3 | 4.3 |
| S+11 2D | S-bul | 46.0 | 5.0 |
| R+13 1D eq. | core-Sérsic | 55.1 | 5.8 |
| L+14 2D | S-bul + m-c | 96.3 | 9.3 |

Note. L+14 obtained the largest values of $R_{\text{e,sph}}$ and n_{sph} , possibly owing to incorrect sky subtraction (see the “upturn” of the three outermost data points in their Figure 21).

Table 19
Best-fit Parameters for the Spheroidal Component of M106

| Work | Model | $R_{\text{e,sph}}$ (arcsec) | n_{sph} |
|--------------|--|--------------------------------|------------------|
| 1D maj. | S-bul + e-d | 15.3 | 2.0 |
| 1D eq. | S-bul + e-d | 8.3 | 1.2 |
| GD07 1D maj. | S-bul + e-d | 14.9 | 2.0 |
| S+11 2D | S-bul + e-d + G-n | 111.7 | 2.0 |
| V+12 2D (1) | S-bul + e-d + PSF-n | 17.0 | 3.5 |
| V+12 2D (2) | S-bul + e-d + PSF-n + S-bar | 6.3 | 2.2 |
| L+14 2D | S-bul + e-d + PSF-n + e-id + S-bar + spiral arms | 6.3 | 3.3 |

Note. The bulge effective radius obtained by S+11 largely exceeds all the other estimates, behavior noted also in NGC 3031.

Table 20
Best-fit Parameters for the Spheroidal Component of NGC 0524

| Work | Model | $R_{\text{e,sph}}$ (arcsec) | n_{sph} |
|---------|---------------------|--------------------------------|------------------|
| 1D maj. | S-bul + e-d + G-r | 6.0 | 1.1 |
| 1D eq. | S-bul + e-d + G-r | 5.8 | 1.1 |
| L+10 2D | S-bul + e-d + 2 F-l | 8.9 | 2.7 |
| S+11 2D | S-bul + e-d | 26.8 | 3.0 |

Note. S+11 obtained the largest value of the effective radius because their two-component model does not account for the ring. Both L+10 and S+11 estimated a Sérsic index of ~ 3 , three times larger than the value obtained by us.

profiles. Before the software fit a smoothed light profile, the model to be fit was convolved twice: the first time to account for PSF effects, and the second time to account for the artificial Gaussian smoothing applied to the image mosaic.

Table 21
Best-fit Parameters for the Spheroidal Component of NGC 0821

| Work | Model | $R_{\text{e,sph}}$ (arcsec) | n_{sph} |
|--------------|----------------------|--------------------------------|------------------|
| 1D maj. | S-bul + e-id + PSF-n | 36.8 | 5.4 |
| 1D eq. | S-bul + e-id + PSF-n | 20.7 | 6.0 |
| 2D | S-bul + e-id + m-n | 33.8 | 2.5 |
| GD07 1D maj. | S-bul | 44.1 | 4.0 |
| S+11 2D | S-bul | 63.6 | 7.0 |
| B+12 2D | S-bul | 111.3 | 7.7 |
| L+14 2D | S-bul + e-d + S-halo | 3.8 | 3.1 |

Note. L+14 obtained a tiny estimate of the spheroid effective radius and a small Sérsic index because they failed to identify the extent of the intermediate-scale disk. Inaccurate sky subtraction could be the reason why B+12 obtained a large estimate of the effective radius. We could not obtain a successful 2D model that included a nuclear component; therefore, we opted for masking the nuclear region of the galaxy. This resulted in a significantly lower Sérsic index, which we consider underestimated.

Table 22
Best-fit Parameters for the Spheroidal Component of NGC 1023

| Work | Model | $R_{\text{e,sph}}$ (arcsec) | n_{sph} |
|--------------|---------------------|--------------------------------|------------------|
| 1D maj. | S-bul + e-d + F-bar | 9.2 | 2.1 |
| 1D eq. | S-bul + e-d + F-bar | 7.4 | 2.0 |
| 2D | S-bul + e-d + G-bar | 6.6 | 2.3 |
| GD07 1D maj. | S-bul + e-d | 17.7 | 2.0 |
| S+11 2D | S-bul + e-d + G-bar | 24.0 | 3.0 |
| L+14 2D | S-bul + e-d + S-bar | 9.6 | 3.1 |

Note. S+11 obtained the largest value of the bulge effective radius, although they accounted for the bar in their model.

Table 23
Best-fit Parameters for the Spheroidal Component of NGC 1300

| Work | Model | $R_{\text{e,sph}}$ (arcsec) | n_{sph} |
|---------|--|--------------------------------|------------------|
| 1D maj. | S-bul + e-(d+bar) + S-id | 9.9 | 3.8 |
| 1D eq. | S-bul + e-(d+bar) + S-id | 8.1 | 3.6 |
| S+11 2D | S-bul + e-d | 85.4 | 3.0 |
| L+14 2D | S-bul + e-d + PSF-n + e-id + S-bar + spiral arms | 10.4 | 4.3 |

Note. S+11 dramatically overestimated the bulge effective radius mainly because their model does not account for the large-scale bar.

Table 24
Best-fit Parameters for the Spheroidal Component of NGC 1316

| Work | Model | $R_{\text{e,sph}}$ (arcsec) | n_{sph} |
|---------|-----------------------------------|--------------------------------|------------------|
| 1D maj. | S-bul + e-d + F-bar + 2 G-r + G-n | 21.5 | 2.0 |
| 1D eq. | S-bul + e-d + F-bar + 2 G-r + G-n | 15.9 | 1.8 |
| S+11 2D | S-bul + e-d + G-n | 93.0 | 5.0 |

Note. S+11 overestimated the bulge effective radius and Sérsic index because their model does not take into account the bar.

3.5. Identifying and Modeling Subcomponents

In this section we give a general overview of the guidelines that we followed to identify and model the subcomponents that

Table 25

Best-fit Parameters for the Spheroidal Component of NGC 1332

| Work | Model | $R_{\text{e,sph}}$ (arcsec) | n_{sph} |
|---------|--------------------|--------------------------------|------------------|
| 1D maj. | S-bul + S-id + m-c | 34.7 | 5.1 |
| 1D eq. | S-bul + S-id + m-c | 18.0 | 3.7 |

Table 26

Best-fit Parameters for the Spheroidal Component of NGC 1374

| Work | Model | $R_{\text{e,sph}}$ (arcsec) | n_{sph} |
|---------|-------------|--------------------------------|------------------|
| 1D maj. | S-bul + G-n | 25.6 | 3.7 |
| 1D eq. | S-bul + G-n | 24.8 | 4.1 |
| 2D | S-bul + m-n | 25.2 | 3.7 |

Table 27

Best-fit Parameters for the Spheroidal Component of NGC 1399

| Work | Model | $R_{\text{e,sph}}$ (arcsec) | n_{sph} |
|--------------|--------------------------|--------------------------------|------------------|
| 1D maj. | S-bul + m-c + e-id | 405.2 | 10.0 |
| 1D eq. | S-bul + m-c + e-id | 338.1 | 10.0 |
| GD07 1D maj. | S-bul | ... | 16.8 |
| R+13 1D eq. | core-Sérsic + (S+e)-halo | 36.2 | 7.4 |
| L+14 2D | S-bul + m-c | 154.0 | 11.1 |

Note. R+13 used a combination of a Sérsic + exponential profile to model the galaxy’s halo and obtained the smallest estimate of the effective radius, one that is at odds with the fact that central cluster galaxies typically have large sizes.

Table 28

Best-fit Parameters for the Spheroidal Component of NGC 2273

| Work | Model | $R_{\text{e,sph}}$ (arcsec) | n_{sph} |
|---------|---------------------|--------------------------------|------------------|
| 1D maj. | S-bul + e-d + F-bar | 1.6 | 2.1 |
| 1D eq. | S-bul + e-d + F-bar | 1.9 | 2.7 |
| L+10 2D | S-bul + e-d + F-bar | 2.6 | 1.8 |

Table 29

Best-fit Parameters for the Spheroidal Component of NGC 2549

| Work | Model | $R_{\text{e,sph}}$ (arcsec) | n_{sph} |
|---------|----------------------------|--------------------------------|------------------|
| 1D maj. | S-bul + e-d + F-bar + F-id | 6.1 | 2.3 |
| 1D eq. | S-bul + e-d + F-bar + F-id | 3.1 | 1.5 |
| 2D | S-bul + e-d + G-bar + G-id | 5.6 | 2.1 |
| S+11 2D | S-bul + e-d | 11.6 | 7.0 |

Note. The model of S+11 does not account for the large-scale bar and therefore largely overestimates the bulge Sérsic index.

constitute our galaxies. However, given the level of accuracy and detail to which each galaxy decomposition has been performed in our analysis, it is hard to encompass all aspects of this matter in a few paragraphs. The modeling of each galaxy represented a particular and original problem, and we remand the reader to Section 5.1, where we provide individual descriptions of the galaxies that we analyzed.

Table 30

Best-fit Parameters for the Spheroidal Component of NGC 2778

| Work | Model | $R_{\text{e,sph}}$ (arcsec) | n_{sph} |
|--------------|-----------------------------|--------------------------------|------------------|
| 1D maj. | S-bul + e-d + F-bar + PSF-n | 2.3 | 1.3 |
| 1D eq. | S-bul + e-d + F-bar + PSF-n | 2.2 | 1.2 |
| GD07 1D maj. | S-bul + e-d | 2.3 | 1.6 |
| S+11 2D | S-bul + e-d | 2.5 | 2.5 |
| V+12 2D | S-bul + e-d | 1.5 | 2.7 |
| L+14 2D | S-bul + e-d + S-bar | 2.8 | 4.0 |

Table 31

Best-fit Parameters for the Spheroidal Component of NGC 2787

| Work | Model | $R_{\text{e,sph}}$ (arcsec) | n_{sph} |
|--------------|--|--------------------------------|------------------|
| 1D maj. | S-bul + e-d + F-bar + F-id + PSF-nucleus | 4.8 | 1.1 |
| 1D eq. | S-bul + e-d + F-bar + F-id + PSF-nucleus | 3.3 | 1.3 |
| GD07 1D maj. | S-bul + e-d | 4.6 | 2.0 |
| L+10 2D | S-bul + e-d + F-bar + F-l | 4.0 | 1.3 |
| S+11 2D | S-bul + e-d + G-bar + G-n | 15.7 | 3.0 |
| L+14 2D | S-bul + trunc. e-d + trunc. S-bar + S-id + PSF-n | 14.3 | 2.8 |

Note. S+11 found larger estimates of the effective radius and Sérsic index because they did not account for the inner disk. L+14 also reported a larger effective radius and Sérsic index because they employed a truncated exponential disk and truncated Sérsic bar in their galaxy model.

Table 32

Best-fit Parameters for the Spheroidal Component of NGC 2974

| Work | Model | $R_{\text{e,sph}}$ (arcsec) | n_{sph} |
|---------|---------------------------------|--------------------------------|------------------|
| 1D maj. | S-bul + e-d + F-bar + G-n + G-r | 8.3 | 1.4 |
| 1D eq. | S-bul + e-d + F-bar + G-n + G-r | 6.9 | 1.2 |
| 2D | S-bul + e-d + G-bar + m-n | 10.6 | 1.3 |
| S+11 2D | S-bul + G-n | 27.2 | 3.0 |

Note. The model of S+11 does not account for the large-scale disk and thus overestimates the bulge effective radius and Sérsic index.

Table 33

Best-fit Parameters for the Spheroidal Component of NGC 2974

| Work | Model | $R_{\text{e,sph}}$ (arcsec) | n_{sph} |
|---------|---------------------------|--------------------------------|------------------|
| 1D maj. | S-bul + F-(bar+d) + G-n | 6.8 | 1.3 |
| 1D eq. | S-bul + F-(bar+d) + G-n | 4.3 | 1.1 |
| S+11 2D | S-bul + e-d + G-bar + G-n | 74.1 | 2.0 |

Note. It is not clear why S+11 obtained a dramatically larger bulge effective radius.

As stressed in Section 1, our investigation is primarily focused on the central spheroidal components of galaxies. The objects in our sample are either early-type galaxies (elliptical +lenticular) or “early-type spiral” galaxies (i.e., the morphological classification of our spiral galaxies is within Sa–Sc, with the only exception of NGC 4945, which is classified as Scd); therefore—by definition—they all have a bulge/spheroidal component, unlike “late-type spiral” galaxies that can be

Table 34

Best-fit Parameters for the Spheroidal Component of NGC 3091

| Work | Model | $R_{\text{e,sph}}$ (arcsec) | n_{sph} |
|------------------|-------------|--------------------------------|------------------|
| 1D maj. | S-bul + m-c | 100.5 | 7.6 |
| 1D eq. | S-bul + m-c | 51.2 | 6.6 |
| 2D | S-bul + m-c | 67.1 | 6.7 |
| R+13 1D Equation | core-Sérsic | 91.0 | 9.3 |

Table 35

Best-fit Parameters for the Spheroidal Component of NGC 3115

| Work | Model | $R_{\text{e,sph}}$ (arcsec) | n_{sph} |
|---------|----------------------|--------------------------------|------------------|
| 1D maj. | S-bul + e-d + G-r | 43.6 | 4.4 |
| 1D eq. | S-bul + e-d + G-r | 34.4 | 5.1 |
| S+11 2D | S-bul + e-d | 27.1 | 3.0 |
| L+14 2D | S-bul + e-d + S-halo | 3.9 | 3.0 |

Note. L+14 used a model with a bulge encased in a larger disk and attributed the excess of light at large radii to a halo. In doing so, they obviously obtained a smaller bulge effective radius.

Table 36

Best-fit Parameters for the Spheroidal Component of NGC 3227

| Work | Model | $R_{\text{e,sph}}$ (arcsec) | n_{sph} |
|---------|-----------------------------|--------------------------------|------------------|
| 1D maj. | S-bul + e-d + F-bar + G-n | 8.1 | 1.7 |
| 1D eq. | S-bul + e-d + [F-bar] + G-n | 4.6 | 1.1 |
| L+10 2D | S-bul + e-d + F-bar | 1.8 | 2.2 |
| S+11 2D | S-bul + e-d | 82.9 | 4.0 |
| L+14 2D | S-bul + e-d + S-bar | 0.7 | 4.1 |

Note. The models of L+10 and L+14 do not account for the bright nuclear component and thus underestimate the bulge effective radius and overestimate the bulge Sérsic index. The bulge effective radius obtained by S+11 is larger because they did not model the bar.

Table 37

Best-fit Parameters for the Spheroidal Component of NGC 3245

| Work | Model | $R_{\text{e,sph}}$ (arcsec) | n_{sph} |
|--------------|------------------------|--------------------------------|------------------|
| 1D maj. | S-bul + e-d + F-id | 4.4 | 2.9 |
| 1D eq. | S-bul + e-d + F-id | 2.4 | 1.7 |
| 2D | S-bul + e-d + G-id | 1.9 | 1.8 |
| GD07 1D maj. | S-bul + e-d | 11.3 | 4.3 |
| L+10 2D | S-bul + e-(d+l) + F-id | 4.0 | 2.4 |
| S+11 2D | S-bul + e-d | 4.6 | 2.5 |
| V+12 2D | S-bul + e-d | 3.5 | 2.6 |
| B+12 2D | S-bul + e-d | 4.0 | 1.6 |
| L+14 2D | S-bul + e-d + S-bar | 2.0 | 1.6 |

bulgeless (e.g., NGC 300). We modeled spheroids/bulges with a Sérsic profile, without attempting to distinguish between classical and pseudobulges.

Disk were usually fit with the exponential model, although in the case of highly inclined or edge-on systems we preferred using an $n < 1$ Sérsic function. Pastrav et al. (2013a, 2013b) showed that, owing to projection effects, their simulated images of inclined galaxy disks are better fit by a Sérsic

Table 38

Best-fit Parameters for the Spheroidal Component of NGC 3377

| Work | Model | $R_{\text{e,sph}}$ (arcsec) | n_{sph} |
|--------------|-----------------------------|--------------------------------|------------------|
| 1D maj. | S-bul + 2 e-id | 61.8 | 7.7 |
| 1D eq. | S-bul + 2 e-id | 91.7 | 9.2 |
| 2D | S-bul + e-id + m-n | 71.8 | 3.7 |
| GD07 1D maj. | S-bul | 44.1 | 3.0 |
| S+11 2D | S-bul | 55.2 | 6.0 |
| B+12 2D | S-bul | 43.5 | 3.5 |
| L+14 2D | S-bul + e-id + e-d + S-halo | 10.1 | 6.0 |

Note. L+14 obtained the smallest estimate of the effective radius because they oversubtracted a halo. In our 2D fit, we were not successful in modeling the nuclear disk and opted for masking the nuclear region of the galaxy. Such a 2D model resulted in a significantly lower Sérsic index, which we trust being underestimated.

Table 39

Best-fit Parameters for the Spheroidal Component of NGC 3384

| Work | Model | $R_{\text{e,sph}}$ (arcsec) | n_{sph} |
|--------------|------------------------------|--------------------------------|------------------|
| 1D maj. | S-bul + e-d + F-bar + m-n | 5.5 | 1.6 |
| 1D eq. | S-bul + e-d + F-bar + m-n | 5.6 | 1.8 |
| GD07 1D maj. | S-bul + e-d | 2.5 | 1.7 |
| L+10 2D | S-bul + e-d + 2 F-bar | 4.0 | 1.5 |
| S+11 2D | S-bul + e-d + G-bar | 4.4 | 2.5 |
| B+12 2D | S-bul + e-d | 8.3 | 2.3 |
| L+14 2D | S-bul + e-d + 2 S-id + S-bar | 5.9 | 2.5 |

Table 40
Best-fit Parameters for the Spheroidal Component of NGC 3393

| Work | Model | $R_{\text{e,sph}}$ (arcsec) | n_{sph} |
|---------|---------------------|--------------------------------|------------------|
| 1D maj. | S-bul + e-d + F-bar | 1.4 | 3.4 |
| 1D eq. | S-bul + e-d + F-bar | 1.4 | 2.6 |
| 2D | S-bul + e-d + G-bar | 1.2 | 1.9 |

Table 41
Best-fit Parameters for the Spheroidal Component of NGC 3414

| Work | Model | $R_{\text{e,sph}}$ (arcsec) | n_{sph} |
|---------|---------------------|--------------------------------|------------------|
| 1D maj. | S-bul + e-id + G-r | 28.0 | 4.8 |
| 1D eq. | S-bul + e-id + G-r | 25.5 | 4.5 |
| L+10 2D | S-bul + e-d + F-bar | 5.0 | 2.6 |

Note. L+10 used a model with a large-scale exponential disk; thus, they obtained a smaller bulge effective radius and Sérsic index.

Table 42
Best-fit Parameters for the Spheroidal Component of NGC 3489

| Work | Model | $R_{\text{e,sph}}$ (arcsec) | n_{sph} |
|---------|---------------------|--------------------------------|------------------|
| 1D maj. | S-bul + e-d + F-bar | 2.2 | 1.5 |
| 1D eq. | S-bul + e-d + F-bar | 1.7 | 1.3 |
| 2D | S-bul + e-d + G-bar | 1.7 | 2.1 |
| L+10 2D | S-bul + e-d + F-bar | 2.0 | 2.1 |
| S+11 2D | S-bul + e-d | 4.6 | 1.5 |

Table 43

Best-fit Parameters for the Spheroidal Component of NGC 3585

| Work | Model | $R_{\text{e,sph}}$ (arcsec) | n_{sph} |
|---------|--------------|--------------------------------|------------------|
| 1D maj. | S-bul + e-id | 105.0 | 5.2 |
| 1D eq. | S-bul + e-id | 86.3 | 6.3 |
| S+11 2D | S-bul + e-d | 15.5 | 2.5 |

Note. S+11 2D obtained smaller estimates of the effective radius and Sérsic index because they included a large-scale disk in their model.

Table 44

Best-fit Parameters for the Spheroidal Component of NGC 3607

| Work | Model | $R_{\text{e,sph}}$ (arcsec) | n_{sph} |
|---------|--------------|--------------------------------|------------------|
| 1D maj. | S-bul + e-id | 69.3 | 5.5 |
| 1D eq. | S-bul + e-id | 65.5 | 5.6 |
| 2D | S-bul + e-id | 60.0 | 5.3 |
| L+10 2D | S-bul + e-d | 6.5 | 1.5 |
| S+11 2D | S-bul + G-n | 44.6 | 5.0 |
| B+12 2D | S-bul | 56.3 | 4.7 |

Note. L+10 obtained the smallest estimates of the effective radius and Sérsic index because they included a large-scale disk in their model.

Table 45

Best-fit Parameters for the Spheroidal Component of NGC 3608

| Work | Model | $R_{\text{e,sph}}$ (arcsec) | n_{sph} |
|-------------|-------------|--------------------------------|------------------|
| 1D maj. | S-bul | 47.5 | 5.2 |
| 1D eq. | S-bul | 43.4 | 5.7 |
| 2D | S-bul | 62.0 | 7.0 |
| S+11 2D | S-bul | 56.4 | 6.0 |
| B+12 2D | S-bul | 182.2 | 9.0 |
| R+13 1D eq. | core-Sérsic | 56.9 | 6.3 |
| L+14 2D | S-bul | 48.9 | 6.6 |

Note. B+12 obtained the largest estimates of the effective radius and Sérsic index, possibly owing to incorrect sky subtraction.

Table 46

Best-fit Parameters for the Spheroidal Component of NGC 3842

| Work | Model | $R_{\text{e,sph}}$ (arcsec) | n_{sph} |
|-------------|-------------------|--------------------------------|------------------|
| 1D maj. | S-bul + F-l + m-c | 100.7 | 8.1 |
| 1D eq. | S-bul + F-l + m-c | 73.6 | 8.2 |
| R+13 1D eq. | core-Sérsic | 58.8 | 6.3 |

function with $n < 1$ than by a pure exponential model. The inclined, embedded disks of some “elliptical” galaxies were described with Ferrer functions, rather than an $n < 1$ Sérsic function. This choice was partly motivated by the fact that a Sérsic + Ferrer model is less degenerate than a Sérsic + Sérsic model, since the Sérsic profile can assume any concave ($n > 1$) or convex ($n < 1$) curvature, whereas the Ferrer profile can only have a negative curvature as required for an inclined disk.

The presence of large-scale disks, such as those of lenticular and spiral galaxies, was known a priori from the galaxy

Table 47

Best-fit Parameters for the Spheroidal Component of NGC 3998

| Work | Model | $R_{\text{e,sph}}$ (arcsec) | n_{sph} |
|---------|---|--------------------------------|------------------|
| 1D maj. | S-bul + e-d + F-bar + F-l + G-n + G-r | 5.8 | 1.2 |
| 1D eq. | S-bul + e-d + F-bar + F-l + G-n + G-r | 4.8 | 1.3 |
| L+10 2D | S-bul + e-d + F-bar + F-l | 5.0 | 2.0 |
| S+11 2D | S-bul + e-d + G-bar + G-n | 4.7 | 1.5 |
| B+12 2D | S-bul + e-d | 5.7 | 2.3 |
| L+14 2D | S-bul + trunc. e-d + PSF-n + S-bar + S-id | 2.0 | 1.1 |

Table 48

Best-fit Parameters for the Spheroidal Component of NGC 4026

| Work | Model | $R_{\text{e,sph}}$ (arcsec) | n_{sph} |
|---------|----------------------------|--------------------------------|------------------|
| 1D maj. | S-bul + e-d + F-bar + S-id | 3.4 | 2.4 |
| 1D eq. | S-bul + e-d + F-bar + S-id | 6.3 | 2.1 |
| S+11 2D | S-bul + e-d | 11.4 | 3.5 |

Note. S+11 obtained larger estimates of the bulge effective radius and Sérsic index because they did not model the bar.

Table 49

Best-fit Parameters for the Spheroidal Component of NGC 4151

| Work | Model | $R_{\text{e,sph}}$ (arcsec) | n_{sph} |
|---------|-----------------------------|--------------------------------|------------------|
| 1D maj. | S-bul + e-d + S-bar [+ m-n] | 7.6 | 1.4 |
| 1D eq. | S-bul + e-d + S-bar [+ m-n] | 6.8 | 1.9 |
| S+11 2D | S-bul + e-d + G-n | 5.4 | 3.5 |

Table 50

Best-fit Parameters for the Spheroidal Component of NGC 4261

| Work | Model | $R_{\text{e,sph}}$ (arcsec) | n_{sph} |
|--------------|--------------------|--------------------------------|------------------|
| 1D maj. | S-bul + m-c + F-id | 52.6 | 4.7 |
| 1D eq. | S-bul + m-c + F-id | 47.3 | 4.3 |
| 2D | S-bul + m-c + e-id | 50.4 | 4.4 |
| GD07 1D maj. | S-bul | 88.6 | 7.3 |
| S+11 2D | S-bul + e-d + G-n | 22.6 | 4.0 |
| V+12 2D | S-bul + m-c | 24.2 | 3.5 |
| B+12 2D | S-bul | 48.8 | 4.3 |
| R+13 1D eq. | core-Sérsic | 77.1 | 6.3 |
| L+14 2D | S-bul + m-c | 68.4 | 6.5 |

Note. S+11 found the smallest estimate of the effective radius because they added a large-scale disk to their model. V+12 obtained a small estimate of the effective radius because of the limited radial extent of their data.

Table 51

Best-fit Parameters for the Spheroidal Component of NGC 4291

| Work | Model | $R_{\text{e,sph}}$ (arcsec) | n_{sph} |
|--------------|-------------|--------------------------------|------------------|
| 1D maj. | S-bul + m-c | 15.0 | 4.2 |
| 1D eq. | S-bul + m-c | 15.4 | 5.9 |
| 2D | S-bul + m-c | 20.8 | 7.7 |
| GD07 1D maj. | S-bul | 14.8 | 4.0 |
| R+13 1D eq. | core-Sérsic | 15.3 | 5.6 |
| L+14 2D | S-bul + m-c | 21.3 | 8.6 |

Table 52

Best-fit Parameters for the Spheroidal Component of NGC 4388

| Work | Model | $R_{\text{e,sph}}$ (arcsec) | n_{sph} |
|---------|---------------------------|--------------------------------|------------------|
| 1D maj. | S-bul + e-d + F-bar + G-n | 4.6 | 0.6 |
| 1D eq. | S-bul + e-d + F-bar + G-n | 4.2 | 1.3 |

Table 53

Best-fit Parameters for the Spheroidal Component of NGC 4459

| Work | Model | $R_{\text{e,sph}}$ (arcsec) | n_{sph} |
|---------|-------------------|--------------------------------|------------------|
| 1D maj. | S-bul + e-d + G-n | 18.4 | 3.1 |
| 1D eq. | S-bul + e-d + G-n | 13.0 | 2.6 |
| L+10 2D | S-bul + e-d + F-l | 7.0 | 3.0 |
| S+11 2D | S-bul + e-d | 10.3 | 2.5 |
| V+12 2D | S-bul + M-n | 25.0 | 3.9 |
| B+12 2D | S-bul | 155.2 | 7.4 |

Note. B+12 did not model the large-scale disk and thus overestimated the bulge effective radius and Sérsic index.

Table 54

Best-fit Parameters for the Spheroidal Component of NGC 4473

| Work | Model | $R_{\text{e,sph}}$ (arcsec) | n_{sph} |
|--------------|--------------------|--------------------------------|------------------|
| 1D maj. | S-bul + e-id + G-n | 45.9 | 2.3 |
| 1D eq. | S-bul + e-id + G-n | 36.9 | 2.9 |
| GD07 1D maj. | S-bul | 39.6 | 2.7 |
| S+11 2D | S-bul | 49.3 | 7.0 |
| V+12 2D | S-bul + m-c | 21.3 | 4.3 |
| B+12 2D | S-bul + e-d | 10.6 | 2.2 |
| L+14 2D | S-bul | 27.9 | 5.1 |

Note. B+12 obtained the smallest estimates of the effective radius and Sérsic index because they included a large-scale disk in their model.

Table 55

Best-fit Parameters for the Spheroidal Component of NGC 4564

| Work | Model | $R_{\text{e,sph}}$ (arcsec) | n_{sph} |
|--------------|-------------------|--------------------------------|------------------|
| 1D maj. | S-bul + e-d + F-l | 5.0 | 2.6 |
| 1D eq. | S-bul + e-d + F-l | 6.0 | 3.0 |
| GD07 1D maj. | S-bul + e-d | 4.3 | 3.2 |
| S+11 2D | S-bul + e-d | 25.0 | 7.0 |
| V+12 2D | S-bul + e-d | 3.0 | 3.7 |

Note. The most discrepant results are obtained by S+11, although they used the same model as GD07 and V+12.

morphological classification (as listed on NED), although some of them were reclassified by us as having intermediate-scale embedded disks. These were identified in a number of different ways. If highly inclined, they can obviously be spotted from the galaxy image or the unsharp mask. Local maxima in the ellipticity and fourth harmonic profiles can provide footprints of less obvious embedded disks. In particular, the ellipticity profile helps distinguish embedded disks from large-scale disks. Galaxy disks typically have fixed ellipticity, reflecting their inclination to our line of sight. On the other hand, spheroids can have their ellipticities varying with radius, but

Table 56

Best-fit Parameters for the Spheroidal Component of NGC 4596

| Work | Model | $R_{\text{e,sph}}$ (arcsec) | n_{sph} |
|---------|----------------------------------|--------------------------------|------------------|
| 1D maj. | S-bul + e-d + F-bar + G-r + S-id | 6.6 | 2.7 |
| 1D eq. | S-bul + e-d + F-bar + G-r + S-id | 9.0 | 3.0 |
| L+10 2D | S-bul + e-d + F-bar + F-l | 2.8 | 1.4 |
| S+11 2D | S-bul + e-d + G-bar | 28.0 | 3.0 |
| V+12 2D | S-bul + e-d + S-bar | 13.2 | 3.6 |
| B+12 2D | S-bul + e-d | 44.9 | 4.4 |

Note. B+12 fit neither the bar nor the inner disk and obtained the largest estimates of the bulge effective radius and Sérsic index. The models of S+11 and V+12 do not account for the inner disk and thus result in larger estimates of the bulge effective radius.

Table 57

Best-fit Parameters for the Spheroidal Component of NGC 4697

| Work | Model | $R_{\text{e,sph}}$ (arcsec) | n_{sph} |
|--------------|------------------------------|--------------------------------|------------------|
| 1D maj. | S-bul + 2 S-id | 239.3 | 7.2 |
| 1D eq. | S-bul + 2 S-id | 226.4 | 6.7 |
| 2D | S-bul + e-id | 121.4 | 5.0 |
| GD07 1D maj. | S-bul | — | 4.0 |
| S+11 2D | S-bul | 100.5 | 5.0 |
| V+12 (1) 2D | S-bul | 39.1 | 3.8 |
| V+12 (2) 2D | S-bul + e-d | 10.0 | 2.9 |
| L+14 2D | S-bul + e-d + PSF-n + S-halo | 6.3 | 2.1 |

Note. In both their models, V+12 underestimated the effective radius and the Sérsic index because of the small radial range of their data. In an effort to model the curved light profile, L+14 included a large-scale disk plus a halo and thus underestimated the spheroid effective radius and the Sérsic index.

Table 58

Best-fit Parameters for the Spheroidal Component of NGC 4889

| Work | Model | $R_{\text{e,sph}}$ (arcsec) | n_{sph} |
|-------------|-------------|--------------------------------|------------------|
| 1D maj. | S-bul + m-c | 119.7 | 8.1 |
| 1D eq. | S-bul + m-c | 60.8 | 6.8 |
| 2D | S-bul + m-c | 104.3 | 7.8 |
| R+13 1D eq. | core-Sérsic | 169.2 | 9.8 |

Table 59

Best-fit Parameters for the Spheroidal Component of NGC 4945

| Work | Model | $R_{\text{e,sph}}$ (arcsec) | n_{sph} |
|---------|-------------|--------------------------------|------------------|
| 1D maj. | S-bul + e-d | 13.9 | 1.4 |
| 1D eq. | S-bul + e-d | 9.5 | 1.7 |
| 2D | S-bul + e-d | 16.2 | 0.8 |

they are usually rounder than inclined disks; thus, their average ellipticities are lower than those of inclined disks. If the ellipticity profile of a galaxy increases with radius, this can be ascribed to an inclined disk that becomes progressively more important over the spheroid, whereas a radial decrease of ellipticity signifies the opposite case. Therefore, in a situation where a disk is identified from the galaxy image, but its extent

Table 60

Best-fit Parameters for the Spheroidal Component of NGC 5077

| Work | Model | $R_{\text{e,sph}}$ (arcsec) | n_{sph} |
|---------|-------------|--------------------------------|------------------|
| 1D maj. | S-bul + m-c | 23.5 | 4.2 |
| 1D eq. | S-bul + m-c | 23.0 | 5.7 |
| 2D | S-bul + m-c | 30.5 | 6.8 |
| S+11 2D | S-bul + G-n | 29.2 | 6.0 |

Table 61

Best-fit Parameters for the Spheroidal Component of NGC 5128

| Work | Model | $R_{\text{e,sph}}$ (arcsec) | n_{sph} |
|---------|----------------------|--------------------------------|------------------|
| 1D maj. | S-bul + e-halo + G-n | 61.3 | 1.2 |
| 1D eq. | S-bul + e-halo + G-n | 60.8 | 2.2 |
| S+11 2D | S-bul + e-d + G-n | 103.6 | 3.5 |

Table 62

Best-fit Parameters for the Spheroidal Component of NGC 5576

| Work | Model | $R_{\text{e,sph}}$ (arcsec) | n_{sph} |
|---------|-------|--------------------------------|------------------|
| 1D maj. | S-bul | 61.5 | 3.3 |
| 1D eq. | S-bul | 49.3 | 3.7 |
| 2D | S-bul | 45.9 | 8.3 |
| S+11 2D | S-bul | 34.3 | 7.0 |
| V+12 2D | S-bul | 16.9 | 5.1 |
| B+12 2D | S-bul | 77.6 | 8.7 |

Note. The results obtained by S+11 and B+12 agree best with the results from our 2D model, in which we did not mask the inner region of the galaxy. The small radial extent of the data used by V+12 led them to underestimate the effective radius.

Table 63

Best-fit Parameters for the Spheroidal Component of NGC 5845

| Work | Model | $R_{\text{e,sph}}$ (arcsec) | n_{sph} |
|--------------|-------------|--------------------------------|------------------|
| 1D maj. | S-bul + e-d | 3.6 | 2.5 |
| 1D eq. | S-bul + e-d | 3.1 | 2.3 |
| 2D | S-bul + e-d | 2.8 | 2.4 |
| GD07 1D maj. | S-bul | 4.1 | 3.2 |
| S+11 2D | S-bul | 3.7 | 3.0 |
| V+12 2D | S-bul | 3.5 | 2.6 |
| B+12 2D | S-bul | 4.1 | 3.5 |
| L+14 2D | S-bul | 3.5 | 2.8 |

(large or intermediate scale) is ambiguous, the shape of the ellipticity profile can be decisive. Another way to establish the presence of an embedded disk is to look at the velocity map of a galaxy, following the approach of Arnold et al. (2014). A local angular momentum decrease with increasing radius is indicative of an intermediate-scale disk that fades toward larger radii. Savorgnan & Graham (2015a) extensively discuss the topic of galaxies with intermediate-scale disks and show that, when these disks are misclassified and modeled as large-scale disks, the luminosity of the spheroidal component is underestimated, which makes these galaxies falsely appear as

Table 64

Best-fit Parameters for the Spheroidal Component of NGC 5846

| Work | Model | $R_{\text{e,sph}}$ (arcsec) | n_{sph} |
|-------------|-------------|--------------------------------|------------------|
| 1D maj. | S-bul + m-c | 105.1 | 6.4 |
| 1D eq. | S-bul + m-c | 83.4 | 5.7 |
| 2D | S-bul + m-c | 85.1 | 5.2 |
| S+11 2D | S-bul | 36.4 | 3.0 |
| V+12 2D | S-bul + m-c | 46.3 | 3.7 |
| R+13 1D eq. | core-Sérsic | 113.2 | 5.3 |

Note. S+11 did not mask the core and thus underestimated the effective radius and Sérsic index.

Table 65

Best-fit Parameters for the Spheroidal Component of NGC 6251

| Work | Model | $R_{\text{e,sph}}$ (arcsec) | n_{sph} |
|--------------|-------------|--------------------------------|------------------|
| 1D maj. | S-bul + m-c | 41.7 | 6.8 |
| 1D eq. | S-bul + m-c | 30.1 | 5.6 |
| 2D | S-bul + m-c | 39.3 | 7.1 |
| GD07 1D maj. | S-bul | 173.9 | 11.8 |
| S+11 2D | S-bul + G-n | 42.4 | 7.0 |
| L+14 2D | S-bul | 20.6 | 5.0 |

Note. It is not clear why GD07 obtained the largest estimates of the effective radius and Sérsic index (possibly the AGN was bright in their R-band image and added to the central cusp).

Table 66

Best-fit Parameters for the Spheroidal Component of NGC 7052

| Work | Model | $R_{\text{e,sph}}$ (arcsec) | n_{sph} |
|--------------|-------------|--------------------------------|------------------|
| 1D maj. | S-bul + m-c | 59.4 | 4.2 |
| 1D eq. | S-bul + m-c | 37.0 | 5.6 |
| 2D | S-bul + m-c | 36.2 | 4.0 |
| GD07 1D maj. | S-bul | 70.4 | 4.6 |
| S+11 2D | S-bul | 39.3 | 5.0 |
| V+12 2D | S-bul + e-d | 4.3 | 1.8 |
| L+14 2D | S-bul | 26.6 | 4.2 |

Note. The model of V+12 2D includes an artificial large-scale disk and thus results in the lowest estimates of the effective radius and Sérsic index.

Table 67

Best-fit Parameters for the Spheroidal Component of NGC 7619

| Work | Model | $R_{\text{e,sph}}$ (arcsec) | n_{sph} |
|-------------|--------------|--------------------------------|------------------|
| 1D maj. | S-bul + e-id | 63.2 | 5.3 |
| 1D eq. | S-bul + e-id | 58.0 | 5.2 |
| R+13 1D eq. | core-Sérsic | 100.1 | 9.3 |

extreme outliers in the black hole mass–spheroid stellar mass diagram.

Bars are usually recognizable from galaxy images and unsharp masks, although local maxima/minima or abrupt changes in the radial profiles of the isophotal parameters can provide additional evidence for less obvious bars. As noted, we were able to successfully fit bars with a Ferrer function (NGC

Table 68
Best-fit Parameters for the Spheroidal Component of NGC 7768

| Work | Model | $R_{\text{e,sph}}$ (arcsec) | n_{sph} |
|-------------|-------------|--------------------------------|------------------|
| 1D maj. | S-bul + m-c | 92.9 | 8.4 |
| 1D eq. | S-bul + m-c | 42.1 | 6.7 |
| R+13 1D eq. | core-Sérsic | 46.1 | 6.2 |

Table 69
Best-fit Parameters for the Spheroidal Component of UGC 03789

| Work | Model | $R_{\text{e,sph}}$ (arcsec) | n_{sph} |
|---------|---------------------------|--------------------------------|------------------|
| 1D maj. | S-bul + e-d + F-bar + G-r | 1.8 | 1.9 |
| 1D eq. | S-bul + e-d + F-bar + G-r | 2.4 | 1.4 |

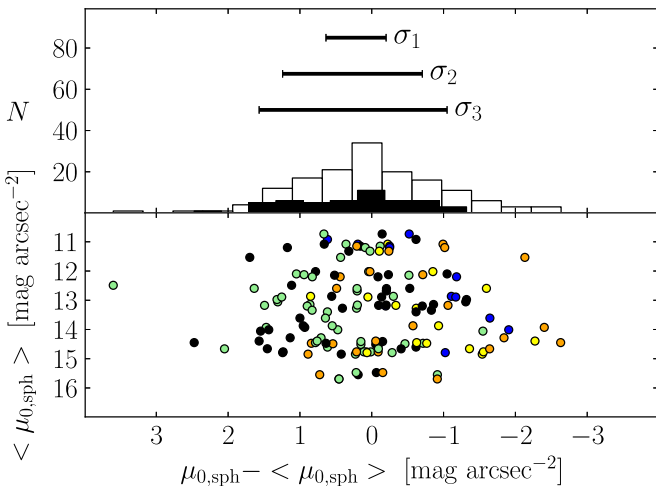


Figure 13. Bottom panel: 49 galaxies for which at least one measurement of the spheroid central surface brightness $\mu_{0,\text{sph}}$ —either in the K band or at $3.6 \mu\text{m}$ —is available from the literature (Table 3), in addition to that measured by us. The K -band magnitudes were converted into $3.6 \mu\text{m}$ magnitudes (see Section 4.2 for details). The average value $\langle \mu_{0,\text{sph}} \rangle$ is plotted against the difference between the individual measurements of a galaxy and the average value for that same galaxy. See Figure 9 for color description and explanation of the top panel.

4151 is the only case for which we described the bar with an $n \sim 0.2$ Sérsic model). Disk-like components embedded in the bulges of spiral galaxies were described with an $n \lesssim 1$ Sérsic model or, in a few cases, with a Ferrer function.¹⁵ This approach is similar to that of Laurikainen et al. (2010), who fit bars with a Ferrer function and inner disks with a Sérsic model. Given that our galaxy sample lacks “late-type spiral” galaxies, it is not surprising (Gadotti & de Souza 2006) that we did not find bars with exponential profiles (e.g., Elmegreen & Elmegreen 1985; Gadotti 2008; Kim et al. 2015). The bars in our sample were found to have rather flat inner profiles, as is commonly found for bars in “early-type spiral” galaxies (Gadotti & de Souza 2006).

The presence of a nuclear component—either resolved or unresolved—was generally expected in (but not restricted to) galaxies that host an optical AGN and circumnuclear dust.

¹⁵ One advantage of choosing a Ferrer function over a Sérsic profile to fit a disk-like component embedded in the bulge is to reduce degeneracies with the Sérsic profile that describes the bulge.

Nuclear stellar disks and nuclear star clusters fall into the category of nuclear components too, but their identification can be more subtle than for AGNs. Nuclear clusters have typical sizes of a few parsecs; therefore, for the majority of our galaxies they are unresolved in *Spitzer*/IRAC $3.6 \mu\text{m}$ observations. If an identification from high-resolution observations was available from the literature, we relied on that; otherwise, we concluded that a galaxy was nucleated from an excess of nuclear light in the residuals of the fit.¹⁶ Unresolved nuclear components were fit with our optimal Moffat PSF, whereas resolved nuclear components were modeled with (PSF-convolved) narrow Gaussian functions (for a discussion of the importance of fitting nuclear components, see Wadadekar et al. 1999; Ravindranath et al. 2001; Peng et al. 2002; Gadotti 2008). Rings were identified from galaxy images and unsharp masks and modeled with symmetric Gaussian ring profiles (e.g., Sheth et al. 2010; Kim et al. 2014).

As an illustration, we consider the galaxy NGC 2974, a spiral galaxy that has been misclassified as an elliptical galaxy in the RC3 catalog (de Vaucouleurs et al. 1991). This galaxy hosts a Seyfert AGN (Véron-Cetty & Véron 2006) and filamentary dust in its center (Tran et al. 2001). NGC 2974 is classified as a fast rotator by the ATLAS^{3D} survey, and indeed the velocity map obtained by the SLUGGS survey shows that the galaxy kinematics is rotation dominated well beyond three effective radii ($R > 150''$), as expected from a large-scale disk. From an inspection of the unsharp mask, we identified a ring at $R \sim 50''$, which might be a residual of two tightly wound spiral arms, and an elongated bar-like component within $R \lesssim 30''$, which is in addition to the more spherical bulge and produces a peak in the ellipticity and position angle profiles at $R \sim 20''$. Our 1D galaxy decomposition for NGC 2974 (Figure 4) consists of a Sérsic bulge, an exponential large-scale disk, a Ferrer bar, a Gaussian nuclear component (AGN), and a Gaussian ring. Although the ring is extremely faint, it is important to account for it in the galaxy decomposition. A model without the ring component results in a “steeper” exponential profile for the disk (i.e., the exponential model has a smaller scale length and a brighter central surface brightness) and produces bad residual structures within $R \lesssim 40''$. Our best-fit model returns a $3.6 \mu\text{m}$ bulge major-axis effective radius $R_{\text{e,sph}}^{\text{maj}} = 8.3$ arcsec, equivalent-axis Sérsic index $n_{\text{sph}}^{\text{eq}} = 1.2$, and apparent magnitude $m_{\text{sph}} = 8.65$ mag. Sani et al. (2011) modeled NGC 2974 with a Sérsic bulge and a Gaussian nuclear component (AGN), but did not account for the large-scale disk. From their best-fit 2D model, they obtained a three times larger $3.6 \mu\text{m}$ bulge major-axis effective radius ($R_{\text{e,sph}}^{\text{maj}} = 27.2$ arcsec), a 2.5 times larger Sérsic index ($n_{\text{sph}} = 3$), and a significantly brighter apparent magnitude ($m_{\text{sph}} = 7.28$ mag).

3.6. 2D Fits

2D decompositions were carried out using the software IMFIT (Erwin 2015). For each galaxy, we built a 2D model that was consistent with the corresponding 1D model in terms of

¹⁶ This conclusion was drawn after going through the following steps. First we identified all the subcomponents of a galaxy (assuming that the galaxy was not nucleated), built a model accordingly, and fit it to the data. If the residuals of the fit showed a nuclear light excess, we repeated the fit by excluding the data points within the nuclear region. Only after checking that the outcome of the last fit was consistent with a fit that included a small nuclear component did we infer the presence of a stellar nuclear component.

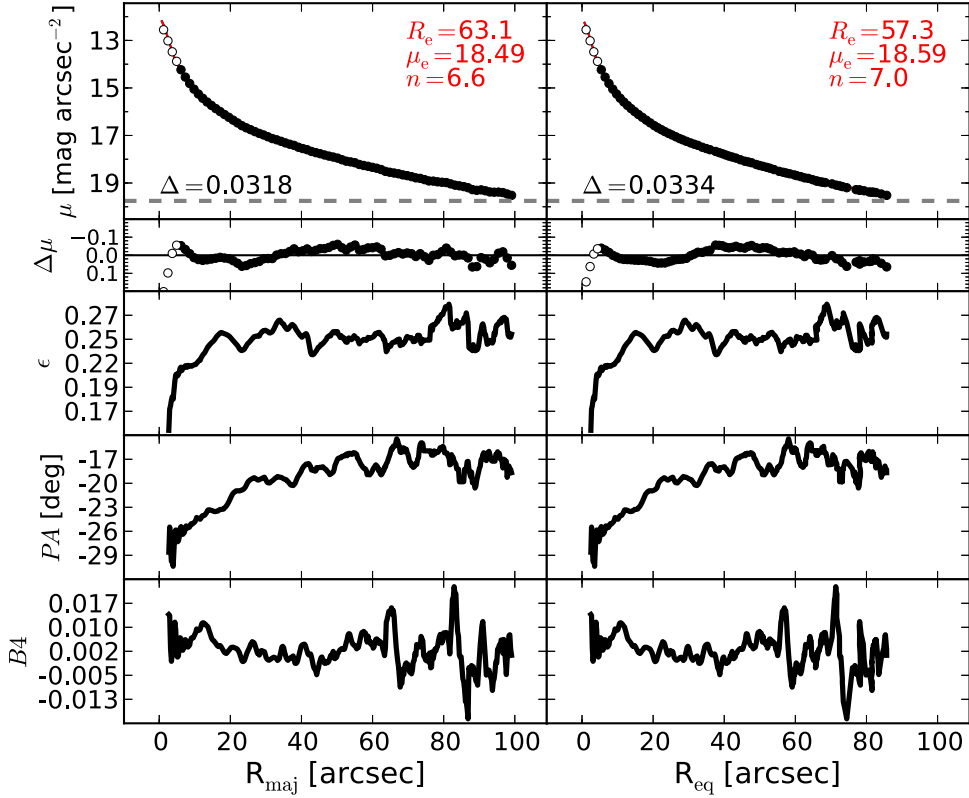


Figure 14. IC 1459: an elliptical galaxy with a fast counterrotating stellar component (Franx & Illingworth 1988; Cappellari et al. 2002), nuclear dust, and indications of a nuclear stellar disk (Forbes et al. 1994). The kinematically decoupled component cannot be identified as a separate structure in photometric observations. This galaxy also has an unresolved partially depleted core (Rusli et al. 2013a). Our isophotal analysis confirms a simple morphology for IC 1459, with no evident embedded components. After masking the innermost $6''$, we fit this galaxy with a Sérsic profile.

number and type of components. The only difference between our 1D and 2D models pertains to the description of bars: because the Ferrer profile is not made available in IMFIT, bars were fit with a 2D Gaussian function.

The 2D decomposition of NGC 2974 is presented in Figure 5. The galaxy was modeled with a Sérsic bulge, an exponential disk, and a Gaussian bar. The nuclear component was masked, and the ring was not modeled.¹⁷ Our best-fit 2D model returns a bulge major-axis effective radius $R_{e,\text{sph}}^{\text{maj}} = 10.5$ arcsec, a bulge Sérsic index $n_{\text{sph}} = 1.3$, and a $3.6 \mu\text{m}$ bulge apparent magnitude $m_{\text{sph}} = 8.39$ mag, in fairly good agreement with our 1D decomposition. Fits and descriptions for the other galaxies are available online.

4. RESULTS

For each galaxy, after we identified its various components and built a model accordingly, we simultaneously performed a set of four 1D fits. All four fits use a Moffat-convolved model. Two fits use the major-axis surface brightness profile, and the remaining two use the equivalent-axis surface brightness profile. For each of these pairs, we use a logarithmically sampled surface brightness profile and a linearly sampled surface brightness profile. Because our fitting routine intentionally does not employ an error-weighting scheme on the data

points that constitute the surface brightness profile, a fit to a logarithmically sampled profile puts more weight on the inner region of the galaxy and poorly constrains the outskirts. On the other hand, a fit to a linearly sampled surface brightness profile equally treats inner and outer regions, but is more susceptible to sky-background subtraction issues.

We found that the fits are, in general, more sensitive to the choice of the initial parameters when using logarithmically sampled profiles than linearly sampled profiles. In addition, a visual examination of the residuals revealed that the quality of the fit within one galaxy effective radius is superior when tighter constraints are put on the galaxy outskirts. In other words, the better quality of the residuals led us to prefer the fits that use linearly sampled surface brightness profiles, although the results were usually very similar, as might be expected.

Among the initial sample of 75 galaxies, we did not attempt to model three galaxies: M32, NGC 4486A, and the Circinus galaxy. The first two have been stripped by their massive companions and thus have uncertain morphology. The Circinus galaxy lies at only 4° from the Galactic plane; therefore, its image mosaic is contaminated by a large number of foreground stars. Of the remaining 72 galaxies, we obtained satisfactory 1D decompositions for 66, whereas the models of 6 galaxies were judged not reliable and were thus excluded. We also performed reliable 2D decompositions for 31 galaxies.

A galaxy-by-galaxy comparison between our best-fit models and those from the previous literature helped identify the optimal decompositions and past problems. We compared our best-fit models with those of Graham & Driver (2007a), Sani et al. (2011), Beifiori et al. (2012), Vika et al. (2012), and Läsker et al.

¹⁷ We built the 2D model first including and then omitting a Gaussian ring component, but both models converged to the same solution, i.e., the fit “ignored” the presence of the faint ring. This did not happen in the 1D decomposition because of the different weighting scheme used by the fitting routines.

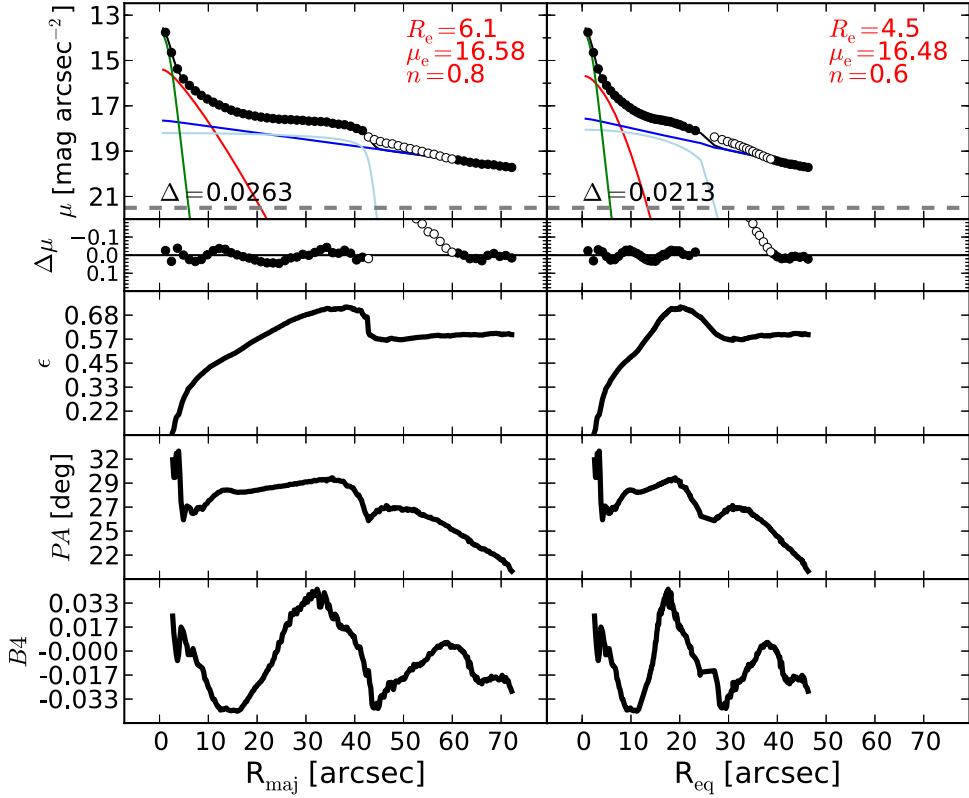


Figure 15. IC 2560: a barred spiral galaxy with a Seyfert AGN (Véron-Cetty & Véron 2006) and dust within the central $2''.5$ (Martini et al. 2003). A visual inspection of the image of IC 2560 reveals a boxy bulge and a large-scale bar that extends out to $R_{\text{maj}} \lesssim 43''$. The disk appears to be slightly lopsided along the direction of the bar, owing to two nonsymmetric ansae, but it becomes symmetric beyond $R_{\text{maj}} \gtrsim 60''$. This is why the surface brightness profile deviates from a perfect exponential in the radial range $42'' \lesssim R_{\text{maj}} \lesssim 60''$, which is excluded from the fit. Motivated by the presence of a strong optical AGN and dust in the nucleus (which adds rather than obscures at $3.6 \mu\text{m}$), we account for an excess of nonstellar light by adding a central Gaussian component to the model.

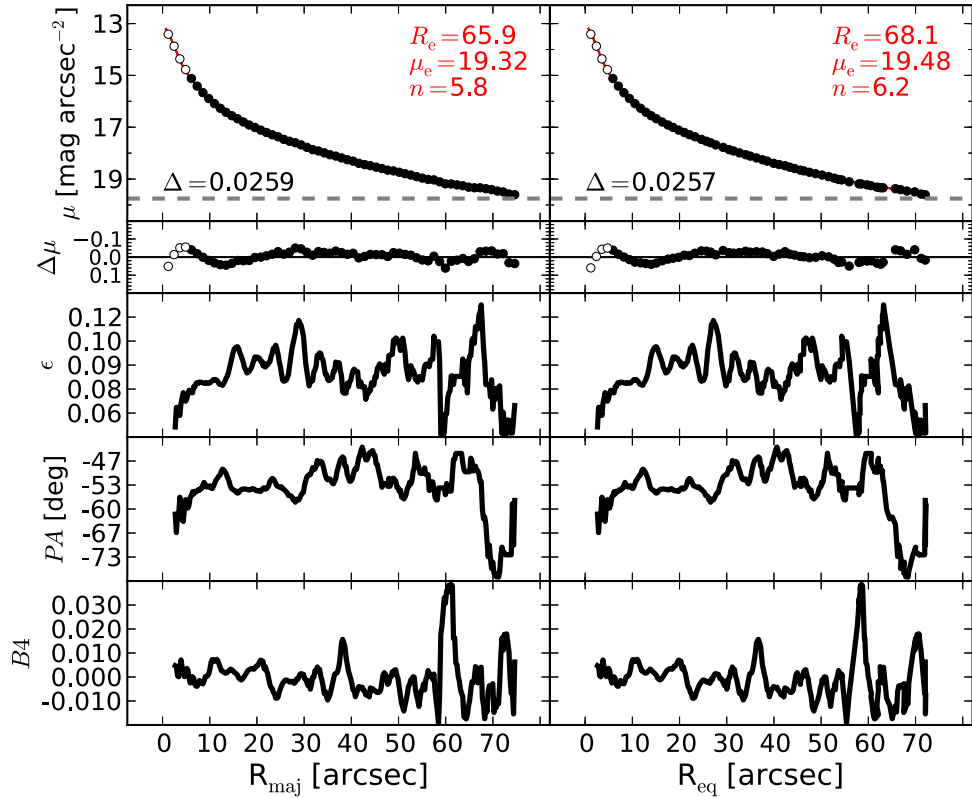


Figure 16. IC 4296: an elliptical galaxy. Owing to its high stellar velocity dispersion, this galaxy is expected to host a partially depleted core. After masking the innermost $6''.1$, we find that a single Sérsic profile provides a good description of this galaxy.

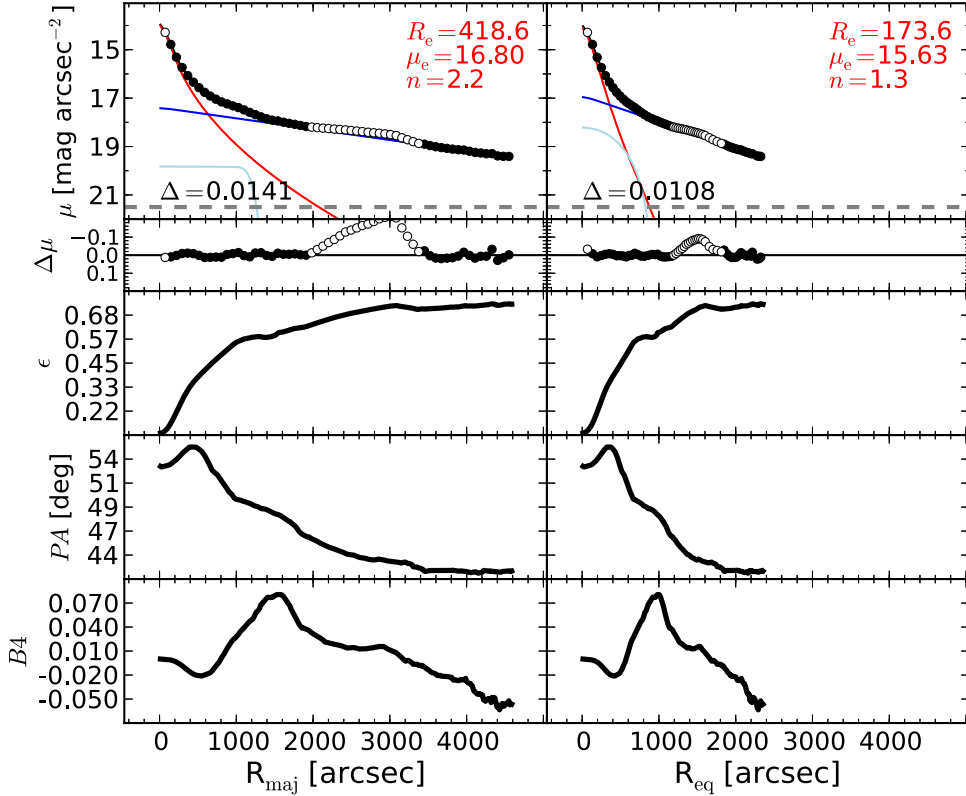


Figure 17. M31 (Andromeda galaxy): a spiral galaxy. Although for decades this galaxy had been classified as an unbarred spiral, recent works have revealed the presence of a bar (Athanioula & Beaton 2006; Beaton et al. 2007; Morrison et al. 2011), seen as the plateau at $800'' \lesssim R_{\text{maj}} \lesssim 1000''$. M31 also features a broad ring-like structure at $R_{\text{maj}} \sim 50'$ (Athanioula & Beaton 2006). We applied the *smoothing* technique described in Section 3.4 to the analysis of M31. The region $2000'' \lesssim R_{\text{maj}} \lesssim 3400''$, where the pseudoring is observed, is excluded from the fit. A Sérsic + exponential fit is not adequate to describe the light profile of M31, as the residuals of such a fit display a structure in correspondence of the bar ($R_{\text{maj}} \lesssim 1500''$). The addition of a Ferrer function to account for the bar notably improves the fit.

(2014a). We also considered the best-fit models of Laurikainen et al. (2010) and Rusli et al. (2013a) because, although they did not specifically deal with black hole—galaxy scaling relations, their galaxy samples significantly overlap with ours.

Table 2 lists the results from both the 1D and 2D fits.

4.1. 1D versus 2D Decompositions

Here we explore how 1D and 2D decompositions compare with each other. Readers not interested in our practical knowledge, having dealt with 1D and 2D techniques of galaxy modeling at the same time, can skip to Section 4.2. We summarize our experience in the following points.

1. A visual inspection of galaxy images and their unsharp masks is often not sufficient to accurately identify all of a galaxy’s components. Weak bars and some embedded disks can easily be missed. Other (inclined) embedded disks can be confused with large-scale disks. In this regard, the 1D isophotal analysis is extremely helpful. Local minima/maxima or abrupt changes in the ellipticity, position angle, and fourth harmonic profiles contain precious information about a galaxy’s constituents.
2. The ellipticity and position angle of triaxial spheroids can vary with radius. The analytic functions used by 2D decomposition codes to fit galaxy components have fixed ellipticity and position angle; thus, they cannot account for these radial gradients. This problem is overcome with 1D decomposition techniques because the ellipticity and

additionally the deviations from elliptical isophotes are efficiently included in the equivalent-axis fit (see the Appendix of Ciambur 2015).

3. The interpretation of the residual surface brightness profile is often crucial to identify the optimal decomposition for a galaxy. In our experience, we found that interpreting 1D residuals was easier and more productive than 2D residuals.

Although we attempted 2D modeling for the 72 galaxies in our sample, more than half of the 2D decompositions were not successful or did not converge to a meaningful solution. This should serve as a tip to users of 2D fitting codes. When physically meaningful spheroid parameters are required, the output may not be reliable and should be inspected. For the 31 galaxies that had successful 2D decompositions, we compare with their 1D parameters in Figures 6–8. The agreement between 1D and 2D effective radii and magnitudes is remarkable, whereas a larger amount of scatter in the Sérsic indices can be caused by the fact that 2D measurements do not exactly correspond to 1D equivalent-axis measurements. No systematic effects are observed in any of these three plots, which indicates that 1D and 2D techniques of galaxy modeling—when performed on the same galaxy—can give consistent results.

In conclusion, since we found that the best-fit parameters do not depend on the decomposition method (1D or 2D) used, and given that we obtained more successful 1D decompositions than 2D, we will base our analysis on the results from the 1D fits.

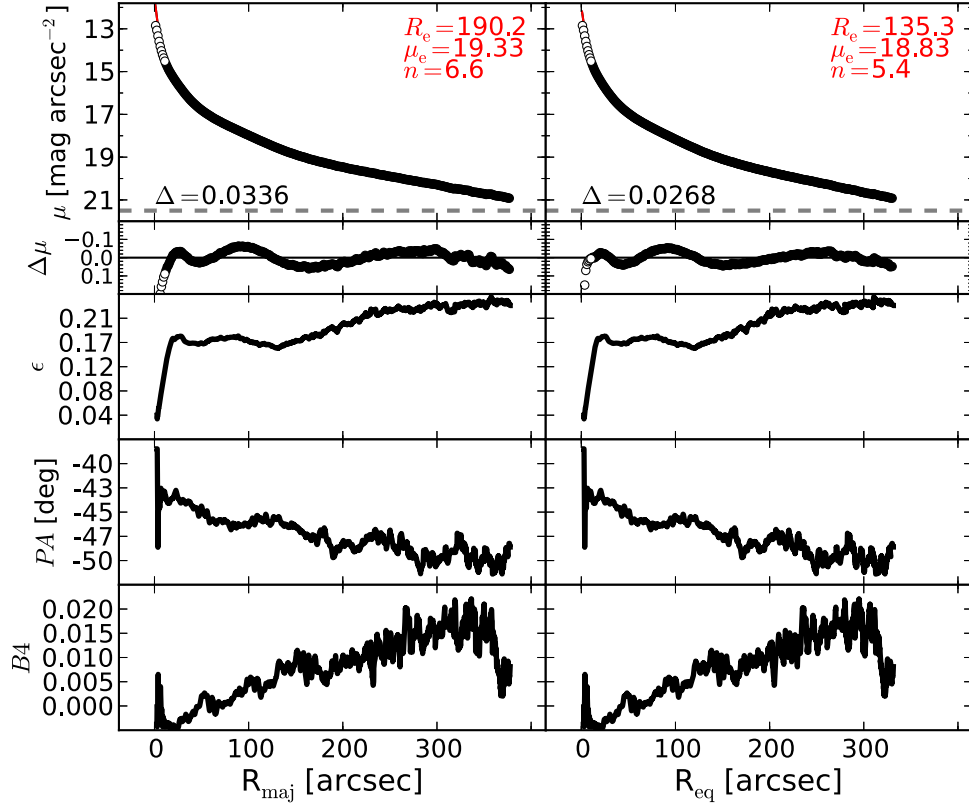


Figure 18. M49: the brightest member of the Virgo Cluster, a giant elliptical galaxy with a slightly resolved partially depleted core (Rusli et al. 2013a). The data within the innermost $12''$ are excluded from the fit. We fit M49 with a single Sérsic profile.

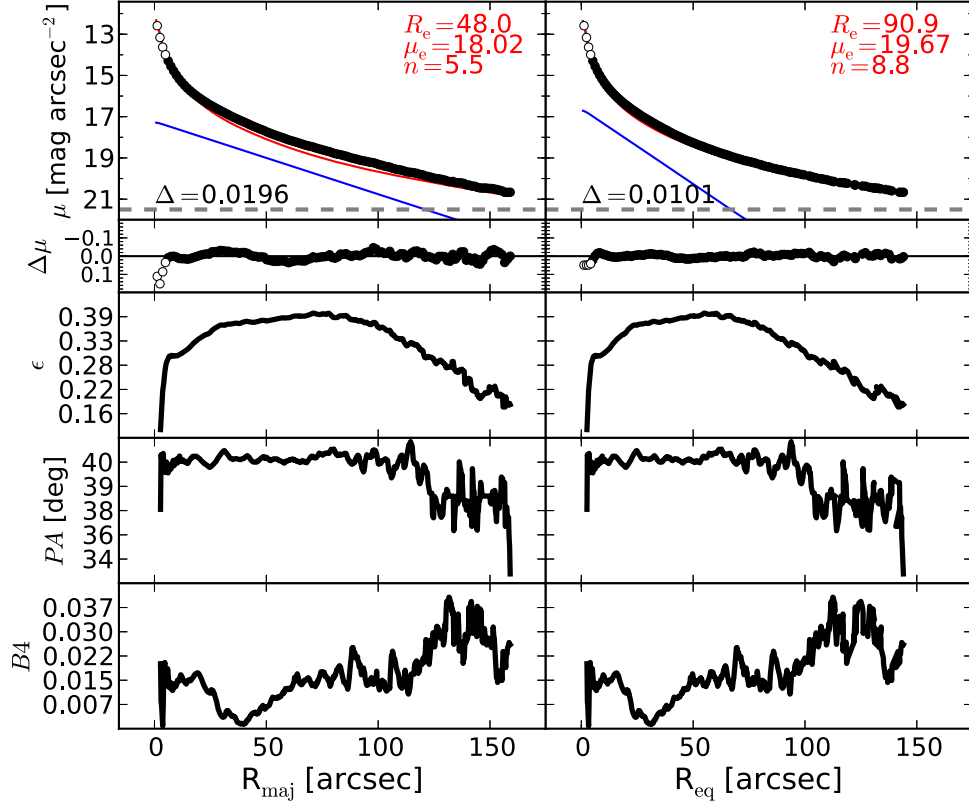


Figure 19. M59: an elliptical galaxy with an edge-on, intermediate-scale embedded disk (Scorza & Bender 1995) and a thin, faint nuclear stellar disk (Ferrarese et al. 2006; Ledo et al. 2010). The intermediate-scale embedded disk is clearly visible in our unsharp mask image (not shown), and the velocity map (ATLAS 3D) confirms the presence of this rapidly rotating component, which is modeled with an exponential function. We choose not to account for the nuclear stellar disk by excluding the innermost $6.1''$ from the fit.

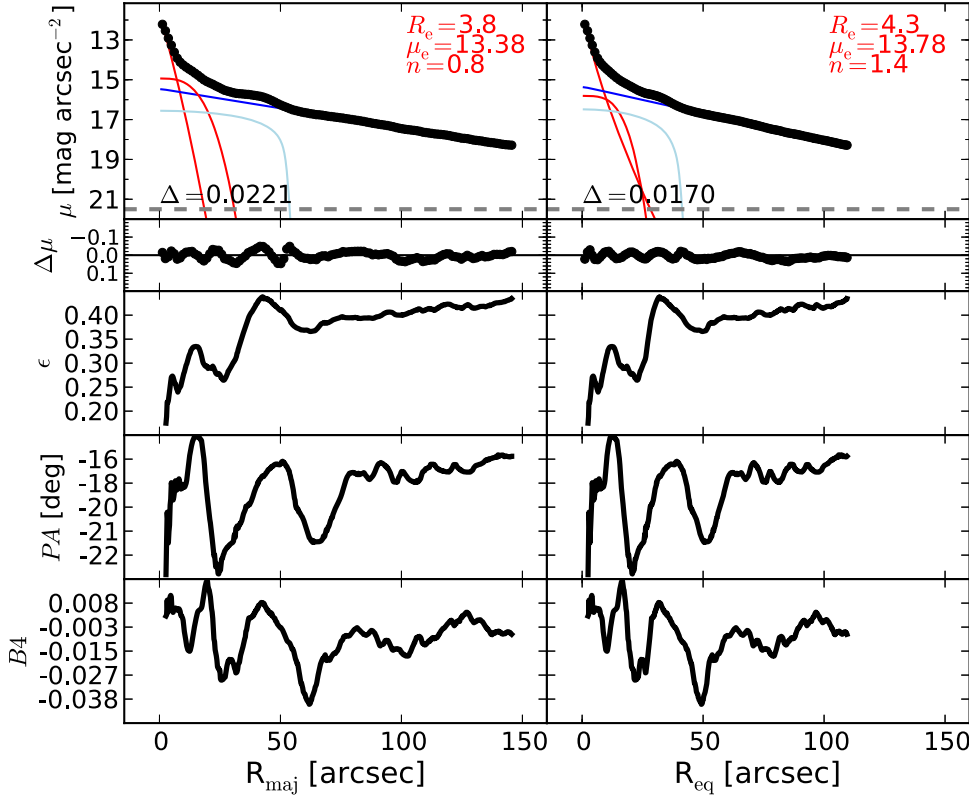


Figure 20. M64: a dusty spiral galaxy with a Seyfert AGN (Véron-Cetty & Véron 2006). A large-scale bar ($R_{\text{maj}} \lesssim 50''$) can be identified in the unsharp mask and produces corresponding peaks in the ellipticity, PA, and $B4$ profiles. This is modeled with a Ferrer function. Additional peaks in the ellipticity, PA, and $B4$ profiles at $R_{\text{maj}} \sim 15''$ signal the presence of an embedded disk component, which we describe with a low- n Sérsic function. Although the galaxy is dusty and hosts an AGN, we do not observe any nuclear excess of light in the fit residuals, and therefore we found it unnecessary to add a nuclear component to our model.

4.2. Parameter Uncertainty

Estimating the uncertainties associated with the best-fit parameters of our 1D galaxy decompositions is not straightforward. Monte Carlo simulations could be used for this purpose, but they would take into account only random errors and not unknown systematic errors. Systematic errors include incorrect sky subtraction, inaccurate masking of contaminating sources, imprecise description of the PSF, erroneous choice of model components (for example, when failing to identify a galaxy subcomponent and thus omitting it in the model, or when describing a galaxy subcomponent with an inadequate function), the radial extent of the surface brightness profile, and its sampling. These factors are not included in popular 2D fitting codes, which report only the random errors associated with their fitted parameters. Moreover, when performing multi-component decomposition of high-S/N images of nearby—and therefore well-resolved—galaxies, errors are dominated by systematics rather than Poisson noise. For this reason, we decided to estimate the uncertainties of the spheroid best-fit parameters with a method that took into account systematic errors.

4.2.1. Goodness of the Spheroid Modeling

For each of our fits, we calculated the associated rms scatter using

$$\Delta = \sqrt{\frac{\sum_{i=0}^N (\mu_i^{\text{obs}} - \mu_i^{\text{mod}})^2}{N_{\text{dof}}}}, \quad (2)$$

where N_{dof} is the number of degrees of freedom, μ_i^{obs} is the observed surface brightness, and μ_i^{mod} is the model surface brightness at each data point i . Although useful to evaluate the overall quality of a galaxy decomposition, the rms scatter alone cannot be used to assess the goodness of the fit for the spheroidal component only, unless the galaxy is a pure spheroid and has consequently been modeled with a single Sérsic profile. To illustrate this point with an example, one can imagine a situation in which a galaxy is thought to be made of a small bulge and a much more extended disk. This galaxy is decomposed with a Sérsic + exponential model. The exponential function provides an excellent description of the light profile of the disk, whereas the Sérsic function does not do the same for the bulge. The residuals of the fit will then be flat and close to zero at large radii, where the emission of the disk dominates over that of the bulge, while they will display significant departures at small radii, in correspondence with the poorly fit spheroidal component. In the case of linear sampling, because the part of the surface brightness profile pertaining to the disk may contain more data points than the part pertaining to the bulge, the global rms scatter will be relatively small, but it obviously will not reflect the accuracy of the fit to the spheroidal component only.

A simple but powerful way to get a feeling of how precisely the global model and its spheroidal component have fared is to look at the major- and equivalent-axis fits of each galaxy and visually inspect the structures of the residual surface brightness profile (i.e., the second row in Figure 4) within $\sim 1\text{--}2$ spheroid

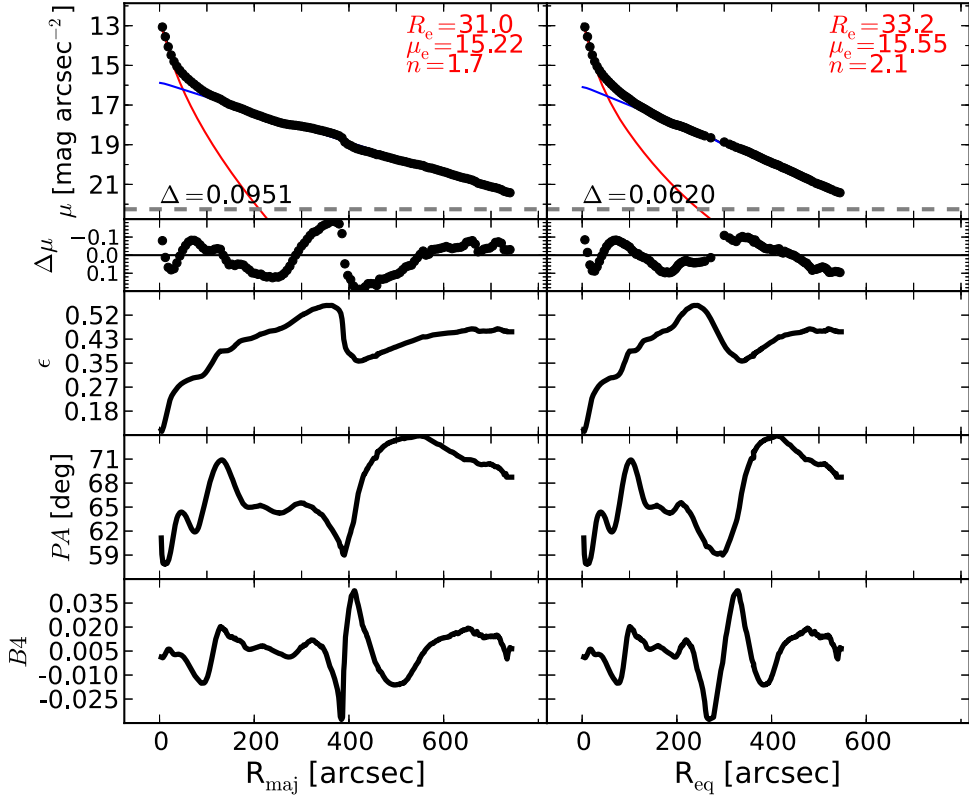


Figure 21. M81: an early-type spiral galaxy. This galaxy features a nuclear bar at $R_{\text{maj}} \lesssim 17''$ and a large-scale bar at $R_{\text{maj}} \lesssim 130''$ (Elmegreen et al. 1995; Gutiérrez et al. 2011; Erwin & Debbattista 2013). We applied the smoothing technique described in Section 3.4 to the analysis of M81. The bars are not particularly evident in the galaxy image or in the unsharp mask. The bump at $R_{\text{maj}} \lesssim 400''$ is due to spiral arms. Attempts to account for the bars in the fit were unsuccessful. For this reason, we use a simple Sérsic + exponential model.

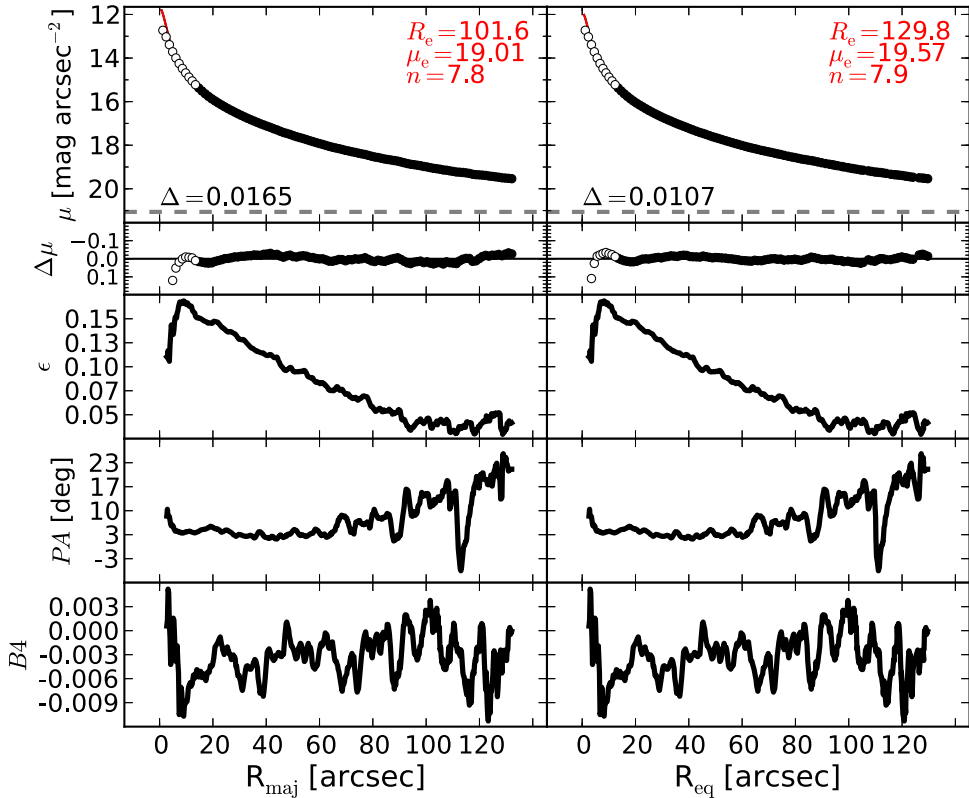


Figure 22. M84: an elliptical galaxy with a slightly resolved partially depleted core (Rusli et al. 2013a). The unsharp mask reveals a faint inner component ($R_{\text{maj}} \lesssim 12''$). We exclude the data within $R_{\text{maj}} < 13.8''$ and model the galaxy with a Sérsic profile.

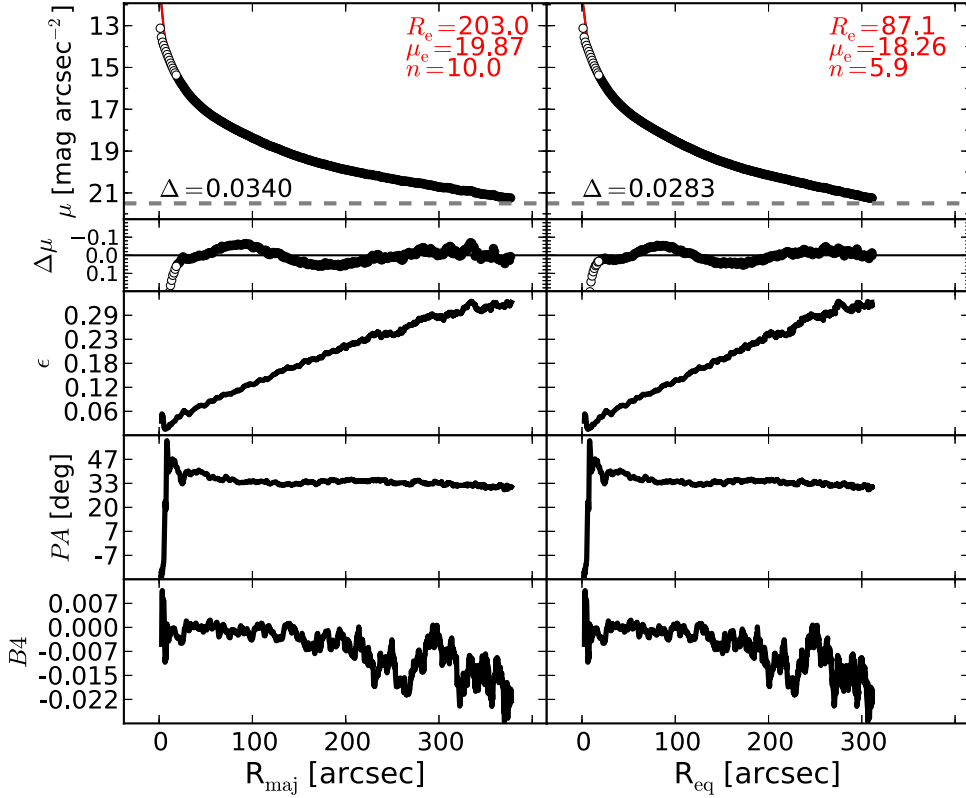


Figure 23. M87: a giant elliptical galaxy belonging to the Virgo Cluster. This galaxy has a large ($>7''$), partially depleted core (Ferrarese et al. 2006). The morphology of M87 is similar to that of M49. The innermost $18''$ are excluded, and a Sérsic model is used to fit M87. We note that the effective radius obtained from our 1D major-axis fit is more than a factor of two larger than that obtained from our 2D fit. This is due to the fact that the 2D model has fixed ellipticity and cannot account for the strong ellipticity gradient of the galaxy, which serves as a warning to some 2D fits in the literature.

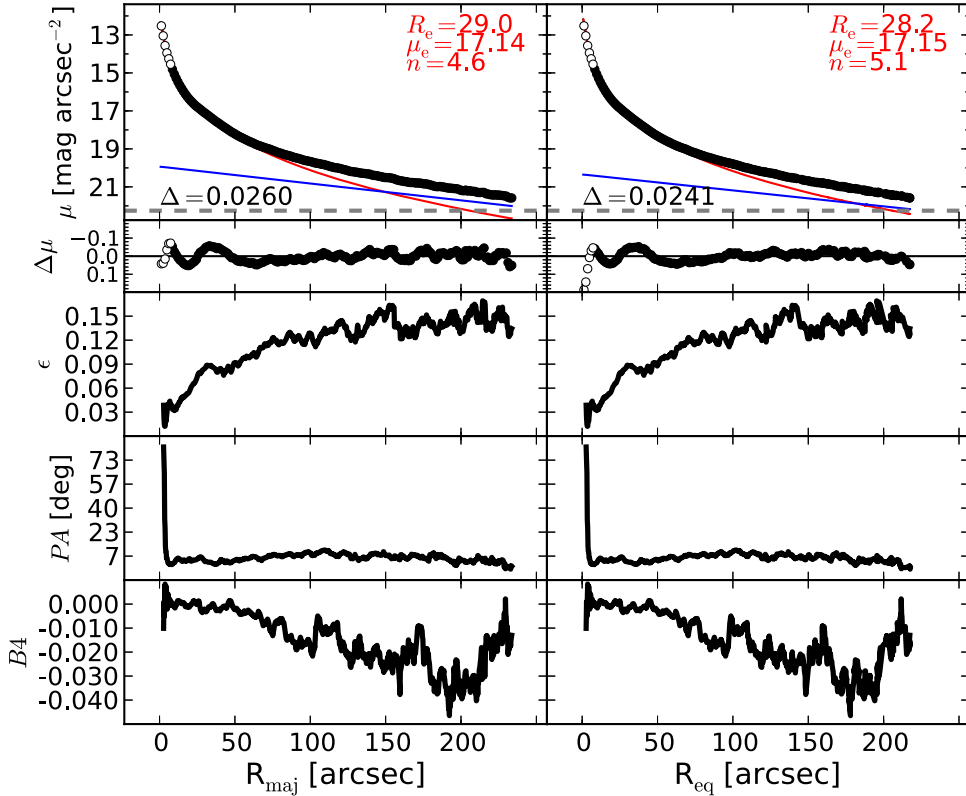


Figure 24. M89: an elliptical galaxy with an unresolved partially depleted core (Rusli et al. 2013a). The galaxy halo dominates the light at large radii, where the isophotes are significantly more elliptical than in the inner part of the galaxy. The halo is modeled with an exponential function.

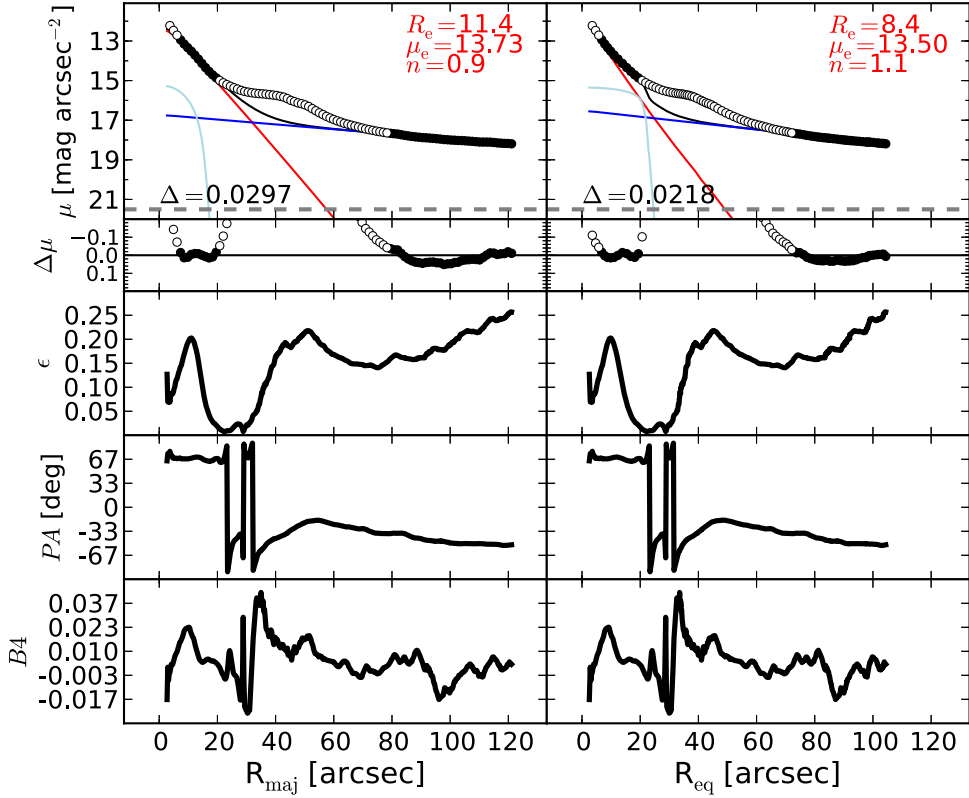


Figure 25. M94: a face-on spiral galaxy, with a Seyfert AGN (Véron-Cetty & Véron 2006) and circumnuclear dust (Elmegreen et al. 2002; Peebles & Martini 2006). This galaxy has a ring-like structure at $R_{\text{maj}} \sim 50''$ (Muñoz-Tunon et al. 1989). The ellipticity and $B4$ profiles display a local maximum at $R_{\text{maj}} \sim 10''$, indicating the presence of a disk-like component embedded in the bulge, as already noted by Fisher & Drory (2010). We model this component with a Ferrer function. We exclude the data within the innermost $6''/7$, owing to the AGN contribution. Attempts to model the ring were unsuccessful, resulting in a degenerate model; therefore, we exclude the data in the range $20'' \lesssim R_{\text{maj}} \lesssim 80''$.

effective radii. We did this using a grade from 1 to 3, assigned according to the following criteria.

1. A grade of 1 was given to the best fits, i.e., fits that do not exhibit any of the problems listed below.
2. A grade of 2 was issued in the following cases: the residuals in correspondence with the radial extent of the spheroidal component are not randomly distributed around zero, being symptomatic of a Sérsic model having a curvature (regulated by the Sérsic index n) that does not quite match the real “shape” of the spheroid; when we identified but were not able to model a galaxy subcomponent with the same accuracy dedicated to the other components; in the case of apparent inconsistencies between the model and the observed galaxy properties (e.g., an embedded disk modeled with an exponential function, whose scale length does not quite match the size of the disk as expected from the ellipticity profile or the velocity map); and when the Sérsic model used to describe the spheroidal component has a size—as measured by the effective radius—comparable to a few times the FWHM of the PSF. Galaxies in this category are reasonably well fit despite these issues.
3. A grade of 3 was assigned to the poorer and more anomalous fits, or those affected by an obvious degeneracy between the spheroid Sérsic profile and the remaining model components (e.g., when the spheroid Sérsic index varies by as much as 50% among the four different realizations of the fit, or when the output of

the fit strongly depends on the choice of the initial parameters).

As a result, we classified 27 galaxies (38% of the 72 galaxies for which we attempted a 1D decomposition) with grade 1, 29 galaxies (40%) with grade 2, and 10 galaxies (14%) with grade 3. Six galaxies could not be modeled. We report the assigned grades in Table 2 (column 10).

4.2.2. Uncertainties on n_{sph}

In Figure 9, for 58 galaxies, we compare the measurements of the spheroid Sérsic index obtained by different authors with those obtained by us. For each galaxy, we computed the average value $\langle \log(n_{\text{sph}}) \rangle$ of the available measurements, and we plot it against the scatter of the individual measurements around each spheroid’s $\langle \log(n_{\text{sph}}) \rangle$. The measurements are heterogeneous, in the sense that they were obtained from 1D or 2D decompositions of data in different wavelengths, and they refer either to the major axis, the equivalent axis, or some 2D average. In Figure 9, the black histogram shows the distribution of the scatter around $\langle \log(n_{\text{sph}}) \rangle$ for our measurements; 38% of this distribution lies within $-\sigma_1^- = -0.08$ dex and $+\sigma_1^+ = +0.06$ dex, 78% lies within $-\sigma_2^- = -0.21$ dex and $+\sigma_2^+ = +0.17$ dex, and 92% lies within $-\sigma_3^- = -0.25$ dex and $+\sigma_3^+ = +0.25$ dex. We elect to use $\pm\sigma_1^\pm$, $\pm\sigma_2^\pm$, and $\pm\sigma_3^\pm$ as 1 σ uncertainties for our measurements of $\log(n_{\text{sph}})$ obtained from “grade 1,” “grade 2,” and “grade 3” fits, respectively. This means that if the fit to a galaxy was classified as “grade 1,” the (logarithmic) value of the spheroid Sérsic

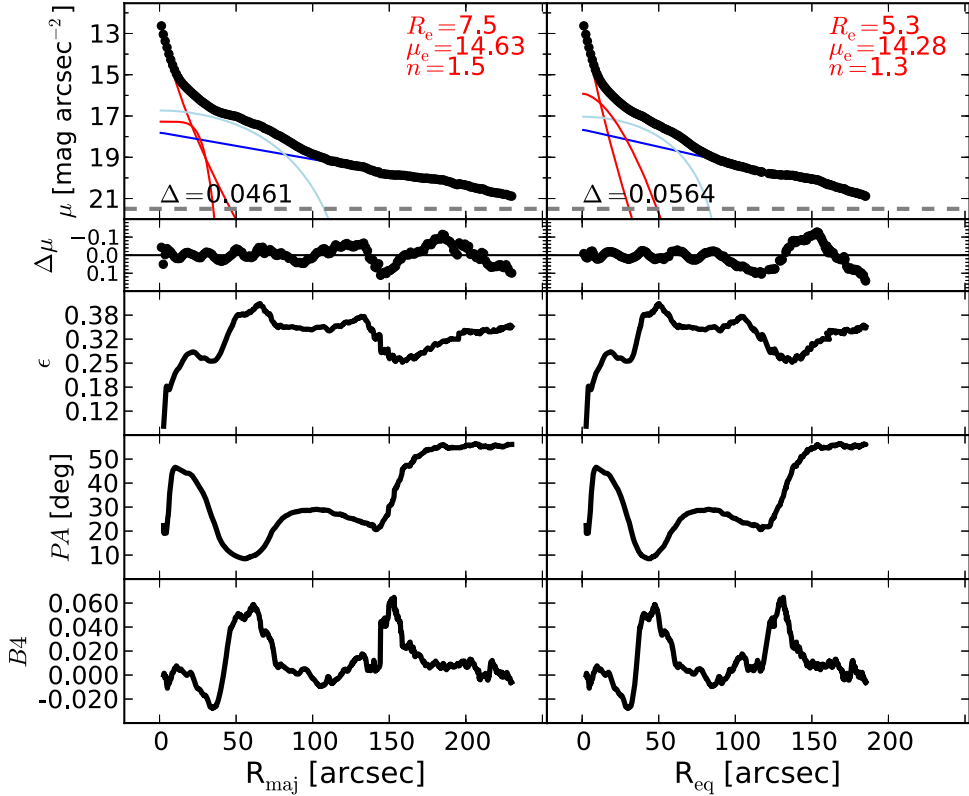


Figure 26. M96: a spiral galaxy with a large-scale bar and no AGN activity (Martini et al. 2003; Nowak et al. 2010). Erwin (2004) observed the presence of two bars in this galaxy. Nowak et al. (2010) reported the presence of a large pseudobulge and a tiny classical bulge ($R_{\text{e,sph}} = 1''\text{.}6$, $n_{\text{sph}} = 2.3$). However, they came to this conclusion by modeling only the innermost $8''/5$ of the light profile of M96 with a Sérsic-classical bulge and an exponential pseudobulge, but without subtracting the contribution of the large-scale disk and the large-scale bar. They also acknowledged the presence of a secondary inner bar, but did not include it in their fit. M96 has a complex morphology. The large-scale disk does not exhibit a perfect exponential profile, mainly because of wound spiral arms resembling a ring ($R_{\text{maj}} \sim 185''$), which however, are too faint and irregular to be described with a Gaussian ring model. The large-scale bar extends out to $R_{\text{maj}} \lesssim 80''$ and is modeled with a Ferrer function. A peak at $R_{\text{maj}} \sim 25''$ in the ellipticity profile reveals an inner disk component embedded in the bulge, which we model with a low- n Sérsic profile.

index \tilde{n}_{sph} and associated uncertainties would be $\log(\tilde{n}_{\text{sph}})^{+\sigma_1^+}_{-\sigma_1^-} = \log(\tilde{n}_{\text{sph}})^{+0.06}_{-0.08}$; if the fit to that galaxy was classified as “grade 2,” then one would have $\log(\tilde{n}_{\text{sph}})^{+\sigma_2^+}_{-\sigma_2^-} = \log(\tilde{n}_{\text{sph}})^{+0.17}_{-0.21}$; and so on.

4.2.3. Uncertainties on $R_{\text{e,sph}}$

The uncertainties on the spheroid effective radii were computed using the same methodology as employed for the Sérsic indices. However, in Figure 10 we include only major-axis measurements of $R_{\text{e,sph}}$. The associated 1σ uncertainties for our measurements of $\log(R_{\text{e,sph}})$ are $-\sigma_1^- = -0.11$ dex and $+\sigma_1^+ = +0.07$ dex, $-\sigma_2^- = -0.30$ dex and $+\sigma_2^+ = +0.32$ dex, and $-\sigma_3^- = -0.39$ dex and $+\sigma_3^+ = +0.42$ dex.

4.2.4. Uncertainties on m_{sph}

To estimate the uncertainties on the spheroid magnitudes, we compared (see Figure 11) only those literature measurements coming from K -band or $3.6\text{ }\mu\text{m}$ observations. To do this, the $3.6\text{ }\mu\text{m}$ magnitudes were converted into K -band magnitudes by applying an additive factor of 0.27 mag, which was estimated using the stellar population models of Worthey (1994), assuming a 13 Gyr old single-burst stellar population with solar metallicity. The associated 1σ uncertainties for our measurements of m_{sph} are $-\sigma_1^- = -0.11$ mag and $+\sigma_1^+ =$

+0.18 mag, $-\sigma_2^- = -0.58$ mag and $+\sigma_2^+ = +0.66$ mag, and $-\sigma_3^- = -0.66$ mag and $+\sigma_3^+ = +0.88$ mag.

4.2.5. Uncertainties on $\mu_{\text{e,sph}}$

As for the spheroid magnitudes, we estimated the uncertainties on the spheroid effective surface brightnesses $\mu_{\text{e,sph}}$ by comparing only K -band or $3.6\text{ }\mu\text{m}$ measurements (see Figure 12) and accounting for the mean color difference of 0.27 mag. Not explicitly reported in the literature, effective surface brightnesses were calculated by us using

$$\begin{aligned} \mu_{\text{e,sph}} = m_{\text{sph}} + 5 \log & \left(R_{\text{e,sph}}^{\text{maj}} \sqrt{(b/a)_{\text{sph}}} \right) \\ & + 2.5 \log \left[2\pi n_{\text{sph}} e^{b_n} b_n^{-2n_{\text{sph}}} \Gamma(2n_{\text{sph}}) \right], \end{aligned} \quad (3)$$

where b_n and $\Gamma(2n_{\text{sph}})$ are defined in the Appendix and $(b/a)_{\text{sph}}$ is the spheroid axis ratio. While Laurikainen et al. (2010) and Sani et al. (2011) reported their estimates of $(b/a)_{\text{sph}}$, Vika et al. (2012) and Läsker et al. (2014a) did not. For the last two studies, we used the values of $(b/a)_{\text{sph}}$ reported by Sani et al. (2011). The associated 1σ uncertainties for our measurements of $\mu_{\text{e,sph}}$ are $-\sigma_1^- = -0.33$ mag and $+\sigma_1^+ = +0.57$ mag, $-\sigma_2^- = -0.84$ mag and $+\sigma_2^+ = +1.59$ mag, and $-\sigma_3^- = -1.06$ mag and $+\sigma_3^+ = +1.74$ mag.

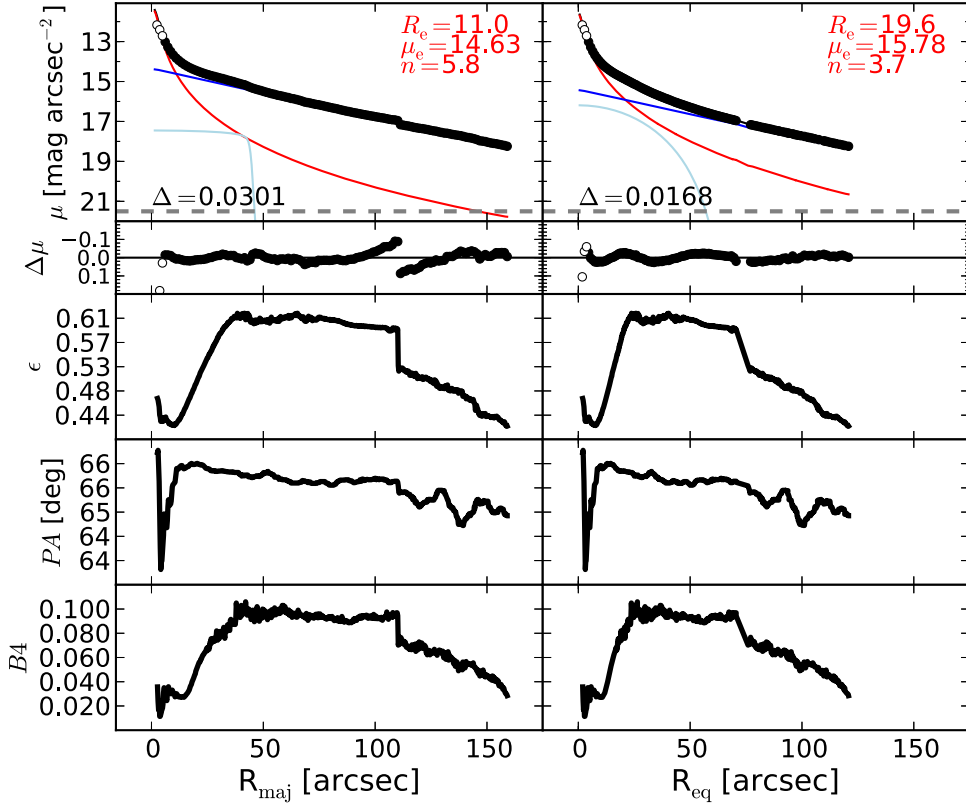


Figure 27. M104: a lenticular/spiral galaxy with a partially depleted core (Jardel et al. 2011). The data within the innermost $6''$ are excluded from the fit, and the most obvious elongated feature of this galaxy is modeled with a Ferrer function. The ellipticity profile indicates that the disk is of intermediate scale (for a thorough analysis of this galaxy, see Gadotti & Sánchez-Janssen 2012).

4.2.6. Uncertainties on $\mu_{0,\text{sph}}$

From the values of $\mu_{e,\text{sph}}$, we derived the central surface brightnesses $\mu_{0,\text{sph}}$ from the equation

$$\mu_{0,\text{sph}} = \mu_{e,\text{sph}} - \frac{2.5b_n}{\ln(10)}. \quad (4)$$

The associated 1σ uncertainties for our measurements of $\mu_{0,\text{sph}}$ are $-\sigma_1^- = -0.20$ mag and $+\sigma_1^+ = +0.64$ mag, $-\sigma_2^- = -0.70$ mag and $+\sigma_2^+ = +1.24$ mag, and $-\sigma_3^- = -1.05$ mag and $+\sigma_3^+ = +1.57$ mag.

5. CONCLUSIONS

The widespread presence of embedded components—in particular intermediate-scale disks—in massive early-type galaxies makes galaxy decomposition an essential tool to properly investigate the scaling relations between black hole masses and host spheroid properties.

Past studies often used different model components for the same galaxy and obtained significantly discrepant results, which led them to draw contrasting conclusions about the black hole–spheroid correlations. These inconsistencies motivated our effort to refine and secure the measure of spheroid properties in a sample of 66 galaxies with a dynamical estimate of the black hole mass. Using $3.6\mu\text{m}$ *Spitzer* satellite images, we performed state-of-the-art galaxy decompositions. The $3.6\mu\text{m}$ band is an excellent tracer of the stellar mass, superior to optical bands and the K band. Considerable care has been taken in the data reduction, image mosaicking, sky subtraction, and component model fitting to the galaxy light. We have

compared our best-fit models with those from the literature, to identify and explain discrepancies when present. Our analysis additionally benefited from recourse to kinematical information—not previously used—to aid in the identification of somewhat face-on disks, or the distinction between intermediate-scale disks and large-scale disks, missed in some past investigations and decompositions. Table 3 summarizes the main characteristics of the five past studies that, since 2007, attempted galaxy decompositions in order to derive black hole–spheroid scaling relations, and it highlights, in part, why our endeavor represents a substantial improvement over the past literature.

We reveal that 1D and 2D techniques of galaxy decomposition return the same results when applied to the same galaxy. However, in our practical experience, the failure rate of 2D decompositions is a factor of two higher than the failure rate of 1D decompositions, either because the fit does not converge or because the result is unphysical. A strong limitation of 2D codes is their inability to accommodate the radial gradients of ellipticity and position angle often observed in galaxy spheroids. The interpretation of 1D residual surface brightness profiles is easier than that of 2D residual images. A 1D isophotal analysis was extremely helpful and sometimes even necessary to accurately identify galaxy components. A correct interpretation of the residuals is fundamental to understand and determine the optimal model for a galaxy. Given the level of detail to which each galaxy decomposition was performed, we believe that our analysis cannot be reproduced by current automatic routines. The uncertainties associated with the literature best-fit parameters of the spheroid are dominated by

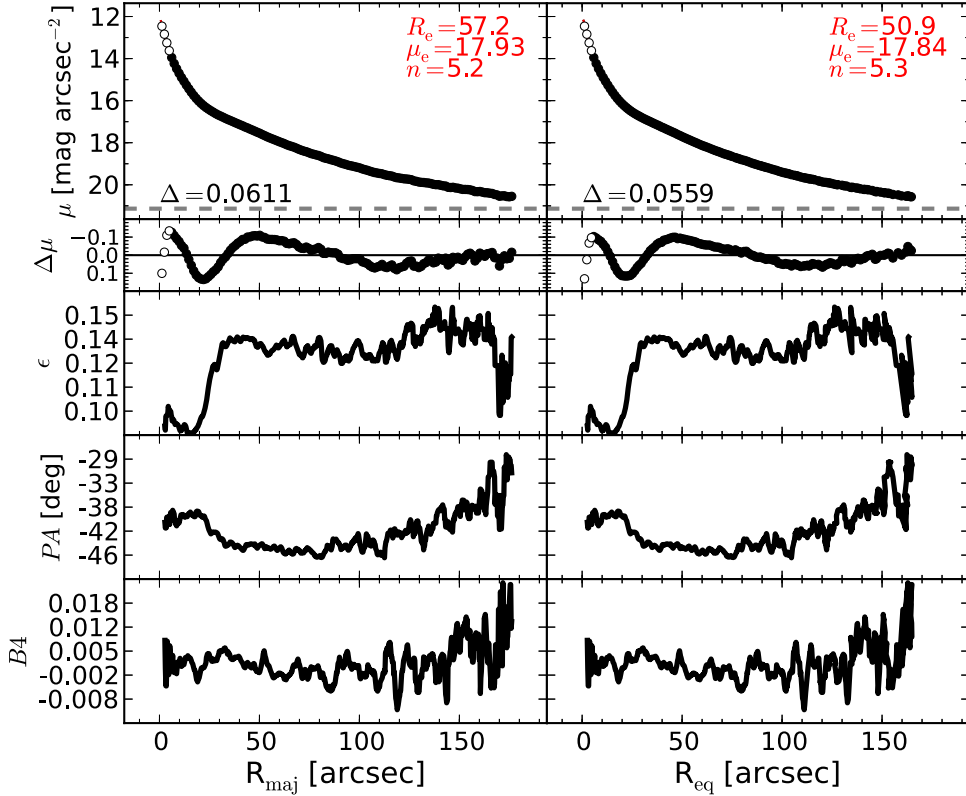


Figure 28. M105: an elliptical galaxy with an unresolved partially depleted core (Rusli et al. 2013a). M105 exhibits a mild isophotal twist and an abrupt change of ellipticity at $R_{\text{maj}} \sim 30''$. The velocity map (ATLAS^{3D}) shows rotation at least within $R_{\text{maj}} \lesssim 30''$, but no embedded disk can be recognized in the unsharp mask, and the ellipticity profile is quite unusual for a spheroidal system with an inner disk. The data within the innermost $6''/1$ are excluded from the fit. A single Sérsic model does not provide a good description of the galaxy light profile. However, the addition of a second function (of any analytic form) to the model does not improve the fit. We conclude that the galaxy may not yet be fully relaxed, and we fit it with a single Sérsic profile.

systematic errors (e.g., incorrect sky subtraction, inaccurate masking of contaminating sources, erroneous choice of model components) and only marginally affected by random errors. For this reason, we developed a method to estimate the uncertainties on the best-fit parameters that takes into account systematic errors (see Figures 9–13).

We will use the results from our 1D galaxy decompositions to obtain improved black hole mass scaling relations. These results will be presented in a series of forthcoming papers.

5.1. Individual Galaxy Decompositions

For each galaxy, we show a figure (Figures 14–79) and a table (Tables 4–69). The figure illustrates our 1D model and the galaxy isophotal parameters. The left panels refer to the major-axis R_{maj} , while the right panels refer to the equivalent-axis R_{eq} , i.e., the geometric mean of the major (a) and minor (b) axis ($R_{\text{eq}} = \sqrt{ab}$), equivalent to a circularized profile. The top panels display the galaxy surface brightness (μ) radial profiles obtained with a linear sampling. The black points are the observed data used in the fit, and the open points are the observed data excluded from the fit. The colored lines represent the individual (PSF-convolved) model components: red = Sérsic; dark blue = exponential; green = Gaussian; cyan = Ferrer; gray = Gaussian ring; pink = PSF. The parameters for the Sérsic spheroid model are inset. The total (PSF-convolved) model is shown with a black dashed line. The residual profile ($\text{data} - \text{model}$) is shown as $\Delta\mu$ in the second row. The horizontal gray dashed line corresponds to an intensity equal to

three times the rms of the sky background fluctuations ($3 \times \text{rms}_{\text{sky}}$). Δ denotes the rms scatter of the fit in units of mag arcsec^{-2} . The lower six panels show the ellipticity (ϵ), position angle (PA), and fourth harmonic ($B4$) radial profiles from the ellipse. The tables report a comparison between our results (from both our 1D and 2D decompositions) and those obtained by the following authors: GD07 = Graham & Driver (2007a, who performed 1D fits along the major-axis), L+10 = Laurikainen et al. (2010, who performed 2D fits), S+11 = Sani et al. (2011, who performed 2D fits), B+12 = Beifiori et al. (2012, who performed 2D fits), V+12 = Vika et al. (2012, who performed 2D fits), R+13 = Rusli et al. (2013a, who performed 1D fits along the equivalent axis), and L+14 = Läsker et al. (2014a, who performed 2D fits). Each galaxy model is the sum of its individual components, which are expressed with the following nomenclature: (analytic function)-(physical component). The analytic functions can be: S = Sérsic, e = exponential, G = Gaussian, F = Ferrer, M = Moffat, and PSF. The physical components can be: bul = bulge (or spheroid), d = disk, id = inner disk, bar, n = nucleus, l = lens or oval, r = ring, halo, and spiral arms. When a nuclear component or a partially depleted core has been masked, we signal it as “m-n” or “m-c,” respectively. For example, the model “S-bul + e-d + e-id + m-n + G-r” reads “Sérsic-bulge + exponential-disk + exponential-(inner disk) + mask-nucleus + Gaussian-ring.” The core-Sérsic model used by Rusli et al. (2013a) is always implicitly associated with the galaxy spheroidal component. Graham & Driver excluded the innermost data points when fitting their

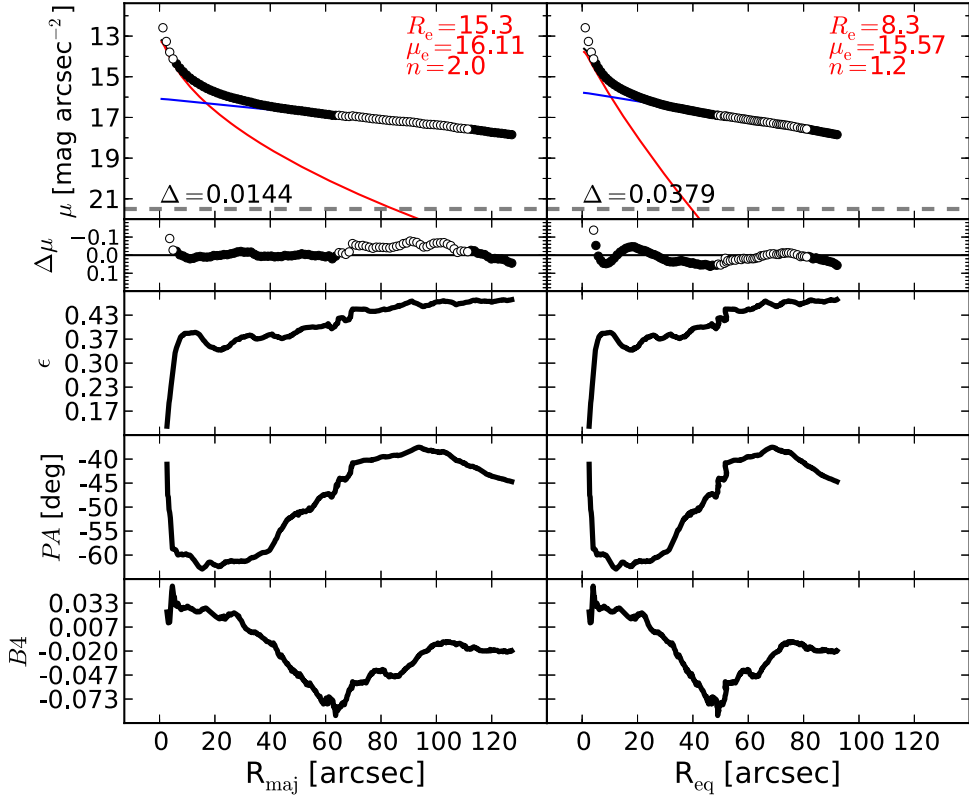


Figure 29. M106: a barred spiral galaxy, harboring a Seyfert AGN (Véron-Cetty & Véron 2006) with circumnuclear dust (Martini et al. 2003). We exclude from the fit the innermost $6.^{\prime\prime}1$ because it is affected by the AGN emission. The boxy bar, responsible for the minimum in the $B4$ profile at $R_{\text{maj}} \sim 65^{\prime\prime}$, is fainter than the large-scale disk, and in the light profile it is only detectable as a slight swelling within $65'' \lesssim R_{\text{maj}} \lesssim 110''$. This region is excluded from the fit. A peak in the ellipticity profile at $R_{\text{maj}} \sim 10''$ suggests the presence of a disky component embedded in the bulge, but a model that accounts for this component is degenerate with the other fitted components.

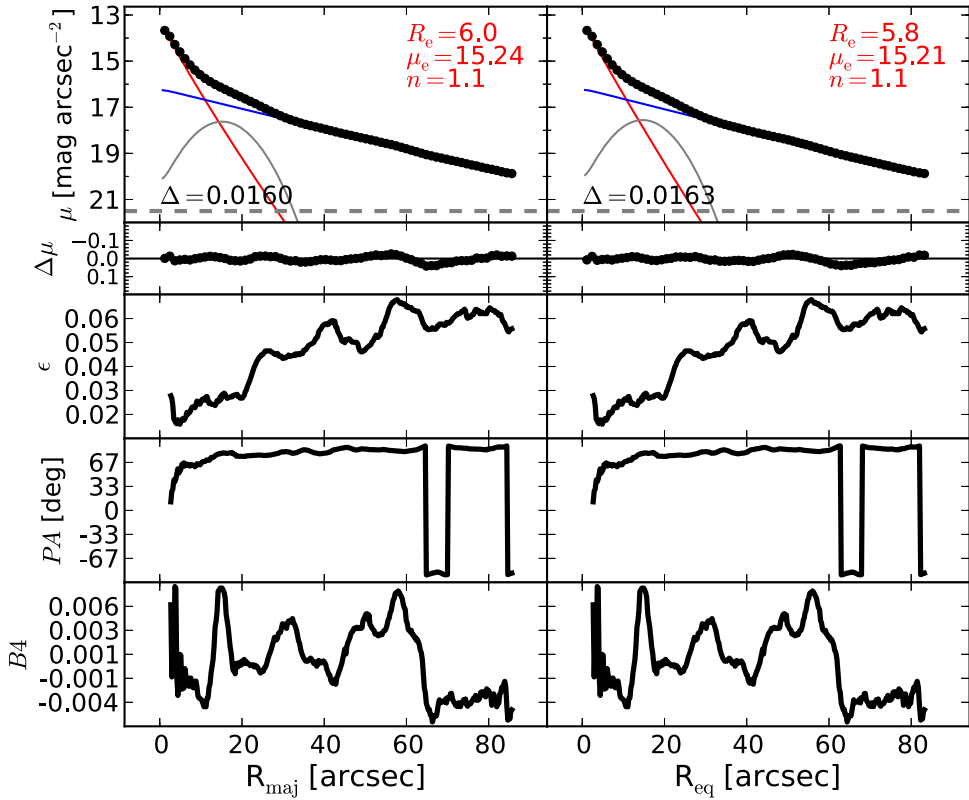


Figure 30. NGC 0524: an unbarred face-on lenticular galaxy. The unsharp mask of NGC 0524 reveals a faint multi-ring structure in the galaxy disk, with a substantial ring peaking at $R_{\text{maj}} \sim 20''$. We account for this brightest ring using a Gaussian ring profile.

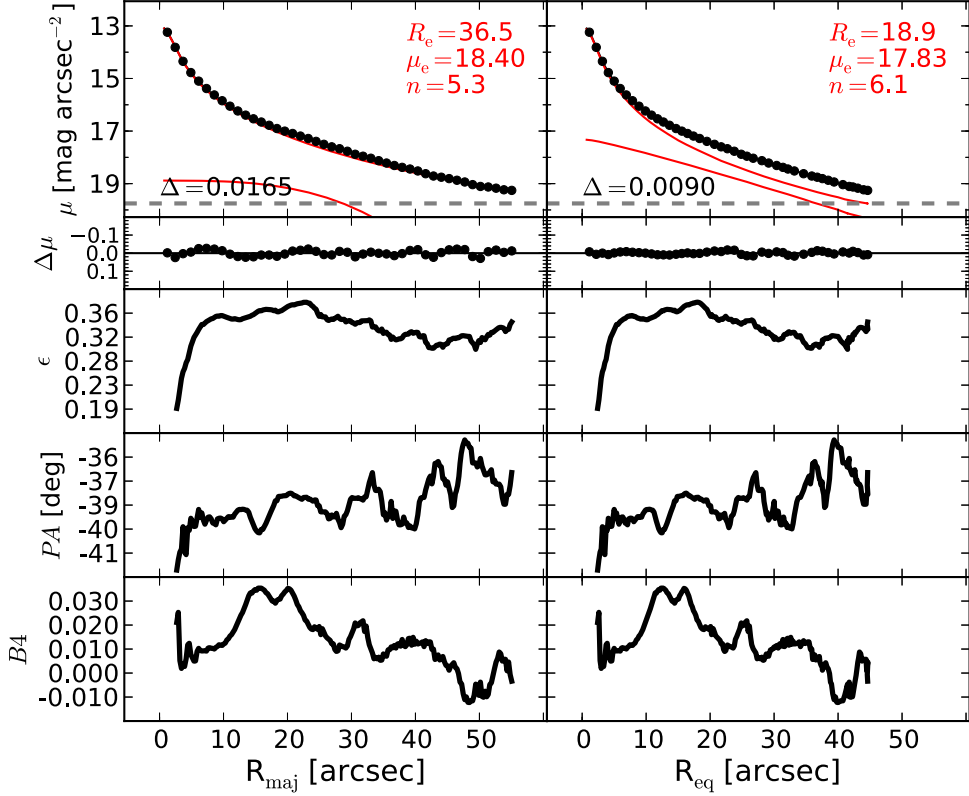


Figure 31. NGC 0821: an elliptical galaxy with an edge-on embedded disk. The ellipticity profile and the velocity map (ATLAS^{3D}, SLUGGS) show the presence of the faint intermediate-scale disk. Given its edge-on inclination, the disk is modeled with a low- n Sérsic function.

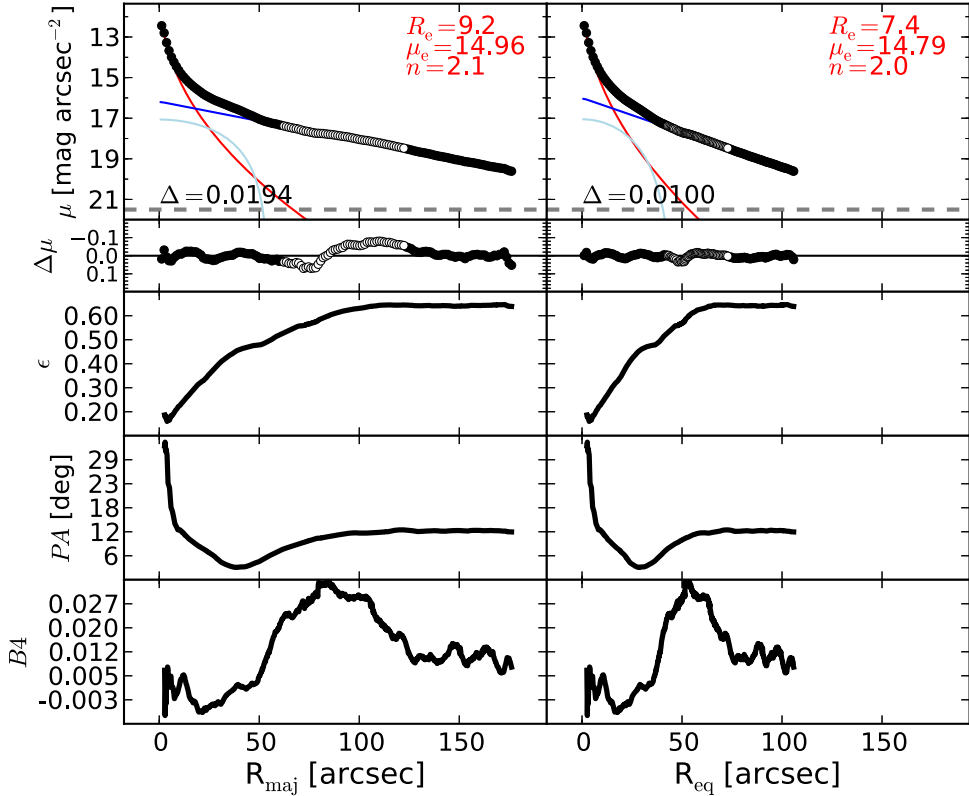


Figure 32. NGC 1023: a barred lenticular galaxy. The bar extends out to $R_{\text{maj}} \lesssim 40''$. Small deviations of the disk from a perfect exponential profile, within $60'' \lesssim R_{\text{maj}} \lesssim 125''$ (the data in this range are excluded from the fit), can be ascribed to faint residual spiral arms, also noticeable in the 2D residual image. The peak at $R_{\text{maj}} \sim 10''$ in the $B4$ profile signals the presence of an embedded (and faint) disk. The 1D residuals show a structure within $R_{\text{maj}} \lesssim 10''$ caused by this unsubtracted component, as also noted by Läsker et al. (2014a). Our attempts to account for the inner disk by adding a fourth function to the model did not significantly change the bulge best-fit parameters; thus, we elect not to model this embedded disk.

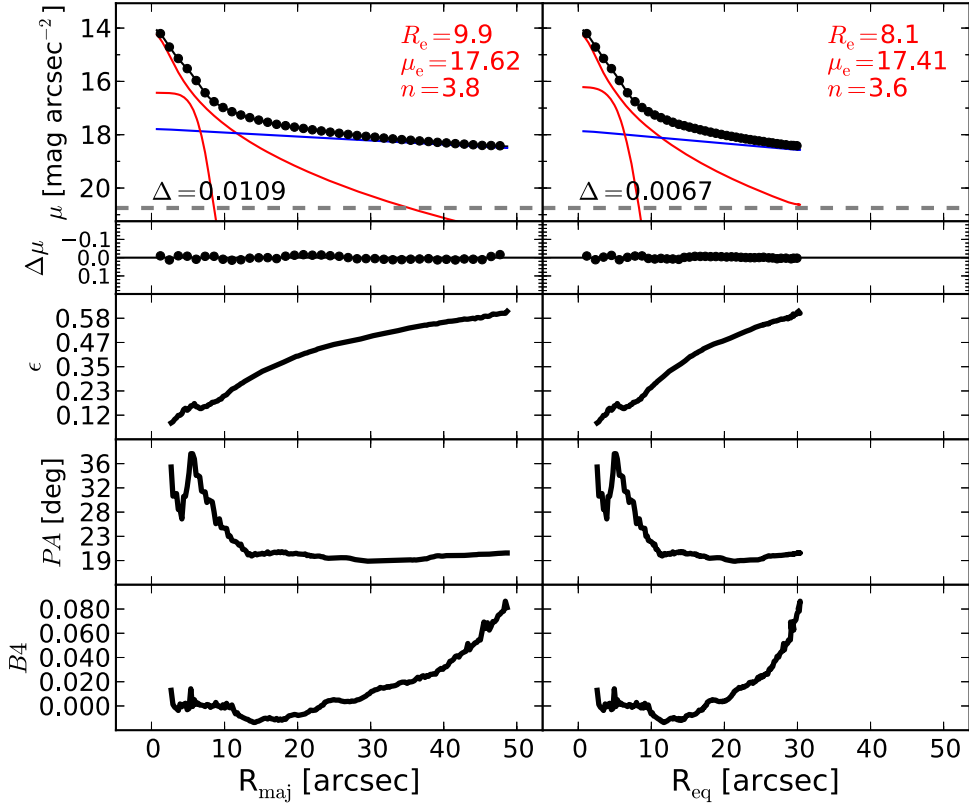


Figure 33. NGC 1300: a face-on, barred spiral galaxy. The morphology of NGC 1300 is quite complex. In addition to a large-scale disk and a bulge, the galaxy is composed of a large-scale bar that extends up to $R_{\text{maj}} \lesssim 90''$, two prominent spiral arms, and an inner disk-like component ($R_{\text{maj}} \lesssim 5''$), disclosed by the peaks in the ellipticity and PA profiles. We truncate the light profile at $R_{\text{maj}} \sim 50''$, and we fit the inner combination of the large-scale bar and the disk as a single component, using an exponential function. The embedded component is described with a low- n Sérsic profile.

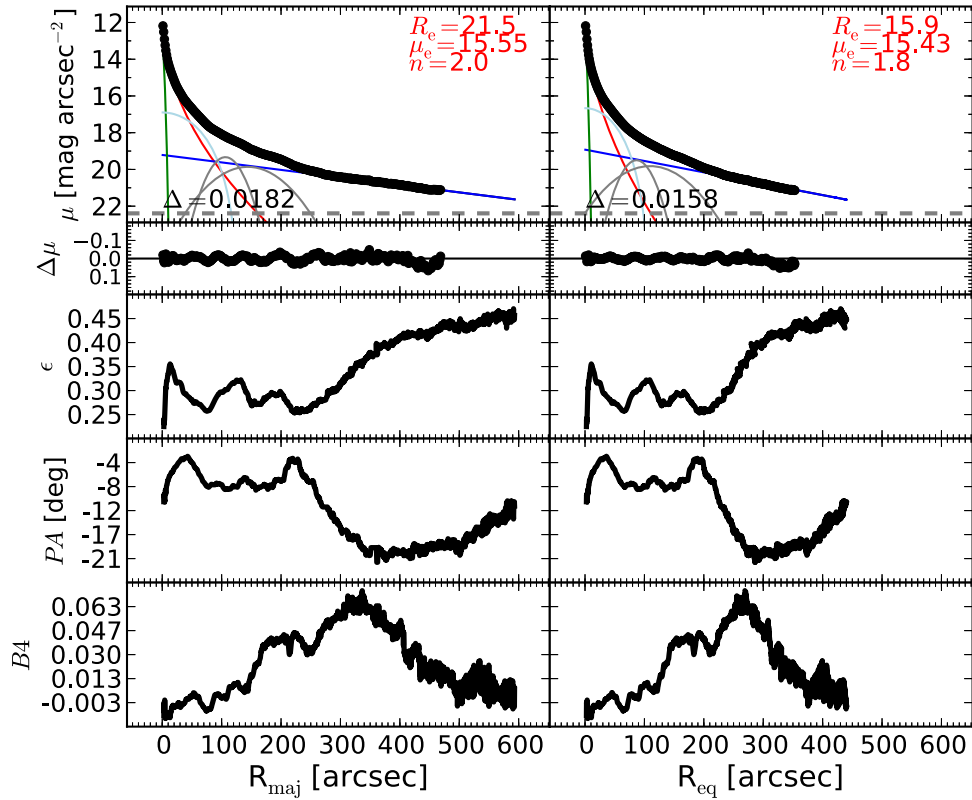


Figure 34. NGC 1316: a merger. The galaxy is composed of a bulge, an elongated structure that can be identified with a bar, two obvious rings, an outer exponential disk or halo, and a bright nuclear component.

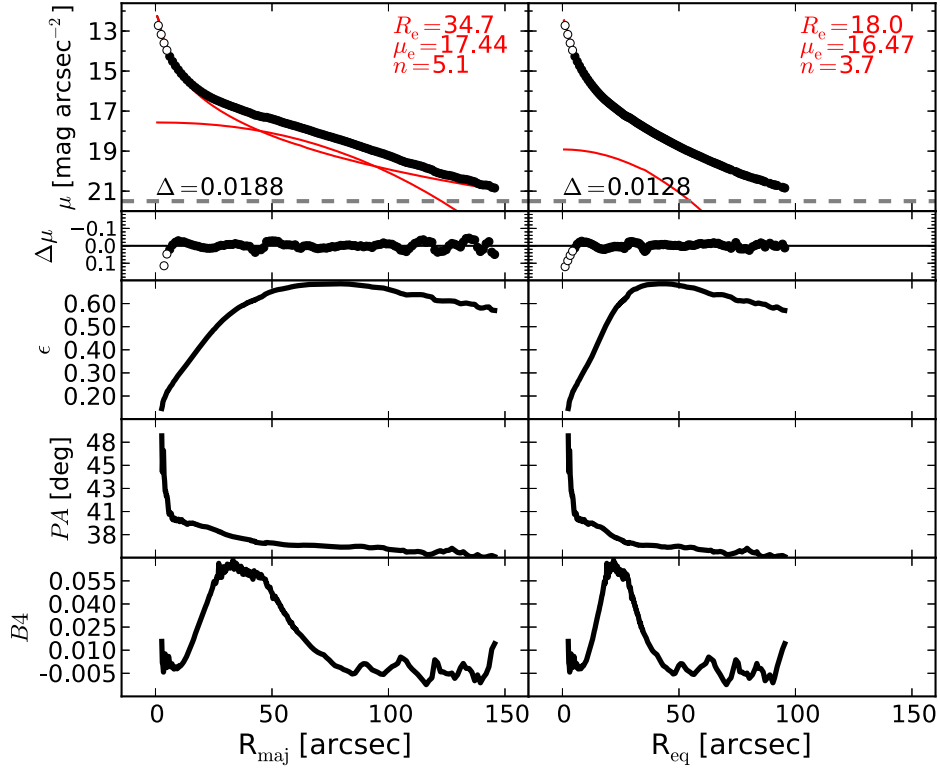


Figure 35. NGC 1332: an edge-on elliptical/lenticular galaxy. The identification of a disk is trivial owing to its edge-on orientation, although a visual inspection of the galaxy image is not enough to establish the radial extent of this disk. The ellipticity profile indicates that the disk is indeed intermediate-sized, i.e., it does not dominate at large radii. Given the edge-on inclination of this disk, we model it with a low- n Sérsic profile. The data within the innermost $6''.1$ are excluded from the fit. Our equivalent-axis decomposition returns a spheroidal component accounting for 95% of the total light, and an embedded disk accounting for the remaining 5%. In passing, we note that the bulge-disk decomposition performed by Rusli et al. (2011) on NGC 1332 is significantly different from our best-fit model. Rusli et al. (2011) did not identify the intermediate-scale embedded disk, but instead proposed a model featuring a Sérsic bulge ($n_{\text{sph}} \sim 2.3$, $R_{e,\text{sph}} \sim 8''$), accounting for 43% of the total light, and a large-scale exponential disk. This result led them to the conclusion that NGC 1332 is a disk-dominated lenticular galaxy and is displaced from the $M_{\text{BH}}-L_{K,\text{sph}}$ (black hole mass vs. K-band spheroid luminosity) relation of Marconi & Hunt (2003) by an order of magnitude along the M_{BH} direction. Instead, the galaxy spheroid is a factor of two more luminous than claimed by Rusli et al. (2011), and NGC 1332 is not an outlier in our $M_{\text{BH}}-L_{\text{sph}}$ diagram.

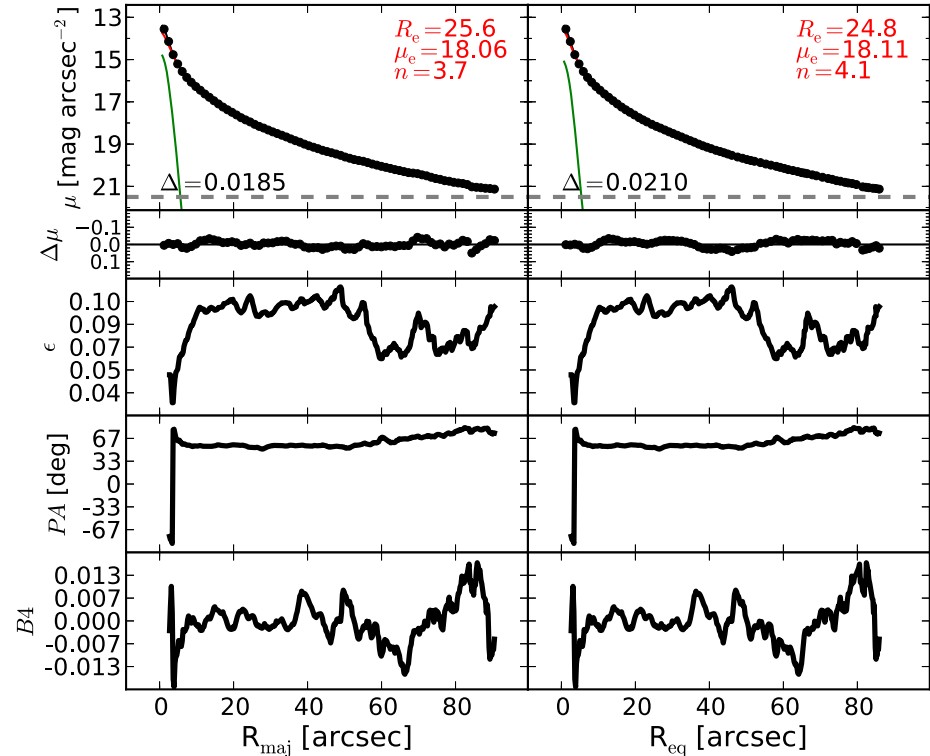


Figure 36. NGC 1374: an elliptical galaxy. A Gaussian function in our model accounts for the relatively faint additional nuclear component.

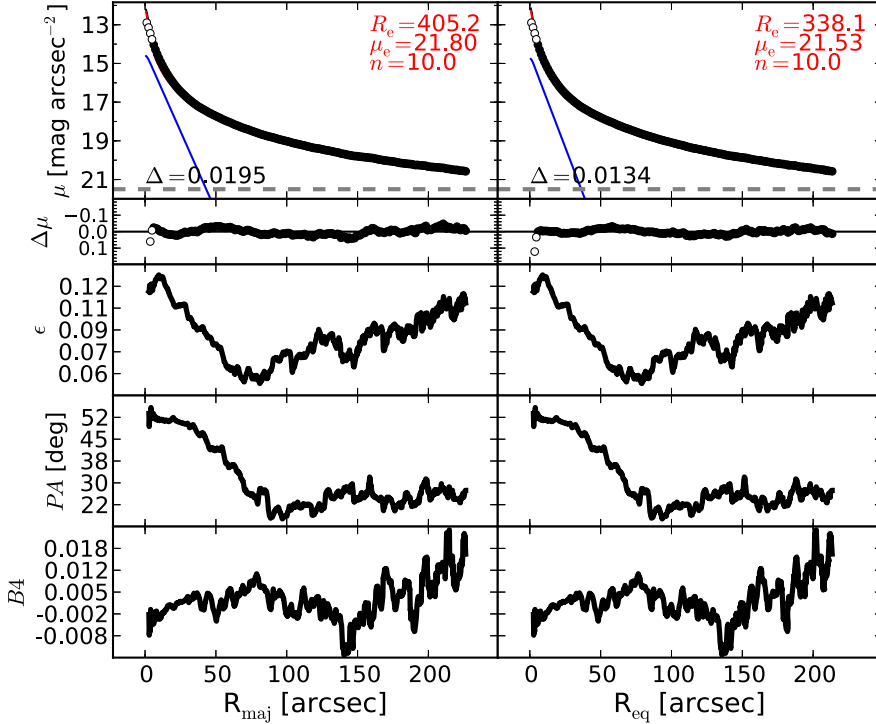


Figure 37. NGC 1399: the central galaxy of the Fornax Cluster, an elliptical galaxy with a slightly resolved partially depleted core (Rusli et al. 2013a; Dullo & Graham 2014). The nuclear activity of NGC 1399 is classified as Seyfert (Véron-Cetty & Véron 2006), but the galaxy lacks dust emission (Tran et al. 2001). The ellipticity and PA profiles display a steep decline with increasing radius within $R_{\text{maj}} \lesssim 60''$, suggesting the presence of an embedded disk. This inner component is also visible, although faint, in the unsharp mask. We note that, after excluding the innermost $6.''1$, a single Sérsic profile is not sufficient to describe the whole galaxy light profile. The addition of an inner exponential function to model the disk notably improves the fit.

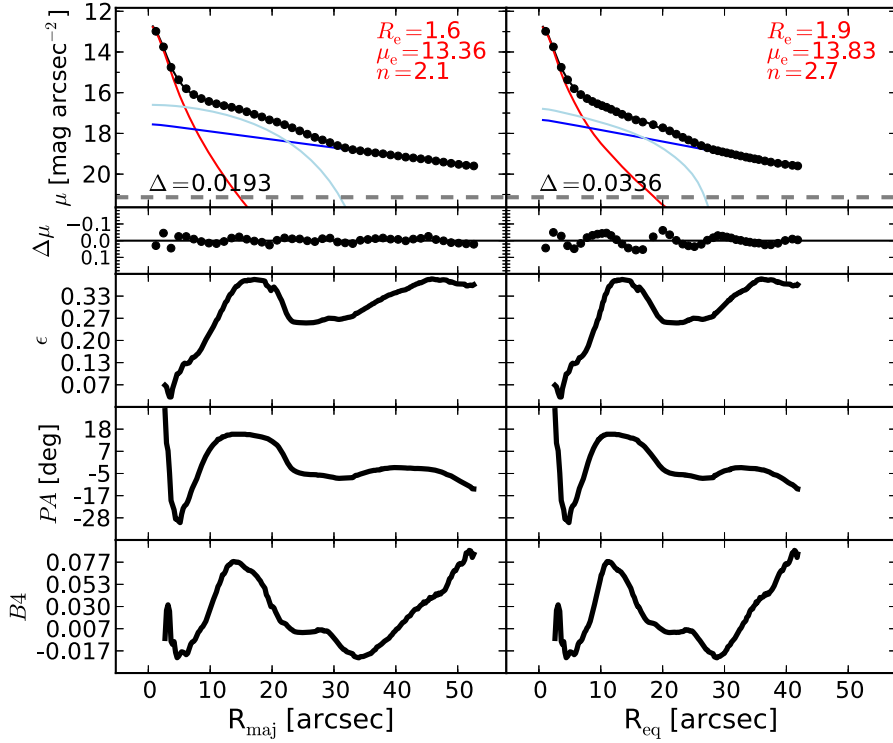


Figure 38. NGC 2273: a barred spiral galaxy with a Seyfert AGN (Contini et al. 1998) and circumnuclear dust (Simões Lopes et al. 2007). Its bar is surrounded by two tightly wound star-forming spiral arms that resemble a ring (Comerón et al. 2010). The bar of NGC 2273 extends out to $R_{\text{maj}} \lesssim 25''$. The pseudoring does not produce any evident swelling in the light profile; therefore, we do not account for it in the galaxy model. The isophotal parameters confirm the presence of a nuclear disk-like component within $R_{\text{maj}} \lesssim 5''$. However, as noted by Laurikainen et al. (2005), any attempt to account for the embedded disk resulted in a degenerate model. This is not surprising if one considers the poor spatial resolution of the galaxy image, with the effective radius of the bulge comparable to the FWHM of the instrumental PSF. Although NGC 2273 hosts an optical AGN and nuclear dust, no central excess of light is observed in the 1D residuals. The addition of a nuclear component to the model does not significantly improve the fit or change the bulge parameters.

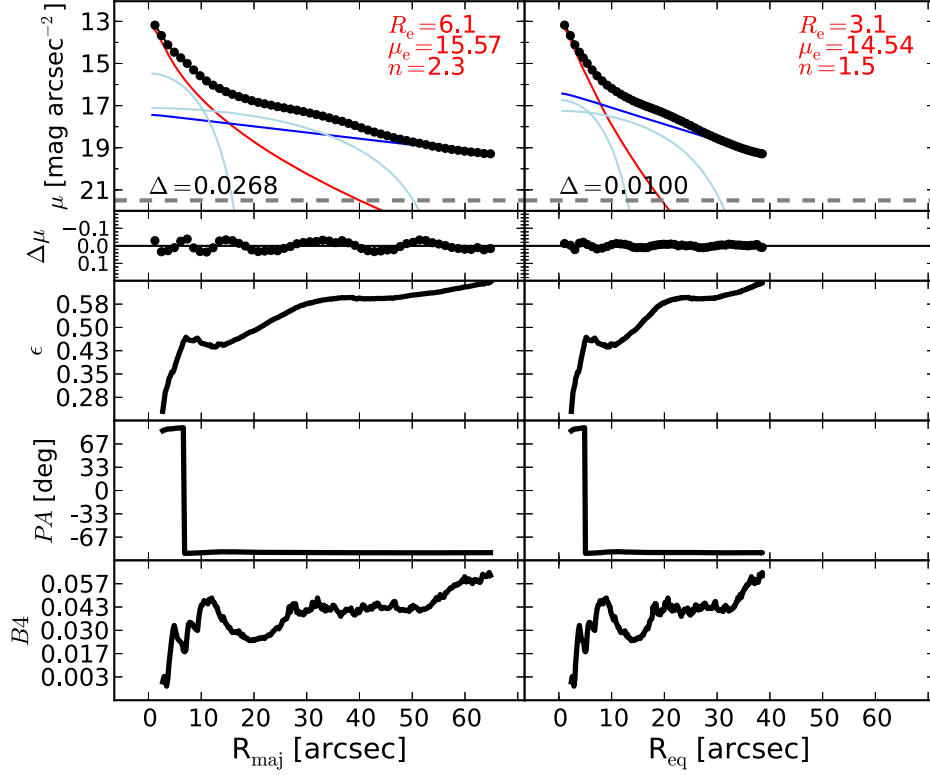


Figure 39. NGC 2549: an edge-on barred lenticular galaxy. Although the edge-on inclination of NGC 2549 complicates the identification of additional embedded components, a large-scale bar ($R_{\text{maj}} \lesssim 45''$) can be recognized in the galaxy image and—more easily—in the light profile. We model the large-scale bar with a Ferrer function. A peak in the ellipticity profile discloses the presence of a disk-like component embedded in the bulge ($R_{\text{maj}} \lesssim 10''$). This inner component can be spotted also by looking at the velocity map (ATLAS 3D), and we fit it with a Ferrer function.

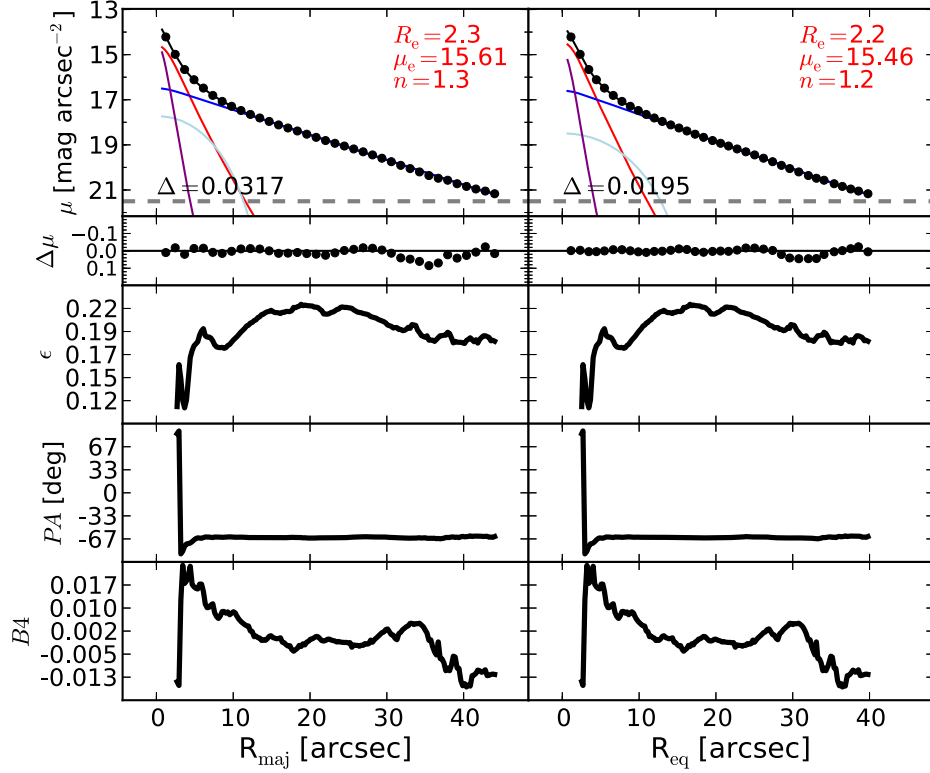


Figure 40. NGC 2778: a face-on lenticular galaxy. The peak in the ellipticity profile at $R_{\text{maj}} \sim 5''$ reveals the existence of a nuclear component embedded in the galaxy bulge. After an inspection of the unsharp mask, we identified this component with a small bar, which we model with a Ferrer function. We also account for some nuclear light excess by adding a PSF component to the model. We note that excluding the PSF component from our model does not significantly change the bulge effective radius, but it does increase the bulge Sérsic index to $n_{\text{sph}} \sim 2$.

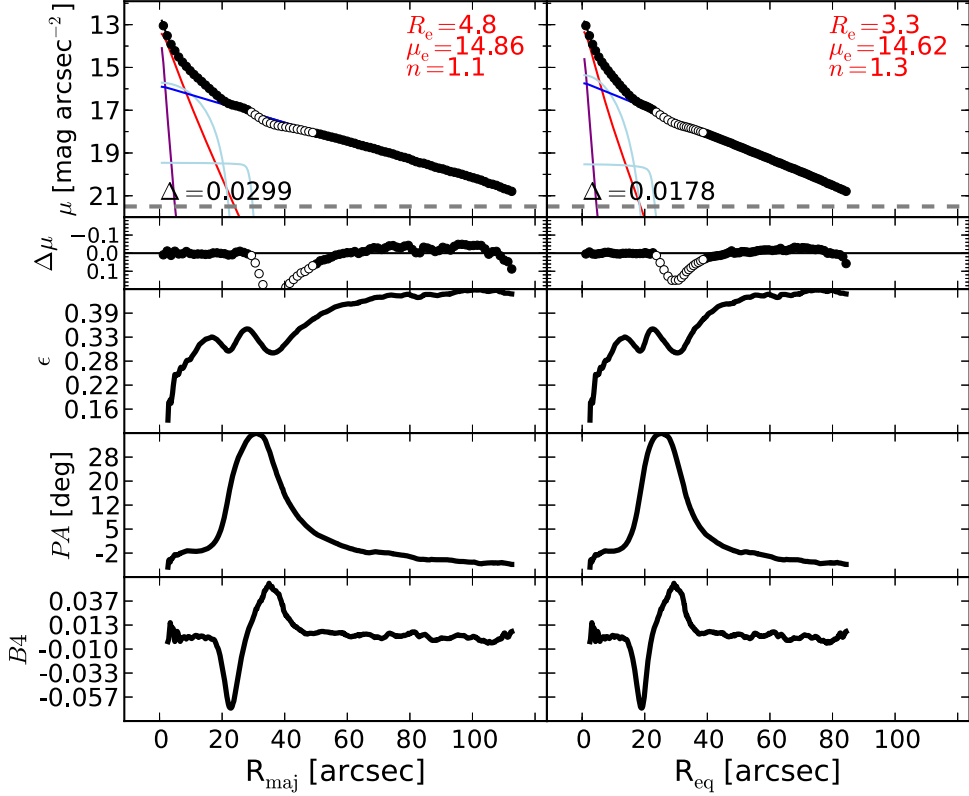


Figure 41. NGC 2787: a barred lenticular galaxy with LINER nuclear activity (Véron-Cetty & Véron 2006). An inner disk is embedded in the bulge of this galaxy (Erwin et al. 2003). NGC 2787 features a spectacular structure of dust rings at its center (Erwin & Sparke 2003) and a nuclear stellar disk (with size $\lesssim 1''.8$; Ledo et al. 2010). NGC 2787 has an undoubtedly complex morphology. This galaxy is composed of a bulge, a large-scale disk, a bar (see the peaks in the ellipticity, PA, and $B4$ profiles at $R_{\text{maj}} \sim 30''$) with two ansae, an inner disk (or bar?) embedded in the bulge (see the peak in the ellipticity profile at $R_{\text{maj}} \sim 17''$), and a bright nucleus. After masking the data affected by the ansae within $30'' \lesssim R_{\text{maj}} \lesssim 50''$, we use a Ferrer function for the bar, a second Ferrer function for the inner disk (or bar), and a PSF component for the nucleus.

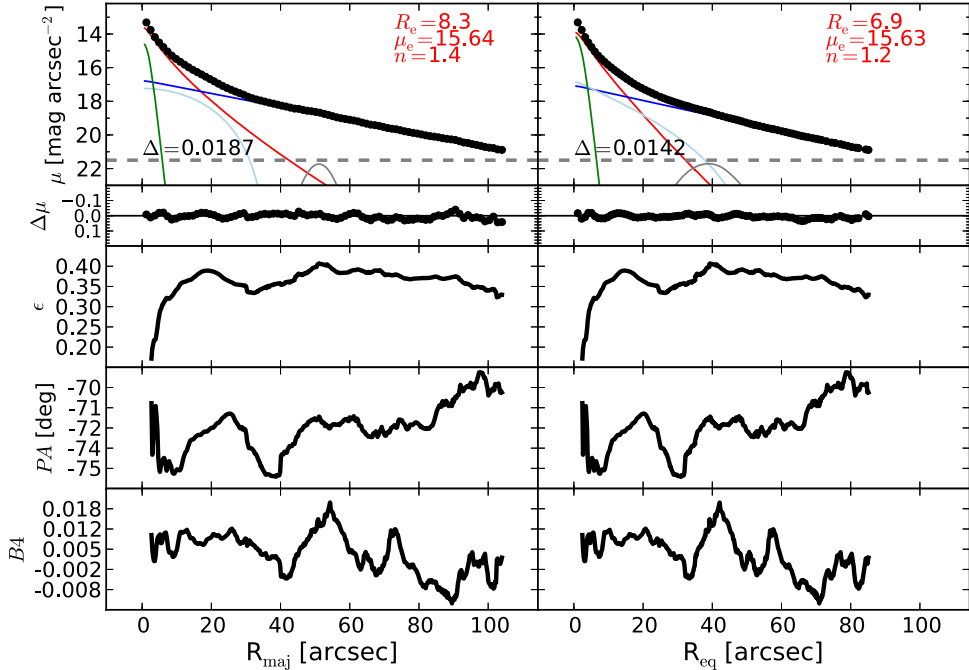


Figure 42. NGC 2974: a spiral galaxy that has been misclassified as an elliptical galaxy in the RC3 catalog. The galaxy hosts a Seyfert AGN (Véron-Cetty & Véron 2006) and filamentary dust in its center (Tran et al. 2001). From an inspection of the unsharp mask, we identified a ring structure at $R_{\text{maj}} \sim 50''$, probably a residual of two tightly wound spiral arms, and an elongated bar-like component within $R_{\text{maj}} \lesssim 30''$, which we fit with a Ferrer function. The pseudoring produces a peak in the $B4$ profile at $R_{\text{maj}} \sim 50''$, and the bar produces a peak in the ellipticity profile at $R_{\text{maj}} \sim 20''$. Although the ring is extremely faint, it is important to account for it in the galaxy decomposition. A model without the ring component results in a “steeper” exponential disk (i.e., the disk would have a smaller scale length and a brighter central surface brightness) and produces poor residuals within $R_{\text{maj}} \lesssim 40''$. The nuclear component is fit with a Gaussian profile.

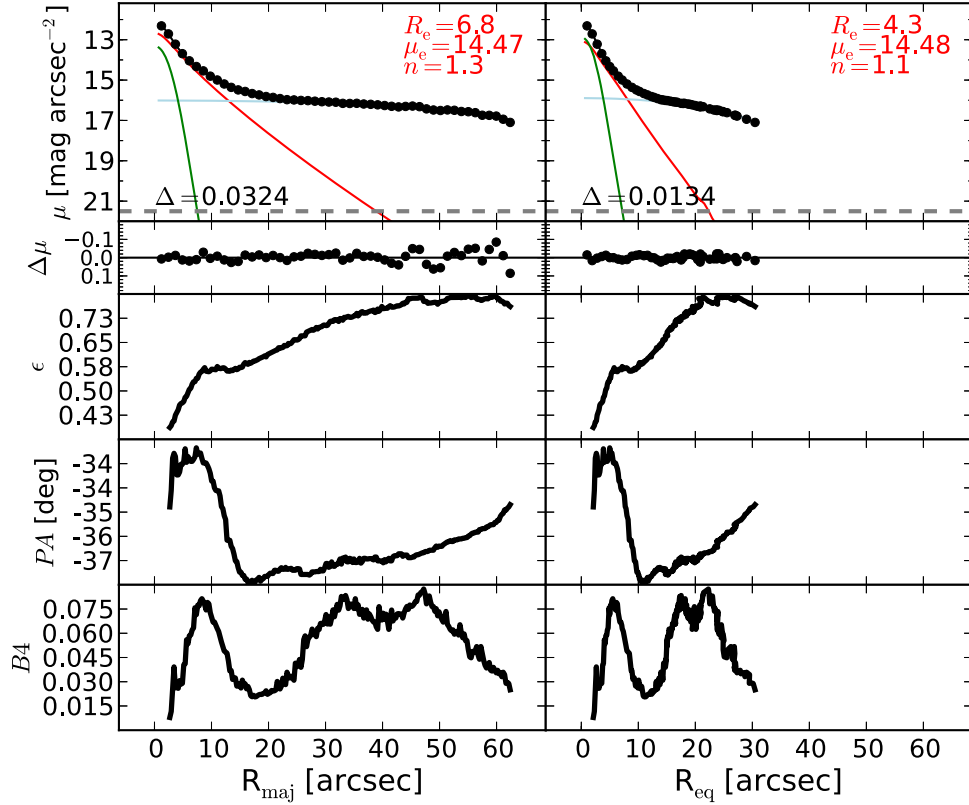


Figure 43. NGC 3079: an edge-on, late-type barred spiral galaxy with a Seyfert AGN (Véron-Cetty & Véron 2006) and circumnuclear dust (Martini et al. 2003). The bar extends out to $R_{\text{maj}} \lesssim 70''$. We truncate the light profile at $R_{\text{maj}} \sim 65''$, before the “edge” of the bar, and we successfully model the combination of the disk and the bar with a Ferrer function. A Gaussian function accounts for the AGN emission.

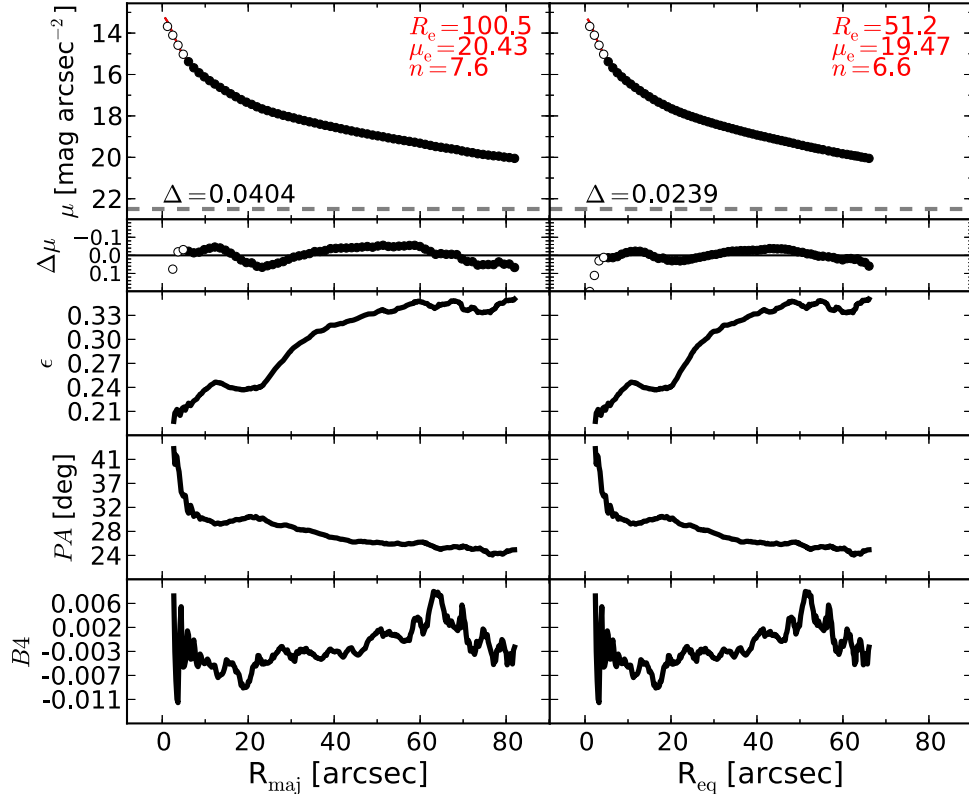


Figure 44. NGC 3091: an elliptical galaxy with an unresolved partially depleted core (Rusli et al. 2013a). The data within the innermost $6''$ are excluded from the fit. A faint embedded component ($R_{\text{maj}} \lesssim 10''$) can be recognized in the unsharp mask and has a corresponding peak in the ellipticity profile. This extra component is clearly visible in the residual image obtained by subtracting a 2D Sérsic model from the galaxy image. However, any attempt to account for the embedded component resulted in an unsatisfactory fit and did not significantly change the bulge parameters. We thus elect not to model the inner component.

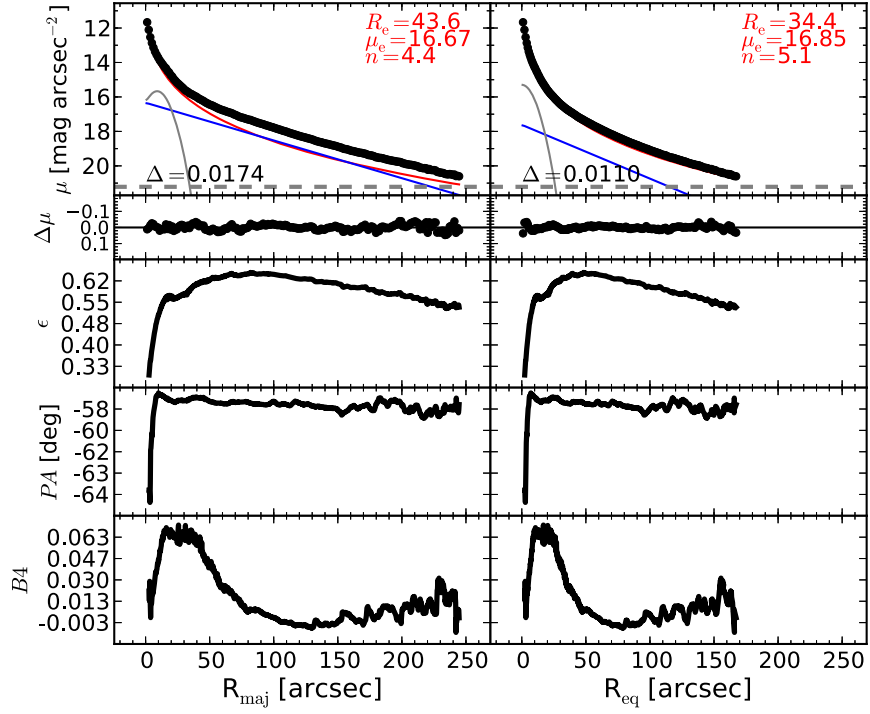


Figure 45. NGC 3115: an edge-on elliptical/lenticular galaxy. This galaxy features an intermediate-scale disk and a nuclear stellar disk (with size $\sim 1''$; Scorz & Bender 1995; Ledo et al. 2010). The presence of the intermediate-scale disk is immediately evident by looking at the ellipticity and $B4$ profiles. From the galaxy center to the outskirts, the ellipticity increases until it reaches a maximum ($\epsilon \sim 0.65$) at $R_{\text{maj}} \sim 90''$. After this point, it starts declining, being as low as $\epsilon \sim 0.55$ at $R_{\text{maj}} \sim 240''$. The galaxy isophotes display a positive diskyness within $R_{\text{maj}} \sim 90''$, but become perfect ellipses ($B4 \sim 0$) beyond that point. Because galaxy disks typically have fixed ellipticity, reflecting their inclination to our line of sight, the previous observations tell us that, going from the galaxy center to the outer regions, the disk of NGC 3115 becomes increasingly important relative to the spheroid light, reaching its maximum at $R \sim 90''$. Beyond $R_{\text{maj}} \gtrsim 90''$, the contribution from the disk light starts declining more rapidly than the spheroid light. This interpretation is supported by the results of Arnold et al. (2011), who found that, within $R_{\text{maj}} \sim 110''$, the bulge of NGC 3115 is flattened and rotates rapidly ($v/\sigma \gtrsim 1.5$), whereas at larger radii the rotation declines dramatically (to $v/\sigma \sim 0.7$), but remains well aligned with the inner regions. From an inspection of the unsharp mask, we identify a faint nuclear edge-on ring ($R_{\text{maj}} \sim 15''$), which produces a corresponding peak in the ellipticity profile. We do not observe any nuclear excess of light in the 1D residuals. The addition of a PSF component to the final model does not significantly change the outcome of the fit.

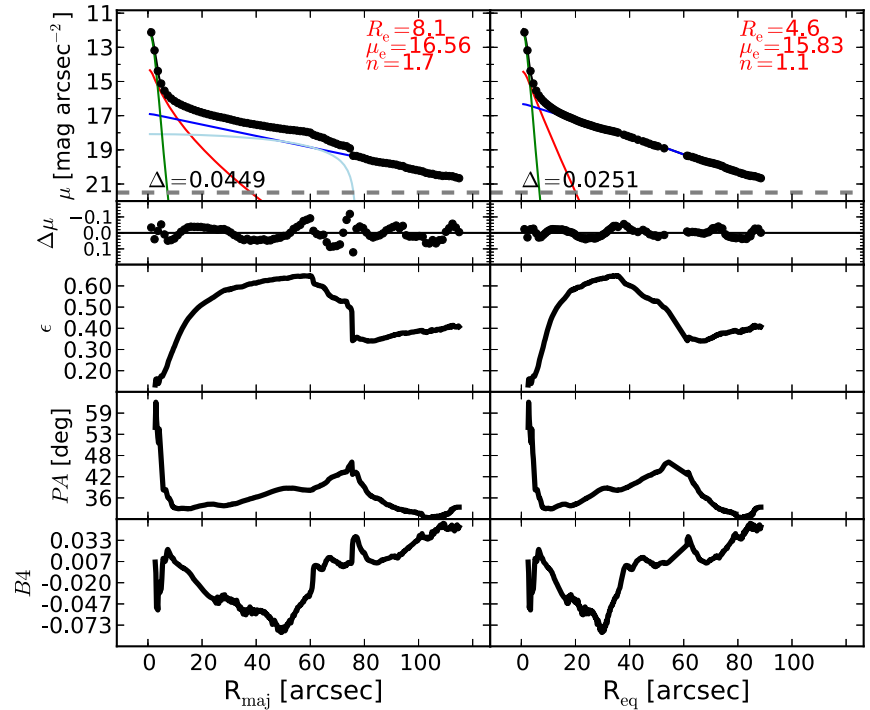


Figure 46. NGC 3227: a spiral galaxy with a large-scale bar. This galaxy hosts a Seyfert AGN (Khachikian & Weedman 1974) and circumnuclear dust (Martini et al. 2003). The large-scale bar produces an evident bump in the major-axis surface brightness profile, which is absent in the equivalent-axis profile. We model the bar with a Ferrer function and the nucleus with a Gaussian function. The Ferrer component is rejected by the equivalent-axis fit.

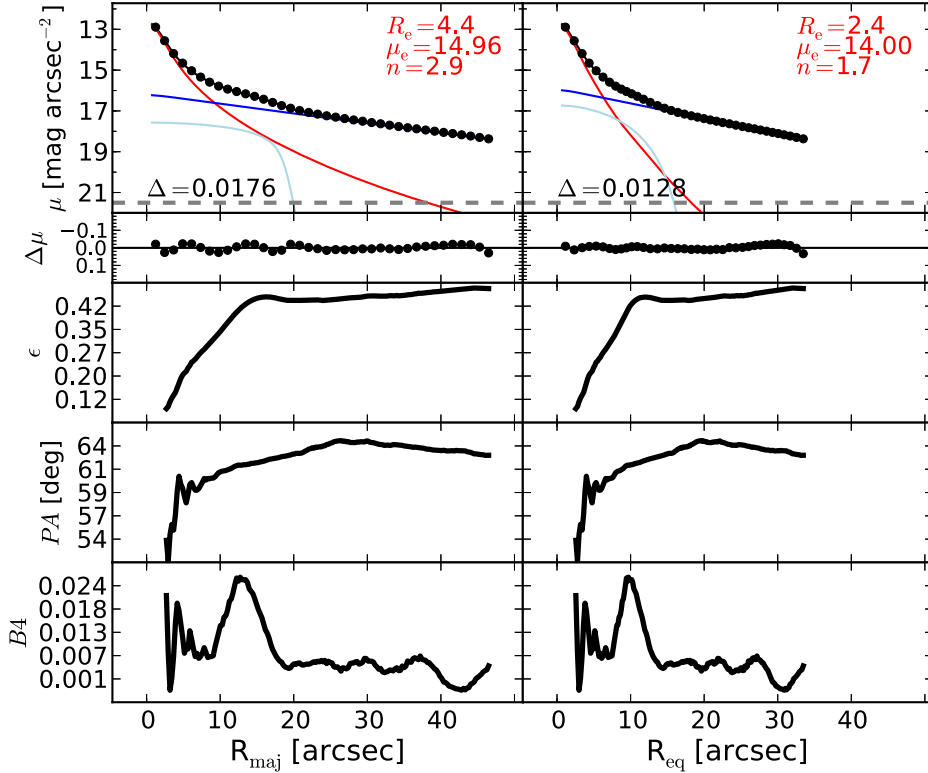


Figure 47. NGC 3245: a lenticular galaxy. The unsharp mask reveals the presence of an embedded disk ($R_{\text{maj}} \lesssim 15''$), confirmed by the corresponding peaks in the ellipticity and B_4 profiles. We model this inner component with a Ferrer function.

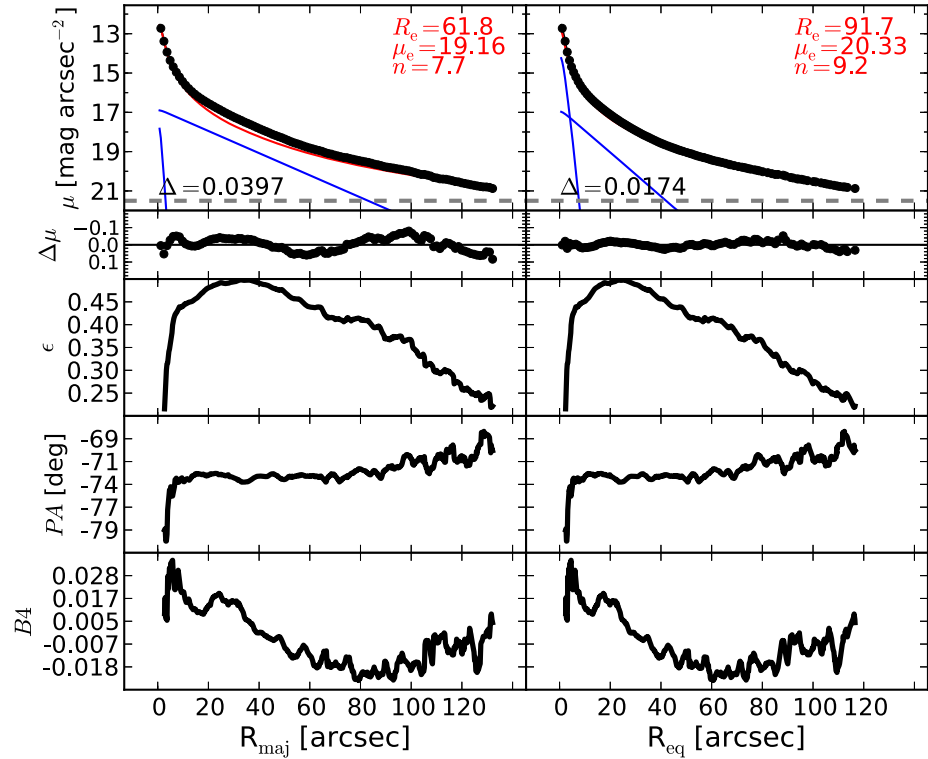


Figure 48. NGC 3377: an elliptical galaxy with an intermediate-scale disk and a nuclear stellar disk (Ledo et al. 2010). For this galaxy, Arnold et al. (2014) reported a strong decline in local specific angular momentum beyond $\sim 35''$, with a disk-to-bulge transition occurring at about $R_{\text{maj}} \sim 50''$. Arnold et al. (2014) attempted a three-component decomposition (accounting for a bulge, an embedded disk, and a central cusp), but unfortunately they fit the spheroidal component with a limited two-parameter $R^{1/4}$ function rather than a three-parameter $R^{1/n}$ Sérsic function. Here we use a surface brightness profile twice as extended as that used by Arnold et al. (2014), and we identify a nuclear disk and an intermediate-scale disk, both embedded in a larger spheroidal component. The presence of the intermediate-scale disk is also evident in the unsharp mask of the image mosaic and also from the ellipticity, which increases with increasing radius until $R_{\text{maj}} \sim 45''$ and then drops at larger radii. The nuclear stellar disk can be spotted from the peak at $R_{\text{maj}} \sim 5''$ in the B_4 profile. Each of the two disks is modeled with an exponential profile.

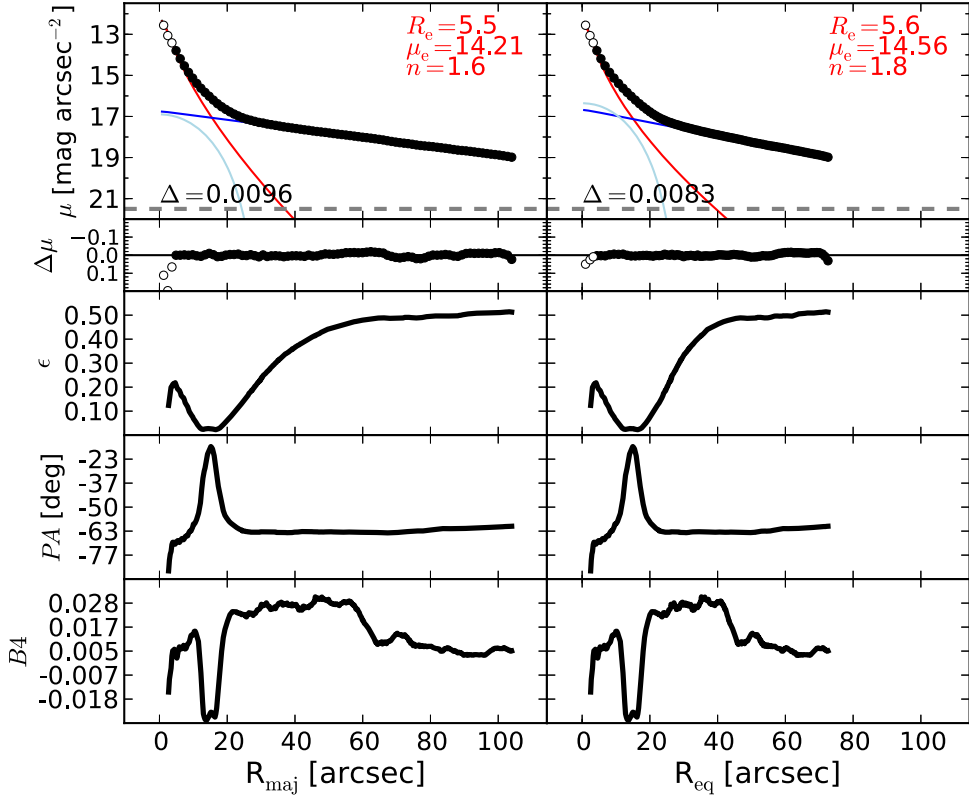


Figure 49. NGC 3384: a barred lenticular galaxy that hosts an embedded disk (with size $\lesssim 11''$; Erwin 2004) and a nuclear stellar disk (with size $\lesssim 0''.8$; Ledo et al. 2010). The isophotal parameters show clearly the presence of a boxy bar that extends out to $R_{\text{maj}} \lesssim 18''$. We model the bar with a Ferrer function. An embedded disk can be seen in the unsharp mask and produces the peak in the ellipticity profile at $R_{\text{maj}} \sim 4''$. However, any attempt to account for this component resulted in a degenerate model. We elect to fit neither the embedded disk nor the nuclear disk, by excluding from the fit the data within $R_{\text{maj}} < 3''7$.

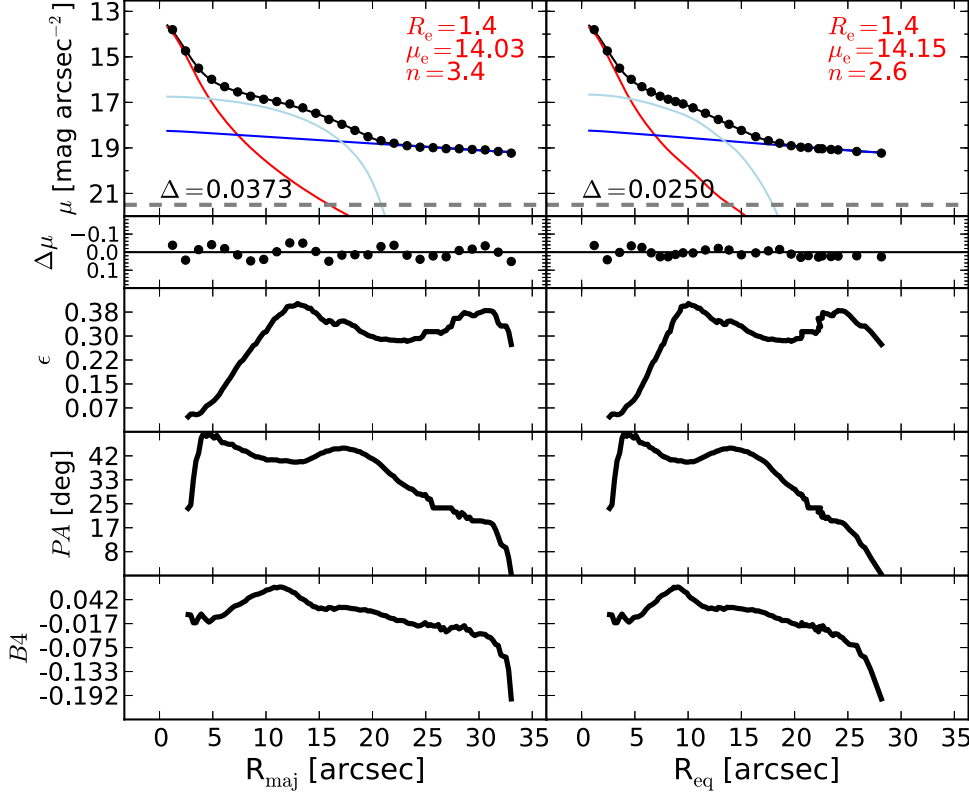


Figure 50. NGC 3393: an edge-on spiral galaxy hosting a Seyfert AGN (Diaz et al. 1988) and circumnuclear dust (Martini et al. 2003). The galaxy has a large-scale bar and a nuclear bar (with size $\lesssim 3''$, Erwin 2004). The large-scale bar ($R_{\text{maj}} \lesssim 20''$) is modeled with a Ferrer function. We do not model the nuclear bar and the AGN component because the poor spatial resolution of the data does not allow us to fit them.

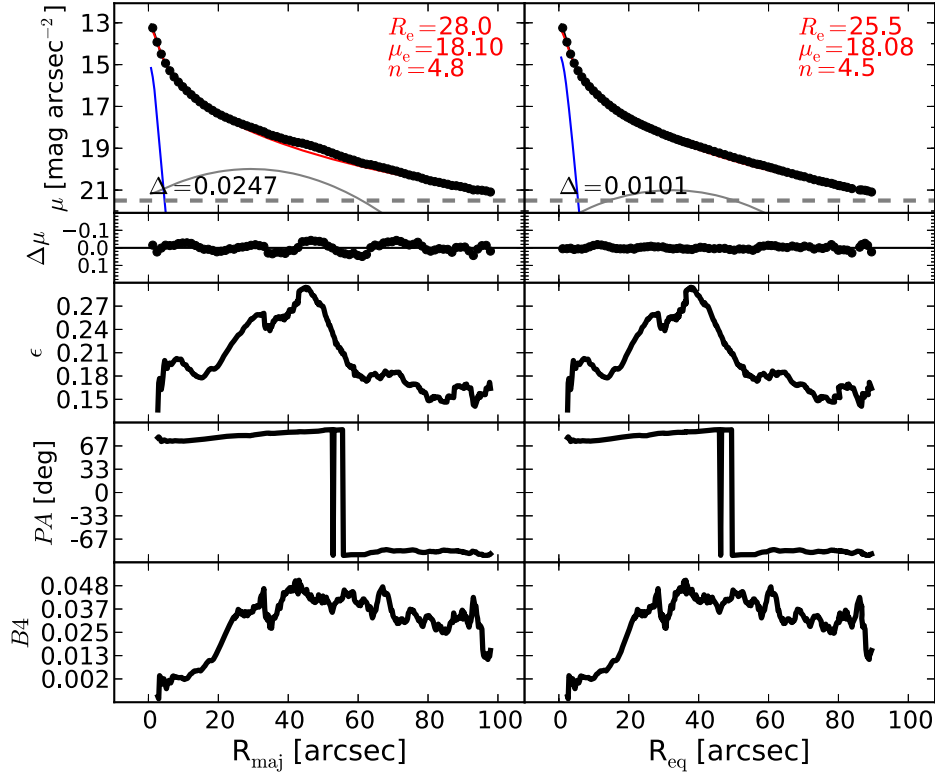


Figure 51. NGC 3414: a peculiar lenticular/elliptical galaxy. Different interpretations have been proposed about the morphology of this galaxy. Whitmore et al. (1990) suggested that NGC 3414 is a spheroidal galaxy with a large-scale edge-on polar ring, rather than a face-on barred lenticular galaxy. Laurikainen et al. (2010) decomposed NGC 3414 as a barred lenticular galaxy, but they cautioned against the uncertainty of their solution owing to the possible misinterpretation of the galaxy morphology. The unsharp mask clearly shows that an embedded component does not extend all the way through the center of the galaxy, but instead it is truncated at $R_{\text{maj}} \sim 20''$. However, an elongated structure in the galaxy center resembles a nuclear edge-on disk ($R_{\text{maj}} \lesssim 5''$). The velocity map (ATLAS^{3D}) shows rotation within $R_{\text{maj}} \lesssim 5''$, no rotation within $5'' \lesssim R_{\text{maj}} \lesssim 15''$, and counterrotation beyond $R_{\text{maj}} \gtrsim 15''$. The velocity pattern is consistent with the galaxy being a spheroidal system containing an edge-on polar ring and an edge-on nuclear disk.

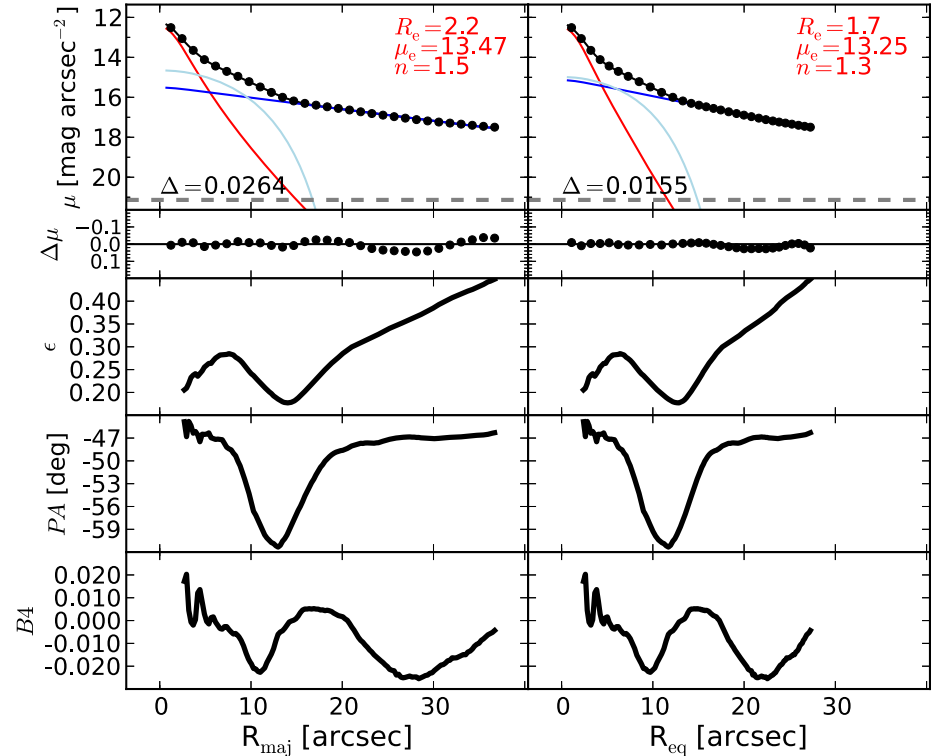


Figure 52. NGC 3489: a barred lenticular galaxy. Its disk has a smooth antitruncation at $R_{\text{maj}} \sim 85''$ (Erwin et al. 2008). The bar is fit with a Ferrer function.

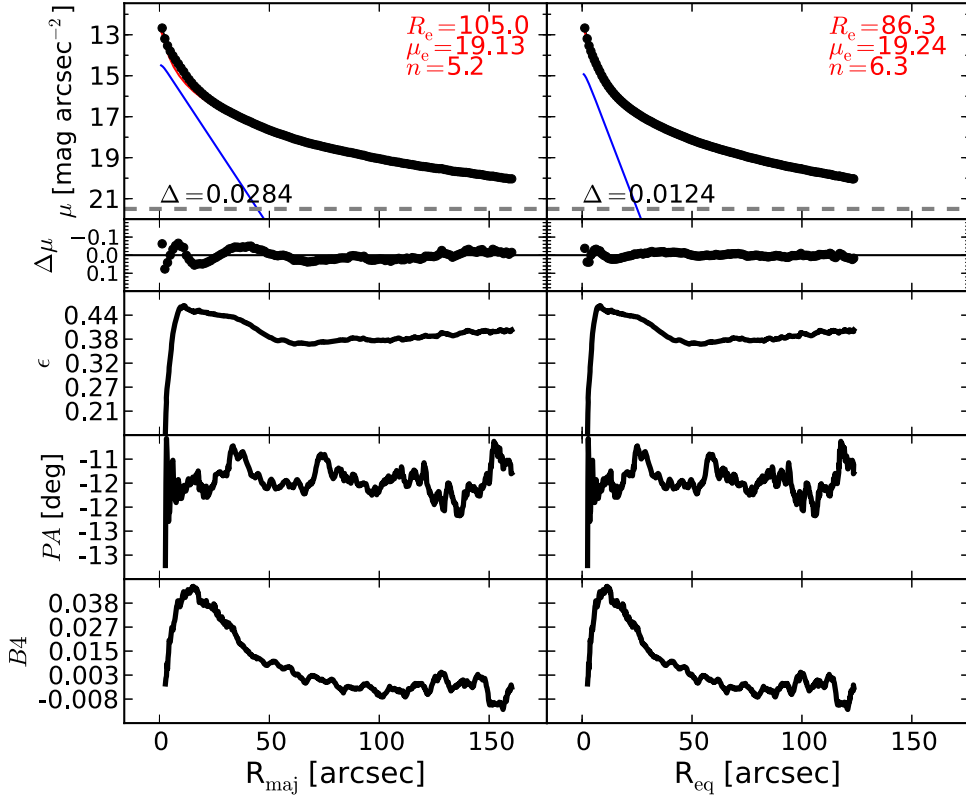


Figure 53. NGC 3585: an elliptical galaxy with an embedded disk (Scorza & Bender 1995). The embedded disk is visible in the unsharp mask and modeled with an exponential function.

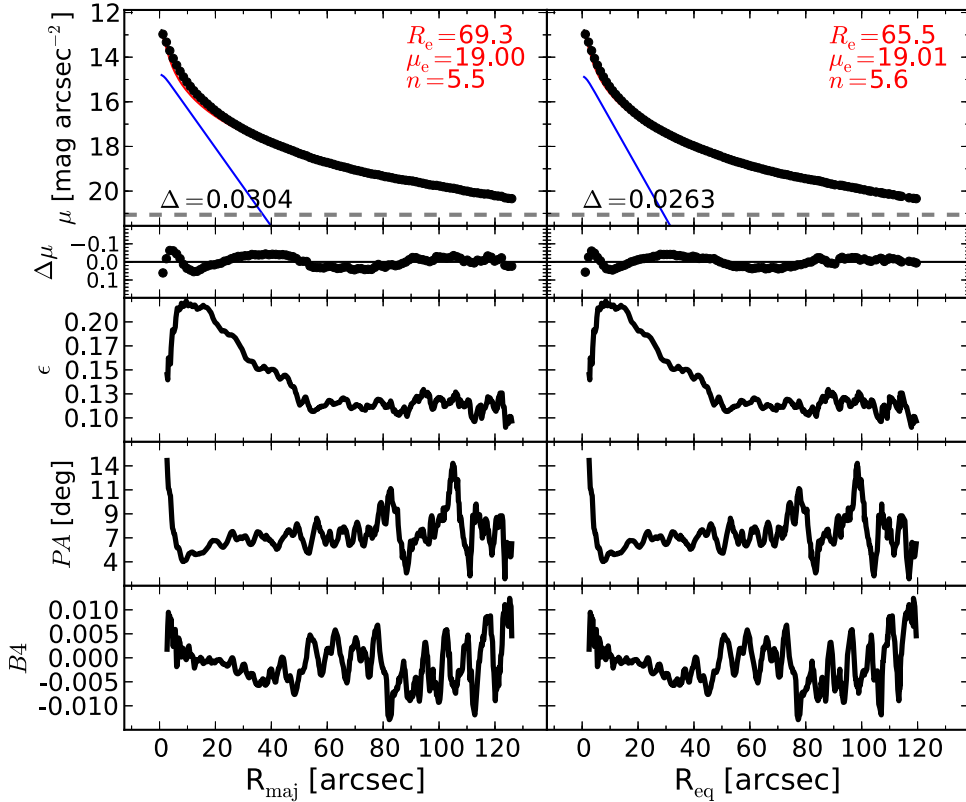


Figure 54. NGC 3607: an elliptical galaxy with an embedded disk. The velocity map (ATLAS^{3D}) shows rotation only within $R_{\text{maj}} \lesssim 20''$.

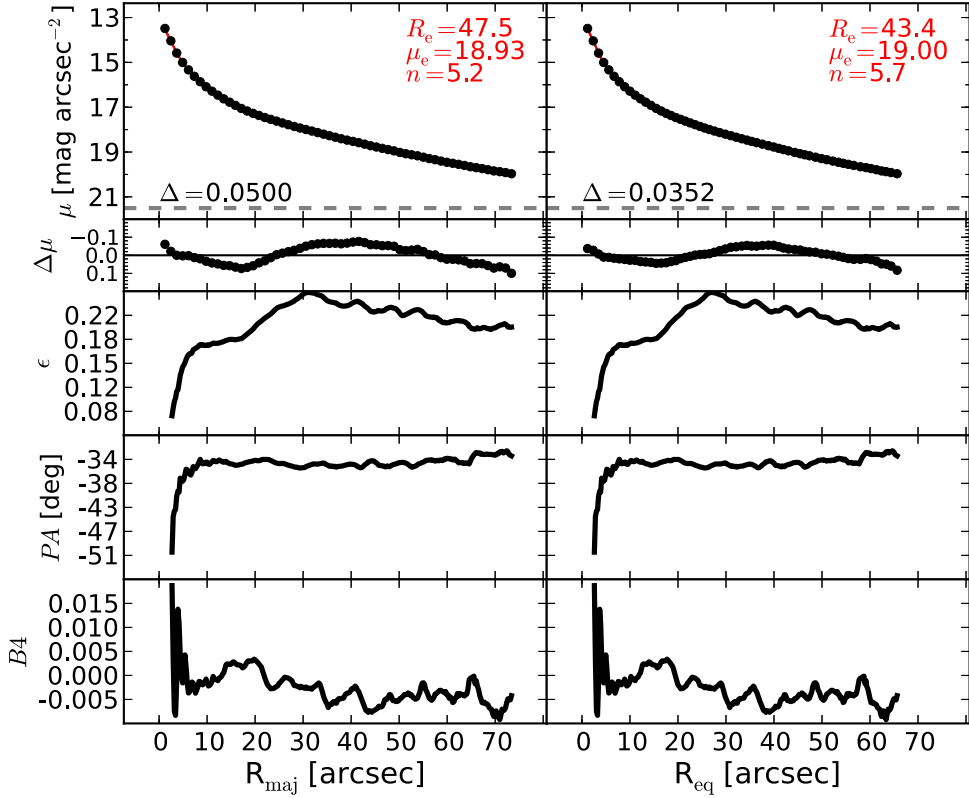


Figure 55. NGC 3608: an elliptical galaxy with an unresolved partially depleted core (Rusli et al. 2013a) and a kinematically decoupled core (ATLAS^{3D}, SLUGGS). We find that masking the nuclear region of this galaxy is unnecessary, and we fit the light profile with a single Sérsic model.

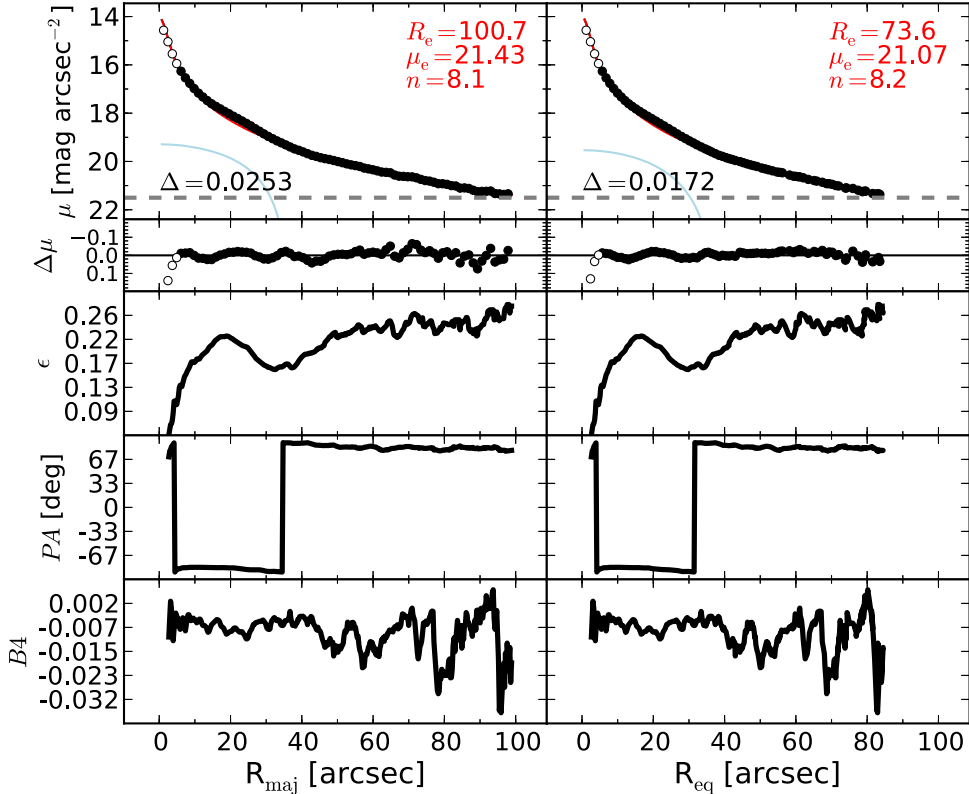


Figure 56. NGC 3842: the brightest member of the Leo Cluster (Abell 1367), an elliptical galaxy with an unresolved partially depleted core (Rusli et al. 2013a; Dullo & Graham 2014). The light profile presents a swelling at $R_{\text{maj}} \sim 20''$, and the ellipticity profile has a peak in the same position. One can also glimpse a faint elongated oval in the unsharp mask. The innermost $6.''1$ are excluded from the fit. A single Sérsic model is not sufficient to provide a good description of the galaxy light profile; therefore, we add a second component (Ferrer function) to account for the embedded lens.